

Department of Physics  
Indian Institute of Technology Guwahati  
Ph.D. Thesis



# **Equilibrium, Non-equilibrium and Topological Phases of Strongly Correlated Bosons**

**Suman Mondal**

Thesis Supervisor: Dr. Tapan Mishra  
September, 2020



# **Equilibrium, Non-equilibrium and Topological Phases of Strongly Correlated Bosons**

A  
Thesis Submitted  
in Fulfillment of the Requirements  
for the Degree of  
PHD  
By

**SUMAN MONDAL**  
Under the Supervision of **Dr. TAPAN MISHRA**



**Department of Physics**  
**Indian Institute of Technology Guwahati**  
**September, 2020**

©Suman Mondal

# **Declaration**

This is to certify that the thesis entitled "**Equilibrium, Non-equilibrium and Topological Phases of Strongly Correlated Bosons**", submitted by me to the *Indian Institute of Technology Guwahati*, for the award of the degree of PhD, is a bonafide work carried out by me under the supervision of Dr. Tapan Mishra. The content of this thesis, in full or in parts, have not been submitted to any other University or Institute for the award of any degree or diploma. I also wish to state that to the best of my knowledge and understanding nothing in this report amounts to plagiarism.

Signed:

---

**Suman Mondal**  
Department of Physics,  
Indian Institute of Technology Guwahati,  
Guwahati-781039, Assam, India.

Date:

---



# **Disclaimer**

The bibliography included in this thesis is, by no means complete but contains the ones which are consulted thoroughly by me. I apologize for inadvertently missing out some of the research papers, review articles and other scientific documents pertaining to the focus of this thesis which should also have been cited. For illustration purpose some of the figures in this thesis are taken from other sources and properly cited.



# Certificate

This is to certify that the thesis entitled "**Equilibrium, Non-equilibrium and Topological Phases of Strongly Correlated Bosons**", submitted by Suman Mondal (166121004), a research scholar in the *Department of Physics, Indian Institute of Technology Guwahati*, for the award of the degree of PhD, is a record of an original research work carried out by him under my supervision and guidance. The thesis has fulfilled all requirements as per the regulations of the institute and in my opinion has reached the standard needed for submission. The results embodied in this thesis have not been submitted to any other University or Institute for the award of any degree or diploma.

Signed:

---

**Supervisor: Dr. Tapan Mishra**  
**Department of Physics,**  
**Indian Institute of Technology Guwahati,**  
**Guwahati-781039, Assam, India.**

Date:

---



*To my parents...*



# Acknowledgement

It would have been impossible to write this thesis without the direct and indirect support and the help of the people around me throughout the journey. The list is endless, it is only possible to mention some of them.

I would like to express my sincere gratitude to my supervisor, Dr. Tapan Mishra, for his continuous guidance, support, enthusiasm and giving me freedom and motivation. I also thank him for introducing me to the collaborators and exciting new problems which helped me to learn and gain experience in the field of my research. His dedication, hard work and immense knowledge always inspire me to learn new things.

I wish to show my appreciation to Dr. Sebastian Greschner, one of our collaborators, for his immense and valuable input in my work. I wish to extend my special thanks to Prof. Luis Santos, Prof. B. K. Sahoo, Dr. Manpreet Singh and Dr. Augustine Kshetrimayum for collaborating in my projects and making them more effective and rich.

I would also like to show my deep appreciation to my doctoral committee members, Prof. Saurabh Basu, Dr. Kanhaiya Pandey and Dr. Manabendra Sarma, for the useful suggestions and yearly evaluations of my research work. I acknowledge the academic help of HODs, Prof. Poulose Poulose and Prof. Subhradip Ghosh. I thank technical assistants, academic and non-academic staff of our department for various helps in my research period. I am also thankful to Param Ishan, IIT Guwahati for the supercomputer facility.

I gratefully acknowledge the support from our group members, Sayan Lahiri, Mrinal Kanti Giri and Ashirbad Padhan. I had wonderful learning sessions with them.

I am grateful for having beautiful friendships with Lopamudra, Kajal, Dibyendu, Sayandeep and Abhisek. Also, I feel lucky to meet the most joyful persons, Sayan Da, Sovan Da, Charu sir and Kumar Sir. I have many precious memories with them. I thank all my batch mates Mousumi, Abhilasha, Apurba, Dangka, Nilamoni, Ritu-

---

pan, Priyanka, Mahananda, Abdelsalam and Ogaro for their friendship throughout the years. I also thank my school close friends, Smita, Debasish and Suman for supporting me in every possible way.

Last but not least, I want to thank my family specially my parents, Samar Mondal and Mina Mondal for their love, support, sacrifices and patience.

September, 2020

Suman Mondal

# Abstract

In this thesis, we study the equilibrium, non-equilibrium and topological properties of interacting bosons in periodic potentials. In this context, we systematically address the physics of interacting bosons in various scenarios using numerical methods such as the cluster mean-field theory approach, exact diagonalization and density matrix renormalization group method.

We first explore the possible quantum phase transitions in a multi-body interacting Bose-Hubbard model in two dimensions. By keeping up to four-body onsite interactions we predict the existence of two-body repulsive bound bosonic pairs in the presence of attractive three-body and repulsive four-body interactions. We also explore the physics of two- and three-body hardcore constrained dipolar bosons in the non-locally coupled one-dimensional lattices and obtain the physics arising from the competing long-range interaction as well as local constraints.

We further explore the dynamical properties of interacting bosons in the context of the quantum walk. In our studies, we analyze the quantum walk of Mott insulator defects (particle and/or hole) in a one-dimensional lattice in the presence of onsite two and three-body interactions. Our analysis predicts an interesting phenomenon of quantum walk reversal of a pair of repulsive bosons as a function of attractive three-body interaction. We extend our analysis for two nearest-neighbor defects in the presence of nearest-neighbor interaction and show the property of antibunching in two-particle correlation function in vanishing interaction limit whereas for large interaction they form nearest-neighbor pair.

The last part of the thesis focuses on the topological phase transitions of interacting bosons in the Su-Schrieffer-Heeger (SSH) model which is one of the simplest one-dimensional models exhibiting the topological phase transitions. In this context, we first explore the bulk properties of the three-body constrained bosons in an SSH model predicting the groundstate phase diagram in the limit of repulsive and attractive two-body interactions using the DMRG method. The phase diagram is shown to exhibit various gapped dimer phases at densities  $1/2$ ,  $1$  and  $3/2$ . In-

---

terestingly on the attractive side, we find a phase transition to a dimer phase of bound bosonic pairs at unit filling. After analyzing the bulk properties of three-body constrained bosons, we study the topological phase transition of these bound bosonic pairs at unit filling. In our analysis, we show that these bound bosonic pairs undergo a trivial to topological phase transitions exhibiting non-trivial edge states. We concretely establish this fact by exploring various topological properties such as edge polarization, winding number and Thouless charge pumping. In the end, we predict the phenomenon of topological inheritance in the case of a half-SSH-Hubbard model. This system represents a model of two components hardcore bosons where one of the components experiences a dimerized hopping similar to the SSH model and the other component resides in a homogeneous lattice. The Hubbard interaction is inter-species interaction. We show that by tuning the inter-species interaction it is possible to induce the topological properties of one component on the other which originally does not possess any topological order. We show that the threshold for full inheritance occurs at weak interactions, for which the components are not yet paired. We illustrate this inheritance by discussing both bulk and edge properties, as well as dynamical observables such as mean chiral displacement and charge pumping.

# List of Publications

## Publications included in the thesis

1. Manpreet Singh, **Suman Mondal**, B. K. Sahoo and Tapan Mishra, *Quantum phases of constrained dipolar bosons in coupled one-dimensional optical lattices*, Phys. Rev. A **96**, 053604(2017).
2. **Suman Mondal**, Sebastian Greschner and Tapan Mishra, *Three-body constrained bosons in double-well optical lattice*, Phys. Rev. A **100**, 013627(2019).
3. Sebastian Greschner, **Suman Mondal** and Tapan Mishra, *Topological charge pumping of bound bosonic pairs*, Phys. Rev. A **101**, 053630(2020).
4. **Suman Mondal** and Tapan Mishra, *Quantum walks of interacting Mott insulator defects with three-body interactions*, Phys. Rev. A **101**, 052341(2020).
5. **Suman Mondal**, Augustine Kshetrimayum and Tapan Mishra, *Two-body repulsive bound pairs in a multibody interacting Bose-Hubbard model*, Phys. Rev. A **102**, 023312(2020).
6. **Suman Mondal**, Sebastian Greschner, Luis Santos and Tapan Mishra, *Topological inheritance in half-SSH Hubbard models*, arXiv, 2008.07224(2020).

## Publications outside thesis

7. Sayan Lahiri, **Suman Mondal**, Manpreet Singh and Tapan Mishra, *Mott insulator phases of nonlocally coupled bosons in bilayer optical superlattices*, Phys. Rev. A **101**, 063624(2020).

8. Sayan Lahiri, **Suman Mondal**, Kanhaiya Pandey and Tapan Mishra, *Emergent photon pair propagation in circuit QED with superconducting processors*, arXiv, 2002.12405(2020).
9. Mrinal Kanti Giri, **Suman Mondal**, and Tapan Mishra, *Quantum walk of two interacting bosons with mass imbalance*, arXiv, 2008.11142(2020).

## **Schools/Workshops/Conferences attended**

1. Attended *SERB School on Frontiers in Quantum Optics*, December 2017, Department of Physics, IIT Guwahati, India.
2. Attended *Recent Trends in Cold and Ultracold Matter*, March 2018, Department of Physics, IIT Guwahati, India.
3. Presented poster at, *2nd Annual conference on quantum condensed matter*, July 2019, Department of Physics, IISc Bangalore, India.
4. Presented poster at, *Novel Phases of Quantum Matter*, December 2019, ICTS Bangalore, India.

# Contents

<b>List of publications</b>	<b>xiii</b>
<b>1 Introduction</b>	<b>1</b>
1.1 Quantum phase transitions . . . . .	1
1.2 QPT in optical lattices . . . . .	3
1.2.1 Optical lattice . . . . .	3
1.2.2 Ultracold bosons in optical lattice: The Bose-Hubbard model .	5
1.2.3 Superfluid to Mott-insulator transition . . . . .	9
1.2.4 QPT in multi-body interacting BH model . . . . .	11
1.2.5 Long-range interaction in optical lattices . . . . .	12
1.3 Quantum walk . . . . .	13
1.3.1 Discrete-time quantum walk (DTQW) . . . . .	14
1.3.2 Continuous-time quantum walk (CTQW) . . . . .	16
1.4 Topological phase transitions . . . . .	18
1.4.1 The Su-Schrieffer-Heeger (SSH) model . . . . .	18
1.4.2 Edge States . . . . .	21
1.5 Numerical methods . . . . .	23
1.5.1 Exact Diagonalization (ED) . . . . .	23
1.5.2 Cluster Mean-field Theory (CMFT) approach . . . . .	24
1.5.3 Matrix product states (MPS) . . . . .	27
1.5.4 Density Matrix Renormalization Group (DMRG) . . . . .	30
1.5.5 Time dependent simulation . . . . .	32
1.6 Chapterwise outline of the thesis . . . . .	34
<b>2 Quantum phases of multi-body interacting bosons in optical lattices</b>	<b>37</b>
2.1 Introduction . . . . .	37
2.2 Multi-body interacting bosons in two-dimensional optical lattice . .	38

---

## CONTENTS

2.2.1	Results . . . . .	40
2.2.2	Effect of density induced tunneling . . . . .	45
2.3	Conclusions . . . . .	47
<b>3</b>	<b>Quantum phases of constrained dipolar bosons in a two-leg ladder</b>	<b>49</b>
3.1	Introduction . . . . .	49
3.2	Results . . . . .	52
3.2.1	TCBs with vanishing on-site interaction . . . . .	54
3.2.2	TCBs with finite on-site interaction . . . . .	56
3.2.3	Effect of an external harmonic confinement . . . . .	62
3.3	Conclusions . . . . .	64
<b>4</b>	<b>Quantum walk of interacting Mott-insulator defects</b>	<b>65</b>
4.1	Introduction . . . . .	65
4.2	QW of a single defect . . . . .	66
4.3	QW of two particle defects . . . . .	68
4.3.1	Density evolution . . . . .	69
4.3.2	Bloch oscillation . . . . .	70
4.3.3	Two particle correlations . . . . .	72
4.3.4	Two-particle QW with three-body repulsion . . . . .	73
4.4	Quantum walk of two particle defects with nearest neighbor interaction	74
4.4.1	Density evolution . . . . .	75
4.4.2	Two particle correlations . . . . .	75
4.5	Experimental feasibility . . . . .	76
4.6	Conclusions . . . . .	77
<b>5</b>	<b>Interacting bosons in optical double wells</b>	<b>79</b>
5.1	Introduction . . . . .	79
5.2	Results . . . . .	80
5.2.1	Hardcore limit ( $U = \infty$ ) . . . . .	81
5.2.2	Isolated Double Wells . . . . .	82
5.2.3	Vanishing two-body interaction ( $U = 0$ ) . . . . .	83
5.2.4	Finite U and $t_2 = 0.2$ case . . . . .	84
5.2.5	Finite U and $t_2 = 0.6$ case . . . . .	93
5.2.6	Parity order . . . . .	94
5.3	Conclusions . . . . .	96

<b>6 Topological properties of bound bosonic pairs in the SSH model</b>	<b>99</b>
6.1 Introduction . . . . .	99
6.2 Results . . . . .	100
6.2.1 Bulk properties . . . . .	101
6.2.2 Phase diagram . . . . .	101
6.2.3 Topological properties . . . . .	105
6.2.3.1 Edge states . . . . .	106
6.2.3.2 Winding number . . . . .	108
6.2.3.3 Thouless charge pumping of bound pairs . . . . .	109
6.2.4 Experimental realization . . . . .	113
6.3 Conclusions . . . . .	115
<b>7 Topological inheritance in multi-component bosons</b>	<b>117</b>
7.1 Introduction . . . . .	117
7.2 Half-SSH Hubbard (HSSHH) model . . . . .	118
7.3 Induced bulk properties . . . . .	119
7.4 Induced topollogical properties . . . . .	121
7.4.1 Edge states . . . . .	122
7.4.2 Mean chiral displacement . . . . .	123
7.4.3 Thouless charge pumping . . . . .	125
7.4.4 Inheritance threshold . . . . .	127
7.5 Experimental feasibility . . . . .	128
7.6 Conclusions . . . . .	129
<b>8 Conclusions and Future Directions</b>	<b>131</b>
8.1 Future Directions . . . . .	133
<b>Bibliography</b>	<b>137</b>



# List of Figures

1.1	The schematic diagram for multi-dimensional optical lattice potential formed by the superimposition of counter propagating lasers. (a) The array of potential tubes formed by two standing waves orthogonal to each other. (b) A three dimensional lattice potential created by superimposing three orthogonal standing waves. The figure is taken from Ref. [15]. . . . .	4
1.2	(a) Shows the role of interaction and hopping in the BH model. Particle tunnel with tunneling amplitude $t$ and the energy offset $U$ results from two particle occupations. (b) A sketch of the energy levels of an isolated site. . . . .	7
1.3	Particle distribution for (a) SF and (b) MI phase with $\rho = 1$ . Figure (a) shows one of the many states whose superposition represent the SF phase. . . . .	9
1.4	The mean-field phase diagram of the BH model (1.14) in $\mu/U - zt/U$ plane. Here MI $n$ is the MI with density $n$ . . . . .	10
1.5	Experimental result of the first observation of SF-MI transition(taken from [19]). The figure shows the absorption images of matter-wave interference pattern for different initial states prepared for different lattice depth( $V_0$ ). Here $V_0$ are, in (a) $0E_r$ , (b) $3E_r$ , (c) $7E_r$ , (d) $10E_r$ , (e) $13E_r$ , (f) $14E_r$ , (g) $16E_r$ and (h) $20E_r$ . . . . .	11
1.6	The figure shows polarized dipoles where the arrows represent the dipole moment. (a) Depicts the two polarized dipoles separated by a distance $r$ and they make angle $\theta$ with the connecting line. The configurations (b) and (c) show repulsive and attractive dipoles. . . . .	13
1.7	The figure compares the probability distributions of CRW and DTQW after 100 time steps. The figure also depicts the dependence of the QW on the initial states. The figure is taken from Ref. [107]. . . . .	15

## LIST OF FIGURES

---

1.8	The figure shows the evolution of (a) density ( $n_i$ ) and (b) entanglement entropy ( $S_i$ ) for CTQW of a boson on a one dimensional graph.	17
1.9	The figure shows a one dimensional lattice with staggered hopping ( $t_1$ and $t_{22}$ ) along the chain. $A_i$ and $B_i$ are the sublattices of $i$ -th unit-cell.	19
1.10	Figure (a-c) shows the band structure and (d) shows how to visualize the winding number. In both the calculations, the dashed line, the dot-dashed and solid line represent the parameters $(t_1, t_2) = (1.0, 0.2)$ , $(0.6, 0.6)$ and $(0.2, 1.0)$ respectively. From (d) we can see that, when $t_1 > t_2$ the circle does not wind around the origin( $O$ ), when $t_1 = t_2$ the circle touches the $O$ which closes the gap evident from the figure (b) and when $t_1 < t_2$ the circle winds the $O$ .	20
1.11	(a) Shows the single-particle energy spectrum of the model (1.34) for a system of length $L = 20$ where $t_2 = 1$ . (b-c) Show the wavefunctions for the parameters marked by the green plus signs in (a). This shows the appearance of the edge state for $t_1/t_2 < 1$ and the gap-closing at the topological transition point $t_1 = t_2$ .	21
1.12	A two-dimensional square lattice is partitioned with the $2 \times 2$ clusters. The dotted box represents a unit cluster by the repetition of which the entire lattice is made. In the CMFT approach, the solid lines are treated exactly and the dashed lines connecting clusters are treated in a mean-field way.	25
1.13	Figure portrays the graphical representation of a general state and matrix product state as defined in Eqs. 1.53 and 1.59 respectively for a system of length $L = 8$ . The top row of the figure shows the elements of the product state.	28
1.14	The graphical representation of the left canonical MPS formation using SVD process for a system of length $L = 8$ .	29
1.15	The graphical representation of a mixed canonical MPS for a system of length $L = 8$ following Eq. 1.61.	29
1.16	The graphical representation of the algorithm for finding the ground state in the DMRG process is shown for a system of length $L = 8$ with open boundary conditions. (a-d) Show the creation of an arbitrary MPS using an infinite DMRG process. (e-l) Show one complete sweep of finite size algorithm of variational search. If we repeat (e-l) several times, the initial state (d) converges to the ground state of the Hamiltonian.	30

---

1.17	The graphical representation of the TEBD algorithm is shown. Here the Suzuki-Trotter decomposed (first-order) evolution operator operates on the initial MPS for a system of $L = 8$ . Here the initial state is evolved by $2\delta t$ time. . . . .	34
2.1	CMFT phase diagram for $t = 1$ , $U_3/U_2 = -2.0$ and $U_4/U_3 = -3.0$ . Solid lines show the boundaries of MI phases and dashed line separates the empty state. Inset shows the PSF-SF boundary marked by green line with circles. . . . .	41
2.2	(a) $\rho$ vs. $\mu/U_2$ and (b) $\rho_s$ vs. $\mu/U_2$ plots for several cuts through the phase diagram of Fig.2.1 corresponding to 0.02(green solid line), 0.04(red dashed) and $1/U_2 = 0.06$ (black dot-dashed). . . . .	42
2.3	Correlation functions $\Gamma_n(i, j)$ for a cut along $1/U_2 = 0.02$ in the phase diagram Fig.2.1. The corresponding values of $\rho$ (blue down triangles) are shown for comparison. . . . .	43
2.4	(a) iPEPS data for $\rho$ , $O_{SF}$ and $O_{PSF}$ for $1/U_2 = 0.015$ showing the MI1, MI3 and the PSF phases. (b) Similar calculations for a cut passing through the normal Superfluid (SF) region at $1/U_2 = 0.04$ . This phase is characterized by a non-vanishing value of both $O_{SF}$ as well as $O_{PSF}$ while the PSF phase is characterized by a vanishing $O_{SF}$ and non-zero $O_{PSF}$ . . . . .	44
2.5	The figure shows the existence of the PSF phase in the presence of density-induced tunneling( $P$ ). Here we plot particle density( $\rho$ ) in (a) and pair correlation function( $\Gamma_2$ ) in (b) for $P = 0.1$ (black lines with circles) and 0.2(blue lines with triangles). The other parameters are same as considered in Fig 2.1 at $U_2 = 1/0.015$ . . . . .	45
2.6	Figure shows the existence of PSF phase for different values of density dependent hopping amplitude $P$ . Here we plot $\rho$ (solid lines), $O_{SF}$ (dashed lines) and $O_{PSF}$ (dot-dashed lines) for $P = 0.1$ and 0.2, which indicate that the PSF survives for finite values of $P$ . . . . .	46
3.1	Two one dimensional optical lattices are coupled by a non-local interaction which is equivalent to a two leg ladder model. Leg-a and leg-b contain two- and three-body constrained bosons, respectively. The particles on both the chain interact among themselves with the non-local dipole-dipole interaction $V$ . The Hamiltonian for this system is given in Eq.3.1. . . . .	51

## LIST OF FIGURES

---

3.2 Phase diagram for TCBs in both the chains for $ V /U = 0.75$ in the $t/U - \mu/U$ plane as considered in Ref. [184]. Red squares, green triangles, the black solid curve and blue diamonds represent the phase boundaries obtained using 4-, 6-, 8- and 10-sites cluster respectively. Scaled critical point for MI-SF transition $(t/U)_c (= 0.1395)$ is shown by a solid black circle. . . . .	52
3.3 Scaling of the MI-SF transition critical point $(t/U)_c$ with respect to the different cluster sizes at $ V /U = 0.75$ . Green solid circles represent the $(t/U)_c$ values for respective cluster sizes, red dashed lines represents the scaling and the black solid circle on Y-axis denotes the value of $(t/U)_c$ scaled to thermodynamic limit ( $= 0.1395$ ). . . . .	53
3.4 Phase diagram for model given in Eq.3.1 in $\mu/ V $ vs. $t/ V $ plane, with leg-a (leg-b) containing HCB (TCB with $U = 0$ ) with varying $t/ V $ . . . . .	54
3.5 (a) $\rho$ vs. $\mu$ (b)Dimer and trimer correlations and (c)Renyi entropy corresponding to a vertical cut along $U/ V  = 0.0$ in Fig.3.8. Inset shows the zoomed in region in which REE is finite at first (HCBMI+ASF) and then gradually drops to 0 as the system approaches saturation. . . . .	55
3.6 Phase diagram for model given in Eq.3.1 in $\mu/U$ vs. $t/U$ plane, with leg-a (leg-b) containing HCB (TCB with finite two-body interaction). . . . .	57
3.7 $\rho$ vs. $\mu$ plot corresponding to the cut shown by dashed line across the phase diagram shown in Fig.3.6. . . . .	58
3.8 Phase diagram for model given in Eq.3.1 in $\mu/U$ vs. $t/U$ plane, with leg-a (leg-b) containing HCB (TCB with finite two-body interaction) at $V = -10.0$ . . . . .	59
3.9 (a) $\rho$ vs. $\mu$ (b)Dimer and trimer correlations and (c)Renyi entropy corresponding to a vertical cut along $U/ V  = 1.0$ in Fig.3.8. Inset shows the zoomed in region where there is a phase transition from MI to HCBMI+SF phase and a change in slope of REE is visible. . . . .	60
3.10 Phase diagram for model given in Eq.3.1 in $\mu/ V $ vs. $U/ V $ plane, with leg-a and leg-b containing HC and three-body constrained bosons for $t/ V  = 0.03$ . . . . .	61
3.11 HCB and TCB confined in harmonic trap with $V_{tr} = 0.002$ at $U = 0.0$ , $t/ V  = 0.225$ and $\mu/ V  = -0.6$ , corresponding to Fig.3.4. . . . .	62

---

3.12 HCBs and TCBs confined in harmonic trap with $V_{tr} = 0.002$ at $ V /U = 0.75$ , $t/U = 0.1$ and $\mu/U = 0.0$ , corresponding to the cut shown in Fig.3.6. . . . .	63
4.1 The figure shows the QWs of single-particle or hole defect in MI of different filling. (a) Density evolution of a single particle on the empty lattice. (b-e) Density evolutions corresponding to the initial states $ \Psi(0)\rangle_1$ , $ \Psi(0)\rangle_2$ , $ \Psi(0)\rangle_3$ and $ \Psi(0)\rangle_4$ respectively. Here, the dashed lines indicate the boundary of the propagation. . . . .	67
4.2 Figure shows the initial state which is two particles on top of a bosonic Mott insulator in one dimension at unit filling i.e. $(a_0^\dagger)^2  \text{MI1}\rangle$ . Here, $J$ denotes the hopping strength. . . . .	69
4.3 Figure shows the phenomenon of QW reversal of the pair of defects shown in terms of the density evolution on a homogeneous(a-g) and tilted(h-n) lattice. In the case of tilted lattice the period doubling in the Bloch oscillation clearly indicates the QW of bound defect pair. . . . .	70
4.4 Figure shows the normalized two particle correlation functions $\Gamma_{ij}$ plotted with respect to the positions $i$ and $j$ after a time evolution of $t = 11.25$ (in units of $1/J$ ) for $J = 0.2$ , $U = 10$ . Results of different values of $W/U = -0.5, -0.8, -0.9, -1.0, -1.1, -1.2, -1.5$ on a homogeneous one dimensional lattice of length $L = 29$ are shown in (a) to (g). Corresponding real space density distribution is shown on top of each correlation plot. . . . .	72
4.5 Figure shows the density evolutions for the QWs of two particle defects on the MI1 state for different repulsive three-body interactions ( $W$ ). . . . .	73
4.6 Density evolutions in the QWs for different values of $V$ . Here (a-f) correspond to $V = 0, 2, 4, 6, 8$ and $10$ respectively. . . . .	74
4.7 Two particle normalized correlation functions are shown for nearest-neighbor defects at time $t = 2.0$ (in units of $1/J$ ) for different values of $V$ . On top of each panel, the corresponding normalized density distribution is shown. Here the densities and correlation functions are calculated in the reduced basis to eliminate the contribution from the MI1 background. . . . .	75
5.1 One dimensional double well optical superlattice with staggered hoppings $t_1 > t_2$ . . . . .	79

## LIST OF FIGURES

---

5.2	Phase diagram of hardcore bosons in the $\mu$ - $t_2$ plane with $t_1 = 1.0$ . The points correspond to extrapolated DMRG data with $L = 300$ , which accurately lie on top of the analytical curves (solid lines). The region included by the blue circles is the gapped BO phase at half filling. The gap opens up for any finite dimerization $t_2/t_1$ . The black curves represent the empty and full states. . . . .	81
5.3	Phase diagram of isolated doublewells showing three gapped phases at $\rho = 0.5, 1$ and $1.5$ . . . . .	83
5.4	Figure shows the behaviour of $\rho$ with respect to $\mu$ for $U = 0$ (left red curve) and $U = 5$ (right blue curve) for $t_2 = 0.2$ . Plateaus indicate the gapped phases. . . . .	84
5.5	The phase diagram for three-body constrained bosons as a function of $t_2$ for $U = 0$ obtained from polynomial extrapolation of gap. The BO phase at $\rho = 1$ and $\rho = 1.5$ appear at $t_2 \sim 0.4$ and $t_2 \sim 0.9$ respectively. . . . .	85
5.6	Phase diagrams for $t_2 = 0.2$ . The region bounded by the green curves are the gapped phases at $\rho = 1$ (middle) which consists of the MI(PBO) phases in the strong repulsive(attractive) regimes. The regions bounded by the blue dashed curves are the gapped BO phases at $\rho = 0.5$ (upper) and $\rho = 1.5$ (lower). On the attractive side the PSF is separated from the SF phase by the red circles. (Inset) Shows the phase diagram in the limit of isolated double-wells for comparison. . .	86
5.7	Bond operator $B_{i,n}$ are shown for the BO(blue circles) and PBO(red squares) phases for $\rho = 1$ and $t_2 = 0.2$ . (a) $B_{i,n}$ for $U = -4$ . (b) $B_{i,n}$ for $U = 0$ . (c) $B_{i,n}$ for $U = 8$ . . . . .	87
5.8	Bond operator $B_{i,n}$ are shown for the BO(blue circles) and PBO(red squares) phases for $t_2 = 0.2$ . (a) $B_{i,n}$ for $U = 4$ and $\rho = 0.5$ . (b) $B_{i,n}$ for $U = 2$ and $\rho = 1.5$ . . . . .	88
5.9	Behaviour of $\rho$ with respect to $\mu$ for $U = -4.0$ (left red curve) and $U = -1.5$ (right blue curve) at $t_2 = 0.2$ . The insets show the enlarged regions of the SF and PSF phases where the density jumps in steps of one and two particles respectively. . . . .	88
5.10	The extrapolated values of bond order structure factor for single particle (blue circles) and pairs (red squares) for different values of $U$ at $\rho = 1$ (see text for details). Here $t_2 = 0.2$ . . . . .	89

---

5.11 Fidelity susceptibility $\chi_{FS}$ as function of the interaction strength $U$ ( $\rho = 1$ , $t_2 = 0.2$ ) for $L = 40$ , 80 and 160. . . . .	90
5.12 Single particle correlation function $\Gamma( i - j )$ (black circles) and pair correlation functions $\Gamma_{pair}( i - j )$ for $t_2 = 0.2$ are plotted for $U = -4.0$ at $\rho = 1.5$ for a system of length $L = 160$ (see text for details). . . . .	90
5.13 The peak heights of $N(k = 0)$ (blue circles) and $N_{pair}(k = 0)$ (red squares) at $\rho = 0.5$ using $L = 160$ for $t_2 = 0.2$ show the transition from PSF to SF and then to BO phases as discussed in the text. . . . .	91
5.14 Finite size scaling of $N(k = 0)$ for $t_2 = 0.2$ shows that the curves for different lengths ( $L = 40$ , 80, 120, 160) intersect at the critical point $U \sim 0.44$ for the SF-MI transition at $\rho = 0.5$ . . . . .	92
5.15 Behaviour of $\rho$ with respect to $\mu$ for $U = 1$ , $t_2 = 0.2$ and $W = 0$ (black curve), $W = 5$ (red curve) and $W = 10$ (green curve) for the case of softcore bosons. Here maximum number of particle per site is taken to be 5. Inset shows the zoomed in view of $\rho = 1$ and 0.5 regions. . . . .	93
5.16 Phase diagrams for $t_2 = 0.6$ . The region bounded by the continuous green curves are the gapped phases at $\rho = 1$ and the regions bounded by the blue dashed curves are the gapped bond order phases at $\rho = 0.5$ (upper) and 1.5 (lower). On the negative $U$ side the PSF is separated from the SF phase by the red circles. The black dot-dashed lines represent the empty and full states. . . . .	94
5.17 Order parameters depicting different phases for $t_2 = 0.6$ . The red circles, green squares and black down triangles show the values of $O_{P,e}^2(i, j)$ , $E_G(L)$ and $S_{BOP}(k = \pi)$ respectively for different values of $U$ . . . . .	95
5.18 Parity order $O_P^2(i, j)$ for odd and even distances $ i - j  \gg 1$ are plotted for different values of $t_2$ with respect to $U$ . $t_2 = 0$ lines correspond to the analytical results as discussed in the main text, $t_2 = 0.2$ and $t_2 = 0.6$ curves depict the data obtained for $L = 160$ sites. . . . .	95
5.19 $O_{P,e}^2$ at $\rho = 0.5$ , 1.0 and 1.5 for $t_2 = 0.2$ is plotted for different values of $U$ . . . . .	96

## LIST OF FIGURES

---

- 6.1 Phase diagram of the bosonic three-body constraint SSH model at unit filling  $n = 1$  as function of  $t_2/t_1$  and  $U/t_1$  (on the left) and  $t_1/t_2$  and  $U/t_2$  (right part). The solid line with black diamonds marks BKT phase transitions between gapped and gapless phases. The dashed line depicts the crossing between single and two particle excitations and defines the crossover between MI and PBO phases. The dotted line depicts the emergence of polarized edge states due to the non-trivial effective topology of the model in the attractive regime (see text). . . . . 102
- 6.2 Single and two particle energy gaps  $G_1$ (red dashed lines) and  $G_2$  (blue solid lines) respectively are shown as function of  $U/t$ . We show the data for system size of  $L = 160$  (light filled squares) together with the extrapolation to the thermodynamic limit (open square for  $G_1$  and cross for  $G_2$ ) using  $L = 40, 80, 120$  and  $160$  sites. DMRG data for (a)  $t_2/t_1 = 0.6$  and (b)  $t_2/t_1 = 0.3$ . The arrow marks the crossing between  $G_1$  and  $G_2$ . The Inset in (a) shows the BKT-compatible scaling of the single particle energy gap with a critical value of  $U_c = -2.9t_1$  (see text). The Inset in (b) depicts the fidelity susceptibility  $\chi_{FS}/L$  for  $t_2/t_1 = 0.3$  as function of  $U$ . Panel (c) shows the neutral excitation gap  $G_N$  at  $t_2/t_1 = 0.2$  for  $L = 20, 40, 80$  and  $160$  sites (top to bottom curve). The inset in (c) shows the extrapolation of the gap-minimum for system sizes up to  $L = 200$  sites which extrapolates to a finite value  $G_N \sim 0.26t_1$ . . . . . 103
- 6.3 Estimate of the central charge for the PSF to PBO phase transition ( $U = -8$ ) for different system sizes. The figure shows results of a fit to the bipartite entanglement entropy  $S_{vN}(j)$ , as shown in the inset for  $L = 160$  for two examples  $t_2 = t_1$  (top curve) and  $t_2 = 0.98t_1$  (bottom curve). . . . . 105
- 6.4 Polarized edge states for the RM model at (a)  $U = -10$  and (b)  $U = -2$  ( $t_1 = 1, t_2 = 0.2$ ) after subtracting the overall density modulation  $\bar{n}_i = \langle n_{L/2+(i \bmod 2)} \rangle$  for clarity. The different curves are for different values of  $\tau = 0.0$ (blue dash-square),  $0.25\pi$ (red plus-solid),  $0.5\pi$ (green dot-cross). . . . . 106
- 6.5 Polarization  $P$  for  $t_1/t_2 = 0.1, 0.3$  and  $0.6$  as function of the interaction strength for  $L = 160$  and  $L = 80$  sites (light colored lines). . . . 107

---

6.6 Estimates of the winding numbers (a) $\omega$ and (b) $\omega_{1/2}$ from small system size simulation ( $L = 8$ sites, exact diagonalization) for the SSH-model as function of $U/t$ and $t_1/t_2$ as well as $t_2/t_1$ . Black lines correspond to the lines of Fig. 6.1. . . . .	108
6.7 Sketch of a charge pumping cycle of the RM model in a one dimensional optical superlattice. The SSH-model corresponds to a dimerized hopping $\delta t = (t_1 - t_2)/2$ as shown in the configurations $\tau = 0$ and $\tau = \pi/2$ . The cases of $\tau = \pi/4$ and $\tau = 3\pi/4$ depict a staggered potential with $\delta\Delta = \Delta_2 - \Delta_1$ . . . . .	109
6.8 The figure depicts the charge pumping in the Rice-Mele model. Figure (a) shows the single-particle energy spectrum of model (6.13) for a system of length $L = 20$ where $\delta t = \delta\Delta = 0.4$ and $t = 0.6$ . (b-c) Show the wavefunctions for the parameters indicated by the green plus signs in figure(a). . . . .	110
6.9 Polarization $P$ for the RM model (6.13) as function of the adiabatic parameter $\tau$ for several values of $U$ ( $\delta\Delta = \delta t$ ). Note that, $\tau = 0$ and $\pi$ correspond to $t_1 = 0.2$ and $t_2 = 1$ and for $\tau = \pi/2$ we have $t_1 = 1.0$ and $t_2 = 0.2$ . We consider system size of $L = 180$ sites and for comparison we consider $L = 80$ (not shown) for $U = -1$ and observe no change in the result. For $U = 4$ we plot $10 \times P$ for clarity. . . . .	111
6.10 Largest values of the entanglement spectrum $\lambda_\mu$ of the reduced density matrix in the center of a finite system of size $L = 160$ for the RM model shown in Eq. (6.13) of the main text as a function of the adiabatic parameter $\tau$ for (a) $U = -10$ , (b) $U = -2$ , (c) $U = -1$ and (d) $U = 4$ (compare Ref. [276]). The eigenvalues $\lambda_\mu$ have been sorted by the particle number sector $N_\mu$ in the center of the chain and for convenience labeled by $\Delta N_\mu = N_\mu - L/2$ . . . . .	112

## LIST OF FIGURES

---

- 6.11 Pumping of repulsively bound pairs along different paths A and B (sketched in the inset of (a) as parametric plot in  $\tau$ ). (a) Fully adiabatic evolution (ground state calculation of the effective model of attractively bound pairs,  $L = 120$  sites). (b) Simulation of an actual real time evolution, which is sufficiently slow to stay close to the adiabatic regime in path  $B$  but too fast for path  $A$  (exact diagonalization,  $L = 6$  sites,  $N = 6$  particles,  $U_q = 36t$ , time evolution initialized at  $\tau = \pi/4$ ). Up to  $\tau = 1$  the curve for path B resembles well the one for the fully adiabatic evolution and totally pumped polarization is close to 1. . . . . 113
- 6.12 Pumping of repulsively bound pairs for different values of the quenched interactions  $U_q = 16t$ ,  $20t$  and  $36t$  (real-time evolution,  $L = 6$ ,  $N = 6$ , initialized at  $\tau = \pi/4$ ). The dash-dotted line depicts the fully adiabatic evolution of the effective model of attractively bound pairs ( $L = 120$  sites). . . . . 114
- 7.1 Two different species  $\{\uparrow, \downarrow\}$  in the Model (7.1). Whereas  $\uparrow$  experiences SSH hopping dimerization with  $t_1 \neq t$ ,  $\downarrow$  is in a homogeneous lattice with uniform hopping amplitude  $t$ . The inter-component interaction is denoted as  $U$ . . . . . 117
- 7.2 The dimer order parameters ( $D_{i\sigma}$ ) are plotted with respect to the bond index  $i$  for different values of interaction (a)  $U = -5$  (b)  $U = 0$  and (c)  $U = 5$  with  $t_1 = t = 1$  and  $t_2 = 0.2$  using a system of length  $L = 120$ . Here black square (red circle) stand for spin- $\uparrow$  ( $\downarrow$ ) component. 119
- 7.3 Bulk gaps  $\Delta_\sigma$  (blue dotted and red continuous), and dimer structure factors  $S_{D\sigma}(\pi)$  (blue dashed and red dot-dashed) for  $\uparrow$  and  $\downarrow$  components, respectively, as a function of  $U$ . The observables are extrapolated to  $L \rightarrow \infty$  using our DMRG results for system sizes of length  $L = 40$ ,  $60$ ,  $80$ ,  $100$  and  $120$ . . . . . 120
- 7.4 Pairing  $\eta$  as a function of  $U$ . . . . . 121
- 7.5 (a-b) Edge states for both component for  $U = -5$  and  $5$  for a system with  $L = 120$ ; (c) Polarization  $P_\sigma$  for  $\uparrow$  (blue squares) and  $\downarrow$  (red circles) as a function of  $U$ , obtained for  $L = 120$ . . . . . 123

---

LIST OF FIGURES

- |      |   |     |
|------|---|-----|
| 7.6  | (a) MCD for a system with $L = 6$ for $U = 0$ for $\uparrow$ (filled symbols) and $\downarrow$ (hollow symbols); (b) Same for $U = -15$ (red circles) and $U = -5$ (black triangles). Here solid and empty symbols are corresponding to $\uparrow$ and $\downarrow$ respectively. For $ U  = 5(15)$ the MCD evolution curves are marked by symbol triangle(circle). In all cases we employ as initial state $ \Psi(0)\rangle = c_{0\uparrow}c_{0\downarrow} \Psi_{GS}\rangle$ . . . . . | 124 |
| 7.7  | Polarizations $P_\uparrow(\tau)$ (a) and $P_\downarrow(\tau)$ (b) for different $U$ values and $L = 120$ .126   |     |
| 7.8  | Initial gradient of polarization $m_\downarrow = \frac{dP_\downarrow}{d\tau}(\tau = 0)$ as a function of $U < 0$ shows the signature of topological inheritance. . . . .  | 127 |
| 7.9  | Fidelity susceptibility $\chi$ as a function of $U$ for different $L$ . The inset shows the extrapolation of the value $U$ at which $\chi/L$ has a maximum. This value marks the onset of full topological inheritance. Here, the filled red triangle corresponds to the extrapolated position of the peak.128  |     |
| 7.10 | (a) Experimental scheme to realize Model (7.1) using two-leg optical ladder systems of hardcore dipolar bosons using dipolar particles (see text); (b) Induced polarization for a three-species system in a state-dependent super-lattice in the presence of on-site all-to-all ( $SU(3)$ -symmetric) interactions. The inset shows the replication of the edge state to the second and third species for $U_{SU(3)} = 6$ . . . . .   | 129 |



# Chapter 1

## Introduction

### 1.1 Quantum phase transitions

Phase transitions are ubiquitous in nature, and the study of phase transitions in various systems is one of the very important areas of research in physics. The phase transition is the phenomenon in which a system undergoes a transition from one phase to another associated with some drastic change in the physical properties has been a topic of paramount interest especially in the context of condensed matter physics. Melting of ice to water is a classic example of phase transition where the phase transition is driven by the temperature and the associated thermal fluctuation. Such phase transitions are known as classical phase transitions. At zero temperature, however, the absence of any thermal fluctuations guarantees no classical phase transitions. Interestingly, in this limit, non-thermal parameters like magnetic field, pressure, uniaxial stress, chemical substitution, etc. can introduce phase transitions in the system - the phenomenon known as the Quantum Phase Transition (QPT). The QPTs are primarily driven by quantum fluctuations, which are the characteristics rooted in the Heisenberg like uncertainty principles. In general, the QPTs occur in many different areas of physics ranging from condensed matter physics, atomic molecular and optical (AMO) physics, high energy physics and astrophysics.

A paradigmatic example that can exhibit both the classical and quantum phase transition is the transverse field Ising model. Bitko, Rosenbaum and Aeppli have experimentally observed [1] the phase transitions in the transverse field Ising model in  $\text{LiHoF}_4$  as a function of magnetic field and temperature.  $\text{LiHoF}_4$  is an ionic crystal and the Holmium atoms represent the only spin degrees of freedom. Without any magnetic field, the ground state of this system is a ferromagnet where the spins orient themselves along the easy axis, i.e., up or down with respect to the crystal

axis. Hence, the state does not have the spin rotation symmetry, and the phase has a finite magnetization  $M$ . Now, increasing the temperature induces fluctuations in the spin and reduces the  $M$ . After a certain critical temperature, known as Curie temperature, the  $M$  completely vanishes, and the system exhibits a paramagnetic phase with spin rotation symmetry. This is a classical phase transition. On the other hand, a magnetic field perpendicular to the easy axis can also induce the fluctuations in the spins at zero temperature. When the magnetic field is applied in the ferromagnetic ground state, the system becomes a paramagnet after a critical value. This transition does not involve the temperature and is completely driven by quantum fluctuations characterizing a QPT.

The curiosity to understand the fundamental physical phenomena, flexibility in making tabletop experiments and demand for technological applications have made the study of QPTs in condensed matter systems an extremely important field of research. The QPTs in condensed matter systems result from the interplay between the inter-particle interactions, geometry, quantum statistics of constituent particles and strong correlations. The systems that comprise of a large number of particles in periodic potentials have revealed a wealth of novel physical phenomena in the last several decades. Due to the successive progress in the experimental fronts, several interesting quantum phases and phase transitions have been observed. However, various constraints related to the flexibility in tuning different system parameters responsible for the QPTs and the presence of defects and/or disorders pose a big challenge to observe a wide range of QPTs in conventional solid-state systems. In such a scenario, several novel quantum simulators have been proposed and experimentally realized to mimic the QPTs in recent years.

The system of ultracold atoms in optical lattices has emerged as a very important field of research as they are able to overcome the obstacles faced by conventional solid-state systems to observe QPTs. These systems consist of ultracold atoms, which are atoms trapped and cooled to the temperature of the order of nano kelvins loaded onto an artificial lattice made up of counter-propagating lasers beams. The new generation of detection techniques in these experiments facilitate to access the fundamental observables [2–9] which includes local observables and complex spatial correlations [8]. The first pioneering observation of the superfluid (SF) to Mott insulator (MI) transition in an optical lattice using cold bosonic atoms demonstrates the precise control over the system parameters [10]. Since the path-breaking observation of the SF-MI transition, the systems of ultracold atoms in optical lattices have proven to be one of the most efficient tools for quantum simulations. The

past two decades have witnessed rapid progress in the field of quantum simulations of condensed matter phenomena using these well-behaved systems leading to many different observations in experiments [10–13]. Due to the flexibility in tuning the interactions, lattice geometry and novel techniques to probe complex quantum systems, the systems of ultracold atoms in optical lattices are considered to be one of the most versatile quantum simulators in recent years.

## 1.2 QPT in optical lattices

### 1.2.1 Optical lattice

An optical lattice is a periodic potential experienced by atoms that are created by the coherent superposition of counter-propagating lasers. When ultracold atoms are loaded onto these artificial lattices, the internal degrees of freedom of the atoms make them visible to the external laser field. Hence, the light-matter interaction becomes key to engineer the optical lattice potential in such systems. Due to a spatially varying ac-Stark shift in off-resonant laser, the spatially varying electric field exerts dipole force on the atoms [14], which also facilitates the atomic cooling and trapping and is given as

$$\mathbf{F} = \frac{1}{2}\eta(\omega) \nabla (|\mathbf{E}(r)|^2) \quad (1.1)$$

where  $|\mathbf{E}(r)|^2$  is the time-averaged intensity,  $\eta(\omega)$  is the polarizability and  $\omega$  is the laser frequency. If the laser frequency  $\omega$  is near the transition frequency ( $\omega_0$ ) of the ground ( $|0\rangle$ ) to an excited state ( $|1\rangle$ ) of the particle, the polarizability takes the form

$$\eta(\omega) \approx \frac{|\langle 1 | \hat{d}_E | 0 \rangle|^2}{\hbar(\omega_0 - \omega)} \quad (1.2)$$

with  $\hat{d}_E$  being the dipole operator in the direction of the field. So, it can be easily seen from Eqs. 1.1 and 1.2 that the direction of force  $\mathbf{F}$  depends on sign of  $\eta(\omega)$ . Thus for red detuned laser ( $\omega > \omega_0$ ), an atom gets attracted towards intensity maxima whereas for blue detuned laser ( $\omega < \omega_0$ ) an atom gets repelled. If the detuning  $\delta = \omega - \omega_0$  is small compared to two-level transition frequency  $\omega_0$  ( $\omega_0 \gg |\delta|$ ) and large compared to the decay rate ( $\Gamma$ ) of the excited state ( $|\delta| \gg \Gamma$ ), the dipole

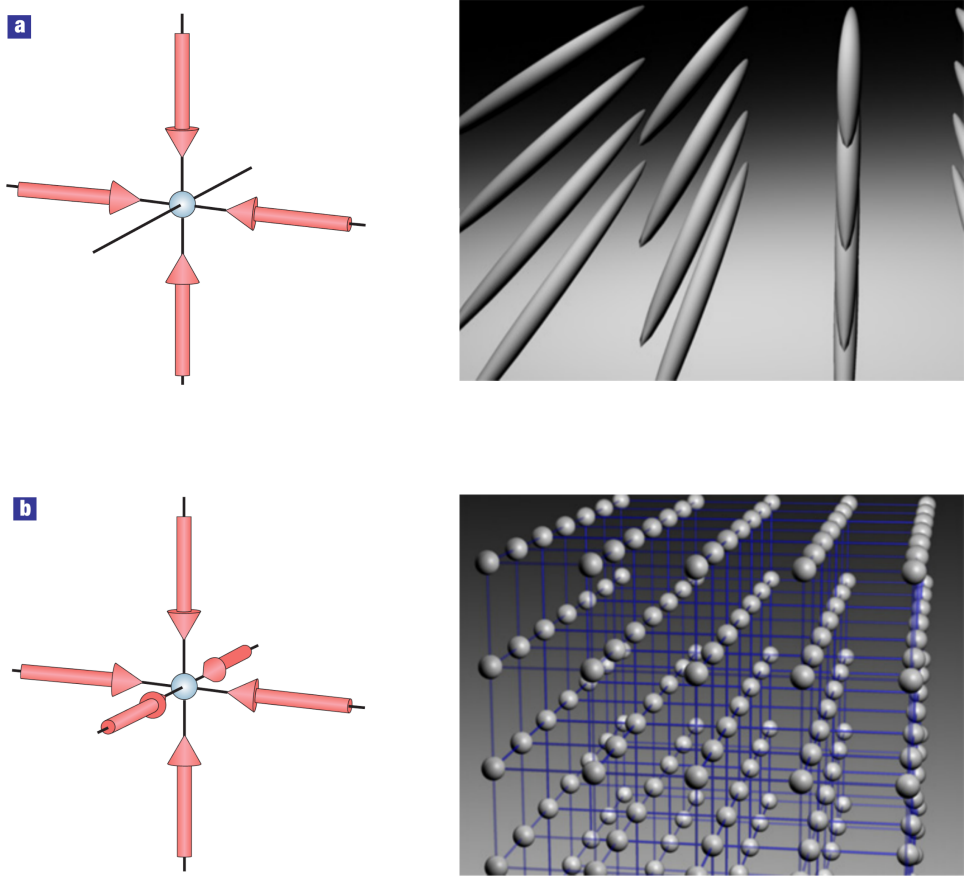


**Figure 1.1:** The schematic diagram for multi-dimensional optical lattice potential formed by the superimposition of counter propagating lasers. (a) The array of potential tubes formed by two standing waves orthogonal to each other. (b) A three dimensional lattice potential created by superimposing three orthogonal standing waves. The figure is taken from Ref. [15].

potential can be written as [14]

$$V_{dip}(x) \approx \frac{\Omega(r)^2}{4\delta}. \quad (1.3)$$

Here  $\Omega(r)$  is the Rabi-frequency proportional to the intensity of the field i.e.  $\Omega(r)^2 \propto |\mathbf{E}(r)|^2$ . So the atoms experience attractive or repulsive potential depending on the detuning of the laser.

Eq. 1.3 gives rise to the periodic optical lattice potential in the presence of the standing wave pattern of electric fields  $\mathbf{E} = \mathbf{e} \sin(kx + \omega t)$  of interfering lasers in

one dimension. This results in the formation of an optical potential of the form

$$V_{lat}(x) = -V_x \sin^2(kx). \quad (1.4)$$

Here  $V_x$  is the lattice depth defined in units of recoil energy  $E_R = \hbar^2 k^2 / 2m$  and the lattice period is half the wavelength of the laser ( $\lambda$ ). It is also possible to engineer two- and three-dimensional optical lattices by considering two or more pairs of laser beams (Fig. 1.1). The general three-dimensional optical lattice potential can be written as ,

$$V_{lat}(x) = -V_x \sin^2(kx) - V_y \sin^2(ky) - V_z \sin^2(kz). \quad (1.5)$$

Note that one can emulate one- and two-dimensional lattice from a three-dimensional one by making the lattice deep enough in two and one directions respectively.

Various lattice geometries can be created apart from the square and cubic lattice, such as triangular and kagome structures [16] with an appropriate number of laser beams arranged in proper directions. Another way to generate the optical lattice is by the holographic projection that has been observed in the context of the single-site microscopy [5].

The importance of the systems of ultracold atoms in optical lattices was realized after the first prediction of superfluid (SF) to Mott insulator (MI) phase transition of bosons in periodic potential as well as optical lattices were made [17, 18]. Following these predictions, the SF to MI phase transition of ultracold bosons was achieved in a path-breaking experiment in a three dimensional optical lattice [19]. This finding opened up a new direction to simulate various complex quantum systems in systems of ultracold quantum gases in optical lattices. In the last several years of nearly two decades have witnessed a growing interest in the field of QPTs in optical lattices leading to novel findings that were absolutely unachievable in conventional solid-state systems.

### 1.2.2 Ultracold bosons in optical lattice: The Bose-Hubbard model

Ultracold atoms are the atoms cooled to the nano-Kelvin regime created using the techniques of cooling and trapping of atoms with magnetic and optical traps [20]. At this low temperature, the quantum mechanical properties of atoms become dominant, which makes the system of ultracold atoms suitable to study various quantum

mechanical phenomena such as the QPTs, superfluidity, Bose-Einstein condensation etc. Due to the flexibility and experimental control, the systems of ultracold atoms are now being pursued as one of the most promising platforms for quantum computation and simulations.

Due to extremely low temperatures, the ultracold atoms possess weak inter-particle interaction arising from the *s*-wave scattering between the particle. However, in order to study the QPTs in strongly correlated systems, an optical lattice is used, which enables the tuning of the potential and kinetic energies associated with the system with absolute flexibility. One of the simplest systems, which exhibit such strong correlations between bosonic atoms, is the system of ultracold bosons in optical lattices which is represented by the famous Bose-Hubbard (BH) model. The BH model was first introduced in 1962 by Gersch and Knollman [21], which is closely related to the Fermi-Hubbard model originally proposed by Hubbard in 1963 [22] to describe the motion of electrons in a crystalline solid and superconducting systems. In the late 1980's, the BH model started to gain eminence after it was able to describe SF-MI transition. In the following, we will formulate the Bose-Hubbard model in detail.

In the second quantized form, the interacting bosonic Hamiltonian can be given by

$$\begin{aligned} \hat{\mathcal{H}} = & \int \hat{\Psi}^\dagger(\vec{x}) \left[ -\frac{\hbar^2}{2m} \nabla^2 + V(\vec{x}) \right] \hat{\Psi}(\vec{x}) d^3x \\ & + \frac{1}{2} \int \int d^3x d^3y \hat{\Psi}^\dagger(\vec{x}) \hat{\Psi}^\dagger(\vec{y}) U(|\vec{x} - \vec{y}|) \hat{\Psi}(\vec{x}) \hat{\Psi}(\vec{y}) \end{aligned} \quad (1.6)$$

where  $V(x)$  is the trapping potential, which is the combined effect of the lattice potential and the external confining potential,  $U(|\vec{x} - \vec{y}|)$  is the two-particle interaction.  $m$  represents the mass of the atom and  $\hat{\Psi}$  are the field operators of bosons that satisfy the standard commutation relation of bosons

$$[\hat{\Psi}(\vec{x}), \hat{\Psi}^\dagger(\vec{x}')] = \delta^3(\vec{x} - \vec{x}') \quad (1.7)$$

$$[\hat{\Psi}(\vec{x}), \hat{\Psi}(\vec{x}')] = [\hat{\Psi}^\dagger(\vec{x}), \hat{\Psi}^\dagger(\vec{x}')] = 0. \quad (1.8)$$

The two-body interaction term in the Hamiltonian shown in Eq. 1.6 is primarily governed by *s*-wave scattering between the ultracold bosons. In this limit the interaction  $U(|\vec{x} - \vec{y}|)$  is essentially the effective contact potential determined by the

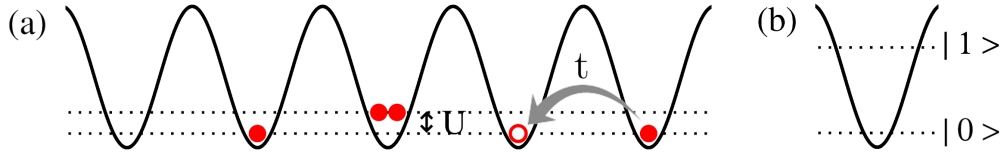


**Figure 1.2:** (a) Shows the role of interaction and hopping in the BH model. Particle tunnel with tunneling amplitude  $t$  and the energy offset  $U$  results from two particle occupations. (b) A sketch of the energy levels of an isolated site.

$s$ -wave scattering length  $a_0$  and is given as

$$U(|\vec{x} - \vec{y}|) = U_0 \delta^3(\vec{x} - \vec{y}) \quad (1.9)$$

where  $U_0 = \frac{4\pi\hbar^2 a_0}{m}$ .

In a system of periodic potential it is convenient to introduce the Wannier functions, which are localized in the lattice sites unlike the delocalized Bloch wavefunctions. Wannier functions are represented by the Fourier transform of Bloch states:

$$W_{ni}(\vec{x}) = \frac{1}{\sqrt{M}} \sum_k e^{i\vec{k} \cdot (\vec{x} - \vec{R}_i)} u_{nk}(\vec{x}). \quad (1.10)$$

Here, the set of  $\{W_{ni}(\vec{x})\}$  form a complete orthonormal basis named as Wannier basis, satisfying the orthogonality relation

$$(W_{mj}(\vec{x}), W_{ni}(\vec{x})) = \int_V d^3x W_{mj}^*(\vec{x}) W_{ni}(\vec{x}) = \delta_{mn} \delta_{ji} \quad (1.11)$$

The bosonic field operators expanded in this Wannier basis are then:

$$\hat{\Psi}(\vec{x}) = \sum_{n,i} W_{ni}(\vec{x}) a_{ni} \quad \hat{\Psi}^\dagger(\vec{x}) = \sum_{n,j} W_{nj}(\vec{x}) a_{nj}^\dagger. \quad (1.12)$$

Here, the operators  $a_i$  and  $a_j^\dagger$  are known as the annihilation and creation operators respectively at site  $i$  and they satisfy the standard bosonic commutation relations:

$$[a_{ni}, a_{nj}^\dagger] = \delta_{ij} \quad [a_{ni}, a_{nj}] = 0 = [a_{ni}^\dagger, a_{nj}^\dagger]. \quad (1.13)$$

Assuming deep enough lattice and the localized nature of the Wannier functions, the tight-binding approximation of the Hamiltonian shown in Eq. 1.6 can be

appropriately written as;

$$H = - \sum_{\langle i,j \rangle} t_{i,j} (a_i^\dagger a_j + H.c.) + \frac{U}{2} \sum_i n_i(n_i - 1) - \sum_i \mu_i n_i \quad (1.14)$$

and this famously represents the BH model. The parameters in the BH model such as  $t_{i,j}$  are the hopping amplitudes between the sites  $i$  and  $j$ ,  $U$  is the onsite two-particle interaction energy, and  $\mu$  is the onsite potential, which can be considered to be the chemical potential. The individual parameters can be expressed in terms of the Wannier function as:

$$t_{i,j} = - \int W^*(x - x_i) \left[ \frac{\hbar^2}{2m} \nabla^2 + V(x) \right] W(x - x_i) \quad (1.15)$$

and

$$U = a_0 \frac{4\pi\hbar^2}{m} \int dx^3 |W(x)|^4 \quad (1.16)$$

Note that due to the lowest band approximation, the band index from the Wannier functions has been dropped. In the deep lattice with lattice depth  $V_0$ , the hopping amplitude can be obtained by one dimensional Mathieu equation [23]

$$t \approx \frac{4}{\sqrt{\pi}} \left( \frac{V_0}{E_R} \right)^{3/4} e^{-2\sqrt{\frac{V_0}{E_R}}} E_R \quad (1.17)$$

However, for optical lattice defined by eq. 1.5, the Wannier function takes the form  $W(x, y, z) = W_x(x)W_y(y)W_z(z)$  and  $t$  becomes independent of the dimension of the lattice. On the other hand, the two-particle interaction can be written under harmonic approximation as

$$U_{har} = \sqrt{\frac{8}{\pi}} \left( \frac{V_0}{E_R} \right)^{3/4} E_R \quad (1.18)$$

As already mentioned, by tuning the lattice depth, the ratio between the hopping strength  $t$  and two-body interaction  $U$  can be controlled in optical lattices. On the other hand, the two-particle interaction strength can be independently tuned using the Feshbach resonances. The concept of Feshbach resonance was initially introduced in the context of nuclear physics [24].

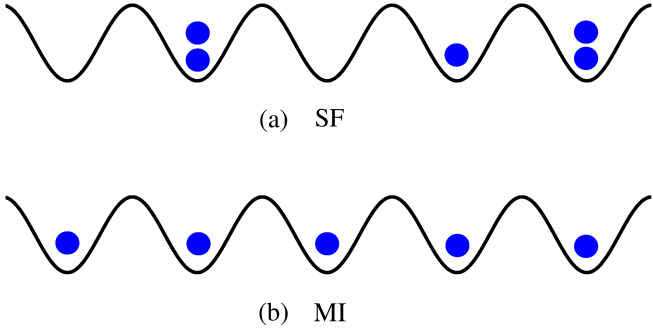


**Figure 1.3:** Particle distribution for (a) SF and (b) MI phase with  $\rho = 1$ . Figure (a) shows one of the many states whose superposition represent the SF phase.

### 1.2.3 Superfluid to Mott-insulator transition

The most famous QPT exhibited by the BH model is the SF to MI phase transition, which we will highlight in this section. The key quantity that drives this QPT is the ratio between the boson tunneling amplitude and the onsite repulsion between two bosonic particles, i.e  $t/U$ . The SF-MI transition in a single species bosonic atoms in a periodic potential was first reported in the year 1989 by Fisher *et al.*[17]. This phase transition was shown to occur exactly at integer densities  $n = N/L$ , which represents the number of particles per site. For large values of ratio  $t/U \gg 1$ , the bosonic kinetic energy is dominant, which ensures the overlap of individual particle wavefunctions resulting in the free motion of the atoms throughout the lattice. In such a scenario, the ground state of a system of size  $L$  and  $N$  number of bosons can be written as

$$|\Psi_{SF}\rangle \propto \left( \sum_i^L a_i^\dagger \right)^N |0\rangle \quad (1.19)$$

where  $|0\rangle$  represents the vacuum state. Eq. (1.19) describes the wavefunction of the SF phase, which is known to exhibit off-diagonal long-range order (ODLRO). Figure 1.3(a) shows one of the many states whose superposition gives rise to Eq. (1.19) e.g. for  $N = L$  in one dimension. On the other hand, in the limit of  $t/U \ll 1$ , number fluctuations on sites are energetically very expensive, and the system minimizes it's energy by localizing the particles (fixed number of particles per lattice sites). Thus, the many-body ground state becomes a zero entangled product state given by

$$|\Psi_{MI_n}\rangle \propto \prod_i^L (a_i^\dagger)^n |0\rangle \quad (1.20)$$

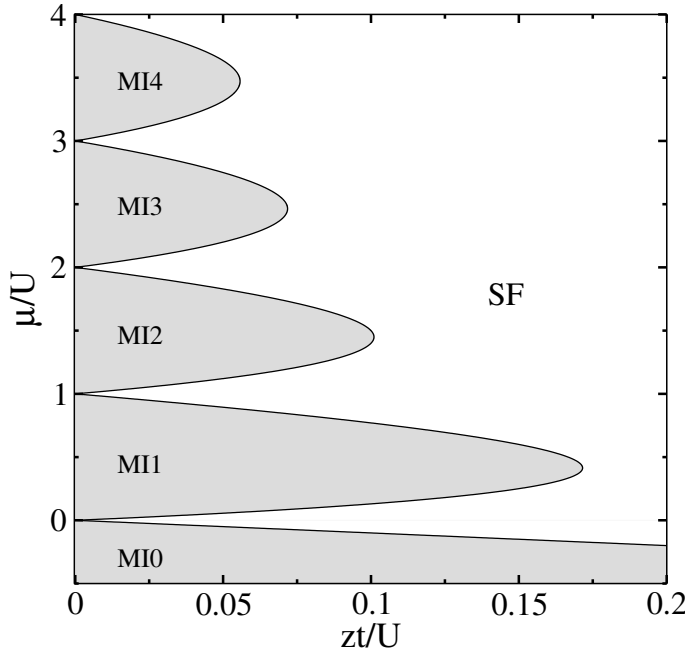


**Figure 1.4:** The mean-field phase diagram of the BH model (1.14) in  $\mu/U - zt/U$  plane. Here  $MIn$  is the MI with density  $n$ .

where,  $n = N/L$  is an integer. The Eq. (1.20) represents the  $MIn$  phase (MI phase with density  $n$ ) as shown in Fig. 1.3(b) for  $n = 1$  in an one dimensional case. By varying the value of  $t/U$  continuously from small to large values, one gets the SF-MI phase transition at a critical value  $(t/U)_c$ . The phase diagram depicting this QPT was first obtained using the simple mean-field approximation for a  $d$ -dimensional lattice [17], which is depicted in Fig. 1.4. The phase diagram shows different  $MIn$  lobes (shaded regions) in the strong interaction regime corresponding to different integer densities  $n$  in the  $\mu/U - zt/U$  plane. Here,  $z$  stands for the coordination number. Whereas, in the limit of weak interaction (strong hopping), the system is in the SF phase (white area). By changing the ratio of  $t/U$ , the system reaches a critical point where the SF-MI transition occurs. The mean-field estimation of the critical point is  $U = 5.8zt$  for  $n = 1$  (Fig. 1.4) [17, 25, 26].

Achieving such a QPT in a conventional solid-state system was out of reach and therefore, a new proposal had been made by Jaksch *et al.* in 1998 to simulate this interesting phenomenon in a system of ultracold bosonic atoms in optical lattices [18]. This was later observed in a seminal experiment [19] by Greiner *et al.* in 2002 using the BEC of  $^{87}\text{Rb}$  atoms in a three-dimensional cubic optical lattice. The observation of the SF-MI phase transition was made by looking at the absorption images obtained after ballistic expansion from a lattice with different potential depth  $V_0$

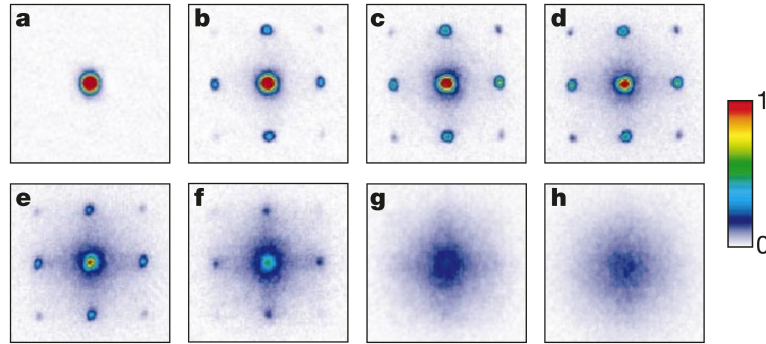


**Figure 1.5:** Experimental result of the first observation of SF-MI transition(taken from [19]). The figure shows the absorption images of matter-wave interference pattern for different initial states prepared for different lattice depth( $V_0$ ). Here  $V_0$  are, in (a) $0E_r$ , (b)  $3E_r$ , (c)  $7E_r$ , (d)  $10E_r$ , (e)  $13E_r$ , (f)  $14E_r$ , (g)  $16E_r$  and (h)  $20E_r$ .

which is shown in Fig. 1.5. The sharp peak in the interference pattern for small  $V_0$  reflects the fact that the system is phase coherent, whereas for larger  $V_0 > 13E_r$ , the interference maxima start to fade away, which is the result of incoherence in the system. This coherent to incoherent features in the interference pattern indicates the SF to MI QPT.

#### 1.2.4 QPT in multi-body interacting BH model

The SF-MI transition discussed above is purely due to the two-body interaction, which is the dominant interaction in the systems of weakly interacting Bose gas. Recently, however, effective higher-order interactions have been observed in optical lattice experiments [27, 28]. These effective interactions are due to the virtual population of occupation dependent higher Bloch bands. Although these effects are small compared to the original two-body interactions, they provide enough motivation to explore the physics of ultracold matter in the presence of multi-body interactions in optical lattices. With these types of interactions, the standard BH model gets modified accordingly and one gets a more general BH model with the on-site multi-body interactions given as;

$$\begin{aligned}
 H = & -t \sum_{\langle i,j \rangle} (a_i^\dagger a_j + H.c.) \\
 & + \sum_{p=2}^M \left( U_p \sum_i \frac{(n_i)!}{p!(n_i-p)!} \right) - \mu \sum_i n_i
 \end{aligned} \tag{1.21}$$

where  $U_p$  is the on-site  $p$ -body interaction strength and  $M$  is the highest order of the multi-body interaction.

In the literature, for the above model truncated to three-body interaction term, has been studied in various context [29–39]. In the presence of repulsive  $U_3$ , the MI lobes with density  $n > 1$  get affected drastically [32, 40]. In the absence of  $U_2$ , the model (Eq.1.21) exhibits the Mott lobes at higher densities repulsive  $U_3$  [37, 41]. Besides repulsive  $U_3$ , the case of attractive  $U_3$  has also been studied, which results in shrinking of the MI lobes [40, 42]. On the other hand, finite attractive two-body interaction between bosons results in the occupation of a single site of an optical lattice by all the bosons leading to collapse [43]. This difficulty can be overcome by including a very strong three-body on-site repulsion which prevents the occupation of a lattice site by more than two atoms and hence the collapse. A recent proposal rigorously shows that an infinitely strong three-body repulsion can arise due to the three-body loss process resulting from the elastic scattering of atoms [29]. This infinite three-body repulsion, which is termed as the three-body hardcore constraint, facilitates the formation of attractively bound bosonic pairs. The superfluid of these composite pairs is called the pair superfluid (PSF) phase in optical lattice [29, 30, 44, 45], which is an interesting manifestation of competing two and three-body interactions.

Several theoretical proposals have been made recently to control the three-body interactions in various ways in optical lattices [35, 46, 47]. Moreover, a recent proposal by D. Petrov [48] reveals the possibilities to simultaneously manipulate the higher-order multi-body interactions along with the two-body one in atomic systems [48, 49]. This prediction is one step forward in the directions of exploring physics arising due to the on-site interactions in optical lattices.

### 1.2.5 Long-range interaction in optical lattices

Apart from on-site interaction, the effect of long-range interactions in dipolar quantum gases have attracted a great deal of attention [50]. Degenerate quantum gases of atoms with large dipole moments have been realized in experiments, for example the BEC of chromium [51], dysprosium [52] and erbium [53]. Rydberg dressed atomic gases [54–59] and polar molecules [60, 61] in contrast show a very strong electric dipole moment.

The interaction between two polarized dipoles separated by a distance  $r$  is of the

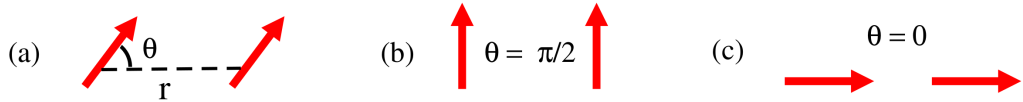


**Figure 1.6:** The figure shows polarized dipoles where the arrows represent the dipole moment. (a) Depicts the two polarized dipoles separated by a distance  $r$  and they make angle  $\theta$  with the connecting line. The configurations (b) and (c) show repulsive and attractive dipoles.

form

$$V_{dd} = \frac{C_{dd}}{4\pi} \frac{1 - 3\cos^2(\theta)}{r^3}. \quad (1.22)$$

Here  $\theta$  is the angle between the polarization direction and the line connecting them. The long-range interaction  $V_{dd}$  can be attractive and repulsive depending on the angle  $\theta$  between the dipoles (see Fig. 1.6). When loaded onto an optical lattice, it is convenient to assume the effect of  $V_{dd}$  up to the nearest neighbor site due to the  $1/r^3$  nature of the potential. In this limit, the Hamiltonian shown in Eq. 1.14 can be written as:

$$H_{EBH} = -t \sum_{\langle i,j \rangle} (a_i^\dagger a_j + H.c.) + \frac{U}{2} \sum_i n_i(n_i - 1) + V \sum_{\langle i,j \rangle} n_i n_j. \quad (1.23)$$

and is called the Extended-Bose-Hubbard (EBH) model.

Theoretically, the EBH model has been extensively studied in different lattice geometries leading to various quantum phases such as the crystalline phases and the exotic supersolid phases [50, 62, 63]. The presence of long-range interactions also hosts the possibilities to study other fundamental physics and technological applications [64, 65]. The recent experimental observation of the EBH model using dipolar quantum gases [66] has opened up avenues to explore novel quantum phase transitions in optical lattices.

## 1.3 Quantum walk

While the equilibrium properties of the strongly correlated many-body systems have been widely explored in the past decades, the systems out of equilibrium are comparatively less explored. There are many ways to drive a system out of equilibrium, such as pumping energy, applying a driving field, injecting particles through external reservoirs in the system and so on. One of the very clean settings is local or

global quench. Here, one prepares an initial state, which can be a ground state of a Hamiltonian, and quickly change a system parameter locally or globally, which takes the system out of equilibrium. The time evolution of the initial state is considered unitary under the final Hamiltonian. One of the interesting manifestations of dynamical systems is that the entanglement propagation is bounded by Lieb-Robinson bounds, where the information propagation outside a light-cone is suppressed exponentially [67–69].

The systems of ultracold atoms in optical lattices have proven to be extremely promising platforms to simulate the nonequilibrium dynamics. Current technologies can be used to study dynamics of a variety of systems such as the Bose-Hubbard model, Fermi-Hubbard model and spin chains [70–81]. Now it is even possible to address and control individual atoms in optical lattices [9, 82, 83]. Several observations have revealed many interesting phenomena in terms of nonequilibrium and relaxation dynamics in the ultracold atomic systems such as the transport phenomena [75, 84], quench dynamics from the MI to SF phases [77], relaxation dynamics of density waves in optical superlattice [71] and Light-cone-like spreading of correlations in many-body system [74].

Apart from the dynamical evolution of a many-body ground state, a great deal of physics can be explored from the time evolution of a few particle state subjected to a quantum mechanical Hamiltonian. The phenomenon which facilitates this process has been introduced as the Quantum Walk (QW), which is the quantum analog of the classical random walk [85]. The study of QW has attracted a great deal of attention recently, not only in the context of studying dynamical properties but also due to its possible application in quantum technologies [86–96]. Numerous studies have been performed in recent years, both theoretical and experimental, to investigate the QW of quantum mechanical particles at the single-particle level and also with few interacting particles [9, 97–106].

QW can be of two different types depending on the time evolution, namely (i) the discrete-time QW (DTQW) and (ii) the continuous-time QW (CTQW). In the following, we briefly discuss both types of QWs.

### 1.3.1 Discrete-time quantum walk (DTQW)

In a classical random walk on a one-dimensional graph (say), the motion of a walker is decided by the outcome of a tossed coin. Depending on the outcome, the walker moves in the forward or backward direction after every toss. Analogous to this, a

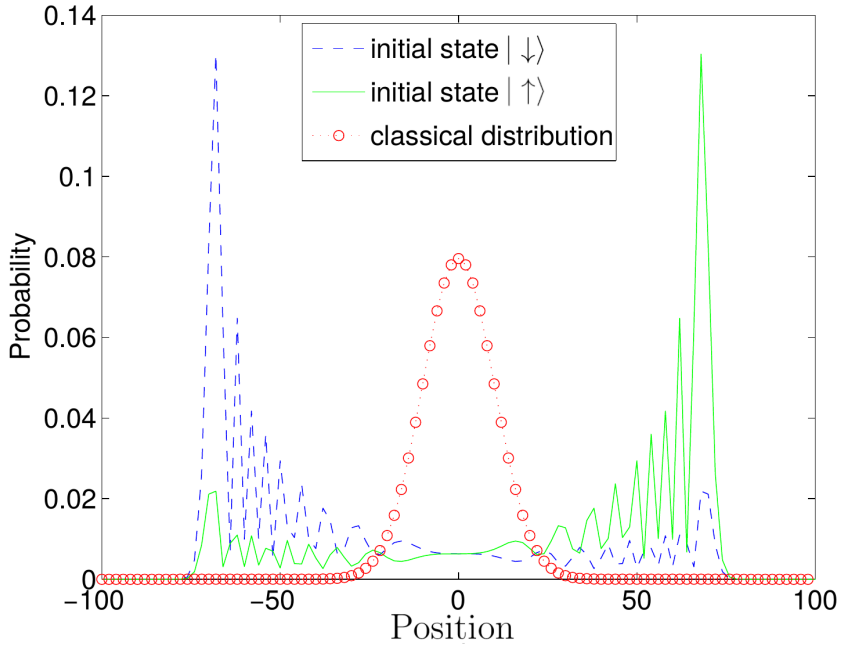


**Figure 1.7:** The figure compares the probability distributions of CRW and DTQW after 100 time steps. The figure also depicts the dependence of the QW on the initial states. The figure is taken from Ref. [107].

qubit is used in the case of DTQW of a quantum walker, which can be considered as spin with states  $|\uparrow\rangle$  and  $|\downarrow\rangle$ . There exists a unitary coin operator ( $\hat{C}$ ) that decides the state of the qubit. After operating the coin operator ( $\hat{C}$ ), a shift operator translates the qubit on the graph. The shift operator that delocalizes the qubit can be written as:

$$\hat{S} = |\uparrow\rangle\langle\uparrow| \otimes \sum_i |i+1\rangle\langle i| + |\downarrow\rangle\langle\downarrow| \otimes \sum_i |i-1\rangle\langle i| \quad (1.24)$$

where  $\{|i\rangle\}$  defines the position Hilbert space. So, the walker evolves a single step on the graph by following the mathematical structure

$$|\Psi(\tilde{t}_2)\rangle = \hat{S}(\hat{C} \otimes 1)|\Psi(\tilde{t}_1)\rangle = \hat{W}|\Psi(\tilde{t}_1)\rangle \quad (1.25)$$

where the  $|\Psi(\tilde{t}_1)\rangle$  is the state of the walker at time  $\tilde{t} = \tilde{t}_1$  and  $|\Psi(\tilde{t}_2)\rangle$  is the state after a finite time-step. Now to perform  $n$  steps, one has to operate  $\hat{W}$   $n$  times on the initial state. The probability of finding the qubit at the  $i^{th}$  site at any point of time can be calculated as  $|\langle i|\Psi(\tilde{t})\rangle|^2$ .

Different kinds of coin operators have been used to study the effects on the

DTQW and Hadamard coin is one of them which has the form

$$\hat{C}_H = \frac{1}{\sqrt{2}} \begin{bmatrix} 1 & 0 \\ 0 & -1 \end{bmatrix}. \quad (1.26)$$

Besides the coin operator, the initial state also plays an important role in the QW. For example, if the initial state of the qubit is  $|\uparrow\rangle$ , then the DTQW will yield a very different final state compared to that with the initial state  $|\downarrow\rangle$  or  $\alpha|\uparrow\rangle + \beta|\downarrow\rangle$ . In Fig. 1.7, we plot the probability distribution of finding the walker in position space after 100 steps, which results from the DTQW with the initial states  $|\downarrow\rangle$  and  $|\uparrow\rangle$  using the Hadamard coin. For comparison, the results using the classical random walk is also shown. It can be seen that the probability distribution in the case of QW spreads much faster compared to the classical random walk. It has also been shown that in the case of the classical random walk, the spreading is defusive in time i.e., the probability of finding the walker at a specific distance from the initial point is proportional to  $\sqrt{\tilde{t}}$ . However, for the DTQW, the expansion is ballistic in nature, where the probability spread is proportional to  $\tilde{t}$ .

### 1.3.2 Continuous-time quantum walk (CTQW)

The evolution process under the CTQW can be formulated from the time-dependent Schrödinger equation. Here, an initial state of the walker ( $\Psi(0)$ ) is evolved in time  $\tilde{t}$  using the unitary time-evolution operator  $\mathcal{U}$  as

$$\Psi(\tilde{t}) = \mathcal{U}\Psi(0) = e^{-iH\tilde{t}}\Psi(0), \quad (1.27)$$

where,  $\hbar = 1$  is assumed. Here  $H$  is the time independent Hamiltonian describing the system.

If the Hilbert space is spanned by the basis vectors  $|k\rangle$ , then the transition probability  $p_{k,l}$  can be defined as

$$p_{k,l} = \gamma_{k,l}^2 \quad (1.28)$$

where,

$$\gamma_{k,l}(\tilde{t}) = \langle k|e^{-iH\tilde{t}}|l\rangle. \quad (1.29)$$

is the transition amplitude. It can be shown that the transition probability for a

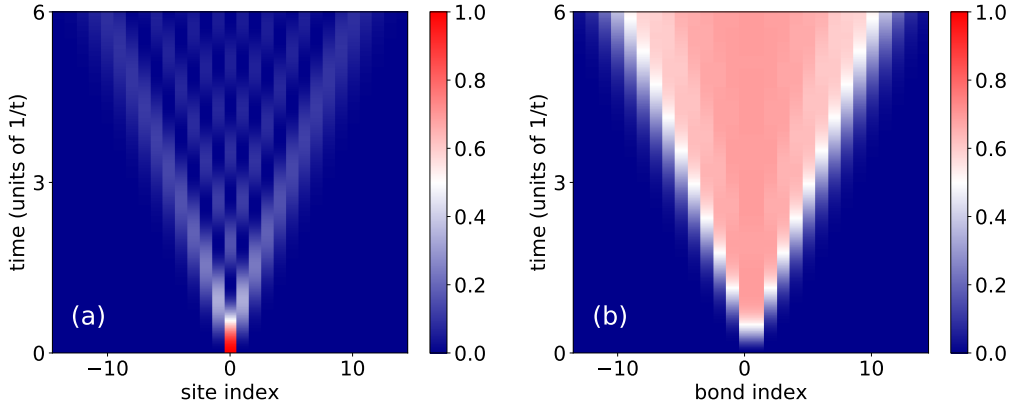


**Figure 1.8:** The figure shows the evolution of (a) density ( $n_i$ ) and (b) entanglement entropy ( $S_i$ ) for CTQW of a boson on a one dimensional graph.

Hamiltonian with nearest-neighbor hopping has the following form,

$$p_{k,l}(\tilde{t}) = [J_{k-l}(2\tilde{t})]^2 \quad (1.30)$$

for a one dimensional graph of length  $L \rightarrow \infty$ [108–110]. Here,  $J_n(x)$  is the Bessel functions of the first kind.

One of the simplest examples of CTQW can be constructed by considering a bosonic particle moving on a one-dimensional lattice. The Hamiltonian describing such a system is the BH model with only the hopping term  $J$  and is given as

$$H = - \sum_{\langle i,j \rangle} J_{i,j} (a_i^\dagger a_j + H.c.). \quad (1.31)$$

The CTQW in such systems can be understood by considering an initial state in which the particle is located at the central site of the lattice and is given as

$$|\Psi(0)\rangle = |\dots 0 0 1 0 0 \dots\rangle \quad (1.32)$$

Now the quenching of the system parameter leads to the time evolution of the initial state  $|\Psi(0)\rangle$  under the influence of the Hamiltonian given in Eq. 1.31. The CTQW in this case, is depicted in Fig. 1.8 in terms of the time evolution of particle density( $\langle n_i \rangle$ ) computed with respect to the time evolved state  $|\Psi(t)\rangle$ . One can also examine the spreading of the entanglement entropy, which is the measure of the

entanglement between two part of the system, defined by

$$S_i = -\text{Tr}(\rho_i \log \rho_i). \quad (1.33)$$

Here  $\rho_i$  is the reduced density matrix defined at the bond and  $i$  indicates the bond that connects the two parts of the system. In Fig. 1.8(a), the light-cone type evolution of density indicates a ballistic spreading of probability. Moreover, similar ballistic spreading can also be seen in the case of entanglement entropy, as shown in Fig. 1.8(b).

## 1.4 Topological phase transitions

Symmetry protected topological (SPT) phase transition is a new class of QPT that does not belong to the well-known Landau-Ginzburg paradigm associated with the spontaneous symmetry breaking. With the pathbreaking observation of the integer [111, 112] and fractional [113] quantum Hall (QH) effects, the abstract mathematical idea of topology enters the field of the condensed matter in a very fundamental way. Remarkably, it is possible to link a robust topological invariant with the energy band of a particle in periodic potentials. Under the continuous change of the system parameter, where the energy gap of the system remains finite and the symmetry of the system is preserved, the topological invariant remains unchanged [114, 115]. In such a scenario, if a phase transition to a topologically different phase happens, it happens through a gap closing.

Since the discovery of QH insulators, over the past few decades, the field of topological insulators has flourished rapidly, both experimentally and theoretically [114–116]. A host of material is shown to be topological insulator in one- two- and three-dimensions [117–120]. Much progress has happened in the optical lattice systems [121], besides real materials, to generate artificial magnetic fields and spin-orbit coupling in neutral atoms [122–124], which led to characterization and realization of topological Bloch bands.

### 1.4.1 The Su-Schrieffer-Heeger (SSH) model

The Su-Schrieffer-Heeger (SSH) model is a one-dimensional tight-binding model which is the simplest model exhibiting the topological phase transitions [125, 126]. This model, which was originally introduced in 1979 in the context of polyacetylene: a linear polymer that has a staggard electronic hopping [125], has gained consider-

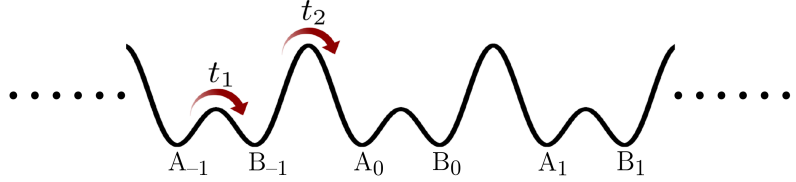


**Figure 1.9:** The figure shows a one dimensional lattice with staggard hopping ( $t_1$  and  $t_2$ ) along the chain.  $A_i$  and  $B_i$  are the sublattices of  $i$ -th unit-cell.

able attention due to the non-trivial topological properties. The model explains a one-dimensional system of free fermions experiencing staggered or dimerized hopping as shown in Fig. 1.9. The Hamiltonian describing the physics of such model is given as

$$H_{SSH} = -t_1 \sum_j (a_j^\dagger b_j + H.c.) - t_2 \sum_j (a_j^\dagger b_{j-1} + H.c.) \quad (1.34)$$

where  $a_j^\dagger (a_j)$  and  $b_j^\dagger (b_j)$  are the creation(annihilation) operators at A and B sublattices of the  $j$ -th unit cell.  $t_1$  and  $t_2$  are the intra and inter-cell hopping amplitudes respectively. The ratio  $t_1/t_2 \neq 1$  defines the hopping dimerization. Here each unit-cell consists of two sublattices  $A_j$  and  $B_j$ , where the subscript  $j$  stands for the position of the unit cells.

Due to translation symmetry, the Hamiltonian 1.34 reduces to a  $2 \times 2$  Hamiltonian in the reciprocal space i.e.

$$H_k = - \begin{bmatrix} 0 & t_1 + t_2 e^{-ika} \\ t_1 + t_2 e^{ika} & 0 \end{bmatrix} \quad (1.35)$$

where  $k$  is the quasi-momentum with the Brillouin zone (BZ)  $-\pi/a < k \leq \pi/a$ . Here,  $a$  is the lattice constant, which we consider equal to one for simplicity. Now the whole problem boils down to finding the eigenvalues and eigenvectors of  $H_k$ . The eigenvalues of  $H_k$  are

$$E_k^\pm = \pm \sqrt{t_1^2 + t_2^2 + 2t_1 t_2 \cos(k)} \quad (1.36)$$

which represents the dispersion relation for a given  $t_1$  and  $t_2$  with gap  $\Delta = 2|t_1 - t_2|$ . In the Fig. 1.10(a-c) we plot the eigenvalues for three different parameter ( $t_1$ ,  $t_2$ ) regimes such as  $t_1 > t_2$ ,  $t_1 = t_2$  and  $t_1 < t_2$  respectively. It can be seen that when  $t_1 \neq t_2$  the system is gapped in both  $t_1 > t_2$  and  $t_1 < t_2$  regimes and gap closes at  $t_1 = t_2$ . Interestingly, two gapped regime  $t_1 > t_2$  and  $t_1 < t_2$  are topologically

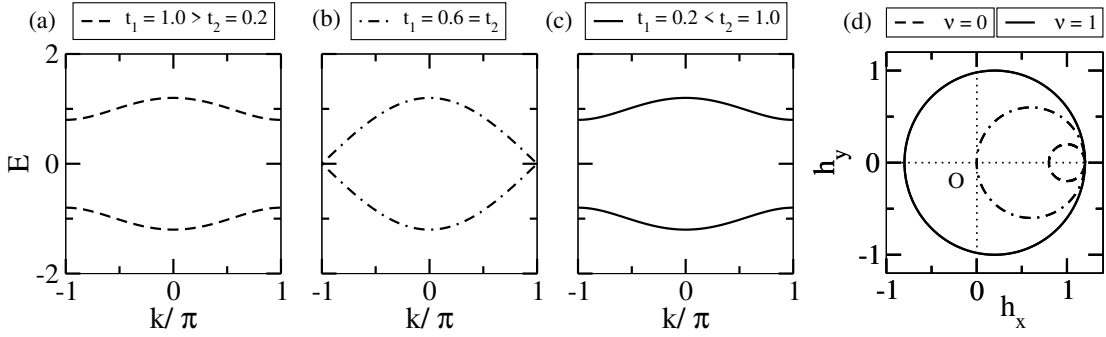


**Figure 1.10:** Figure (a-c) shows the band structure and (d) shows how to visualize the winding number. In both the calculations, the dashed line, the dot-dashed and solid line represent the parameters  $(t_1, t_2) = (1.0, 0.2)$ ,  $(0.6, 0.6)$  and  $(0.2, 1.0)$  respectively. From (d) we can see that, when  $t_1 > t_2$  the circle does not wind around the origin( $O$ ), when  $t_1 = t_2$  the circle touches the  $O$  which closes the gap evident from the figure (b) and when  $t_1 < t_2$  the circle winds the  $O$ .

distinct, and they are disconnected through the gap-closing point  $t_1 = t_2$ .

The topological invariant in this model is defined by the winding number ( $\nu$ ). The winding number ( $\nu$ ) comes from the Zak phase ( $\Phi_z$ ) [127] that is defined by the integral of Berry connection over a closed loop.

$$\nu = \frac{1}{\pi} \Phi_z = \frac{1}{\pi} \int_{BZ} \langle \psi_k | \partial_k | \psi_k \rangle \quad (1.37)$$

where  $|\psi_k\rangle$  is the wave function. The value of  $\nu$  can be obtained from the eigenfunctions of  $H_k$ . Representing the Hamiltonian  $H_k$  (Eq. 1.35) in a more general form we have

$$H_k = -\mathbf{h}(k) \cdot \hat{\sigma} \quad (1.38)$$

where  $\hat{\sigma}_\alpha$  are the Pauli matrices and

$$h_x = t_1 + t_2 \cos(k) \quad h_y = t_2 \sin(k) \quad h_z = 0. \quad (1.39)$$

Here  $h_z = 0$  indicates the chiral symmetry of the model. This shows that the  $\mathbf{h}$  is confined to the  $h_x - h_y$  plane. The  $|\mathbf{h}|$  represents the gap for all  $k$  and one can define  $h_x + i h_y = |\mathbf{h}| e^{i\phi_k}$  where for a finite gap, there is a well defined  $\phi_k$ . The eigenfunctions of the Hamiltonian shown in 1.35 can be written in terms of  $\phi_k$  as

$$\psi_k = \mp \frac{1}{\sqrt{2}} \begin{bmatrix} 1 \\ e^{i\phi_k} \end{bmatrix} \quad (1.40)$$

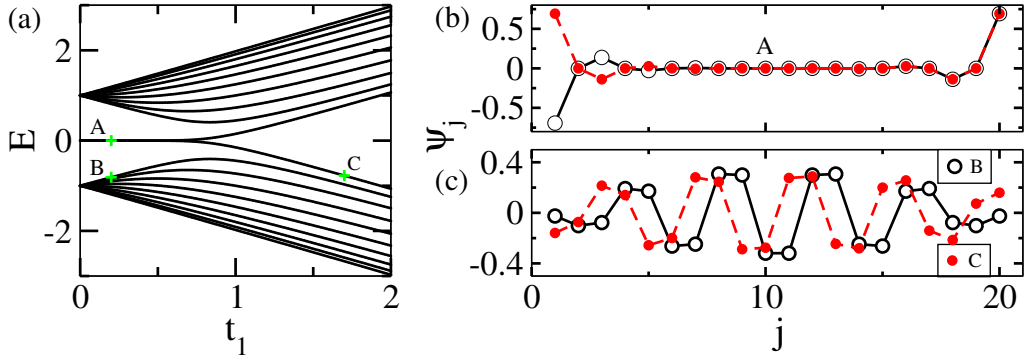


**Figure 1.11:** (a) Shows the single-particle energy spectrum of the model (1.34) for a system of length  $L = 20$  where  $t_2 = 1$ . (b-c) Show the wavefunctions for the parameters marked by the green plus signs in (a). This shows the appearance of the edge state for  $t_1/t_2 < 1$  and the gap-closing at the topological transition point  $t_1 = t_2$ .

Using this wavefunction one can show that the winding number 1.37 turns out to be

$$\nu = \frac{1}{2\pi} \int_{BZ} \frac{\partial \phi_k}{\partial k} dk = 0 \text{ or } 1 \bmod 2. \quad (1.41)$$

and the  $\nu$  is zero if  $t_1 > t_2$  and one if  $t_1 < t_2$ .

The winding number  $\nu$  can be visualized by how many times  $\mathbf{h}$  sweeps around the origin while  $k$  changes from  $-\pi$  to  $\pi$  (BZ). For example, in Fig. 1.10(d) we show the winding of  $\mathbf{h}$  for the parameters used to calculate the bands in Fig. 1.10(a-c). We show that for  $t_1 > t_2$ , the circle (smallest dashed circle) does not wind around the origin ( $O$ ). However, for  $t_1 < t_2$  (biggest solid circle), the circle encloses the origin and hence yields the nontrivial winding number. Here we can check the notion of *continuous transformation*: one cannot continuously transform the smallest circle (dashed circle) staying in  $h_x - h_y$  plane and make the biggest circle (solid circle) without touching the origin where the gap vanishes. This is the concrete evidence that the two gapped phases in two parameter regime ( $t_1 > t_2$  and  $t_1 < t_2$ ) belong to two different topological phases. However, one can avoid touching the origin by lifting up the smallest circle along  $h_z$  axis and smoothly deforming it to the biggest circle. Note that by adding an  $h_z$  term to the Hamiltonian  $H_k$  the chiral symmetry is no longer preserved which is crucial for the topological phase transition.

### 1.4.2 Edge States

One of the hallmark properties of topological insulators is the presence of the edge states in a finite system. In the quantum Hall effect, these states are responsible for

the quantized Hall conductivity. In the SSH model however, being a one-dimensional model, they appear as localized edge states. We can study the existence of these edge states in the SSH model (1.34) from the energy spectrum for a finite system. In Fig. 1.11 we show the energy spectrum for a system of length  $L = 20$  by varying  $t_1$  and fixing  $t_2 = 1$ . The figure shows that when  $t_1 < t_2$ , there exists a pair of degenerate zero energy edge states localized at the edges with zero overlap, which defines the topologically nontrivial phase. At  $t_1 = t_2$ , the bulk gap vanishes where topological phase transition occurs and again the gap opens up when  $t_1 > t_2$ . In this limit, the edge states vanish, defining the trivial phase. This is the phenomenon known as bulk-edge correspondence, where the edge states exist only if the bulk gap is finite for the topologically nontrivial phase, which will be discussed in detail later.

Motivated by all the recent developments, we investigate some of the interesting equilibrium, non-equilibrium and topological phases of interacting bosons in optical lattices in this thesis. In the first part of the thesis, we study the equilibrium properties of ultracold bosons in the presence of two and higher order interactions and long-range interactions that are not explored in the literature. On the other hand, the technique of QW is considered as a new tool to investigate the dynamical properties of interacting systems. Although the QW of a few interacting bosons on empty graphs has been discussed in the literature, the QW of interacting defects offers to uncover the dynamical properties of quantum defects. In the second part of the thesis, we discuss the QW of interacting bosonic defects in one dimension. At the same time, topological phase transitions in interacting many-body systems are also one of the interesting areas of research which provide useful insight about the interaction effect on the topological phase transitions. In the last part of the thesis, we address some of the open problems involving topological phase transitions of interacting bosons in one dimension. Although efforts have been made to understand such interacting many-body systems in various contexts, the topics covered in the thesis address some of the interesting open problems revealing novel phenomena that are accessible in quantum gas experiments.

The QPTs in such complex many-body systems are often intractable using analytical methods, and hence one has to rely on numerical techniques. One obvious method is to solve the many-body Schrödinger's equation using the exact diagonalization (ED) methods. However, due to the exponential growth of the dimension of the Hilbert space with increase in system size, it is absolutely impossible to access the physics of a larger system that can capture the effect of quantum correlations. To circumvent this problem, several powerful methods have been developed to

study the QPTs in the many-body quantum systems, such as the Quantum Monte Carlo (QMC) and the Density Matrix Renormalization Group (DMRG) methods. In this thesis, we will utilize the DMRG and the ED methods to analyze the one-dimensional problems and to address higher dimensional systems, we will employ the self-consistent cluster mean-field theory (CMFT) approach. These methods are among the most suitable methods to analyze strongly correlated systems.

## 1.5 Numerical methods

In this section, we briefly outline the different numerical methods utilized in this thesis.

### 1.5.1 Exact Diagonalization (ED)

In principle, the ED method allows us to calculate the full spectrum of the Hamiltonian describing a particular system. The method is based on three major steps, namely (a) create appropriate basis states, (b) compute the matrix elements of the Hamiltonian using the basis states and (c) diagonalize the Hamiltonian matrix to obtain the eigenspectrum. We use the Fock state basis to span the Hilbert space of the system. For example, for the one-dimensional bosonic system with  $L$  number of sites, the basis vectors can be written as

$$\{|n_1, n_2, n_3, \dots, n_L\rangle\} \equiv |n_1\rangle \otimes |n_2\rangle \otimes |n_3\rangle \otimes \dots \otimes |n_L\rangle \quad (1.42)$$

where  $n_i$  is the number of particles at  $i^{th}$  site. Assuming the on-site dimension to be  $m$ , the full Hilbert space dimension  $D = m^L$  without considering any symmetry in the system. Because of this exponential growth of  $D$ , it becomes impossible to store a single vector for a large system. For example, if we consider hard-core bosons ( $m = 2$ ) and small system of length  $L = 30$  it takes 8GB of memory to store a single  $2^{30}$  dimensional vector with “double” precision. On the other hand, the computational complexity to get all the eigenstate cranks up to  $\mathcal{O}(D^3)$ .

However, one can exploit the use of good quantum numbers of the system to reduce the basis dimension substantially. To get the essence, in the model (1.14) for example, the total number of particles  $N = \sum_j n_j$  is a conserved quantity. This assumption ensures that the Hamiltonian is block diagonal, and each block can be solved separately. This substantially reduces the effective computational cost and

memory needed for the calculations. Note that this process makes the Hamiltonian matrix less sparse, which consumes more time to diagonalize.

Lanczos or Arnoldi method makes it more efficient if we are only interested in lowe-lying states, which is often sufficient for essential studies. In this process, we approximate a Hamiltonian ( $H$ ) in a  $p$ -dimensional orthonormal basis space generated from Krylov space: a vector space created by an arbitrary vector  $v$  and the  $H$ , given by

$$\{v, Hv, H^2v, H^3v, \dots H^{p-1}v\}. \quad (1.43)$$

In this orthonormal basis, the  $H$  becomes  $\tilde{H}$ , whose largest eigenvalue converges rapidly to that of  $H$  with increasing  $p$ . In general, with  $p \ll D$ , the first eigenstate is achieved with high accuracy and to improve the accuracy of excited states, one can increase  $p$  further.

The ED method can also be used to study the dynamics of systems. As mentioned in the beginning, we can have access to the system's dynamical property by solving the corresponding time-dependent Schrödinger-equation. In other words, we need to calculate the time-evolution operator  $\mathcal{U}(t) = e^{-iH(t)t/\hbar}$  and a given state  $|\Psi(t=0)\rangle$  can be evolved in time  $t$  as

$$|\Psi(t)\rangle = \mathcal{U}(t)|\Psi(t)\rangle. \quad (1.44)$$

Note that the exponentiation is a computationally demanding task, which again restricts us to small system sizes.

### 1.5.2 Cluster Mean-field Theory (CMFT) approach

The Cluster Mean-Field Theory (CMFT) approach is one of the simplest methods which utilizes the ED method and the mean-field (MF) decoupling approximations [128] to simplify a many-body problem. In this method, one divides the entire many-body system into small small clusters of finite size, as shown in Fig. 1.12 [129]. While the Hamiltonian of the individual cluster is treated exactly, the couplings between the clusters are treated in a mean-field way.

Let's consider an example of the BH model of interacting bosons as already introduced in Eq. 1.14 as

$$H = - \sum_{\langle i,j \rangle} t_{i,j} (a_i^\dagger a_j + H.c.) + \frac{U}{2} \sum_i n_i(n_i - 1) - \sum_i \mu_i n_i \quad (1.45)$$

Using the MF approximation, one can write the annihilation operator as

$$a_i = \psi_i + \delta a_i \quad (1.46)$$

where  $\psi = \langle a \rangle$  and  $\delta a_i$  is a small fluctuation around the mean value. This approximation transforms the hopping term as

$$a_i^\dagger a_j = a_i^\dagger \psi_j + a_j \psi_i^* - \psi_i^* \psi_j \quad (1.47)$$

by neglecting the terms quadratic in  $\delta a_i$ , which we consider to be infinitesimal. Using Eq. 1.47 the Hamiltonian (1.45) becomes  $H \approx \sum_i H_{MF}$  where

$$H_{MF} = -\mu n + \frac{U}{2}n(n-1) - zt(a^\dagger \psi + a \psi^* - \psi^* \psi) \quad (1.48)$$

This is a single site Hamiltonian. The  $z$  is the lattice co-ordination number. The above Hamiltonian breaks the  $U(1)$  symmetry for all the  $\psi \neq 0$  reflecting the appearance of the SF phase where  $\psi$  represents the superfluid order parameter. The  $\psi$  can be obtained self-consistently through an iterative process to get the ground state of the system. The  $H_{MF}$  estimates the critical point for the SF-MI transition

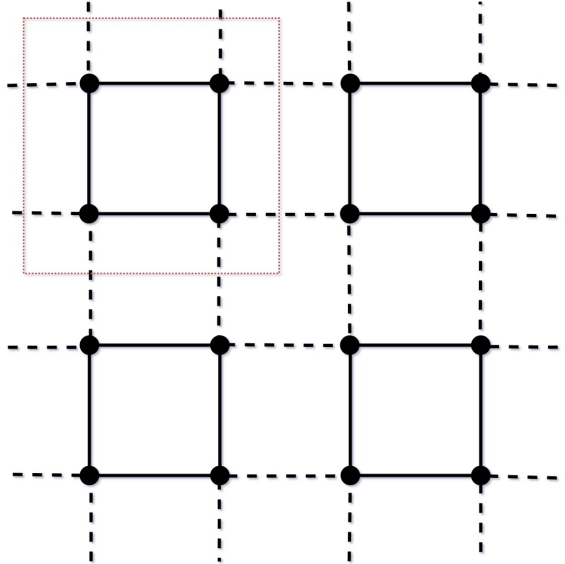


**Figure 1.12:** A two-dimensional square lattice is partitioned with the  $2 \times 2$  clusters. The dotted box represents a unit cluster by the repetition of which the entire lattice is made. In the CMFT approach, the solid lines are treated exactly and the dashed lines connecting clusters are treated in a mean-field way.

corresponding to the BH model to be  $(U/zt)_c = 5.83$ . Note that in the simple MF approach, the entire Hamiltonian is decomposed into single site Hamiltonian and the accuracy of the results increases with the dimension of the system. Being a single site method, this method does not demand computational complexity. However, for the same reason, it ignores the off-site correlations, which are essential to capture useful insights about the system.

The CMFT approach circumvents this problem as one considers a cluster of sites instead of a single site as opposed to the simple MF approach. As shown in Fig. 1.12, the cluster of sites connected by solid lines is treated exactly, whereas the edges connecting two clusters marked by dashed lines are treated in a mean-field way. Using this approximation the resulting BH Hamiltonian can be written as

$$H \approx \sum_c H_{CMF} \quad (1.49)$$

where  $c$  represents the cluster index. Here  $H_{CMF}$  is cluster mean-field Hamiltonian that consists of two parts i.e.

$$H_{CMF} = H_e + H_{mf}. \quad (1.50)$$

Here,  $H_e$  represents the exact part which is given as

$$\hat{H}_e = -t \sum_{\langle i,j \rangle} a_i^\dagger a_j + \frac{U}{2} \sum_i n_i(n_i - 1) - \mu \sum_i n_i, \quad (1.51)$$

where  $i, j$  are sites within the cluster.  $H_{mf}$  represents the mean-field part of the Hamiltonian and is given as

$$H_{mf} = -t \sum_{\langle i,j' \rangle} (a_i^\dagger \phi_{j'} + \phi_i^* a_{j'} - \phi_i^* \phi_{j'}) \quad (1.52)$$

where  $i$  ( $j'$ ) are site indices of the edges of the cluster (neighboring clusters).

Similar to the simple MF approach, the values of  $\psi_i$  are obtained self-consistently in the CMFT approach as well. In this method, the accuracy of the results increases with the cluster size. Unlike the MF approach, the CMFT allows for the calculation of off-site correlation functions within the cluster. This makes the CMFT method more accurate than the simple mean-field theory approach and can capture the qualitative picture of the system with less computing effort than the powerful Quantum Monte Carlo method [44, 129–132].

### 1.5.3 Matrix product states (MPS)

The matrix product states (MPS) are the widely used class of states in quantum information theory and theoretical physics, especially to study the strongly correlated matter. These are simple tensor network representations of the quantum many-body states. An example of such state is one-dimensional AKLT state [133–135] that can be converted to MPS exactly. This powerful way of representing many-body states gives us a perfect variational class to incorporate in the density matrix renormalization group (DMRG) method [136–138]. We briefly explain the salient features of this method in the following.

The transformation of a many-body state to an MPS relies on the well known singular value decomposition (SVD). Consider a one-dimensional system with open boundary condition consists of  $L$  number of sites and a  $d$ -dimensional local state spaces  $\{\sigma_i\}$  where  $i$  is the lattice index. A most general wave function for this system can be written as

$$|\Psi\rangle = \sum_{\sigma_1, \dots, \sigma_L} c_{\sigma_1 \dots \sigma_L} |\sigma_1, \dots, \sigma_L\rangle. \quad (1.53)$$

The number of coefficients  $c_{\sigma_1 \dots \sigma_L}$  is equal to the dimension of the Hilbert space of the system which increases exponentially with  $L$ . Now, a matrix can represent the coefficient vector as [136]

$$c_{\sigma_1 \dots \sigma_L} = c_{\sigma_1, (\sigma_2 \dots \sigma_L)}. \quad (1.54)$$

An SVD performed on this matrix leads to ,

$$c_{\sigma_1 \dots \sigma_L} = c_{\sigma_1, (\sigma_2 \dots \sigma_L)} = \sum_{a_1} U_{\sigma_1, a_1} S_{a_1, a_1} (V^\dagger)_{a_1, (\sigma_2 \dots \sigma_L)}. \quad (1.55)$$

Here  $U$  and  $V$  are unitary matrices and  $S$  is a diagonal matrix containing the so-called *singular values*. Now the  $a_1$  index of the  $S_{a_1, a_1}$  and  $(V^\dagger)_{a_1, (\sigma_2 \dots \sigma_L)}$  can be contructed and transformed into  $c_{a_1, (\sigma_2 \dots \sigma_L)}$ . By renaming  $U_{\sigma_1, a_1}$  with  $A_{a_1}^{\sigma_1}$ , the above equation becomes

$$c_{\sigma_1 \dots \sigma_L} = \sum_{a_1} A_{a_1}^{\sigma_1} c_{a_1, (\sigma_2 \dots \sigma_L)} \quad (1.56)$$

Then, by transforming  $c_{a_1, (\sigma_2 \dots \sigma_L)}$  to  $c_{(a_1 \sigma_2), (\sigma_3 \dots \sigma_L)}$ , and after an SVD we have

$$c_{\sigma_1 \dots \sigma_L} = \sum_{a_1} \sum_{a_2} A_{a_1}^{\sigma_1} U_{(a_1 \sigma_2), a_2} S_{a_1, a_2} (V^\dagger)_{a_2, (\sigma_3 \dots \sigma_L)}. \quad (1.57)$$

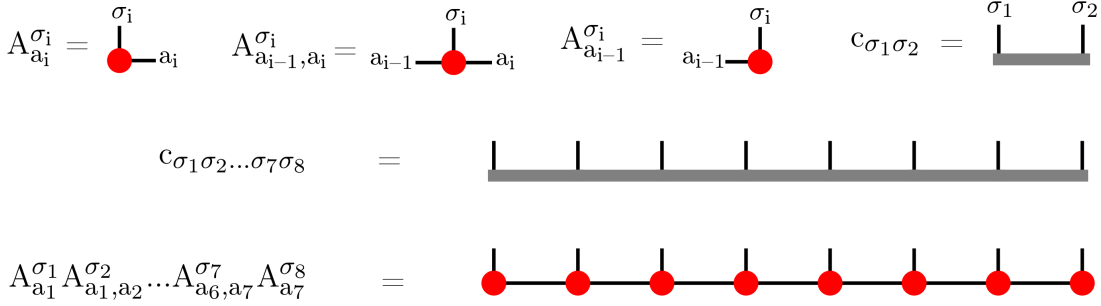


**Figure 1.13:** Figure portrays the graphical representation of a general state and matrix product state as defined in Eqs. 1.53 and 1.59 respectively for a system of length  $L = 8$ . The top row of the figure shows the elements of the product state.

Contracting  $a_2$  in  $S$  and  $V$ , the above equation can be modified as

$$c_{\sigma_1 \dots \sigma_L} = \sum_{a_1} \sum_{a_2} A_{a_1}^{\sigma_1} A_{a_1, a_2}^{\sigma_2} c_{a_2 \sigma_3), (\sigma_4 \dots \sigma_L)}. \quad (1.58)$$

This process is repeated until the other end of the lattice is reached. Finally, the wave function transforms into an MPS which is given by

$$|\Psi\rangle = \sum_{a_1, \dots, a_L} A_{a_1}^{\sigma_1} A_{a_1, a_2}^{\sigma_2} \dots A_{a_{L-2}, a_{L-1}}^{\sigma_{L-1}} A_{a_{L-1}}^{\sigma_L} |\sigma_1, \dots, \sigma_L\rangle. \quad (1.59)$$

In the above equation,  $a_i$  are called bond indices, whereas  $\sigma_i$  are the physical indices. The MPS can be conveniently represented in a graphical way. In Fig.1.13, we depict an MPS and different elements of an MPS in graphical form for a system of length  $L = 8$ . We also represent the above formalism to create the MPS graphically in Fig.1.14.

The MPS representation of states is categorized into three types. The one shown in Eq. 1.59 is called Left-canonical MPS. There are two other representations of the MPS called the right-canonical MPS and the mixed-canonical MPS. The procedure of creating right-canonical MPS is similar to that of the Left-canonical MPS. However, the right-canonical MPS is developed by contracting from right to left instead of left to right. The Right-canonical MPS of  $|\Psi\rangle$  can be written as

$$|\Psi\rangle = \sum_{a_1, \dots, a_L} B_{a_1}^{\sigma_1} B_{a_1, a_2}^{\sigma_2} \dots B_{a_{L-2}, a_{L-1}}^{\sigma_{L-1}} B_{a_{L-1}}^{\sigma_L} |\sigma_1, \dots, \sigma_L\rangle. \quad (1.60)$$

where  $B_{a_{i-1}, a_i}^{\sigma_i}$  are created from the corresponding  $(V^\dagger)$  matrices. The last variant

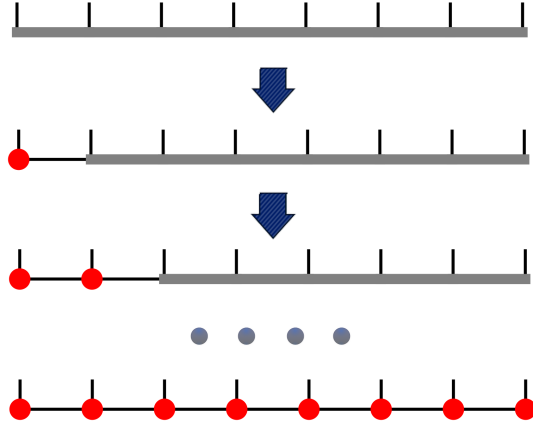


**Figure 1.14:** The graphical representation of the left canonical MPS formation using SVD process for a system of length  $L = 8$ .

that we are going to use in the DMRG method is called the Mixed-canonical MPS. In this scenario, we create an MPS of a state from both left ( $1^{st}$  to the  $l^{th}$  sites) and right ( $L^{th}$  to  $(L - l)^{th}$  sites) ways. A typical Mixed-canonical MPS can be written as

$$|\Psi\rangle = \sum_{a_1, \dots, a_L} A_{a_1}^{\sigma_1} \dots A_{a_l}^{\sigma_l} S_{a_l, a_l} B_{a_l, a_{l+1}}^{\sigma_{l+1}} \dots B_{a_{L-1}}^{\sigma_L} |\sigma_1, \dots, \sigma_L\rangle. \quad (1.61)$$

A graphical representation of a Mixed-canonical MPS for  $L = 8$  is shown in Fig 1.15 where we consider  $l = 4$ . Since the representations discussed above are exact, the total dimension would scale exponentially with  $L$ .

Once we have an MPS, the expectation value of an operator or the overlap with other MPS is very easy to calculate [136]. For example, consider two left-canonical MPSs  $|\Psi\rangle$  and  $|\Phi\rangle$  described by the networks of  $A^{\sigma_l}$  and  $\tilde{A}^{\sigma_l}$  ( $a_i$  indices are hidden) matrices respectively. The overlap between them can be calculated efficiently by contracting the common indices from one boundary to another (say, 1 to  $L$ ):

$$\langle \Phi | \Psi \rangle = \sum_{\sigma_L} \tilde{A}^{\sigma_L \dagger} \left( \dots \left( \sum_{\sigma_2} \tilde{A}^{\sigma_2 \dagger} \left( \sum_{\sigma_1} \tilde{A}^{\sigma_1 \dagger} A^{\sigma_1} \right) A^{\sigma_2} \right) \dots \right) A^{\sigma_L} \quad (1.62)$$

$$S_{a_4, a_4} = \text{---} \diamond \text{---} \quad A_{a_1}^{\sigma_1} \dots A_{a_3, a_4}^{\sigma_4} S_{a_4, a_4} B_{a_4, a_5}^{\sigma_5} \dots B_{a_7}^{\sigma_8} = \text{---} \text{---} \text{---} \text{---} \text{---} \text{---} \text{---} \text{---} \quad \text{---} \text{---} \text{---} \text{---} \text{---} \text{---} \text{---} \text{---}$$

**Figure 1.15:** The graphical representation of a mixed canonical MPS for a system of length  $L = 8$  following Eq. 1.61.

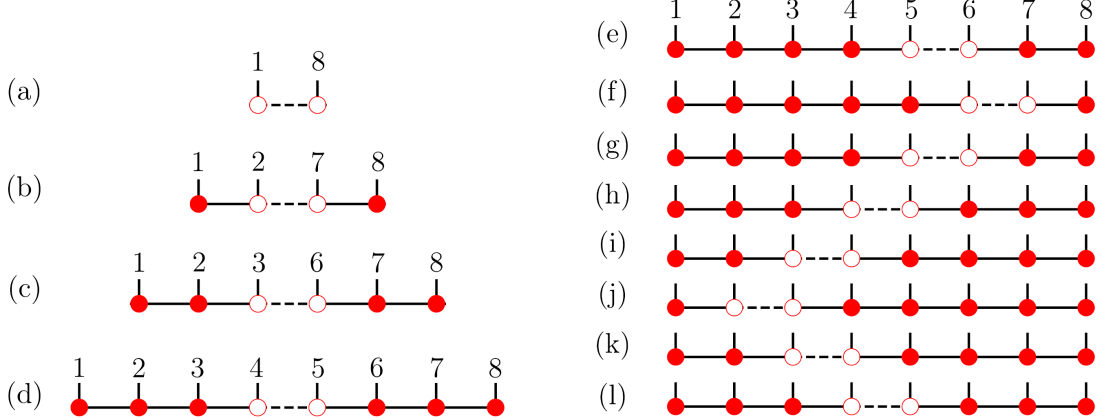


**Figure 1.16:** The graphical representation of the algorithm for finding the ground state in the DMRG process is shown for a system of length  $L = 8$  with open boundary conditions. (a-d) Show the creation of an arbitrary MPS using an infinite DMRG process. (e-l) Show one complete sweep of finite size algorithm of variational search. If we repeat (e-l) several times, the initial state (d) converges to the ground state of the Hamiltonian.

Here we hide the  $a_i$  indices for simplicity.

By using a similar prescription, the expectation value of an operator can also be calculated. As an example consider an  $L$  point operator  $O = O_1 \otimes O_2 \otimes \dots \otimes O_L$ . Note that in most of the cases most of the on-site operators ( $O_i$ ) will be identity operators. Now the expectation value of the operator can be written as

$$\langle \Psi | O | \Psi \rangle = \sum_{\sigma_L \sigma'_L} O_L^{\sigma_L \sigma'_L} A^{\sigma_L \dagger} \left( \dots \left( \sum_{\sigma_2 \sigma_2} O_2^{\sigma_2 \sigma'_2} A^{\sigma_2 \dagger} \left( \sum_{\sigma_1 \sigma'_1} O_1^{\sigma_1 \sigma'_1} A^{\sigma_1 \dagger} A^{\sigma'_1} \right) A^{\sigma_2 \dagger} \right) \dots \right) A^{\sigma'_L} \quad (1.63)$$

#### 1.5.4 Density Matrix Renormalization Group (DMRG)

The Density Matrix renormalization group (DMRG) method is the prescription to prevent the exponential growth of the Hilbert space while providing accurate results for low dimensional systems. Steve White proposed the method in 1992 [137] as an improvement over the numerical renormalization group (NRG). The method finds the ground state of the system by variational approximation through local optimization. As a further development, the DMRG method was then applied to MPSs that increased the flexibility and power of the DMRG method by manyfold. The key idea here is to minimize the bond dimension ( $a_i$ ) of the MPS by eliminating

a part of the singular value spectrum that is negligible in weight. For example, in the low entangled states like the gapped state, the singular values ( $\lambda_k$ ) decrease exponentially with its spectral position ( $k$ ),

$$\lambda_k \propto e^{-\alpha k}, \quad \alpha > 0. \quad (1.64)$$

In a variational process of ground state search, the aim is to minimize the energy functional defined by,

$$E_g = \frac{\langle \Psi_g | H | \Psi_g \rangle}{\langle \Psi_g | \Psi_g \rangle} \leq \frac{\langle \Psi | H | \Psi \rangle}{\langle \Psi | \Psi \rangle} \quad (1.65)$$

However, in the MPS description, this is a high dimensional non-linear problem to solve. In this case, the local update using the DMRG sweep helps to optimize the local tensors. In a so-called two site DMRG process we write the Hamiltonian in the following form

$$H = \sum_k H_L^k \otimes H_{i,j}^k \otimes H_R^k. \quad (1.66)$$

Here, the Hamiltonian is divided into the left and the right part which are called the system parts. In this case, the local minimization becomes an eigenvalue problem

$$\tilde{H}_{a\sigma_i\sigma_j b}^{a'\sigma'_i\sigma'_j b'} X_{a'\sigma'_i\sigma'_j b'} = E X_{a'\sigma'_i\sigma'_j b'} \quad (1.67)$$

where

$$\tilde{H}_{a\sigma_i\sigma_j b}^{a'\sigma'_i\sigma'_j b'} = \sum_k (\tilde{H}_R^k)_a^{a'} (\tilde{H}_L^k)_b^{b'} (H_{i,j}^k)_{\sigma_i\sigma_j}^{\sigma'_i\sigma'_j} \quad (1.68)$$

Here  $\tilde{H}_R^k$  and  $\tilde{H}_L^k$  may be obtained from the previous step and  $X_{a'\sigma'_i\sigma'_j b'}$  describes the local wavefunction. The eigenvalue problem shown in Eq. 1.67 can be solved using the Lanczos algorithm. Using an initial guess that can be extracted from the previous iteration, the process can be made faster, especially when it is close to the convergence. As a next step, the updated MPS is computed from  $X_{a\sigma_i\sigma_j b}$  after truncating it to the desired bond dimension in the SVD process.

To get the ground state of a Hamiltonian, the algorithm starts with an arbitrary MPS formed by an infinite DMRG process with a given bond dimension. A graphical representation is shown in Fig. 1.16(a-d) for convenience. The dotted line shows the connection between the left and the right parts of the system, and the tensors with the empty circles are the resulting tensor we create in that step. The variational optimization of the local tensor is done by sweeping from left to right and vice-versa through the system length. This process is recognized as the finite size DMRG

process. A *two-site DMRG* sweeping process is graphically presented in Fig. 1.16(e-l) for one complete sweep. Here also the dashed line connects the two parts of the system and the local tensors marked with open circles are optimized in the process mentioned above in that step.

There are different sources of error in this process of finding the eigenstates [139]. Most important of them is the *truncation error*

$$p = \sum_{a=M+1}^D S_\alpha^2 = 1 - \sum_{\alpha=1}^M S_\alpha^2. \quad (1.69)$$

which arises due to the discarded part of the singular value spectrum during the DMRG process. It has been shown that the error in the ground-state energy is proportional to  $p$  [139]. Other than the truncation error, there are two more sources of error. One arises from the iterative process of the numerical diagonalization and the other from the lack of convergence within the class of the MPS states. In this thesis, we have implemented the DMRG method for one-dimensional open boundary systems where it works the best. In general, it can be utilized for systems with periodic boundary conditions [140], infinite systems [141, 142] and two-dimensional lattices [143, 144].

### 1.5.5 Time dependent simulation

The time evolution of a quantum state of a strongly correlated many-body system with time-dependent Hamiltonian is a highly nontrivial problem. Because of the tremendous success of the DMRG method in addressing the equilibrium properties of strongly correlated systems, different attempts have been made to study non-equilibrium properties using the time-dependent DMRG method [145–147]. G. Vidal developed an algorithm to simulate the time evolution of the many-body states [148, 149]. In the algorithm, the Hilbert space dynamically adapts itself for better accuracy. This algorithm is called the time-evolving block decimation (TEBD), which fits perfectly with the MPS framework.

The essential technique of TEBD is to write the time evolution operator  $U(\delta t) = e^{-iH\delta t}$  (where  $\hbar$  is considered to be 1), introduced in Eq. 1.44, for a small time  $\delta t$  using Suzuki-Trotter (ST) decomposition [150, 151]. If the Hamiltonian of interest contains only the nearest-neighbor interactions, then the Hamiltonian can be re-

written in terms of local two site terms as

$$H = \sum_i h_{(2i-1),2i} + \sum_i h_{2i,(2i+1)} = H_{odd} + H_{even}. \quad (1.70)$$

Here all  $H_{odd}$  or  $H_{even}$  terms commute among themselves but,  $h_{(2i-1),2i}$  and  $h_{2i,(2i+1)}$  do not commute in general since they share a common site  $2i$ . This non-commutative nature gives rise to an error in the ST decomposed time evolution operator. The first order Suzuki-Trotter (ST(1)) decomposed  $U(\delta t)$  can be written as

$$e^{-iH\delta t} = e^{-iH_{odd}\delta t} + e^{-iH_{even}\delta t} + O(\delta t^2). \quad (1.71)$$

So, the time evolved wavefunction becomes

$$|\Psi(t + \delta t)\rangle = e^{-iH_{odd}\delta t}e^{-iH_{even}\delta t}|\Psi(t)\rangle \quad (1.72)$$

In the MPS description of the wavefunction, the two site operators in  $H_{odd}$  or  $H_{even}$  can be operated independently since they commute with each other. After operating a two-site operator, the local dimension increases by  $d^2$  times and the MPS description vanishes on those two sites. This tells us that at every time step, the dimension increases exponentially. However, applying the SVD technique, one can reduce the dimension by truncating the singular value spectrum as before and also restore the MPS description after each time step. Now, discretizing the total time of evolution  $t = N\delta t$ , the repeated operation of the Eq. 1.72 on the initial state can evolve the state to time  $t$ . An example of this method of time evolution is depicted in figure 1.17 for  $N = 2$ . The ST decomposition described above works if the Hamiltonian only has the nearest-neighbor terms. In general, if the Hamiltonian has the next-nearest-neighbor terms, the ST decomposition of the evolution operator is done with three-site local operators instead of two.

Note that during every step of time evolution, entanglement builds up in the system. In the process of truncation in SVD, the error also builds up in the wavefunction. However, for nonequilibrium evolution, the entanglement increases linearly in the system with time [152], which may not be a problem for most of the systems. Apart from this, errors also arise from the ST decomposition, which is of the order of  $\delta t^2$ . This error can be reduced by considering a very short time step  $\delta t$ . The error in ST decomposition can be further reduced by considering higher-order ST decomposition since in ST( $n$ ), the error comes of the order of  $\delta t^{n+1}$ . In the following,

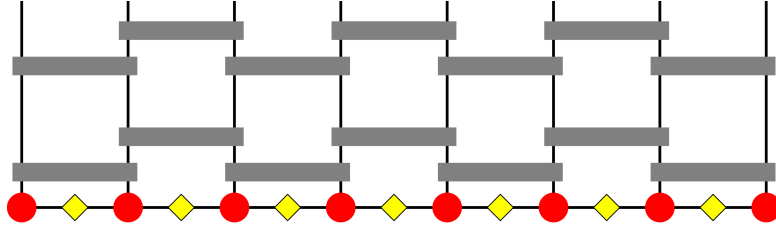


**Figure 1.17:** The graphical representation of the TEBD algorithm is shown. Here the Suzuki-Trotter decomposed (first-order) evolution operator operates on the initial MPS for a system of  $L = 8$ . Here the initial state is evolved by  $2\delta t$  time.

an ST(2) decomposition is shown.

$$e^{-iH\delta t} = e^{-iH_{odd}\delta t/2}e^{-iH_{even}\delta t}e^{-iH_{odd}\delta t/2} + O(\delta t^3). \quad (1.73)$$

Using small time steps and higher-order ST decomposition, this error can also be significantly minimized. Nevertheless, considering all these sources of errors, the accessible time scale allows us to study the system of interest efficiently.

## 1.6 Chapterwise outline of the thesis

In Chapter 1, we have presented an introduction to the topic of QPTs in systems of ultracold bosons in optical lattices with emphasis on the SF-MI transition. Then we have briefly discussed about the role of multi-body interaction and the dipole-dipole interactions in the system. In the next part, we have discussed about the phenomenon of quantum walk, which can be utilized to study the dynamical properties of a quantum mechanical system. We have then discussed the physics of topological phase transition in the context of the SSH model. After giving a brief motivation for our work, we have provided a discussion on the numerical methods used in this thesis.

The rest of the thesis is divided into several chapters, including the outlook. The main chapters are categorized into three parts depending on the topics analyzed in this thesis. The second and third chapters focus on the equilibrium phase transitions, the fourth chapter contains the non-equilibrium studies. The studies based on the topological phase transitions are discussed in the fifth, sixth and seventh chapters. In the following, we briefly discuss the contents of all the chapters.

In Chapter 2, we discuss the quantum phase transition in a system of multi-body interacting bosons on a two-dimensional optical lattice and analyze the formation

of two-body repulsively bound bosonic pairs in the context of the Bose-Hubbard model. In this chapter, we discuss the details about the QPTs obtained using the CMFT method. We also provide a detailed comparison of our results with the results obtained using the Projected Entangled Paired States (PEPS) method.

In Chapter **3**, a system of hardcore and three-body constrained dipolar bosons in a two-leg ladder is analyzed. A brief introduction to the QPT in a two-leg Bose-Hubbard ladder is discussed. Then the modified BH model for a non-locally coupled ladder of constrained dipolar bosons is introduced. The details of the phases and phase transitions obtained using the CMFT based calculation are discussed.

Chapter **4** is completely dedicated to the dynamical properties of systems of interacting bosons in one-dimensional lattices in the framework of the continuous-time quantum walk. In the first part of this chapter, the QW of interacting Mott insulator defects with only two-body interactions is discussed. Following this, a discussion on the QW of Mott insulator defects in the presence of local multi-body interactions is provided. In the end, the effect nearest neighbor interaction on the QW of two nearest-neighbor defects is analyzed.

The focus of the next part of the thesis is mainly on the study of topological phase transition in systems of interacting bosons in one dimensional SSH model. In this context, two different cases are considered in this thesis. In one case, the topological phase transition of a system of three-body constrained bosons is discussed. In the other case, the phenomenon of topological inheritance is studied in a system of two-component hardcore bosons.

Before discussing the topological properties, in Chapter **5**, the bulk properties of a system of three-body constrained bosons in a double-well lattice possessing an SSH model type hopping dimerization is discussed in detail. After briefly discussing the double-well lattice and its importance, the combined effect of three-body constraint and two-body interactions leading to rich phase diagrams are presented.

Chapter **6** is based on the topological phase transitions in a system of bound bosonic pairs in the context of the SSH model. Although the topological phase transitions in the SSH model are based on a system of free fermions at half-filling, this chapter is focused on an effective topological phase transition in the case of attractively bound bosonic pairs. The details of the bulk and topological properties of the bound bosonic pairs are analyzed.

Chapter **7** is based on the topological properties of interacting two-component spinless fermion or hardcore boson in the context of the half SSH-Hubbard model. Assuming one component subjected to the SSH type dimerization and allowing

## Chapter 1. Introduction

uniform hopping for the other component, the physics of topological inheritance is discussed in this chapter.

Finally, Chapter 8 highlights the conclusions drawn from our work. This also includes the possible extension of the results discussed in the thesis as well as a list of new problems that can be done in the future.

## Chapter 2

# Quantum phases of multi-body interacting bosons in optical lattices

### 2.1 Introduction

The physics of the multi-body interacting BH model has been widely discussed in the literature, as already mentioned in the introduction. In a recent proposal in Ref. [35], it was shown that the strength of the three-body interaction could be tuned by coupling it to the Efimov states, which leads to a non-trivial form of the interaction which is given as  $U_3\delta_{n,3}$ , where  $U_3$  represents the strength of the three-body interaction. Analysis of the BH model with such three-body interaction using the single site mean-field theory approach complemented by the Quantum Monte Carlo (QMC) simulations revealed a first order phase transition between the MI1 and MI3 lobes by completely suppressing the MI2 lobe in the limit of  $|U_3|/U_2 > 1$  [35], where  $U_2$  is the strength of the two-body interaction. However, this finding was later found to be inconsistent when compared with the results obtained using the DMRG method and the CMFT approach in one and two-dimensional systems respectively [132]. A careful analysis in Ref. [132] showed that there exists no first order transition between the MI lobes for the parameter choice considered in Ref. [35]. Rather, the competing two and three-body interactions lead to the formation of a non-trivial PSF phase in between the MI1 and MI3 lobes where the bosons tend to move in pairs even in the presence of the two-body repulsive interactions. This reveals a kind of two-body repulsively bound pairs driven by a mechanism completely different from the one already observed in optical lattices by Winkler *et al.* [153] where the pair formation occurs due to the competition between the two-body interaction and the bandwidth associated to the band structure.

Now the question is whether this kind of PSF phase of two-body repulsive bound pairs can be stabilized in a more general BH model with tunable multi-body interaction or not. The interesting proposal by D. Petrov [48], which allows simultaneous manipulation of multi-body interactions in optical lattice [48, 49], promotes the study with multi-body interactions. In this context, we explore physics arising due to these multi-body interacting bosons on a two-dimensional lattice where we search for the PSF phase of the two-body repulsive bound pairs in the presence of higher-order interactions.

## 2.2 Multi-body interacting bosons in two-dimensional optical lattice

As discussed in Sec. 1.2.4, the general Hamiltonian which describes the physics of such system is the multi-body interacting BH model given by

$$H = -t \sum_{\langle i,j \rangle} (a_i^\dagger a_j + H.c.) + \sum_{p=2}^M \left( U_p \sum_i \frac{(n_i)!}{p!(n_i-p)!} \right) - \mu \sum_i n_i \quad (2.1)$$

where  $a_i^\dagger(a_i)$  is the bosonic creation (annihilation) operator,  $n_i$  is the number operator for the  $i^{th}$  site, and  $\langle i, j \rangle$  denotes the nearest neighbor sites. While  $t$  represents the nearest-neighbor hopping amplitude,  $U_p$  is the on-site  $p$ -body interaction strength. Depending on the value of  $M$ , one gets the corresponding multi-body interacting BH model.  $\mu$  is the chemical potential associated to the system in the grand canonical ensemble which decides the number of particles in the system. In our present analysis we consider the combined effect of two-, three- and four-body interaction and the Hamiltonian for this can be obtained by retaining the terms up to  $M = 4$  in Eq.2.1 which is given as

$$H = -t \sum_{\langle i,j \rangle} (a_i^\dagger a_j + H.c.) + \frac{U_2}{2} \sum_i n_i(n_i - 1) + \frac{U_3}{6} \sum_i n_i(n_i - 1)(n_i - 2) + \frac{U_4}{24} \sum_i n_i(n_i - 1)(n_i - 2)(n_i - 3) - \mu \sum_i n_i \quad (2.2)$$

where the terms have their usual meaning as discussed before. We numerically investigate the ground state properties of the model shown in Eq. 2.2 in two-dimension by the self-consistent CMFT approach [129–131], the details of which is discussed in the introduction. In the CMFT approach , we divide the Hamiltonian into several clusters of finite number of sites and each cluster interacts with the rest of the system in a mean-field way i.e.

$$H_{CMF} = \sum_{i,j \in C} H_C - t \sum_{\substack{\langle i,j \rangle \\ i \in B, j \notin C}} (a_i^\dagger \psi_j + H.c.) \quad (2.3)$$

Here,  $H_C$  is the cluster Hamiltonian identical to Eq. 2.2 with index  $i, j$  belonging to the cluster  $C$ . The second term which is the mean-field expression for the hopping term from the  $i^{th}$  site at the cluster boundaries ( $B$ ) to the nearest neighbor [154].  $\psi$  is the superfluid order parameter which is determined self consistently. In order to obtain the insights about various quantum phases we utilize the average density and the superfluid density of the system  $\rho = 1/L \sum_i n_i$  and  $\rho_s = 1/L \sum_i \psi_i^2$  respectively computed from the CMFT ground state where  $L$  is number of sites in a cluster. In this case we consider a four site cluster which is sufficient to predict the relevant physics .

We compare the results obtained using the CMFT approach by the calculations based on the infinite Projected Entangled Pair States (iPEPS) algorithm, which are two-dimensional tensor network techniques [155, 156]. Such techniques are built upon genuine quantum correlations and hence, goes beyond mean field calculations. Besides, we can directly target the thermodynamic limit by assuming translational invariance over some sites. Another advantage is that unlike QMC techniques, it does not suffer from the infamous sign problem for fermionic and frustrated systems [157]. For these reasons PEPS techniques have been used in the past to study hard condensed matter problems such as frustrated kagome antiferromagnets[158–161] and real materials [162–164]. It has been able to beat state-of-the-art QMC calculations in finding the ground state energy of the doped Hubbard model [165], and helped settle controversies that would have otherwise been difficult such as the magnetization plateaus of the Shastry-Sutherland model[166], phase diagrams of steady states of dissipative spin models[167], etc. The technique has now been extended to finite temperature calculations [168–171] and the difficult problem of time evolution in two-dimension [172–175].

For the purpose of this work, we use an iPEPS with a two-site unit cell in the

thermodynamic limit. We approximate the ground state of the Hamiltonian given in Eq. 2.2 using the so-called simple update [176] with bond dimension  $D = 2$  and  $D = 4$  which proves sufficient for our purpose.

### 2.2.1 Results

In this section we move on to discuss our results in detail. The model shown in Eq. 2.2 consists of three different interactions such as  $U_2$ ,  $U_3$  and  $U_4$ . Our goal is to search for the bound pairs in presence of repulsive  $U_2$  (i.e.  $U_2 > 0$ ) and attractive  $U_3$  (i.e.  $U_3 < 0$ ). Due to the attractive nature of the  $U_3$ , we have to consider a large repulsive  $U_4$  (i.e.  $U_4 > 0$ ) in order to prevent the system from collapse and also to stabilize the MI3 phase. For simplicity, we define two ratios such as  $U_4/U_3$  and  $U_3/U_2$  and analyze the ground state phase diagram of the system. In the case of the BH model shown in Eq. 2.2, it is well known that the presence of the interaction up to  $U_3$  largely affects the SF-MI phase transitions with modified Mott lobes at higher densities. While the MI lobes corresponding to  $\rho \geq 2$  get enlarged by the three-body repulsion  $U_3$  [31, 33], an attractive  $U_3$  results in shrinking up of the higher MI lobes [33]. However, in this case we show that a large four-body repulsive interaction  $U_4$  leads to interesting phenomena. We show that as the ratio  $U_3/U_2$  increases the MI3 lobe expands by simultaneously shrinking the MI2 lobe which eventually disappears for some specific ratio. In Fig. 2.1, we depict the phase diagram corresponding to the ground state of Eq. 2.3 using the CMFT approach in the  $\mu/U_2$  and  $1/U_2$  plane for  $U_4/U_3 = -3$  and  $U_3/U_2 = -2$ . The phase diagram clearly shows the MI phases at different densities, the SF and the PSF phases. The MI lobes are denoted by the continuous lines and the dashed line separates the empty state.

The phase diagram is obtained by examining various physical quantities. The SF to MI transitions are characterized by examining the behavior of change in the total density of the system  $\rho$  and the superfluid density  $\rho_s$  with respect to increase in chemical potential  $\mu$ . In the SF phase  $\rho$  increases continuously with increase in  $\mu$ . However, in the MI phase  $\rho$  remains constant for a range of  $\mu$  and at the same time  $\rho_s$  vanishes. In Fig. 2.2(a) we show the  $\rho - \frac{\mu}{U_2}$  plot determined using the CMFT approach for various values of  $1/U_2 = 0.02, 0.04$  and  $0.06$  which cut through different regions of the phase diagram of Fig. 2.1 indicating the MI plateaus and the SF regions. The end points of the plateaus correspond to two different chemical

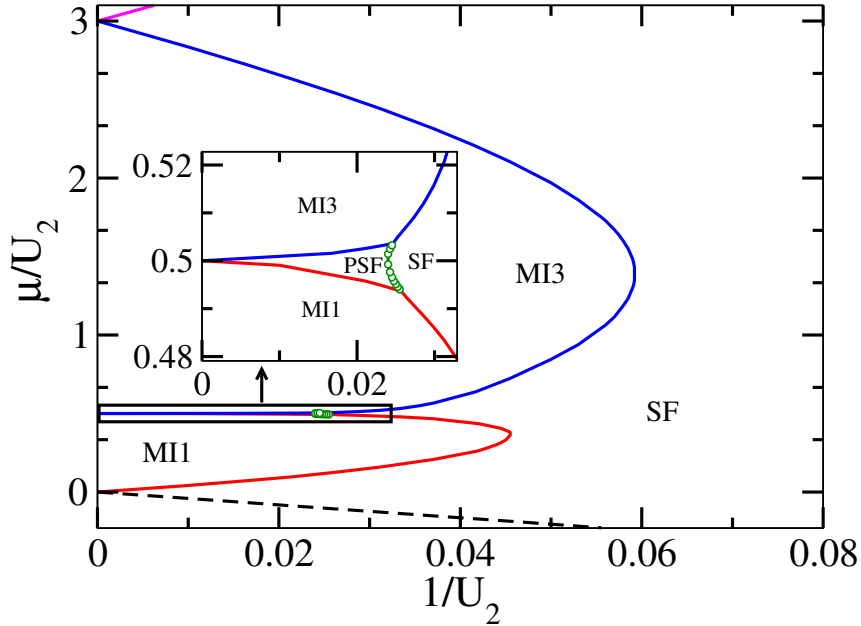


**Figure 2.1:** CMFT phase diagram for  $t = 1$ ,  $U_3/U_2 = -2.0$  and  $U_4/U_3 = -3.0$ . Solid lines show the boundaries of MI phases and dashed line separates the empty state. Inset shows the PSF-SF boundary marked by green line with circles.

potentials  $\mu^+$  and  $\mu^-$  of the system defined as

$$\mu^+ = E_L(N+1) - E_L(N); \quad \mu^- = E_L(N) - E_L(N-1). \quad (2.4)$$

Here,  $E(N)$  denotes the ground state energy of the system with  $N$  particles. The difference  $G = \mu^+ - \mu^-$  quantifies the gap in the MI phase which vanishes in the SF phase. The signatures of the MI and SF phases are also confirmed from the  $\frac{\mu}{U_2} - \rho_s$  plot in Fig. 2.2(b) which shows finite(zero) superfluid density in the SF(MI) phase.

Interesting thing happens in the regime of large interactions. It can be seen from Fig. 2.2 that for  $U_2 = 50$  ( $1/U_2 = 0.02$ ), there are discrete jumps in  $\rho$  in steps of  $\Delta\rho = 0.5$  (blue down triangles) with respect to increase in  $\frac{\mu}{U_2}$  in the region between two plateaus corresponding to the MI1 and MI3 phases. This behaviour indicates a change in the particle number  $\Delta N = 2$  (since we have  $L = 4$  in our CMFT calculation) which is a signature of pair formation. We can identify this phase as the PSF phase which can be confirmed from the pair correlation functions [44, 132, 177]. To this end we compute the  $n$ -particle nearest neighbor correlation functions defined as

$$\Gamma_n = \langle (a_i^\dagger)^n (a_j)^n \rangle. \quad (2.5)$$

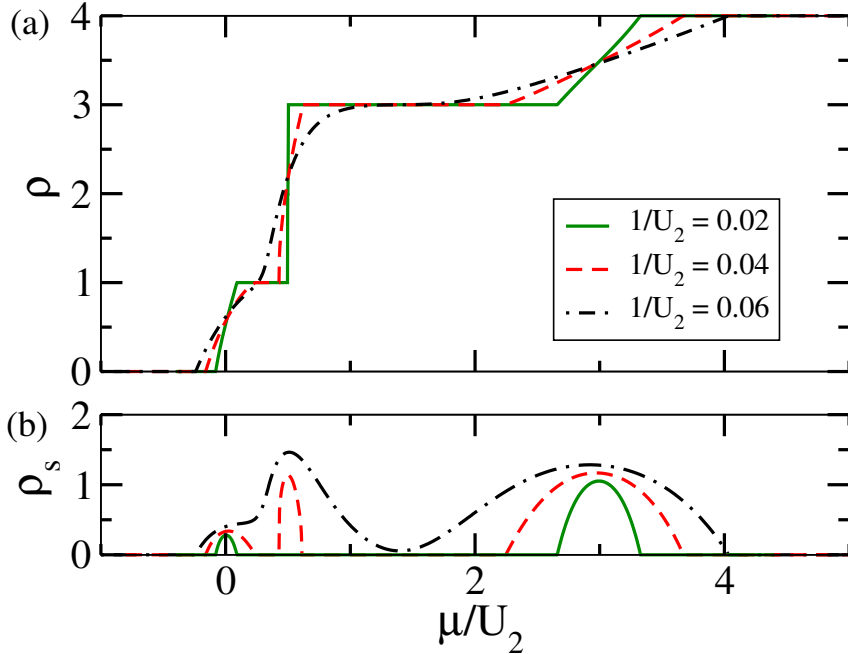


**Figure 2.2:** (a)  $\rho$  vs.  $\mu/U_2$  and (b)  $\rho_s$  vs.  $\mu/U_2$  plots for several cuts through the phase diagram of Fig. 2.1 corresponding to  $0.02$ (green solid line),  $0.04$ (red dashed) and  $1/U_2 = 0.06$ (black dot-dashed).

where  $i$  and  $j$  are the nearest neighbor site index of our four site cluster.

In Fig. 2.3 we also plot the correlation functions  $\Gamma_n$  for  $n = 1, 2$  and  $3$  corresponding to the single- (black circles), two- (red squares) and three-particles (green up triangles) respectively for different values of  $\mu/U_2$  at a fixed  $1/U_2 = 0.02$  of the phase diagram given in Fig. 2.1. It can be seen that at the plateau regions corresponding to the MI1 and MI3 phases, all the correlation functions are vanishingly small. However, for the values of  $\rho$  away from the plateau regions i.e.  $1 < \rho < 3$ ,  $\Gamma_2$  clearly dominates over  $\Gamma_1$  and  $\Gamma_3$ . This is a clear indication of the existence of the PSF phase which is sandwiched between the MI1 and MI3 lobes in the large  $U_2$  regime as shown in Fig. 2.1. There exists a SF-PSF phase transition at these densities indicated by the green circles.

As mentioned before, the CMFT approach can predict the quantum phases qualitatively and efficiently. However, to concretely establish the existence of the PSF phase we compare our CMFT calculation with the results obtained using the iPEPS method. In the iPEPS simulation we use various physical quantities to identify different quantum phases. The gapped MI phases are identified by looking at the behavior of the chemical potential  $\mu$  with respect to the average density  $\rho$ . The SF and the PSF phases are characterized by their respective order parameters defined

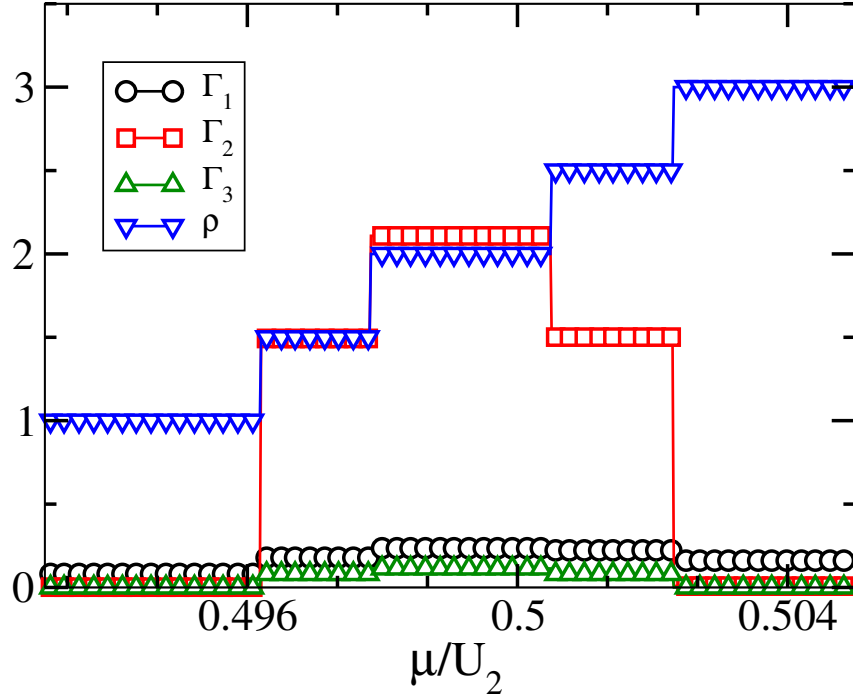


**Figure 2.3:** Correlation functions  $\Gamma_n(i,j)$  for a cut along  $1/U_2 = 0.02$  in the phase diagram Fig.2.1. The corresponding values of  $\rho$ (blue down triangles) are shown for comparison.

as;

$$O_{SF} = |\langle a_i \rangle|^2 \quad (2.6)$$

and

$$O_{PSF} = |\langle a_i^2 \rangle|^2. \quad (2.7)$$

We compute these parameters for several values of  $U_2$  and find signatures of different phases and phase transitions similar to that obtained using the CMFT method. In Fig. 2.4(a), we plot  $\rho$ (black circles),  $O_{SF}$ (red squares) and  $O_{PSF}$ (green triangles) against  $\mu/U_2$  for fixed  $1/U_2 = 0.015$ ,  $U_3/U_2 = -2$  and  $U_4 = \infty$ . Note that the choice of  $U_4$  restricts the local Hilbert space to a maximum of three particles per site and simplifies our iPEPS calculation while retaining the underlying physics of the system. It can be clearly seen from Fig. 2.4(a) that there exists two Mott plateaus at  $\rho = 1$  and  $3$  corresponding to the gapped MI1 and MI3 phases. Inside these plateau regions both the superfluid order parameters vanish. However, in the region between the two MI phases, the value of  $O_{SF}$  remains vanishingly small, whereas  $O_{PSF}$  becomes finite indicating the existence of the PSF phase. We have also performed the same calculation for a different cut that passes through the region of

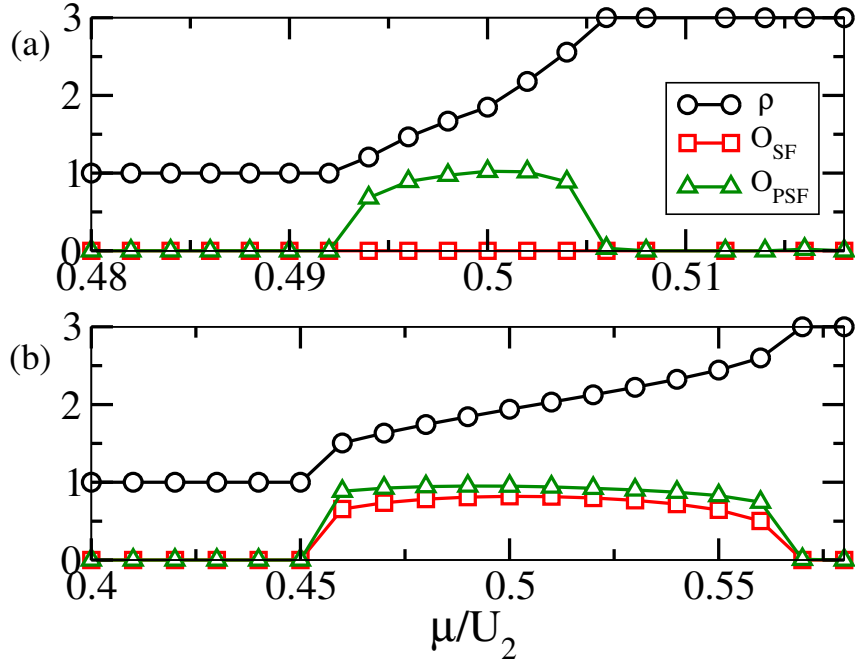


**Figure 2.4:** (a) iPEPS data for  $\rho$ ,  $O_{SF}$  and  $O_{PSF}$  for  $1/U_2 = 0.015$  showing the MI1, MI3 and the PSF phases. (b) Similar calculations for a cut passing through the normal Superfluid (SF) region at  $1/U_2 = 0.04$ . This phase is characterized by a non-vanishing value of both  $O_{SF}$  as well as  $O_{PSF}$  while the PSF phase is characterized by a vanishing  $O_{SF}$  and non-zero  $O_{PSF}$ .

normal superfluid (SF) as shown in Fig. 2.4 (b) for  $1/U_2 = 0.04$ . We find that both the  $O_{SF}$  as well as the  $O_{PSF}$  are non-zero in this region which defines our SF phase.

It is to be noted that the physics obtained using the CMFT approach and the iPEPS method are similar to the one reported in Ref. [132]. The important difference is the choice of the interactions. We explicitly show that in the presence of two-body repulsion the bosons prefer to move in pairs due to the large three-body attraction and four-body repulsion. The physics of the pair formation and the PSF phase on top of the MI1 phase can be understood from the energy consideration as discussed in Ref. [132]. Due to the large three-body attraction the system will tend to acquire two particles at a time to reach the energy minimum by forming a trimer. However, because of the presence of uniform two body repulsion from the MI1 background the added particles tend to move in pairs without affecting the system energy. This leads to the PSF phase in the system. This is indeed an interesting manifestation of the multi-body interactions in the Bose-Hubbard model. We would like to mention that this pair formation is not limited to the region between the MI1 and MI3 lobes. One can in principle create the PSF phase between higher Mott lobes such as between

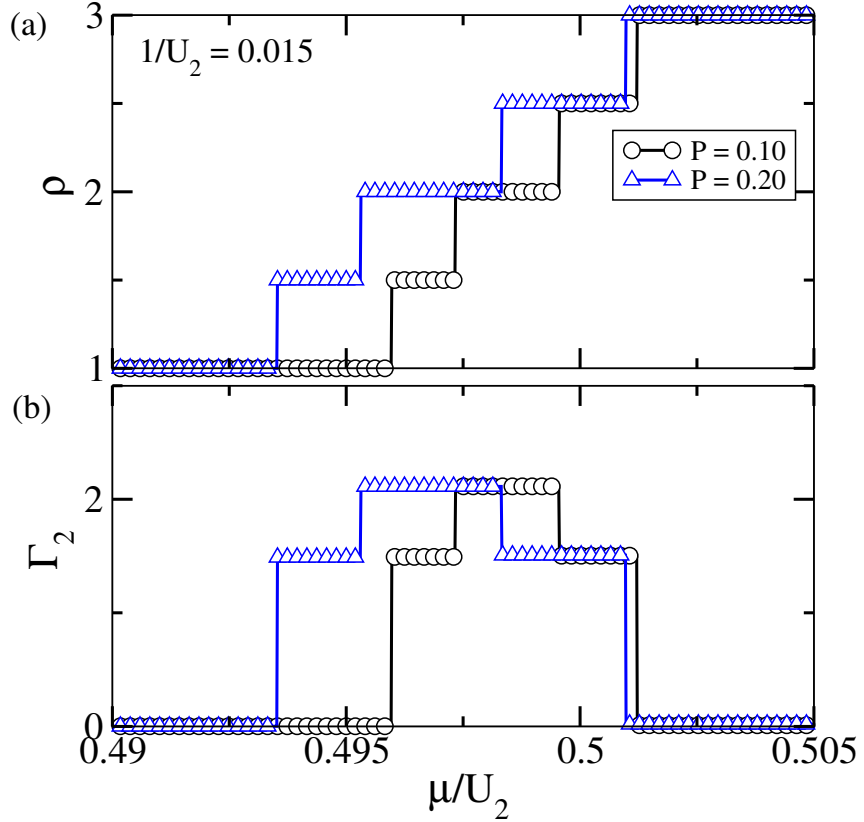


**Figure 2.5:** The figure shows the existence of the PSF phase in the presence of density-induced tunneling( $P$ ). Here we plot particle density( $\rho$ ) in (a) and pair correlation function( $\Gamma_2$ ) in (b) for  $P = 0.1$ (black lines with circles) and  $0.2$ (blue lines with triangles). The other parameters are same as considered in Fig.2.1 at  $U_2 = 1/0.015$ .

the MI2 and MI4 lobes. To achieve this one needs to consider a five-body interaction term by keeping terms up to  $M = 5$  in the model given in Eq. 2.1. Using the CMFT calculation we verify that the PSF in this case can be obtained for suitable choice of repulsive  $U_2$ ,  $U_3$ ,  $U_5$  and attractive  $U_4$  terms in Eq. 2.1. Because of the attractive nature of  $U_4$ , the value of  $U_5$  has to be very strong and repulsive to prevent the collapse.

### 2.2.2 Effect of density induced tunneling

It has been shown that in systems of ultracold atoms in optical lattices, the density induced tunneling plays an important role and has been experimentally observed recently [178]. Although the amplitudes of such tunneling are small compared to the conventional tunneling amplitude  $t$  of the model shown in Eq.2.2, the natural question to ask is whether the narrow region of the PSF phase will survive in the

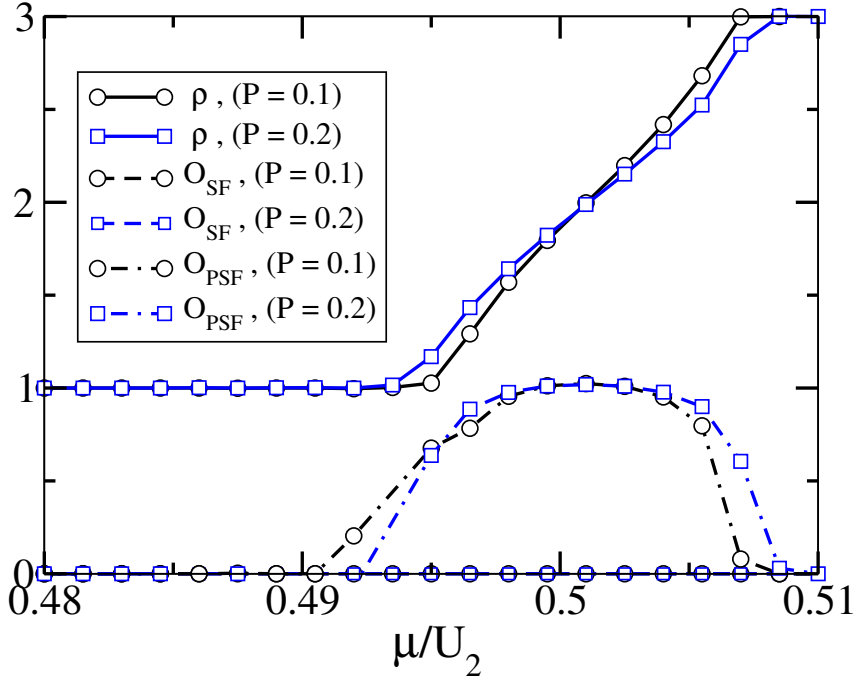


**Figure 2.6:** Figure shows the existence of PSF phase for different values of density dependent hopping amplitude  $P$ . Here we plot  $\rho$ (solid lines),  $O_{SF}$ (dashed lines) and  $O_{PSF}$ (dot-dashed lines) for  $P = 0.1$  and  $0.2$ , which indicate that the PSF survives for finite values of  $P$ .

presence of such density induced tunneling or not. In this subsection, we analyze the effect of density-induced tunneling on the PSF phase [62]. In this context, we introduce the density-induced tunneling term in Eq. 2.2 which is given as

$$H_P = -P \sum_{\langle i,j \rangle} \left( a_i^\dagger (n_i + n_j) a_j + H.c. \right) \quad (2.8)$$

where  $P$  is the density-induced tunneling amplitude. Using the CMFT approach, we show that, indeed, the PSF phase survives up to a finite value of  $P$ . In the CMFT method, the density-dependent tunneling term can be decoupled as

$$a_i^\dagger (n_i + n_j) a_j \approx \psi (a_i^\dagger n_i + n_j a_j) \quad (2.9)$$

where the terms  $O(\psi^3)$  are neglected [179] and  $\psi$  is the superfluid order parameter.

In Fig. 2.5, we plot the behavior of various physical quantities with respect to  $P$  for a cut through the phase diagram of Fig. 2.1 at  $1/U = 0.015$  which passes through the PSF phase. It can be seen from Fig. 2.5(a), where we plot particle

density( $\rho$ ) for  $P = 0.1$  and  $0.2$ , that the  $\rho$  exhibits discrete jumps in steps of  $\delta\rho = 0.5$ , indicating a PSF phase. The corresponding pair correlation function( $\Gamma_2$ ) are plotted in Fig. 2.5(b) which confirm the existence of the PSF phase for finite values of  $P$ . However, when we further increase the  $P$ , the system exhibits a normal SF phase for  $P = 0.3$ . We also analyze this situation using the iPEPS method which is shown in Fig. 2.6. The figure depicts that the  $O_{PSF}(O_{SF})$  is finite(zero) for finite values of  $P$ , indicating the existence of the PSF phase.

## 2.3 Conclusions

In this chapter, we analyze a multi-body interacting BH model and show the possibility of creating two-body repulsive bound bosonic pairs in a two-dimensional optical lattice due to the combined effects of the multi-body interactions. We establish that for a very strong four-body repulsion, a suitable ratio between the three-body attraction and two-body repulsion leads to the bosonic pair formation and hence the PSF phase between the MI1 and MI3 lobes. This fact is concretely demonstrated by analyzing the ground state properties of the BH model using the CMFT approach, which agrees with the results obtained using the iPEPS method. Moreover, we show that this pair formation is stable against the density induced tunneling, which is inevitable in cold gas experiments. Due to the rapid progress in the field of quantum gas experiments in optical lattice, it will be possible to create the repulsively bound pairs in an alternate way as opposed to the already observed one [153] by engineering the multi-body interactions among the bosons. Moreover, this finding may provide scope to create and manipulate the number of bosonic pairs in a controlled manner which may be useful for other relevant studies.



# Chapter 3

## Quantum phases of constrained dipolar bosons in a two-leg ladder

### 3.1 Introduction

In the previous chapter, we discussed the physics arising due to the interplay between different onsite interactions in the BH model. In an optical lattice, large repulsive interaction between the bosons may lead to exotic behavior. For example, very strong onsite two-body repulsion between bosons prevents more than one particle occupation on a single site. This is known as the hardcore constraint and under such circumstances, the bosons are called the hardcore bosons (HCBs) or Tonk gases, which has been observed in cold gas experiment [180]. Similarly, as mentioned in the introduction, large three-body onsite repulsion introduces the three-body hardcore constraints in the system, and the bosons are called three-body constraint bosons (TCBs). The physics of such constrained bosons are widely explored in various context [181, 182].

On the other hand, long-range dipole-dipole interactions among atoms and molecules have also opened up new avenues of research [63, 183] as already mentioned in the introduction. One of the remarkable properties of such off-site interactions is that these can be made repulsive as well as attractive by simply manipulating the directions of the dipoles by suitably applying the external magnetic field. Interestingly, this technique also facilitates to completely reduce the interaction to zero by aligning the dipoles in the so-called magic angles [184]. Due to the long-range nature of the interaction, it is also possible to couple two disconnected systems by adjusting the associated dipole-dipole interactions between the constituents of both the systems. As a result, one can simulate interesting physics in bilayer systems [185].

The one-dimensional analog of this bilayer geometry is the system of two nonlocal chains coupled by the dipole-dipole interactions [184]. This system resembles a two-leg ladder, which is extremely important to study strongly correlated physics in low dimension as many of the solid-state systems exhibit the ladder geometries [186]. Quasi-one-dimensional systems such as the two-leg ladder geometries can be engineered in the optical lattice experiments and manipulation of atomic species in such potentials gives rise to various interesting quantum phases [44, 148, 149, 181, 187–192].

Interestingly, a system of bosons in two non-locally coupled chains can be viewed as a system of binary atomic mixtures as the atoms in individual legs and the interaction between the chains can be thought of as different species of atoms and the inter-species interaction respectively. Binary atomic mixtures in optical lattices promise even richer platforms to study novel quantum phase transitions. Bose-Bose, Bose-Fermi and Fermi-Fermi systems have been shown to exhibit various quantum phases due to the presence of the inter-species interactions along with the interactions within the individual species [193–201]. It has been shown in Bose-Bose mixtures that atoms of different species can form the PSF phase for attractive inter-species interactions [199]. On the other hand, there occurs a spatial phase separation (PS) in the presence of a critical value of repulsive inter-species interaction [196, 202]. Interesting quantum phases with composite fermions, where one fermion is associated with one or several bosons (bosonic holes) for attractive (repulsive) inter-species interaction [195] have been proposed. Recent experimental observations of Bose-Bose and Bose-Fermi mixtures in optical lattices have paved the path to simulate such interesting physics in the laboratory [203–209].

In this chapter, we study the physics of constrained dipolar bosons on a non-locally coupled two-leg ladder, as shown in Fig. 3.1. In this context, we consider atoms in one chain as HCBs and in the other chain as TBCs. We also assume the atoms are arranged in such a way that they attract each other along the rung direction of the ladder and there is no dipole-dipole interaction along the leg direction [44, 184]. By using the selfconsistent CMFT approach, we analyze the groundstate properties of this system and present various possible quantum phases that can arise due to the competition between the attractive dipole-dipole interactions and the onsite interactions. We present a detailed discussion of different quantum phases in a wide parameter regime of the constrained dipolar bosons, which will also reflect the properties of systems of bosons and spin-polarized fermions in depth.

The system considered here can be expressed in the framework of the modified

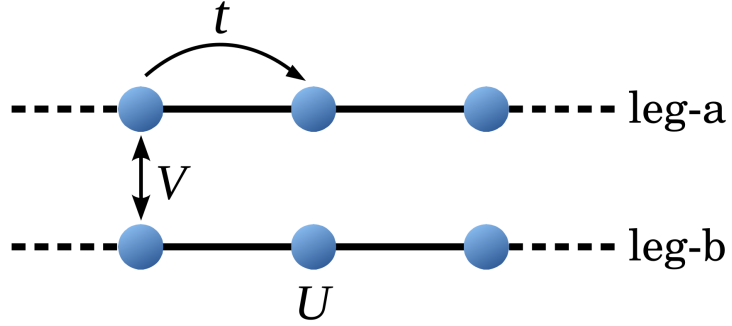


**Figure 3.1:** Two one dimensional optical lattices are coupled by a non-local interaction which is equivalent to a two leg ladder model. Leg-a and leg-b contain two- and three-body constrained bosons, respectively. The particles on both the chain interact among themselves with the non-local dipole-dipole interaction  $V$ . The Hamiltonian for this system is given in Eq.3.1.

EBH model whose Hamiltonian is given as:

$$\begin{aligned}
 H = & - t \sum_{i,\alpha=1,2} (a_{i,\alpha}^\dagger a_{i+1,\alpha} + H.c.) \\
 & + \frac{U}{2} \sum_{i,\alpha=1,2} [n_{i,\alpha}(n_{i,\alpha} - 1)] \\
 & + V \sum_i n_{i,1} n_{i,2} - \mu \sum_{i,\alpha=1,2} n_{i,\alpha}
 \end{aligned} \tag{3.1}$$

where  $a_i^\dagger(a_i)$  is the bosonic creation (annihilation) operator at the site  $i$  of leg-a or leg-b. Index  $\alpha = 1(2)$  represents leg-a (leg-b). The first term corresponds to hopping between the nearest neighbor sites within the same leg. Second and third terms describe the on-site and nearest-neighbor interactions between the legs of the ladder. Last term denotes the chemical potential. As mentioned before we consider that the leg-a of the ladder consists of only HCBs ( $(a^\dagger)^2 = 0$ ) and leg-b contains TCBs ( $(a^\dagger)^3 = 0$ ). On top of that the bosons in leg-b possess repulsive on-site interaction  $U$  and the dipole-dipole interaction  $V$  is attractive in nature. We also assume that the atoms are arranged in such a way that they attract each other along the rung-direction of the ladder and there is no dipole-dipole interaction along the leg direction [44, 184].

## 3.2 Results

Before proceeding further, we first validate our CMFT method by carrying out calculations of the already existing results for a limiting case. The system of two decoupled chains, which are connected only through the non-local dipole-dipole interaction  $V$ , has been studied earlier using strong coupling expansion and the MPS method [184]. It was found that the ground state phase diagram exhibits a direct MI-PSF transition as a function of  $t/U$  for large values of  $|V|$ . Due to the attractive interaction  $V$ , a pairing takes place between the bosons on the two different legs of the ladder at incommensurate densities while at commensurate density, the MI phase appears in both the chains. The lower boundary of the MI lobe gets distorted with an increase in the value of  $|V|$ . As the strength of  $|V|$  increases further, the lower Mott boundary first gets flattened out and then starts bending as we approach the tip of the lobe. The Mott lobe in this case is distorted as a function of hopping and a re-entrant type behavior appears in the phase diagram. This behavior is also clearly visible from another calculation performed using the DMRG method [192].

To reproduce the above findings, we consider exactly the same parameters as considered in Ref. [184] and employ the CMFT approach to obtain the MI-PSF

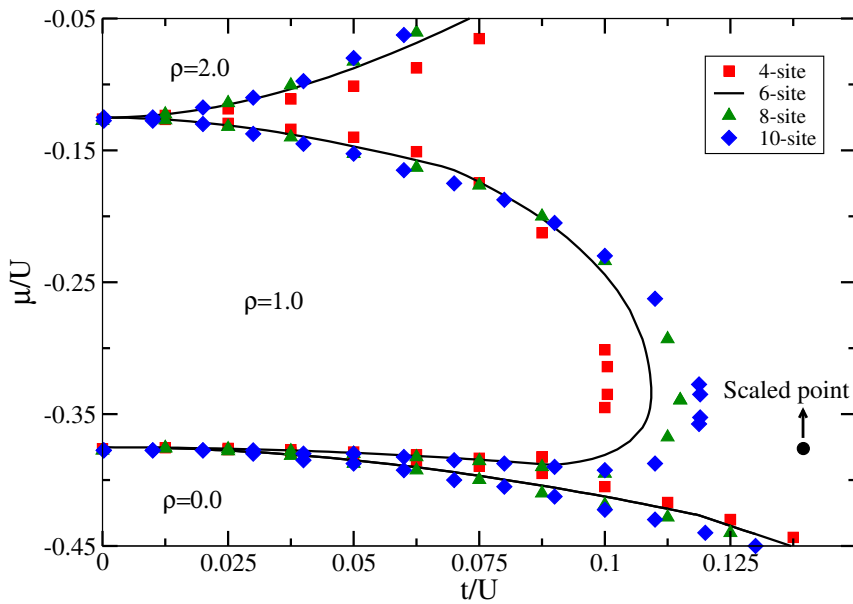


**Figure 3.2:** Phase diagram for TCBs in both the chains for  $|V|/U = 0.75$  in the  $t/U$ - $\mu/U$  plane as considered in Ref. [184]. Red squares, green triangles, the black solid curve and blue diamonds represent the phase boundaries obtained using 4-, 6-, 8- and 10-sites cluster respectively. Scaled critical point for MI-SF transition ( $t/U)_c (= 0.1395)$  is shown by a solid black circle.

phase boundary as shown in Fig. 3.2. The black solid curve shows the MI-PSF phase boundary for a six-site cluster and  $|V|/U = 0.75$ . This already shows the bending of curvature of the lower boundary of the Mott lobe as predicted in Ref. [184]. In order to affirm these result more distinctly we perform calculations with 10-site cluster which are shown by the blue diamonds. We find that the tip of the Mott lobe approaches towards the value obtained using the MPS method. Further, we perform a cluster size extrapolation to estimate the critical value  $(t/U)_c$  at the tip of the Mott lobe as shown in Fig. 3.3. The extrapolated point is shown as the black filled circle in Fig. 3.2. The finite size extrapolation leads to  $(t/U)_c \approx 0.14$  against the value  $(t/U)_c \approx 0.18$ , which was shown in Ref. [184]. The region depicted by  $\rho = 0$  and  $\rho = 2$  correspond to the empty and full states respectively. It is obvious from the above analysis that our CMFT method is able to predict the ground state of the system of TCBs reasonably well and can be used to perform a ground state analysis of the aforementioned model described by Eq. (3.1). We now proceed on to discuss the main results obtained for the case, when one of the linear chains is occupied by the HCBs and the other chain by the TCBs. This situation can also mimic a two leg ladder where one leg of the ladder contains only HCBs (say, leg-a) and the other leg contains only TCBs (say, leg-b). Like previous case these bosons are also considered to be dipolar in nature and the dipole orientation is such that

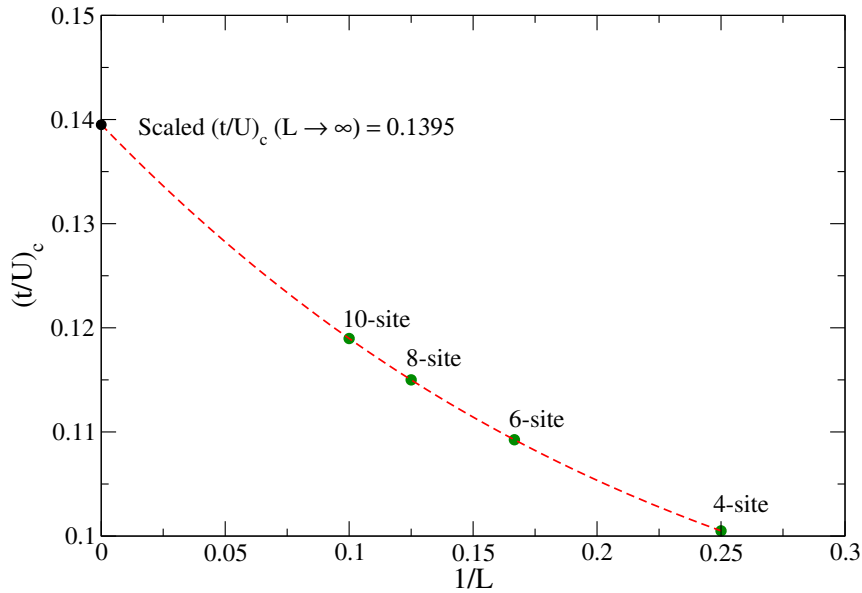


**Figure 3.3:** Scaling of the MI-SF transition critical point  $(t/U)_c$  with respect to the different cluster sizes at  $|V|/U = 0.75$ . Green solid circles represent the  $(t/U)_c$  values for respective cluster sizes, red dashed lines represents the scaling and the black solid circle on Y-axis denotes the value of  $(t/U)_c$  scaled to thermodynamic limit ( $= 0.1395$ ).

both the legs are coupled via attractive dipole-dipole interaction  $V$  and there is no dipole-dipole interaction along the legs. In addition to this, the TCBs interact through a finite on-site interaction term  $U$ . Henceforth,  $U$  will be used to denote the on-site two-body interaction strength for TCBs only (as for HCB,  $U \rightarrow \infty$ ). We consider two scenarios in the following subsections. In the first case  $U = 0$  and in the second case we set  $U \neq 0$ .

### 3.2.1 TCBs with vanishing on-site interaction

First we investigate the effect of an attractive  $V$  on the system in the absence of two-body interaction between the TCBs, i.e.  $U = 0$ . The detailed phase diagram for this case is shown in Fig. 3.4. As the on-site repulsion is absent, the bosons on different legs form a bound state of one HCB and two TCBs (HCB+2TCBs) when  $|V|$  is sufficiently large compared to  $t$ . This happens due to the obvious reason as the two- and three-body constraints prevent more than one and two atoms on a single site of leg-a and leg-b, respectively. When the density is small, these bound state can move freely in the chains giving rise to a SF phase, which we call a trimer superfluid (TSF) phase. The TSF phase is depicted in the cartoon as the bound state of one HCB (green circle) and two TCBs (red circles). For small to moderate values of  $t/|V|$ , the TSF phase is always present but when  $t/|V| \gtrsim 0.25$ , there is a direct transition from vacuum to 2SF phase. For intermediate values of  $t/|V|$ ,

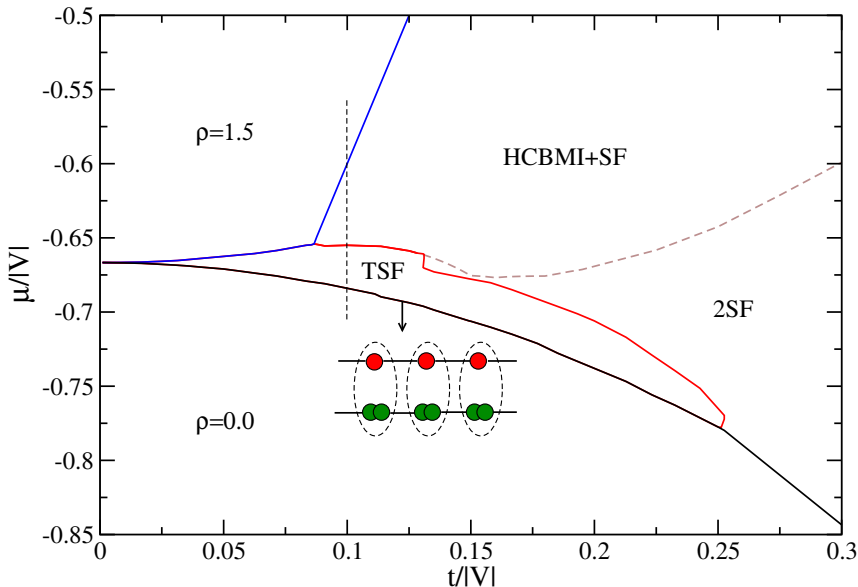


**Figure 3.4:** Phase diagram for model given in Eq.3.1 in  $\mu/|V|$  vs.  $t/|V|$  plane, with leg-a (leg-b) containing HCB (TCB with  $U = 0$ ) with varying  $t/|V|$ .

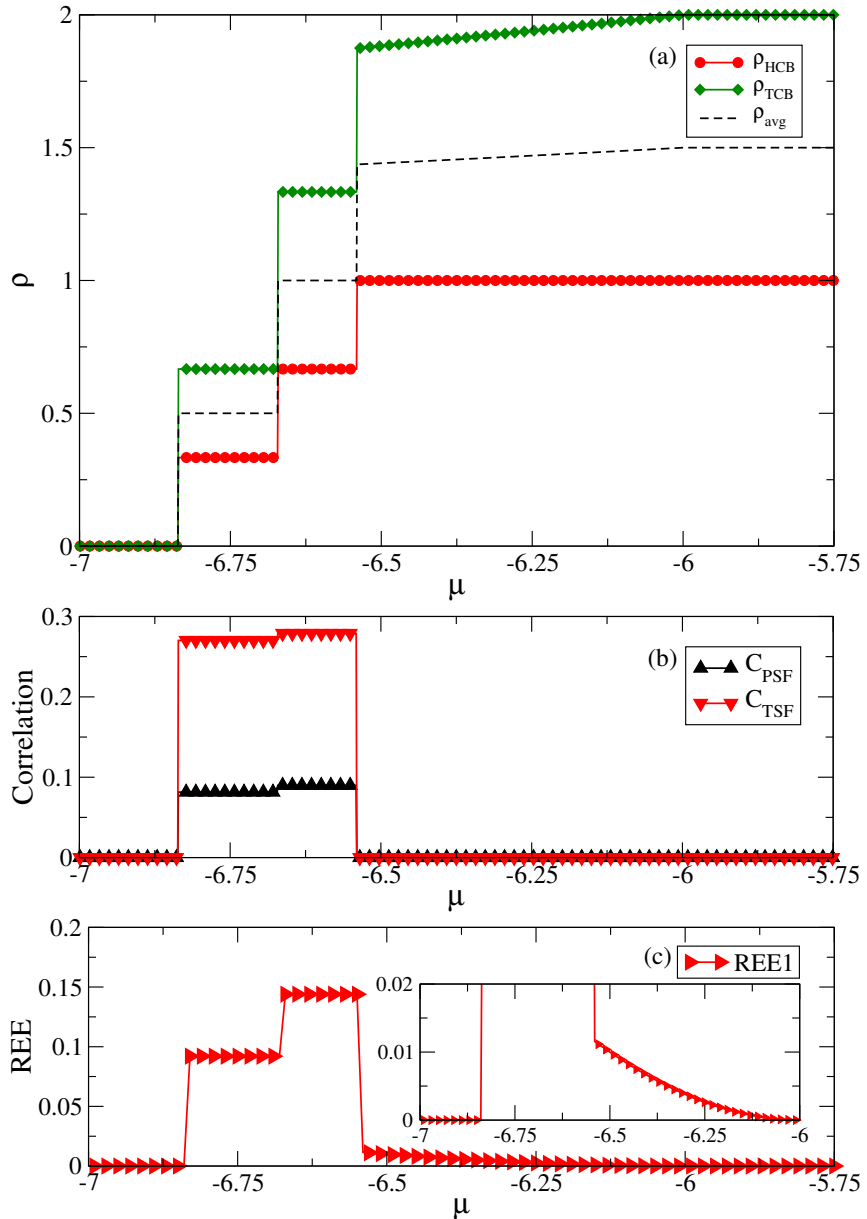


**Figure 3.5:** (a)  $\rho$  vs.  $\mu$  (b) Dimer and trimer correlations and (c) Rényi entropy corresponding to a vertical cut along  $U/|V| = 0.0$  in Fig.3.8. Inset shows the zoomed in region in which REE is finite at first (HCBMI+ASF) and then gradually drops to 0 as the system approaches saturation.

when the density of bosons and hence the value of  $\mu/|V|$  increases, at some point leg-a becomes a Mott insulator with one atom in every site due to the hardcore constraint. In this limit we call this as the hardcore boson MI (HCBMI) phase. At the same time the leg-b shows a SF signature, as the trimer which was formed before can not move in the limit when the leg-a is full. We call this region of the phase diagram as the HCBMI+SF phase. Further increase in density leads to the

saturation at  $\rho = 1.5$ , i.e.  $\rho = 1$  and 2 for HCBs and TCBs respectively. However, for small values of  $|V|$  the system first goes to a 2SF phase from the TSF phase and then to the HCBMI+SF phase before saturating. For very large values of  $|V|$  the system goes directly into the saturation from the TSF phase with increase in density of particles. In Fig. 3.4 , the HCBMI+SF phase is separated from the 2SF phase by the dashed line.

To obtain the phase diagram for this case we analyze the densities and the superfluid order parameter  $\phi$  of the two legs individually as well as of the whole system for different values of  $t/|V|$  as a function of the chemical potential  $\mu$  in a 6-site cluster (3 sites each in leg-a and leg-b). The  $\rho$  vs.  $\mu$  plot across a cut in the phase diagram (dashed vertical line in Fig. 3.4) for  $t/|V| = 0.1$  is shown in Fig. 3.5(a). In Fig. 3.5(a) the HCB, TCB and average density of the system are shown by red circles, green diamonds and black-dashed lines, respectively. It can be seen from this figure that there appears several discontinuous jumps in the densities as a function of  $\mu$ . These step-wise jumps correspond to the formation of bound states. It is to be noted that in the CMFT approach, the formation of bound states can be inferred from these discrete jumps in density for creation of every bound state. This has been confirmed in our earlier work [44]. As  $\mu/|V|$  increases both the legs, hence the system starts filling up. In the case of trimer formation, the filling pattern is such that for every single particle in leg-a, there are two particles in leg-b. As we go on increasing  $\mu$  more particles are introduced and more such bound states are formed. This process continues until both the legs are fully occupied and the system attains its maximum possible density ( $\rho = 1.5$ ). The stepwise jump in the case of HCBs at  $\rho = 0.33, 0.66$  and  $1.0$  corresponds to 1-, 2- and 3-particle states, respectively, of the leg-a. Similarly, the stepwise jump for TCBs at  $\rho = 0.66, 1.33$  and  $2.0$  indicate 2-, 4- and 6-particle states, respectively, of leg-b. The average density of the system also behaves like wise.

### 3.2.2 TCBs with finite on-site interaction

We now discuss the situation for finite on-site two-body interaction  $U$  between the TCBs. In this case the presence of on-site repulsion will play an important role as it will break the trimer phase and stabilize the MI and PSF phases. As mentioned before, in the case of soft-core bosons in both the legs it has been shown that there exists a MI-PSF phase transition as a function of  $(t/U)$  for finite values of  $|V|$  keeping the ratio  $U/|V| = 1.33$  (equitably  $|V|/U = 0.75$  as considered in Ref. [184].

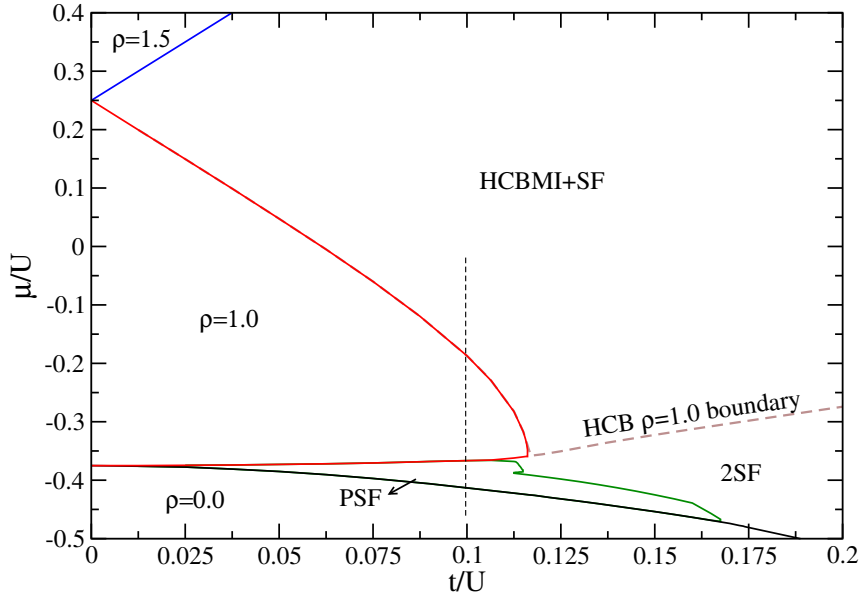


**Figure 3.6:** Phase diagram for model given in Eq.3.1 in  $\mu/U$  vs.  $t/U$  plane, with leg-a (leg-b) containing HCB (TCB with finite two-body interaction).

The PSF phase is the bound state of two bosons each from different legs. In the case of constrained bosons studied in this case, we show that the MI-PSF transition also occurs for large values of  $|V|/U$ . However, the phase diagram in this case shows interesting features due to the two- and three-body constraints. We vary the ratio  $(t/U)$ , while keeping  $V$  fixed to find out the existence of various phases. The phase diagram obtained for this case is shown in Fig. 3.6. Compared to the previous case of TCBs with no local two-body interaction, here we do get an MI phase when the densities of both the legs becomes unity. However, before entering the MI phase the system undergoes a transition from vacuum to a PSF phase. The existence of this PSF phase can be understood with the help of  $\rho$  vs.  $\mu$  plot given in Fig. 3.7 along the dashed vertical line for  $t/U = 0.1$ . For an attractive  $V$ , the system favors a bound state between the bosons of the two legs. If both the legs contain one-particle each a pair is formed. With increase in the chemical potential the number of particle in the system increases. As the system favors the formation of bound pairs, the number of particles in the system increase in steps of two particles at a time. This results in the step wise jump in the  $\rho$  vs.  $\mu$  plot as discussed before. The densities of HCBs, TCBs as well as the average density of the system is plotted in Fig. 3.7(a), (b) and (c) respectively for a 6-site cluster. The jumps in all the three plots signify the existence of the PSF phase. The plateau at  $\rho = 1$  corresponds to the MI phase and the shoulder above the plateau is the gapless SF phase. When the on-site

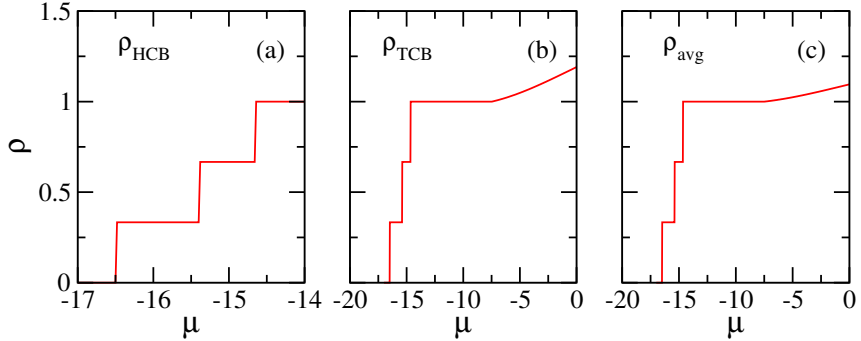


**Figure 3.7:**  $\rho$  vs.  $\mu$  plot corresponding to the cut shown by dashed line across the phase diagram shown in Fig.3.6.

interaction strength  $U$  is small then the system enters into a 2SF phase with the chemical potential. However, for large values of  $U$  the system favors an MI phase at commensurate density of both the legs where the density of both the legs are equal to unity. Further increasing the chemical potential leads to the HCBMI+SF phase for all values of  $t/U$  as discussed in the previous section. The system saturates at  $\rho_{avg} = 1.5$ . It is to be noted that the PSF phase, which appears along the top boundary of the MI lobe, disappears due to the hardcore constraint in one leg. This prevents the motion of the pairs once leg-a is full. As a result the bosons in leg-b can move freely in this region and hence, it is responsible for breaking the pair formation. On the other hand the re-entrant type behavior of the lower MI lobe disappears in this case owing to the fact that the hopping process for the HCBs is restricted in the MI phase and the Mott boundaries are not quadratic anymore [184].

After discussing two cases above it is informative to perform a careful analysis of the competition between repulsive  $U$  and attractive  $V$ , which may reveal a more detailed phase diagram. In this regard, we explore the system by varying the  $U/|V|$  ratio for a large range of values. We investigate how the phase diagram changes when the on-site interaction  $U$  of TCBs in leg-b is changed for a finite value of inter-leg interaction  $V$ . First, we discuss the case for small  $|V|$ . We fix  $t/|V| = 0.1$  and vary  $U/|V|$  to obtain the phase diagram, which is shown in Fig. 3.8. When  $U/|V| = 0$ , this corresponds to the case when the system exhibits the trimer phase as discussed in the previous section. Further increase in the value of  $U/|V|$  does not allow for the formation of the trimer phase as it prevents the two TCBs to occupy the same site in leg-b. Therefore, the TSF phase survives for a range of values of  $U/|V|$  between 0.0 and 0.25. Following which we only see HCBMI+SF phase without any signature of a paired phase or the MI phase. For a relatively larger value of  $U/|V|$  (beyond  $U/|V| = 0.75$ ), the density in both the legs are same. As  $|V|$  is still finite, a dimer

formation occurs between the legs at densities 0.33 and 0.66. This is indicated in the  $\rho$  vs.  $\mu$  plot for  $U/|V| = 1.0$  in Fig. 3.9(a). The particle number in both the legs always jumps in steps of one until the system goes to the HCBMI+ASF phase (for  $0.75 \lesssim U/|V| < 1.0$ ) or the MI phase (for  $U/|V| \gtrsim 1.0$ ).

Now we discuss the case for large  $|V|$ . As before, we obtain the phase diagram by varying  $U/|V|$  while keeping  $t/|V| = 0.03$ , which is shown in Fig. 3.10. The overall phase diagram and phases are similar as found in the previous case. A major difference is seen in the width and phase boundaries of the TSF and the PSF regions. It is seen that the TSF and PSF phase shrink and get reduced to a very small region. For intermediate values of  $U/|V| (\approx 0.4 - 0.6)$ , the repulsion between TCBs is strong enough to break the pairing in the TSF phase. In this range of  $U/|V|$  there is a direct transition from vacuum to the SF phase and then to a fully occupied state. As  $U/|V|$  is increased further, the system exhibits a PSF phase for incommensurate densities as  $V$  is still finite and attractive in nature. At integer densities there is a transition to the MI phase in which both the HCBs and the TCBs have average densities equal to unity. When in the MI phase, as  $\mu$  is increased, the TCBs drive the system first into a SF phase and eventually saturates at  $\rho = 1.5$ .

To confirm the existence of various phase transitions discussed above we calculate correlation functions as well as the Rényi entanglement entropy (REE) of the system.

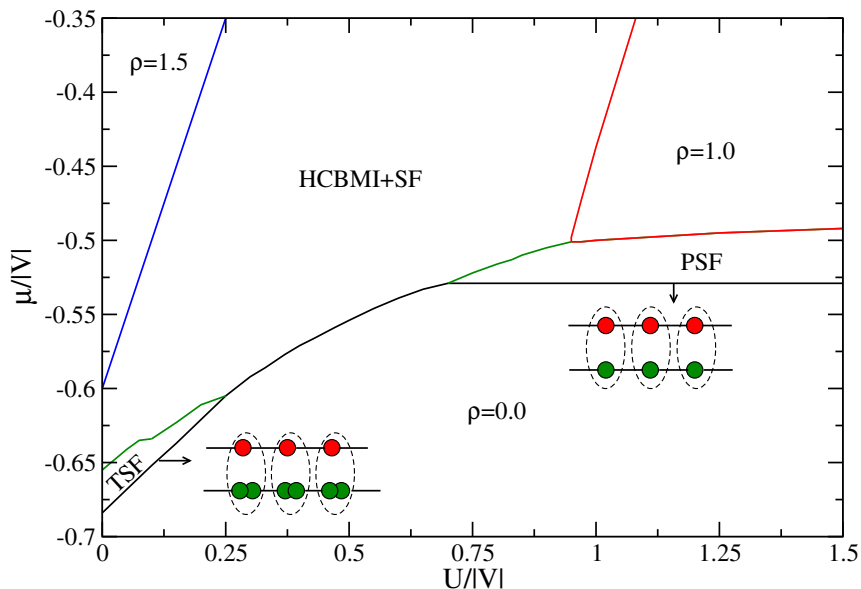


**Figure 3.8:** Phase diagram for model given in Eq.3.1 in  $\mu/U$  vs.  $t/U$  plane, with leg-a (leg-b) containing HCB (TCB with finite two-body interaction) at  $V = -10.0$ .

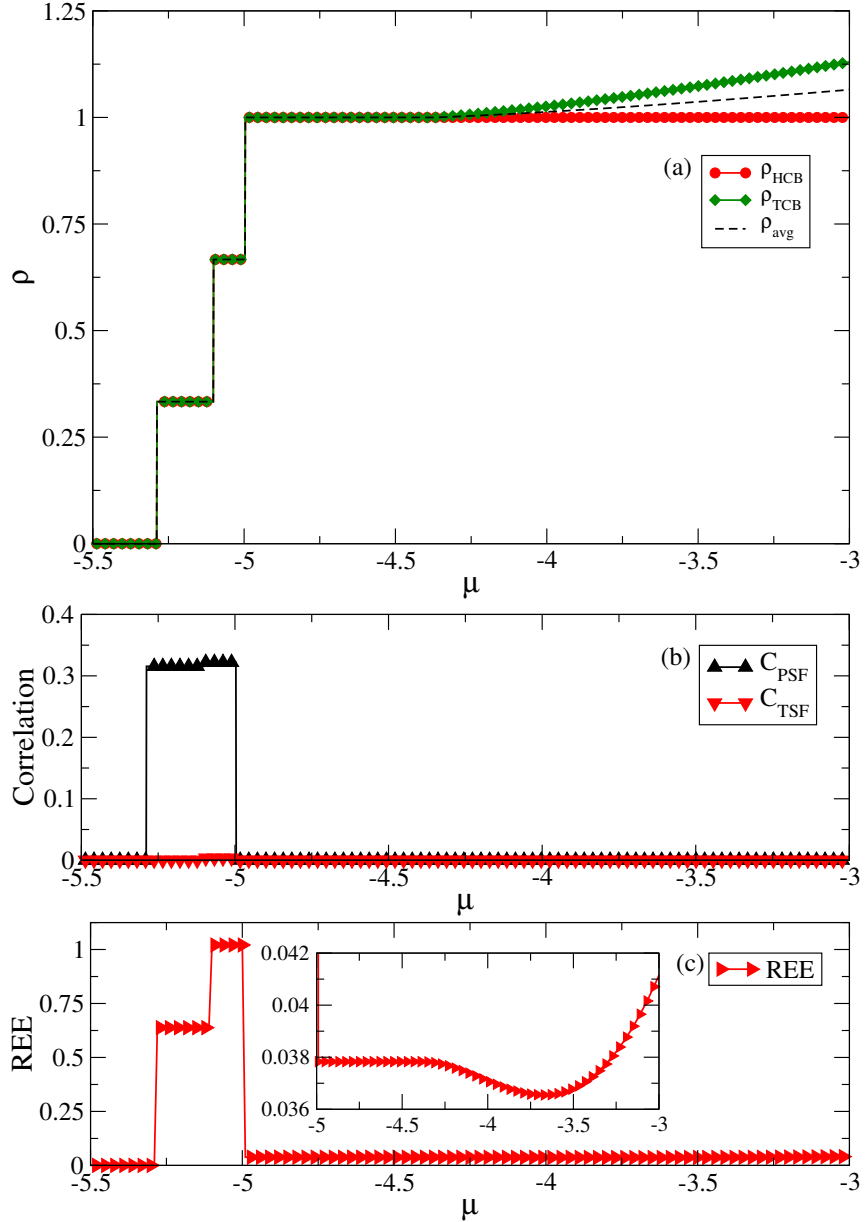


**Figure 3.9:** (a) $\rho$  vs.  $\mu$  (b)Dimer and trimer correlations and (c)Rényi entropy corresponding to a vertical cut along  $U/|V| = 1.0$  in Fig.3.8. Inset shows the zoomed in region where there is a phase transition from MI to HCBMI+SF phase and a change in slope of REE is visible.

We calculate the pair correlation function as

$$C_{PSF} = \langle a_i^\dagger b_i^\dagger a_j b_j \rangle, \quad (3.2)$$

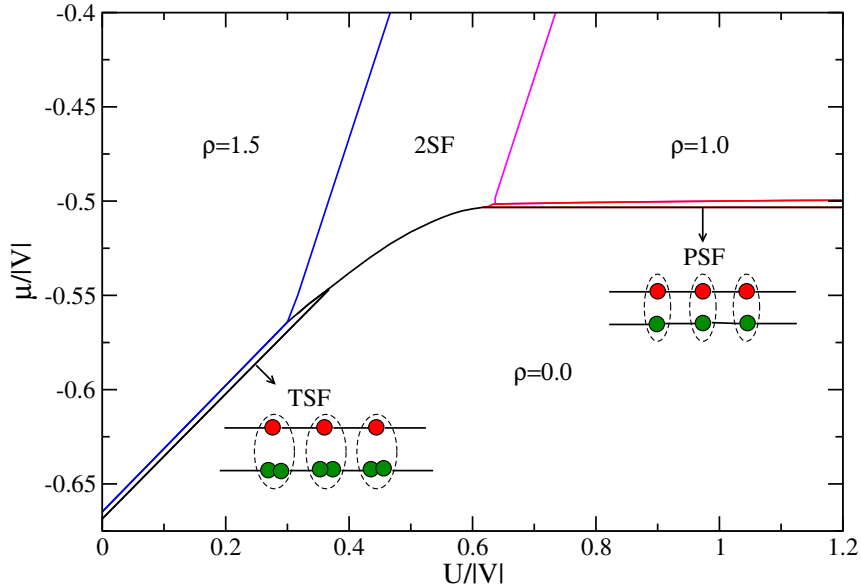


**Figure 3.10:** Phase diagram for model given in Eq.3.1 in  $\mu/|V|$  vs.  $U/|V|$  plane, with leg-a and leg-b containing HC and three-body constrained bosons for  $t/|V| = 0.03$ .

and the trimer correlation function as

$$C_{TSF} = \langle a_i^\dagger(b_i^\dagger)^2 a_j(b_j)^2 \rangle. \quad (3.3)$$

to infer the signatures of the PSF and the TSF phases, respectively. These quantities are plotted with respect to the chemical potential  $\mu$  in Fig. 3.5(b) and Fig. 3.9(b) corresponding to the cuts shown in Fig. 3.4 and Fig. 3.6, respectively. It can be seen from Fig. 3.5(b) that  $C_{TSF}$  (red triangles) clearly dominates  $C_{PSF}$  in the region where the system exhibits a trimer phase as shown in Fig. 3.5(a). Both the correlation functions are zero in the HCBMI+SF phase. On the other hand,  $C_{PSF}$  is larger than  $C_{TSF}$  in the dimer phase as shown in Fig. 3.9(b).

We further calculate the REE to complement our findings in this work. This is an important quantity to probe quantum phase transitions in optical lattices which has been measured recently in an experiment on a Bose-Hubbard system [210]. The REE of  $n^{th}$  order is defined as:

$$S_n(A) = \frac{1}{1-n} \log \text{Tr}(\hat{\rho}_A^n) \quad (3.4)$$

where  $\hat{\rho}_A$  is the reduced-density matrix of a subsystem A entangled with it's complement B. For our calculations we focus only on the  $2^{nd}$  order REE which can then be written as  $S_2(A) = -\log \text{Tr}(\hat{\rho}_A^2)$ . The system considered can be divide into

two subsystems as follows: Four left most sites can form one subsystem and the remaining (right most two sites) form another subsystem. We calculate the REE in this configuration for the cuts along  $U/|V| = 0.0$  and  $1.0$  in the phase diagram shown in Fig. 3.8 and plot it as a function of  $\mu$  in Fig. 3.5(c) and 3.9(c), respectively. As expected we observe finite REE in the SF, PSF and TSF phases. However in the gapped MI phase and in the saturated region, the REE reduces considerably. In Fig. 3.5(c), it can be seen that the REE is finite in the TSF region and as the system moves into the HCBMI+SF phase there is a significant change in REE which indicates a phase transition. As there is a contribution from SF phase REE is still finite, which can be seen in the inset of Fig. 3.5(c). As the system approaches saturation, REE also reduces to 0. Similar features are seen for the transition from the PSF to MI then to HCBMI+ASF phases as shown in Fig. 3.9(c). Our findings from the REE calculations are therefore consistent with the phase transitions indicated by the corresponding  $\rho$  vs.  $\mu$  and correlation function plots.

### 3.2.3 Effect of an external harmonic confinement

Here we discuss the effect of an external harmonic confinement on the quantum phase diagrams that are investigated in this work. For this purpose we consider a harmonic trap along the length of the linear chains with equal potential on both the

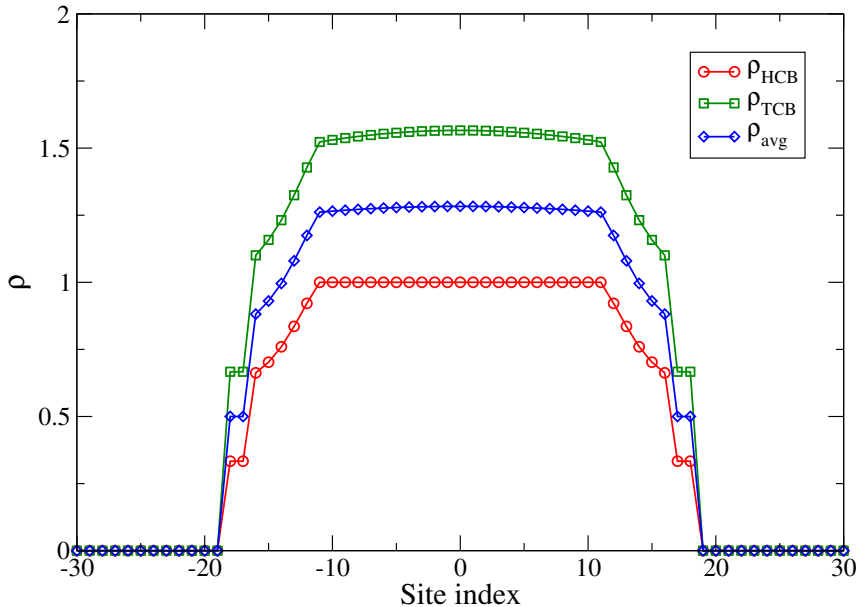


**Figure 3.11:** HCB and TCB confined in harmonic trap with  $V_{tr} = 0.002$  at  $U = 0.0$ ,  $t/|V| = 0.225$  and  $\mu/|V| = -0.6$ , corresponding to Fig.3.4.

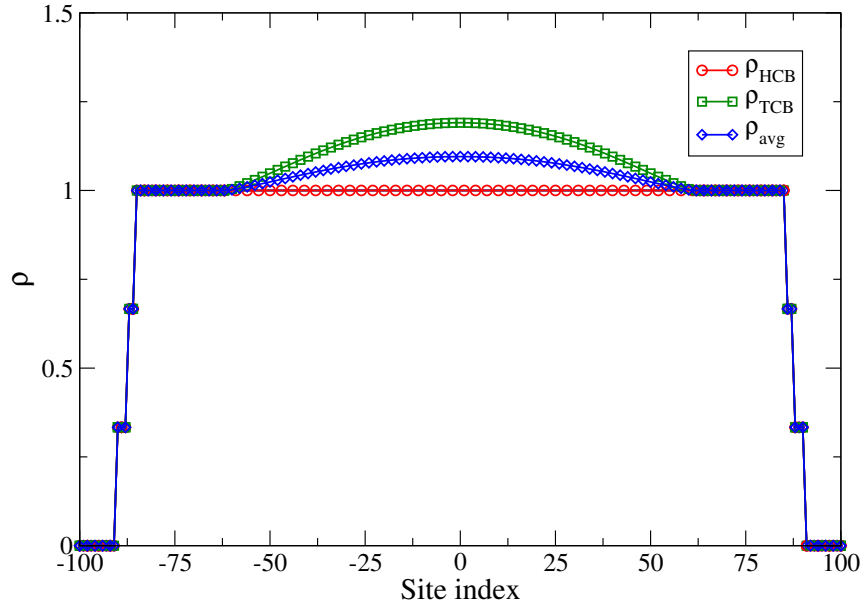


**Figure 3.12:** HCBs and TCBs confined in harmonic trap with  $V_{tr} = 0.002$  at  $|V|/U = 0.75$ ,  $t/U = 0.1$  and  $\mu/U = 0.0$ , corresponding to the cut shown in Fig.3.6.

legs and repeat the calculations. An extra term of the form

$$H_{tr} = V_{tr} \sum nx^2 \quad (3.5)$$

is thus added to the system Hamiltonian, where  $V_{tr}$  is the trap parameter and  $x$  is the site index ( $= 0$  at the center). This is equivalent to redefining the effective chemical potential as  $\mu_x = \mu_0 - V_{tr}x^2$ . For our calculation we set  $(V_{tr}/t) = 0.002$ , which is experimentally achievable. The results obtained are presented in Figs. 3.11 and 3.12. In Fig. 3.11 we analyze the region along  $t/|V| = 0.225$  for  $U = 0.0$  and  $\mu_0/|V| = -0.6$  of Fig. 3.4. The result is very similar to the one obtained for the homogeneous case. It is known obvious that the trap center has comparatively higher density than other sites away from the center. The center of the trap is in the HCBMI+SF phase, which can be clearly seen from the density plot in Fig. 3.11. Moving away from the trap center, we obtain a small region of the 2SF phase and then the TSF phase. This can be identified as the jump in the density in steps of three particles. The overall extent of all the phases is close to 40 sites. The extent of all the phases will increase by considering a shallow trap. When we add the same trap to our system with  $|V|/U = 0.75$ , a comparatively larger region of condensate is seen. This corresponds to a cut along  $t/U = 0.1$  with  $\mu_0/U = 0.0$ . Once again center of the trap exhibits a HCBMI+SF phase. But unlike the previous case, we first obtain an MI phase as we move away from the center of the trap. Farther going

away, it yields the PSF phase where the density changes in steps of two particles. At the trap boundaries the particle number vanishes. All these phases can be probed in the already existing technique of site resolved imaging which has been used to obtain the signature of Mott shells in the optical lattice experiments [6, 211, 212].

### 3.3 Conclusions

In this chapter, we have studied the ground-state phase diagram of two- and three-body constrained dipolar bosons in a system of two one dimensional optical lattices coupled by the dipole-dipole interaction using the self-consistent CMFT approach. We analyze a wide range of parameters and obtain the phase diagrams depicting all the important phases that may arise due to the competition between the on-site two-body repulsion and the nearest neighbor attraction with the two- and three-body constraints. We have found that the system exhibits mainly four types of phases, namely the 2SF, PSF, TSF and the MI phases corresponding to different ranges of parameters. We have showed the signature of different phases using the CMFT calculation, which cannot be obtained using the conventional single-site mean-field theory. By computing the pair correlation along with the trimer correlation functions, we have identified the PSF and the TSF phases. These results are further substantiated by the Rényi entanglement entropy, which is found to be finite in the PSF and the TSF phases and zero in the MI phase. In addition, we have also discussed the effect of external harmonic confining potential, which emphasizes the feasibility of observing these phases in an experiment.

## Chapter 4

# Quantum walk of interacting Mott-insulator defects

### 4.1 Introduction

The last two chapters are focused on the equilibrium properties of the interacting bosons in optical lattices. This chapter will be devoted to investigating the dynamical properties of interacting bosons in the framework of the quantum walk. As mentioned in the introduction, the phenomenon of the quantum walk (QW) provides useful insights about the dynamical behavior of a quantum mechanical system with a bottom-up approach by considering a few particles instead of a large number of particles. The goal of this chapter is to investigate the QW of interacting bosons in the presence of both local and/or nearest neighbor interactions in a one-dimensional lattice.

Considerable efforts have been made to understand the effect of interactions on the QW of more than one indistinguishable particles in various systems such as quantum gases in optical lattice [213], correlated photon pairs [214, 215] and superconducting qubits [216, 217]. In the interacting systems, the combined effect of quantum correlation and interaction may yield novel scenarios in the phenomenon of QW as a result of the Hanbury-Brown and Twiss(HBT) interference and Bloch oscillation [98, 213, 214, 218–224].

Recently, the BH model has been analyzed to understand the QW of interacting particles in different physical systems [87, 98, 213, 215, 217]. In most of the cases, the focus was to study the QW with an initial state of particles in an empty lattice driven by the competing two-body interactions. We are interested in investigating the QW of bosons influenced by a lattice already occupied by interacting particles

instead of empty sites. In this context, we systematically investigate the CTQW of one or more defects on top of a bosonic MI phase in a one-dimensional BH model. Moreover, we also investigate the effects of the three-body interaction and the two-body nearest-neighbor interactions on the QW of the MI defects. This chapter is arranged in three parts. In the first part of the chapter, we will analyze the QW of defects with only two-body interactions. In the second part, we will analyze the influence of both two and three-body onsite interactions on the QW and in the end, we will discuss the effect of nearest neighbor interactions on the QW of defects.

The scenario considered here is completely different from the QW of interacting bosons already discussed in the literature [98, 213, 215]. The very difference here is that the quantum walkers interact with themselves as well as with the background bosons which form the MI state. Although the interactions experienced from the background bosons in the MI state are uniform throughout the lattice, we will show that this background plays an important role in revealing interesting physics in the QW.

## 4.2 QW of a single defect

In this section, we will present the dynamics of single defect on top of an MI phase. The underlying model which describes such a system is the BH Hamiltonian given by:

$$\mathcal{H} = -J \sum_{\langle i,j \rangle} (a_i^\dagger a_j + H.c.) + \frac{U}{2} \sum_i n_i(n_i - 1) \quad (4.1)$$

which has already been introduced in Chapter 1. All the terms have their usual meaning and  $J$  denotes the hopping matrix element. As we have seen in Sec. 1.2.3, after a critical repulsion  $U$ , the system undergoes an SF-MI transition at different integer densities. As already discussed in the introduction, the time evolution is performed on an initial state, defining the system under consideration. In this case, we consider a deep MI state, which is ensured by fixing  $U = 50$ , which is much larger than  $J = 1$ . In order to study the QW of defects on top of the MI state, we consider four different initial states by introducing defect of both hole and particle type, which are given as

1.  $|\Psi(0)\rangle_1 = a_0 |\text{MI1}\rangle = |\dots 1 1 0 1 1 \dots\rangle$ .
2.  $|\Psi(0)\rangle_2 = a_0^\dagger |\text{MI1}\rangle = |\dots 1 1 2 1 1 \dots\rangle$ .

$$3. |\Psi(0)\rangle_3 = a_0 |\text{MI2}\rangle = |\dots 2 2 1 2 2 \dots\rangle.$$

$$4. |\Psi(0)\rangle_4 = a_0^\dagger |\text{MI2}\rangle = |\dots 2 2 3 2 2 \dots\rangle.$$

Due to the large number of particles involved in the system, the exact solution of the Schrödinger equation with the Bose-Hubbard model is difficult. Hence, the dynamical evolution of the initial state is done by using the Time-Evolving Block Decimation(TEBD) method using the Matrix Product States(MPS) [225, 226] with maximum bond-dimension of 500. In our simulation, we consider a system of length  $L = 29$  which is sufficient to exhibit the essential physics discussed. To analyse the QW we compute the time average density  $\langle n_i(t) \rangle$  with respect to the time evolved states  $|\Psi(t)\rangle$ .

In Fig. 4.1(b-e), we plot the QW of a defect based on all the four initial states  $|\Psi(0)\rangle_1$ ,  $|\Psi(0)\rangle_2$ ,  $|\Psi(0)\rangle_3$  and  $|\Psi(0)\rangle_4$  respectively. For comparison, we also show the QW of a single particle in an empty lattice in Fig. 4.1(a). We plot the evolution of density  $\langle n_i(t) \rangle$  in all the cases, which shows a ballistic expansion of the probabilities. It can be seen from Fig. 4.1(a) and (b) that the QW of a single hole is identical to the QW of a single particle on an empty graph, which is obvious as both the excitations are identical in nature. However, a particle excitation on top of an MI1 state ( $|\Psi(0)\rangle_2$ ) results in faster propagation of density in the QW compared to the single hole QW as shown in Fig. 4.1(c). The reason for this faster propagation can be attributed to the Bose enhancement, where the particle excitation experiences uniform repulsion from the background atoms which are already in the MI1 state. For a reason similar to the QW of single hole on an MI1 state, single hole on MI2 state ( $|\Psi(0)\rangle_3$ ) also exhibits QW (Fig. 4.1(d)) identical to the QW of single particle defect on MI1 state ( $|\Psi(0)\rangle_2$ ). This enhancement in propagation speed can further be confirmed by analyzing the QW of particle defect on an MI3 state ( $|\Psi(0)\rangle_3$ ), which is shown in Fig. 4.1(e). It can be seen that in this case, the particle spreading is

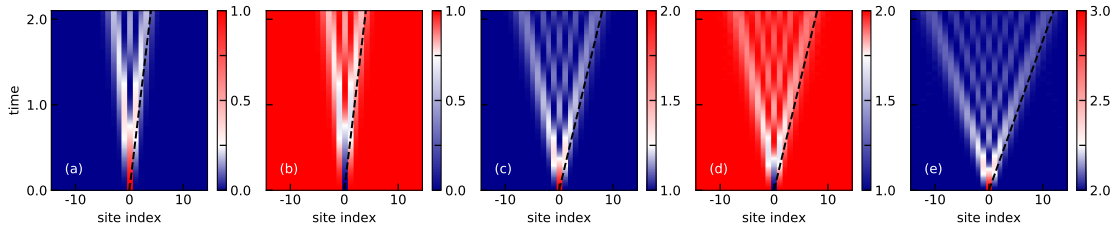


**Figure 4.1:** The figure shows the QWs of single-particle or hole defect in MI of different filling. (a) Density evolution of a single particle on the empty lattice. (b-e) Density evolutions corresponding to the initial states  $|\Psi(0)\rangle_1$ ,  $|\Psi(0)\rangle_2$ ,  $|\Psi(0)\rangle_3$  and  $|\Psi(0)\rangle_4$  respectively. Here, the dashed lines indicate the boundary of the propagation.

much faster compared to all other cases, which is also due to the strong background interaction.

### 4.3 QW of two particle defects

In this section, we discuss the QW of two bosonic particles created on top of an MI1 state in a one-dimensional lattice. As already mentioned before, the QW of two interacting bosons on an empty lattice has been observed in recent experiments [213, 215]. Before proceeding further, we present a brief overview of this physics to compare the similarities and differences with that of the QW of interacting defects.

The initial state for a two-particle QW on empty lattice is given by

$$|\Psi(0)\rangle = a_0^{\dagger 2} |MI0\rangle = |\dots 0 0 2 0 0 \dots\rangle, \quad (4.2)$$

where the two particles are initially placed at the central site. The time evolution of such initial state in the presence of onsite interaction  $U$  leads to interesting phenomena such as the QW of repulsively bound pairs, spatial bunching and anti-bunching and HBT interference etc [213]. For vanishingly small interaction, the two particles exhibit independent particle QW. A gradual increase in the interaction leads to a QW of a composite particle at a reduced propagation speed. This reduction in speed can be attributed to the formation of a repulsively bound pair of atoms. For the same reason, it results in the signature of spatial bunching in the two-particle correlation function for large onsite interaction.

On the other hand, when the initial state is prepared by placing the two particles at the nearest neighbor sites, which is given by

$$|\Psi(0)\rangle = a_0^\dagger a_1^\dagger |MI0\rangle = |\dots 0 0 1 1 0 0 \dots\rangle. \quad (4.3)$$

the system exhibits HBT interference for vanishing interactions. However, for large onsite interactions, spatial anti-bunching in the two-particle correlation function is exhibited, which is also known as fermionization, where the two particles stay separated.

Now, we turn our discussion to a problem where we create two particles on top of an MI1 state in one dimension as depicted in Fig. 4.2. The initial state which explains this situation is given as

$$|\Psi(0)\rangle = (a_0^\dagger)^2 |MI1\rangle = |\dots 1 1 3 1 1 \dots\rangle \quad (4.4)$$

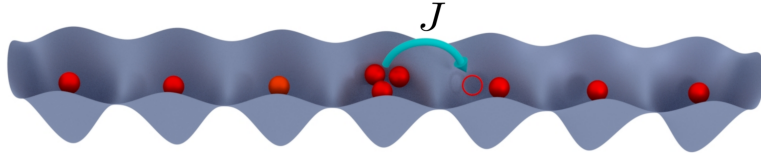


**Figure 4.2:** Figure shows the initial state which is two particles on top of a bosonic Mott insulator in one dimension at unit filling i.e.  $(a_0^\dagger)^2 |\text{MI1}\rangle$ . Here,  $J$  denotes the hopping strength.

Note that the central site now has three particles and the background MI1 state is a result of strong two-body repulsion compared to the hopping  $J$ . Hence, the extra two particles on top of the MI1 state are also subjected to the two-body repulsion. However, as already mentioned in Chapters 1 and 2, one can in principle allow an additional three-body interaction among the bosons leading to interesting physics. In this context, we investigate the QW of the two bosonic defects in the presence of both two and three-body interactions in the framework of the modified BH model given as

$$\mathcal{H} = -J \sum_{\langle i,j \rangle} (a_i^\dagger a_j + H.c.) + \frac{U}{2} \sum_i n_i(n_i - 1) + \frac{W}{6} \sum_i n_i(n_i - 1)(n_i - 2) \quad (4.5)$$

where  $W$  is the three-body interaction term.

Our goal is to understand the signatures of the QW from the average particle density  $\langle n_i(t) \rangle$  obtained using the time evolved state  $|\Psi(t)\rangle$ . We also compute the two particle correlation function given by

$$\Gamma_{ij} = \langle a_i^\dagger a_j^\dagger a_j a_i \rangle \quad (4.6)$$

which are accessible in recent experiments.

### 4.3.1 Density evolution

For our analysis, here we consider  $J = 0.2$  and  $U = 10$  which makes the ratio  $U/J = 50$ . With this ratio, the two-particle repulsion between the bosons are very strong to ensure a deep MI1. First we study the QW of such a system by systematically varying the three-body attraction  $W$  from a very small to a large value compared to  $U$ . In Fig. 4.3(a-g) we show the time evolution of  $\langle n_i(t) \rangle$  for different values of  $W$ . It can be seen that for  $W = -0.5U$ , the density evolution shows a slow propagation of the quantum walkers although it is ballistic in nature.

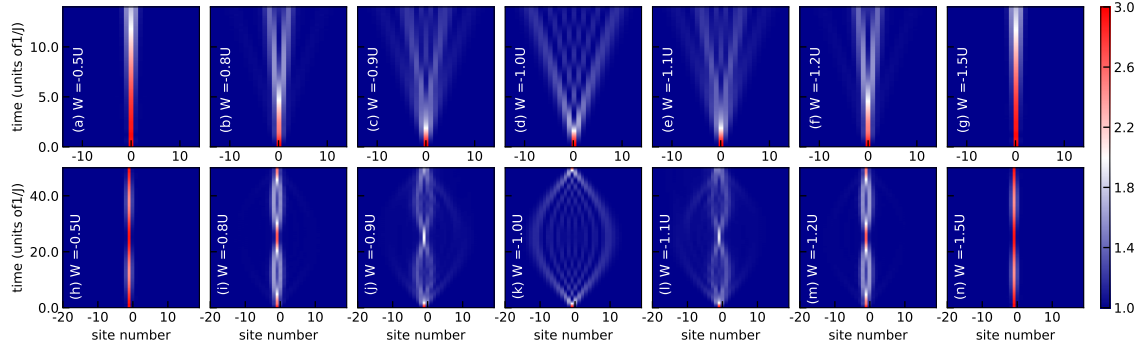


**Figure 4.3:** Figure shows the phenomenon of QW reversal of the pair of defects shown in terms of the density evolution on a homogeneous(a-g) and tilted(h-n) lattice. In the case of tilted lattice the period doubling in the Bloch oscillation clearly indicates the QW of bound defect pair.

This indicates the QW of a slow moving particle in contrast to the independent particle QW. At this point , by increasing the three-body attraction, the density distribution gradually spreads and moves towards the boundaries of the lattice at a faster rate. At some intermediate values of  $W$  ( $W < -U < W$ ), two different cones appear in the QW. In this regime of interactions, the signatures of both slow and fast moving particles emerge. However, at  $W = -U$ , the system exhibits a faster propagation of density which indicates a QW similar to that of the non-interacting particles (compare with Fig. 4.1). Interestingly, further increase in the three-body attraction after  $W = -U$  gradually brings the intermediate phases appeared in  $-W < U$  region to the original scenario (i.e.  $W = -0.5U$ ) at  $U = -1.5W$ . In this limit we see the feature similar to the QW of a slow moving particle. This indicates a scenario where the change in  $W$  in one direction introduces a reversal phenomenon where the system exhibits a sequence of slow-fast-slow QW of the two particle defects.

At this stage it is difficult to ascertain about the nature of different situations shown in Fig. 4.3(a-g). In order to understand this we exploit the physics of the Bloch oscillation, which is the periodic breathing motion of particle in position space.

### 4.3.2 Bloch oscillation

Bloch oscillation is an interesting manifestation of particle motion in a periodic potential subjected to an external force [224]. This external force can be incorporated

in model(4.5) as a constant tilt or gradient of the form

$$\mathcal{H}_{\text{tilt}} = \lambda \sum_i i n_i. \quad (4.7)$$

Under the influence of this tilt potential, the particle undergoes a periodic Bloch oscillation with period  $\tau = 2\pi/\lambda$ . We solve the model(4.5) with this additional term  $\mathcal{H}_{\text{tilt}}$  and study the density evolution for various values of  $W$  as considered in Fig. 4.3(a-g). For this purpose we consider a tilt of strength  $\lambda = 0.02 \times 2\pi$ . Interestingly, we see distinctly different features in the Bloch oscillations and a reversal phenomena as shown in Fig. 4.3(h-n). It is interesting to note that for small and large values of  $W$  the time period of oscillation are half that of the one at  $W = -U$  (which corresponds to a independent particle type evolution). Note that the frequency doubling of the oscillation in this case is a typical signature of the Bloch oscillation of a pair of particles as already discussed in Ref. [98, 213, 227, 228]. For intermediate values of  $W$  ( $W > -U$  and  $W < -U$ ) there exist two types of oscillations with two different time periods. In this regime, it appears that both single and double occupancy states are energetically favorable. From this signature it is now easy to ascertain that the system exhibits a QW of a bound pair in the beginning when  $W = -0.5U$  and gradually the pair tends to dissociate and the defects perform QW independently at  $W \sim -U$ . Counter intuitively, for larger values of  $W$  the QW of pair reappears showing a reversal of QW phenomena as a function of  $W$ .

From the above analysis, it is evident that the quantum walker is a pair of defects for small and large values of  $W$  compared to  $U$ . The pair which appears for  $W \sim 0$  can be thought of as a repulsively bound pair on top of the MI1 state which is similar to the one observed in the quantum gas experiment by Winkler *et. al.* [153]. In this case, the MI1 phase acts as a uniform background and hence the defect pair experiences uniform repulsions from all the sites. In such a case the velocity of the walkers becomes extremely small as can be seen from Fig. 4.3 (upper panel). However, when the value of  $W$  increases, the effective local interaction reduces gradually due to the attractive nature of  $W$ . Hence, the repulsively bound pair tends to dissociate into single particles and therefore, we see enhanced group velocity of propagation which corresponds to independent particle QW. However, we would like to note that the mechanism for the QW of the pair of defects in the large  $W$  regime is completely different from the one for vanishing  $W$ . In this regime, the pairing of defects is due to the combined effect of the interactions  $U$  and

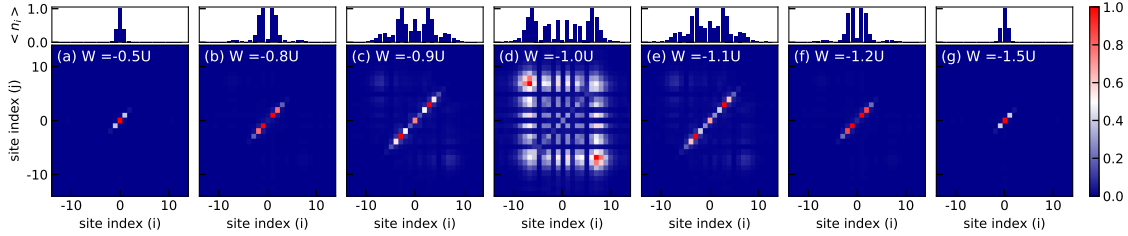


**Figure 4.4:** Figure shows the normalized two particle correlation functions  $\Gamma_{ij}$  plotted with respect to the positions  $i$  and  $j$  after a time evolution of  $t = 11.25$  (in units of  $1/J$ ) for  $J = 0.2$ ,  $U = 10$ . Results of different values of  $W/U = -0.5$ ,  $-0.8$ ,  $-0.9$ ,  $-1.0$ ,  $-1.1$ ,  $-1.2$ ,  $-1.5$  on a homogeneous one dimensional lattice of length  $L = 29$  are shown in (a) to (g). Corresponding real space density distribution is shown on top of each correlation plot.

$W$ . This is altogether a different kind of mechanism to establish repulsively bound pairs, which is already discussed in Chapter 2. The pair formation in this limit can be understood as follows. When  $W$  is very large and attractive compared to the other energy scales of the system then ideally the system prefers to form a trimer (a three particle bound state). This trimer may consists of the two defect bosons and one from the MI background. However, because of the uniform repulsion from all the sites due to the MI1 state, the two defects may rather prefer to move freely throughout the system as a bound pair [229, 230]. It is to be noted that although the pair formation mechanism for both the cases ( $W = 0$  and  $\neq 0$ ) are different, the signatures in the quantum walk are identical in nature.

### 4.3.3 Two particle correlations

At this stage, to further substantiate the physics presented above we utilize the two-particle correlator  $\Gamma_{ij}$  defined in Eq. 4.6, which sheds light on the quantum coherence of the two particles. It is well known that if two particles perform QW together, then the HBT interference occurs which strongly depends on the statistical nature of the particles. However, in the present case, since the quantum walkers originate from the same site, the HBT interference are forbidden. We compute  $\Gamma_{ij}$  after an evolution time of  $t = 11.25$  (in units of  $1/J$ ) for different values of  $W$  which are shown in the bottom panel of Fig. 4.4(a-g). We have considered a reduced basis to define the two particle correlator  $\Gamma_{ij}$  and number operator  $n_i$  where we subtract the contributions from the MI1 background. The mapping between the initial and the reduced on-site basis reads  $\{|n\rangle\} \rightarrow \{|n-1\rangle\}$  for  $n > 0$ . The correlation functions (particle densities) of each plot of Fig.4.4 are normalized by

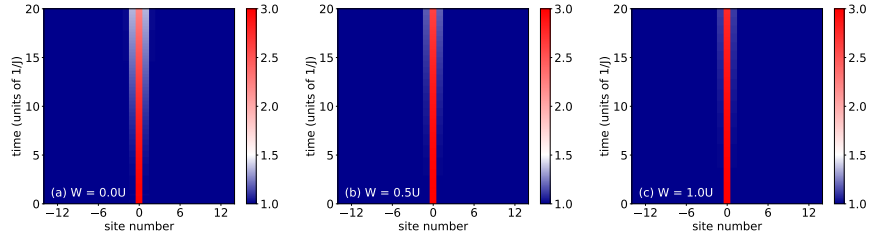


**Figure 4.5:** Figure shows the density evolutions for the QWs of two particle defects on the MI1 state for different repulsive three-body interactions ( $W$ ).

their largest respective values so that each plot can share the same scale from 0 to  $\Gamma_{max}$  (or zero to one). One can clearly see that when the ratio  $W/U$  is very small the diagonal weights of the correlation matrix are dominant indicating the QW of repulsively bound pair (Fig. 4.4(a)). Increasing the value of  $W/U$  to a very large limit recovers the similar behavior in the correlation matrix corresponding to the QW of a bound pair. However, at intermediate values of the ratio  $W/U$ , the off-diagonal weights of the correlation matrix start to increase and eventually show the signature of independent particle QW as shown in Fig. 4.4(d). These signatures in the two particle correlators for independent and pair particle QW are similar to the one obtained in recent experiment on two interacting particle QW in an empty lattice [213]. In the top panel of Fig. 4.4, we plot the normalized densities  $\langle n_i \rangle$  which shows features complementing the two particle correlation behavior.

#### 4.3.4 Two-particle QW with three-body repulsion

After discussing the QW of two particle defects on top of an MI1 state with attractive  $W$ , we turn our discussion to see the effect of repulsive  $W$ . In this regard, we time evolve the initial state (4.4) with for different repulsive three-body interactions  $W$  keeping the other parameters identical to the previous case i.e.  $U = 10$  and  $J = 0.2$ . In Fig. 4.5, we show the density evolution of the system with respect to time. It can be seen that with increasing  $W$ , the spreading of the defects becomes more localized around the origin and remain localized for higher values of  $W$ . This scenario is completely in contrast with the attractive  $W$  case, which exhibits the reversal phenomena. The reason for this localization is again due to the formation of repulsively bound pair of defects as a result of effective onsite repulsion arising from both  $U$  and  $W$ .

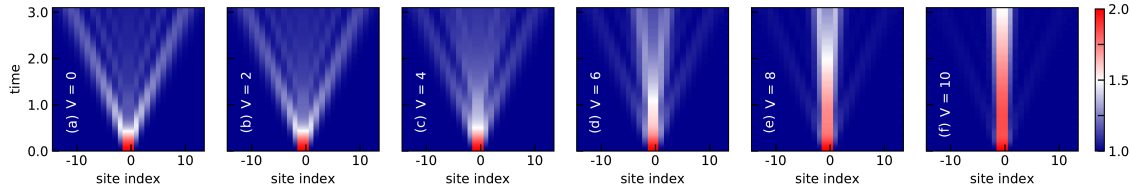


**Figure 4.6:** Density evolutions in the QWs for different values of  $V$ . Here (a-f) correspond to  $V = 0, 2, 4, 6, 8$  and  $10$  respectively.

## 4.4 Quantum walk of two particle defects with nearest neighbor interaction

After discussing the behavior of two particle defects in the presence of onsite interactions only, we discuss the QW of two defects on a MI1 state in the presence of nearest neighbor interaction. As already discussed in the previous section, two defects on the same site in presence of only two-body interaction exhibits the QW of a repulsively bound pair. Now, switching on the nearest neighbor interaction  $V$  which is small compared to  $U$ , the overall QW of defects does not get affected as the underlying MI1 state remains as it is [231]. On the other hand, if two defects stay at the nearest neighbor sites, then the presence of  $V$  plays an important role in the QW of the defects which we discuss in the following.

The Hamiltonian of the system with nearest-neighbor interaction can be defined by the EBH model, which has been introduced in Chapter 1 as:

$$\begin{aligned} \mathcal{H} = & - J \sum_{\langle i,j \rangle} (a_i^\dagger a_j + H.c.) + \frac{U}{2} \sum_i n_i(n_i - 1) \\ & + V \sum_{\langle i,j \rangle} n_i n_j. \end{aligned} \quad (4.8)$$

Here  $V$  is the nearest neighbor interaction energy. The initial state for the present configuration is given as

$$|\Psi(0)\rangle = a_{-1}^\dagger a_0^\dagger |MI1\rangle = |\dots 1 1 2 2 1 1 \dots\rangle \quad (4.9)$$

where the two defects are located at the nearest-neighbor sites on top of a perfect MI1 state. As discussed above, the perfect MI1 state is a result of large onsite repulsion  $U$ . Here we consider  $U = 50$  and  $J = 1$ . Now to study the QW of two defects, we evolve the initial state (4.9) with the system Hamiltonian (4.8) for different values of  $V$  and analyze in terms of density evolution and two-particle correlation function.

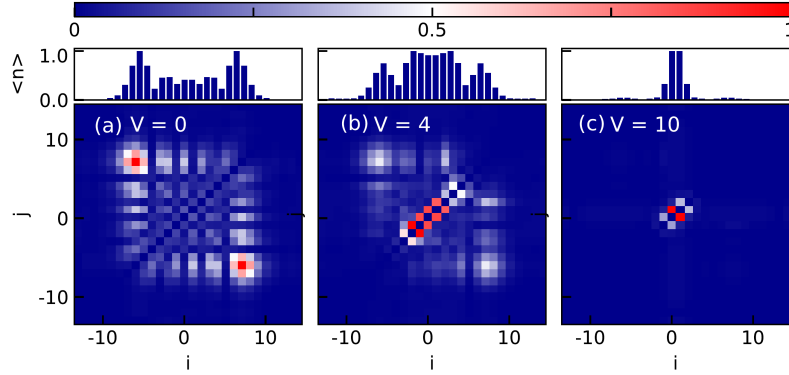


**Figure 4.7:** Two particle normalized correlation functions are shown for nearest-neighbor defects at time  $t = 2.0$  (in units of  $1/J$ ) for different values of  $V$ . On top of each panel, the corresponding normalized density distribution is shown. Here the densities and correlation functions are calculated in the reduced basis to eliminate the contribution from the MI1 background.

#### 4.4.1 Density evolution

In Fig. 4.6, we portray the density evolution for different values of  $V$ , where (a-f) correspond to  $V = 0, 2, 4, 6, 8$  and  $10$ . For  $V = 0$  we see the density spreading is similar to the single particle defects as shown in Sec. 4.2. Now with increasing  $V$ , a slower moving component starts to appear as can be seen from the second cone in the density evolution. For large values of  $V \sim 10$ , the wider cone fades away and only the slow-moving component survives.

#### 4.4.2 Two particle correlations

To ascertain the accurate dynamics of the systems, similar to the previous section, we calculate the two-particle correlation functions of two defects( $\Gamma_{i,j}$ ) in the reduced basis and normalize them. We plot these correlation functions after time  $t = 2.0$  (in units of  $1/J$ ) in Fig. 4.4 for three different regimes of  $V$ : (i) when  $V$  is zero (Fig. 4.7 (a)), (ii) at some intermediate value of  $V$  (Fig. 4.7 (b)) when we see two cones in Fig. 4.6 and (iii) when  $V$  is large compared to  $J$  (Fig. 4.7 (c)). On top of each panel in Fig. 4.4, we show the real space normalized densities calculated in reduced basis. When  $V = 0$ , we see the feature of anti-bunching in the correlation function [213, 215] which is indicated by the two peaks of the correlation function appear in far off-diagonal positions. Due to the large values of  $U$ , two defects stay away from each other, which can be seen from the corresponding density distribution on the top of the panel and this results in the anti-bunching. In the other limit

when  $V$  is large, we see that only the elements  $\Gamma_{i,(i+1)}$  and  $\Gamma_{i,(i-1)}$  are finite which signifies that the defects prefer to stay in pair (nearest-neighbor pair). However, in the intermediate region, both the signatures of anti-bunching and pair formation coexist.

The formation of pair in large  $V$  limits can be thought of as a nearest neighbor repulsively bound pair which is similar to the one described in Ref. [153]. In this case, the bound state has  $V$  amount of energy offset with the scattering states which forms a separate band for large interactions. In this scenario, if two defects are initially prepared at the nearest neighbor, for large  $V$ , they perform QW in the higher band of paired states.

## 4.5 Experimental feasibility

The QWs of defects discussed in this chapter are based on a simple Bose-Hubbard model with two or/and three-body interactions and one of the immediate platform where one can think of observing this QW reversal phenomenon is quantum gas experiment in optical lattices. Moreover, recent observation of QW with single-site addressing in interacting ultracold atoms in optical lattices [213] have broadened the scope by manifold. In the optical lattice setups, it can be possible to create an initial state proposed in this work by creating an MI phase at different densities and selectively removing particles from one site or from all sites except the central site to create all possible initial states. For example, to observe the QW reversal, a pair of particles from every site except the central one can be eliminated from an MI3 phase. With the proposed mechanism to tune the two and three-body interactions in optical lattice, the time evolution of such initial state may reveal the quantum walk reversal phenomenon. On the other hand, quantum simulations in superconducting circuit QED systems have attracted enormous attention in recent years due to the flexibility to design and control strong non-linearities and interactions with microwave radiation and artificial atoms. Very recently, strongly correlated quantum walks with a 12-qubit superconducting circuit has been observed in the experiment [217]. In practice, two-level artificial atoms are considered in the quantum simulations with circuit QED setups. However, a recent experimental proposal shows that it is possible to control the two and three-body interactions by considering a fluxonium qubit [232] where the first and second excitation levels are of equal energy and the third one can be controlled by detuning it from the first two. This scenario results in a two- and three-body interacting BH model. In such a scenario,

the above predicted physics of QW reversal can be observed in the current state-of-the-art experiments based on quantum gases in optical lattice or circuit QED systems. This result also opens up directions to study other interesting quantum mechanical phenomena such as the HBT interference effects [213–215, 218–223] in such multi-body interacting quantum walks of defects. The nearest-neighbor defect pairs are based on the EBH model which has already been simulated using dipolar bosons as discussed in Chapter 1. So, in principle the QW of the nearest neighbor defects can be accessible in cold atoms experiments.

## 4.6 Conclusions

We analyze the QW of one and two defects on a perfect MI state in the context of the BH model in the presence of interaction. When we consider a single particle or hole in strong MI of filling  $n$ , QW's expansion speed is enhanced with the density  $n$  of the MI. Moreover, the particle defect has a higher expansion speed than a hole defect in the same MI $n$ . Then we analyze the case of two interacting defects in MI $_1$  with both two-body repulsive and three-body attractive interactions. By fixing the onsite two-body interaction at a finite value and varying the three-body interaction from zero to large value, we predict the phenomenon of QW reversal. We show that the two defects on top of the MI phase pair up and perform QW for small and large values of  $W$ . At intermediate strength of  $W$ , the defects behave like independent walkers in the QW. This result shows a spontaneous QW reversal process in Mott insulator defects. Finally, we analyze the QW of two nearest-neighbor defects in the presence of nearest neighbor interactions. We find, for vanishing nearest neighbor interaction defects show antibunching nature in the correlation functions. Whereas, in the large interaction, they form the nearest-neighbor pair. We rigorously discuss all these processes in the time evolution of real-space density distribution, Bloch oscillation and also two-particle correlation function.



# Chapter 5

## Interacting bosons in optical double wells

### 5.1 Introduction

A new frontier of research have evolved with the construction of two color superlattices which is an array of double-well potentials [192, 233–239]. Recent experiments on systems of ultracold atoms in these double wells have led to various interesting phenomena in condensed matter physics and also in atom interferometry [240] and quantum information [241]. Particularly in one dimension these double-well lattices exhibit interesting properties due to the staggered or dimerized hopping amplitudes. As discussed in the introduction, the presence of this staggered hopping in double wells resembles the inversion symmetric SSH model [125]. The paradigmatic SSH model is an extremely important system to study topological phase transitions in fermionic systems as already mentioned in the introduction.

In this chapter, we analyze the ground-state properties of interacting bosons in a one-dimensional optical lattice with staggered hoppings analogous to the double-well

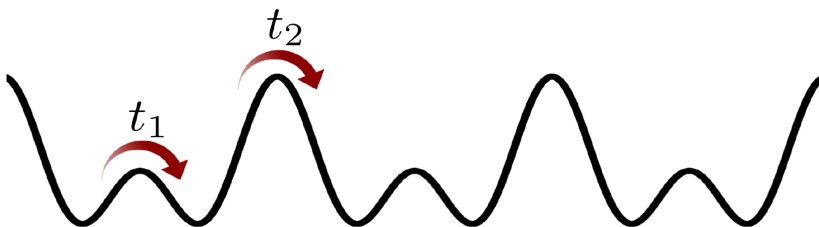


**Figure 5.1:** One dimensional double well optical superlattice with staggered hoppings  $t_1 > t_2$ .

optical lattice shown in Fig. 5.1. By assuming three-body hardcore constraint, we obtain the phase diagram in both attractive and repulsive interaction regime. This chapters builds the foundation to study the topological properties of interacting bosons in Chapter 5.

The physics of ultracold bosons in double well optical lattice can be explained by a modified Bose-Hubbard model with staggered hopping amplitudes(bosonic SSH model) which is given as;

$$\begin{aligned} \mathcal{H} = & -t_1 \sum_{i \in \text{odd}} (a_i^\dagger a_{i+1} + \text{H.c.}) \\ & - t_2 \sum_{i \in \text{even}} (a_i^\dagger a_{i+1} + \text{H.c.}) + \frac{U}{2} \sum_i n_i(n_i - 1) \end{aligned} \quad (5.1)$$

where  $a_i^\dagger$  and  $a_i$  are the creation and annihilation operators for bosons at site  $i$  and  $n_i = a_i^\dagger a_i$  is the number operator at site  $i$ .  $t_1$  and  $t_2$  are the tunneling rates from odd and even sites respectively (compare Fig. 5.1). The onsite contact interactions are characterized by the term  $U$ . The bosons in the lattice enjoy three-body constraint i.e.  $(a_i^\dagger)^3 = 0$ .

At half filling the single particle spectrum of Model(5.1) exhibits gap for any imbalance in hopping between the unit cells  $t_1 \neq t_2$ (see Sec. 1.4) [125]. Hence, the ground state is a dimer phase or bond order (BO) phase for spin polarized fermions or bosons with very large on-site interactions (hardcore bosons). The presence of three-body constraint may lead to interesting phenomena in such dimerized lattice which will be the topic of this chapter. In particular we study the interplay between pairing of particles and dimerization which gives rise to the emergence of a pair-bond-ordered phases with a sharp crossover to the bond-ordered phase. We assume  $t_1 = 1$  (unless stated otherwise) which makes other physical quantities dimensionless. Ground state properties of this system is analysed using the density matrix renormalization group (DMRG) method. We consider system sizes up to 160 sites with a bond dimension up to 800.

## 5.2 Results

We begin our discussion with a short summary of the properties of two analytically solvable limits of model (5.1). These analysis will help in understanding the physics of the system discussed in the chapter.

### 5.2.1 Hardcore limit ( $U = \infty$ )

In the limit of large interactions  $U \rightarrow \infty$ , the bosons are hardcore in nature and in this limit the Model (5.1), after a Jordan-Wigner transformation to free fermions, can be considered as the topological SSH model as mentioned before. Due to the staggered hopping amplitudes, the SSH model at half filling dimerizes naturally due to the Peierls instability and one gets dimerized phase of bosons. In this phase a single boson lives in one of the unit cell composed of two lattice sites in the double-well with larger hopping strength. Doping away from half filling breaks this dimer ordering and a critical SF phase appears. This gapped phase is called the bond-order (BO) phase. Note, that this BO phase, stabilized due a spin-Peierls like mechanism [186], does not exhibit spontaneous symmetry breaking and the BO-order is induced due to the explicitly broken translational symmetry of the model. In the literature this phase is, hence, also called fractional Mott-insulator phase or similar phase [242]. The phase diagram of such system is shown in Fig. 5.2 as a function of  $t_2$  and the filling. The gapped phases are characterized by the finite

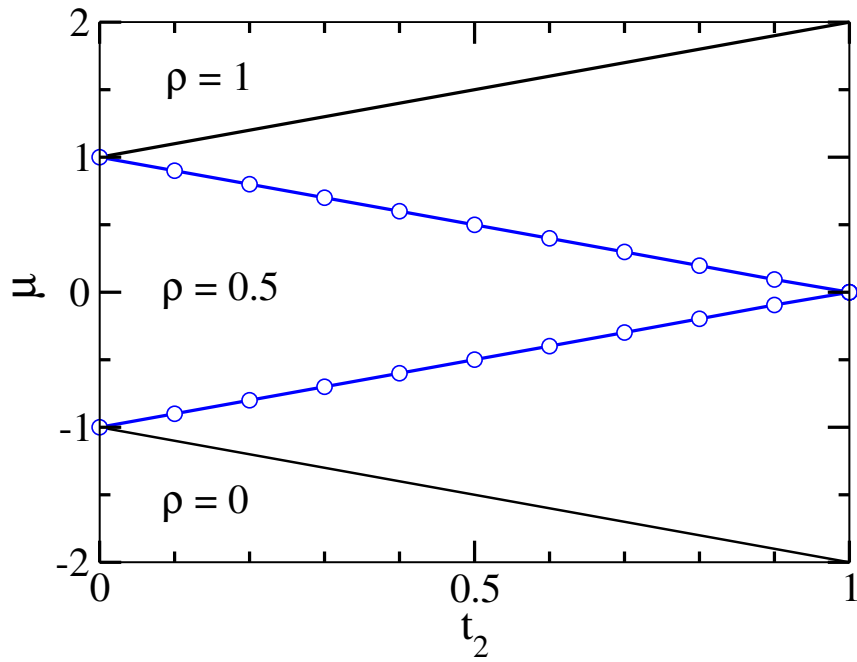


**Figure 5.2:** Phase diagram of hardcore bosons in the  $\mu$  -  $t_2$  plane with  $t_1 = 1.0$ . The points correspond to extrapolated DMRG data with  $L = 300$ , which accurately lie on top of the analytical curves (solid lines). The region included by the blue circles is the gapped BO phase at half filling. The gap opens up for any finite dimerization  $t_2/t_1$ . The black curves represent the empty and full states.

single particle gaps which is defined as

$$E_G = \mu^+ - \mu^-, \quad (5.2)$$

where  $\mu^+$  and  $\mu^-$  are the chemical potentials. As it can be seen from the phase diagram, any finite hopping imbalance leads to the gapped phase which is a BO phase and this phenomenon is also evident from the single particle spectrum.

### 5.2.2 Isolated Double Wells

It is also instructive to discuss the model for the case of trivially disconnected double-wells, corresponding to the case  $t_2 = 0$ . From this limit one can conveniently explain the finite hopping case which is the topic of interest of the chapter. In this limit the model Hamiltonian can be readily diagonalized for a fixed particle number: In the  $n = 1$  ( $n = 3$ ) sector two eigen-energies  $\pm t_1$  ( $U \pm 2t_1$ ) are found. For  $n = 2$ , the eigenvalues are given by  $U$  and  $\frac{1}{2}(U \pm \sqrt{16t_1^2 + U^2})$ . With these eigenvalues in a grand-canonical ensemble three gapped phases at fillings  $\rho = 0.5$ , 1 and 1.5 can be observed as shown in Fig. 5.3 in the strong dimerization limit. In this limit the gap at unit filling is given by

$$E_G = -3t_1 + \sqrt{16t_1^2 + U^2} \quad (5.3)$$

The ground state in the  $n = 1$  sector is given by  $|\psi_1\rangle = \psi_{20}|2, 0\rangle + \psi_{11}|1, 1\rangle + \psi_{02}|0, 2\rangle$ . Here  $|n_1, n_2\rangle$  denotes a Fock-state basis of the isolated double well and  $\psi_{02} = \psi_{20} = 2/\sqrt{16t_1^2 + 2U\varepsilon}$ ,  $\psi_{11} = 2\varepsilon/\sqrt{16t_1^2 + 2U\varepsilon}$  where  $\varepsilon = U/2 + \sqrt{4t_1^2 + U^2}/4$ . For  $U \rightarrow \infty$  this results in a MI like state  $\sim |11\rangle$  and a dimer of pairs  $|20\rangle + |02\rangle$  (pair-bond-ordered or PBO phase) for strong attractive interactions with a smooth crossover between both regimes. Indeed, the decoupled double well ground state for  $U = 0$  resembles a superposition of MI and PBO states. The features of this interesting many-body state for finite hopping  $t_1, t_2 \neq 0$  will be studied in the following sections.

A finite small hopping  $0 < t_2 \ll 1$  will couple the double wells and allow for a melting of the gapped phases due to the energy gain by delocalization of excitations and stabilize superfluids separating the gapped phases. This process may be understood as well from an effective model of coupled dimer-states such as recently discussed in Refs. [243, 244].

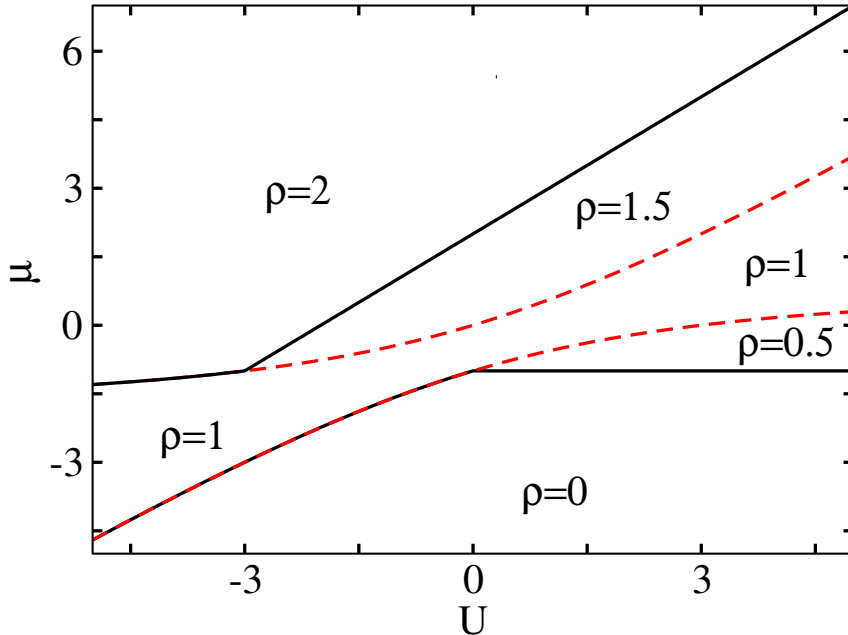


**Figure 5.3:** Phase diagram of isolated doublewells showing three gapped phases at  $\rho = 0.5, 1$  and  $1.5$ .

### 5.2.3 Vanishing two-body interaction ( $U = 0$ )

In the limit of vanishing interactions for a softcore boson without the three-body hardcore constraint one expects an SF phase even for very strong hopping imbalance. In the presence of interaction the physics of the system is governed by the competition between the hopping amplitudes and the onsite interactions which leads to the non-trivial gapped phases at intermediate half integer filling apart from the gapped MI phases [242] as a function of interaction  $U$ . A similar feature is also present in the case of usual two color superlattice potential where the SF phase becomes gapped MI phases at half integer and integer fillings for strong interactions [245].

The situation however, is different in the case of three-body constrained bosons where a maximum of two bosons can occupy a single lattice site. Due to the effect of double well superlattice the motion of particles is restricted to one unit cell. Interestingly, in such a scenario two different gapped phases arise at  $\rho = 1$  and  $\rho = 1.5$  after some critical values of  $t_2$ . The gap in the system can be seen as the finite plateaus in the  $\rho$  vs  $\mu$  diagram as shown in Fig. 5.4. The phase diagram corresponding to this scenario is depicted in Fig. 5.5 where the gapped phases at  $\rho = 1$  and  $\rho = 1.5$  appear at  $t_2 \sim 0.4$  and  $t_2 \sim 0.9$  respectively. The gapped BO regions for  $\rho = 1$  and  $\rho = 1.5$  are bounded by red circles and blue squares respectively. The black lines correspond to the empty and full states. The remaining

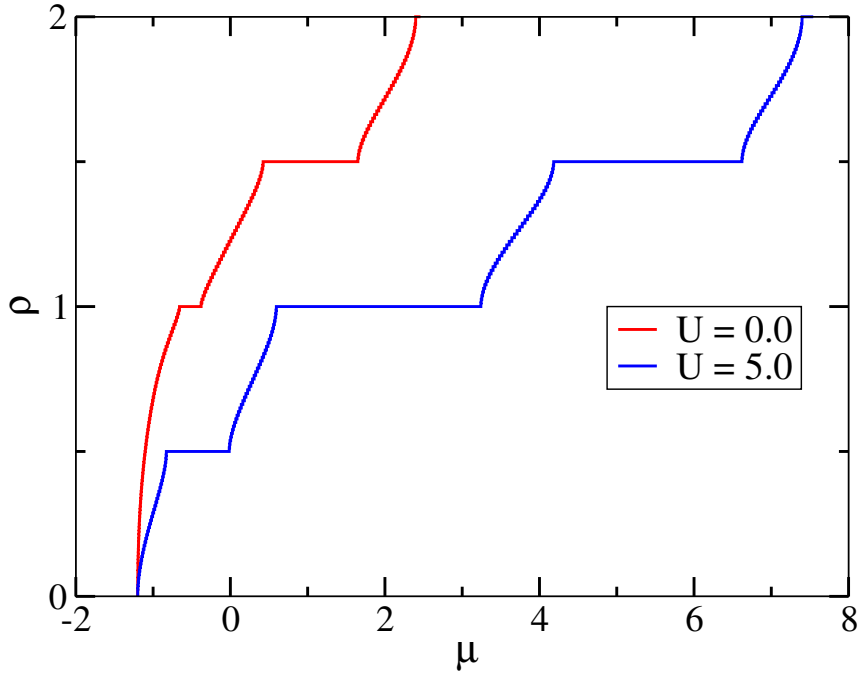


**Figure 5.4:** Figure shows the behaviour of  $\rho$  with respect to  $\mu$  for  $U = 0$  (left red curve) and  $U = 5$  (right blue curve) for  $t_2 = 0.2$ . Plateaus indicate the gapped phases.

part of the phase diagram is the SF phase.

#### 5.2.4 Finite $U$ and $t_2 = 0.2$ case

As the system is already in the gapped BO phase for  $U = 0$  at commensurate densities except at  $\rho = 0.5$ , it is interesting to see the effect of interactions on the ground state of the system. The phase diagram for this case is shown in Fig. 5.6. As we move away from the  $U = 0$  limit along the positive  $U$  axis the gapped phases grow as can be seen from the enlargement of the plateaus in the  $\rho$  vs  $\mu$  plot for  $U = 5$  shown in Fig. 5.4. The gapped phases at  $\rho = 0.5$  and  $\rho = 1.5$  are depicted by the region bounded by the blue dashed curves and the one at  $\rho = 1$  is bounded by the green solid curve in the phase diagram of Fig. 5.6. At  $\rho = 0.5$ , the gap appears after a critical point  $U \gtrsim 0.4$  leading to the BO phase. As anticipated in the discussion of the decoupled double-well case, the excitation gap at  $\rho = 1$  remains finite for all  $U$  even for a small  $t_2 > 0$  leading to a smooth cross-over from the pair-bond-ordered (PBO) phase to the MI phase through the BO phase where every site is occupied by one atom due to large onsite repulsion. The strong onsite repulsion disfavours the dimerization and prohibits two particles occupying a single site. For  $\rho = 1.5$ , the system remains in the BO phase which becomes wider as a function

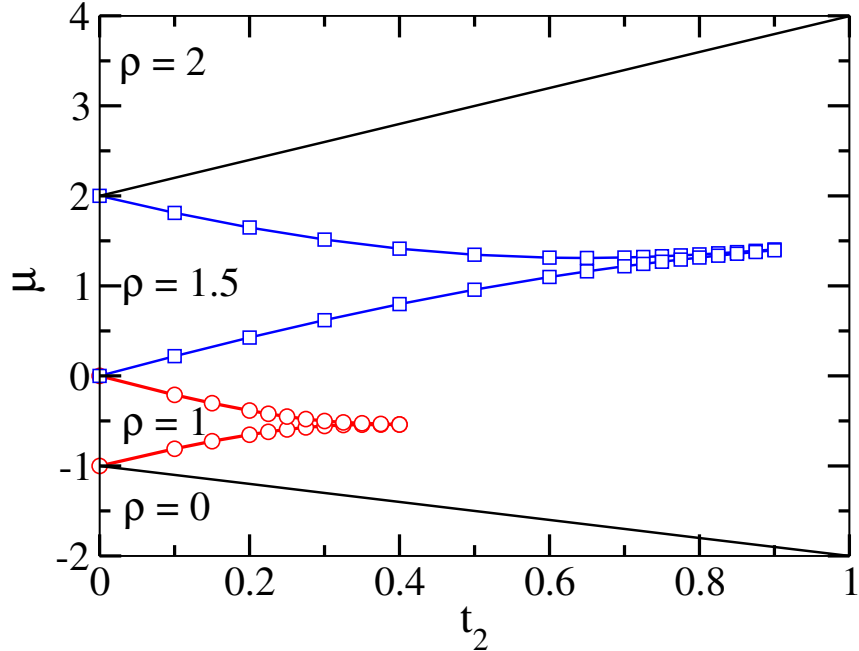


**Figure 5.5:** The phase diagram for three-body constrained bosons as a function of  $t_2$  for  $U = 0$  obtained from polynomial extrapolation of gap. The BO phase at  $\rho = 1$  and  $\rho = 1.5$  appear at  $t_2 \sim 0.4$  and  $t_2 \sim 0.9$  respectively.

of  $U$ . This BO phase is similar to the one for the hardcore bosons at  $\rho = 0.5$  as discussed before. The boundaries for the gapped phases are obtained by computing the chemical potentials  $\mu^+$  and  $\mu^-$  and extrapolating them to thermodynamic limit using system sizes of  $L = 20, 40$  and  $80$ .

The signatures of BO and PBO phases can be seen by plotting the bond operator

$$B_{i,n} = \langle (a_i^\dagger)^n (a_{i+1})^n + H.c \rangle \quad (5.4)$$

for different bonds. Here the exponent  $n = 1$  and  $n = 2$  for the BO and the PBO phases respectively. In Fig.5.7 we plot  $B_{i,n}$  for unit filling which show finite oscillations in the BO and PBO phases. The calculations are done by taking 80 sites and in the figure we show only the central part of the system. Fig.5.7(a), Fig.5.7(b) and Fig.5.7(c) shows the values of  $B_{i,n}$  for  $U = -4, 0$  and  $8$  respectively. The strong oscillation of PBO operator compared to the BO operator for  $U = -4$  shows that the system is dominantly in the PBO phase. Also it can be seen that for  $U = 8$  the oscillation of  $B_{i,n}$  has decreased drastically due to the MI phase. Similarly, in Fig.5.8(a) and Fig.5.8(b) we plot the value of  $B_{i,n}$  for  $\rho = 0.5$  and  $\rho = 1.5$  respectively for the repulsive values of  $U$  where the system is in the BO phase.

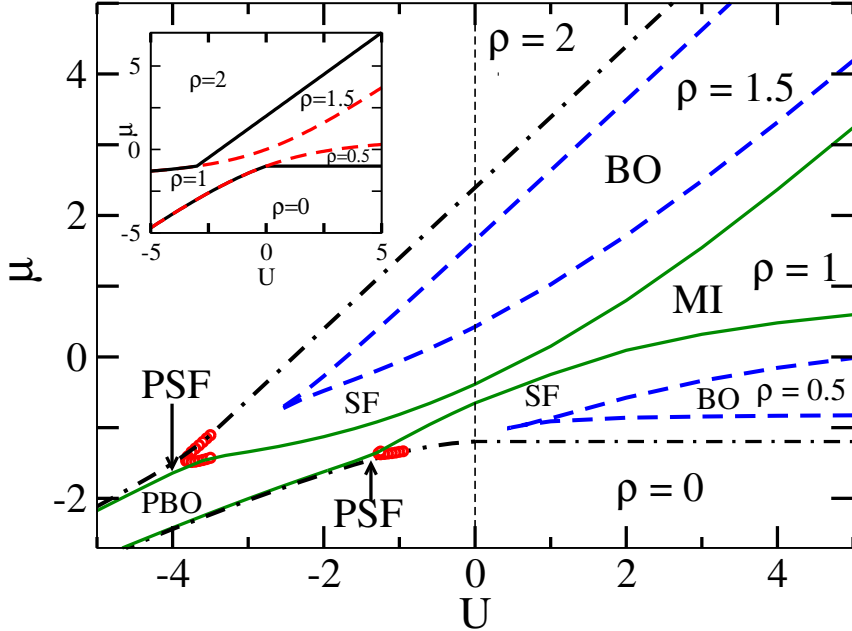


**Figure 5.6:** Phase diagrams for  $t_2 = 0.2$ . The region bounded by the green curves are the gapped phases at  $\rho = 1$ (middle) which consists of the MI(PBO) phases in the strong repulsive(attractive) regimes. The regions bounded by the blue dashed curves are the gapped BO phases at  $\rho = 0.5$ (upper) and  $\rho = 1.5$ (lower). On the attractive side the PSF is separated from the SF phase by the red circles. (Inset) Shows the phase diagram in the limit of isolated double-wells for comparison.

Further we obtain the signature of the BO phases by computing the bond-bond correlation function and the related structure factor which is given as;

$$S_{BO}(k) = \frac{1}{L^2} \sum_{i,j} e^{ikr} \langle B_i B_j \rangle, \quad (5.5)$$

where  $r = |i - j|$  is the distance. In the BO phase the quantity  $B_i$  oscillates in alternate bonds and the structure factor exhibits a finite peak at the zone boundaries. It is to be noted that the BO phases which appear in the phase diagram are not the true BO phase as lattice translational symmetry is not spontaneously broken. However, the signature is similar to the BO phase whose qualitative feature can be seen from the bond order structure factor.

The situation becomes interesting in the attractive regime. Because of the three-body constraint the system is stable against collapse and due to the attractive interaction, the particles start to form pairs. While there is no gapped phase at  $\rho = 0.5$  in this side of the phase diagram, the gap at  $\rho = 1.5$  remains finite up to some finite values of  $U$  and then closes after a critical point of  $U = -2.6$ . The

closing up of the gap is due to the competition between the hopping and attractive interaction which tries to break the dimerization and system becomes a superfluid as shown in Fig. 5.6. However, for  $\rho = 1$ , the gap survives for very large values of  $U$  extending up to infinity. These features can be seen from the plateaus in the  $\rho - \mu$  plot as shown in Fig. 5.9 for two different values of  $U = -1.5$  and  $U = -4.0$ . For  $U = -1.5$ , the gaps appear at  $\rho = 1$  as well as at  $\rho = 1.5$  where as for  $U = -4$ , only the gap at  $\rho = 1$  exists. For sufficiently strong attractive interactions, the particles tend to form pairs and at unit filling it becomes a half filled system of bosonic pairs. It is to be noted that these pairs behave like hardcore bosons due to the three-body constraint. In such a scenario the ground state is similar to the dimerization of the hardcore bosons as discussed in the section for  $U = \infty$  case. The gapped phase for large attractive  $U$  is the BO phase of pairs which can be called as a PBO phase. However, in the weak interaction regime pair formation is not favoured due to the competition between the interaction and kinetic energy. Therefore, the BO phase which appear at  $U = 0$  survives up to a finite value of attractive  $U$  and then there exist a smooth crossover to the PBO phase as the value of  $U$  increases.

The characteristic feature of the PBO phase is seen from the PBO structure factor  $S_{PBO}(k)$  which is similar to the BO structure factor as defined in Eq. (5.5) with  $a^\dagger(a)$  replaced by  $a^{\dagger 2}(a^2)$  which is shown in Fig. 5.10. It can be seen that

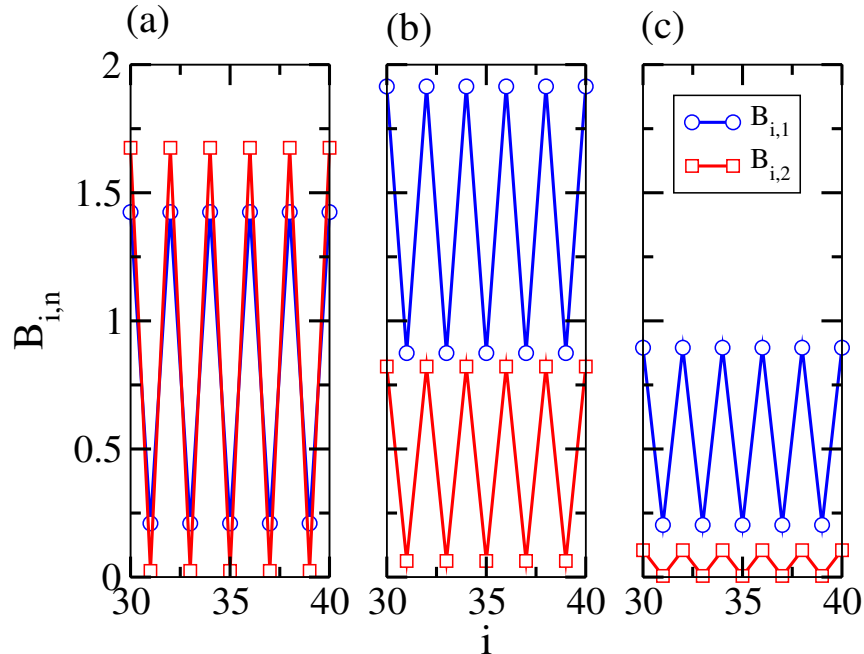


**Figure 5.7:** Bond operator  $B_{i,n}$  are shown for the BO(blue circles) and PBO(red squares) phases for  $\rho = 1$  and  $t_2 = 0.2$ . (a) $B_{i,n}$  for  $U = -4$ . (b) $B_{i,n}$  for  $U = 0$ . (c)  $B_{i,n}$  for  $U = 8$ .

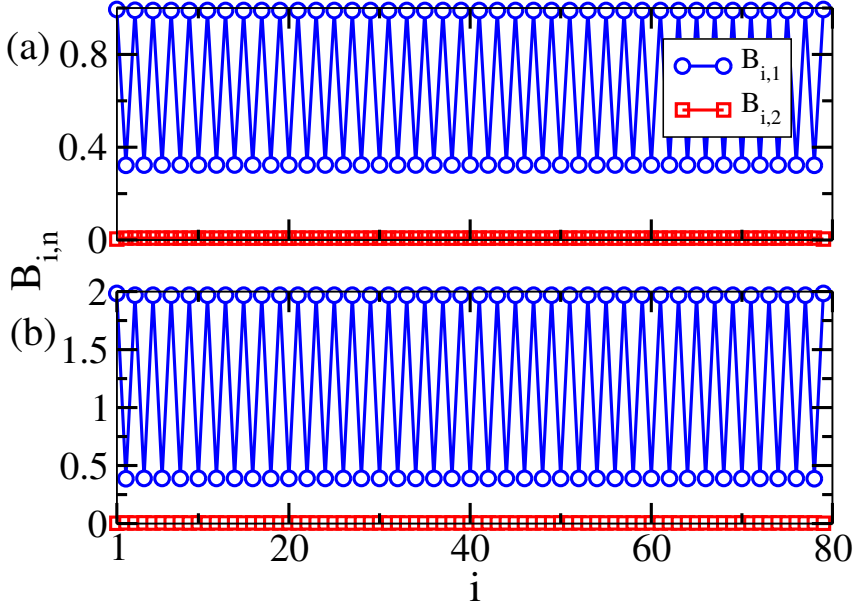


**Figure 5.8:** Bond operator  $B_{i,n}$  are shown for the BO(blue circles) and PBO(red squares) phases for  $t_2 = 0.2$ . (a) $B_{i,n}$  for  $U = 4$  and  $\rho = 0.5$ . (b) $B_{i,n}$  for  $U = 2$  and  $\rho = 1.5$ .

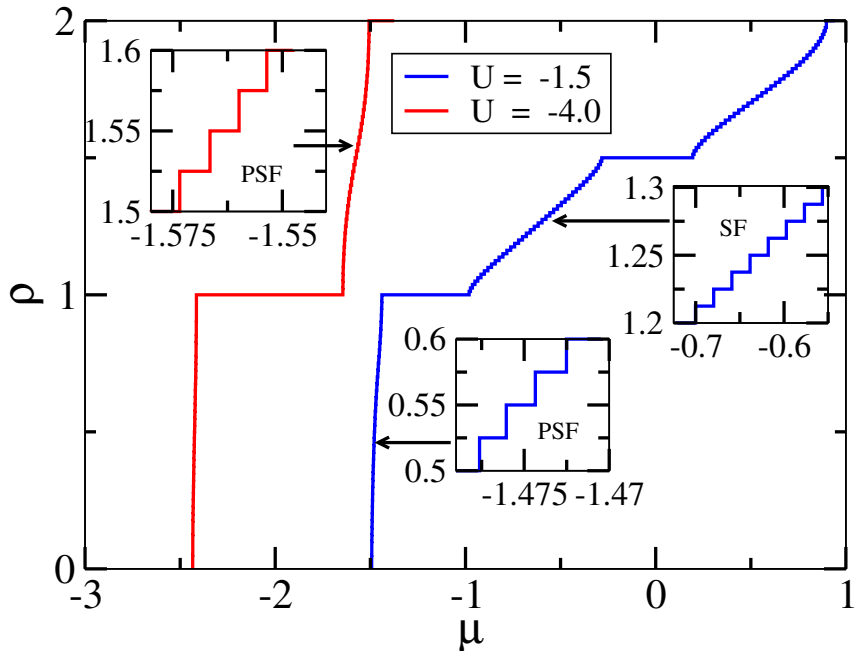


**Figure 5.9:** Behaviour of  $\rho$  with respect to  $\mu$  for  $U = -4.0$  (left red curve) and  $U = -1.5$  (right blue curve) at  $t_2 = 0.2$ . The insets show the enlarged regions of the SF and PSF phases where the density jumps in steps of one and two particles respectively.

the value of  $S_{PBO}(k = \pi)$  increases smoothly as the value of  $U$  becomes more and more attractive. At the same time the BO structure factor  $S_{BO}(k = \pi)$  decreases smoothly after increasing up to a particular value of attractive interaction  $U \sim -2.5$ .

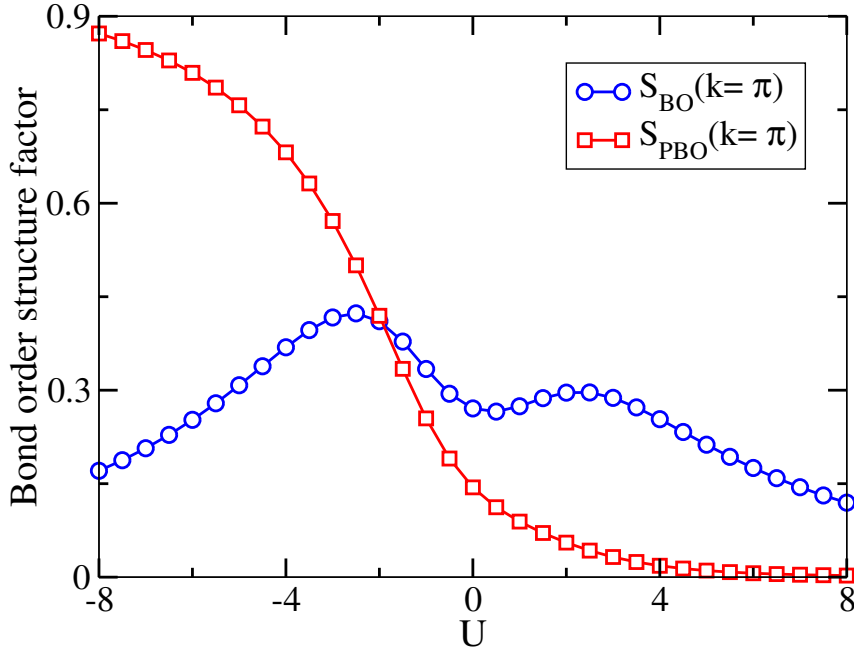


**Figure 5.10:** The extrapolated values of bond order structure factor for single particle (blue circles) and pairs (red squares) for different values of  $U$  at  $\rho = 1$  (see text for details). Here  $t_2 = 0.2$ .

Note that the finite value of  $S_{PBO}(k = \pi)$  for repulsive  $U$  and small attractive  $U$  are due to the finite probability of second order hopping processes in the BO phase. We would like to stress that since the BO phases are the manifestation of the double well geometry of the lattice, the BO structure factor remains finite even in the MI and PBO phase even in the thermodynamic limit. It can be seen from Fig. 5.10 that on the repulsive interaction side the value of  $S_{BO}(\pi)$  smoothly decreases after a particular value of  $U$ . This signals the crossover to the MI phase. The onset of the MI phase can be understood as in the case of large interaction  $U$ , the system prefers to accommodate one particle in each site which is also true in the homogeneous lattice systems. This can be seen from the decreasing trend of the curve shown in the Fig. 5.10.

We may further characterize the position of the phase cross-over by local maximum of the fidelity susceptibility [246] which is defined as

$$\chi_{FS}(U) = \lim_{U-U' \rightarrow 0} \frac{-2 \ln |\langle \Psi_0(U) | \Psi_0(U') \rangle|}{(U - U')^2}, \quad (5.6)$$

with the ground-state wave function  $|\Psi_0\rangle$ . While the phase transitions are often characterized by a peak diverging with the system size  $L$ , here we observe a stable maximum as function of several system sizes as shown in Fig. 5.11.

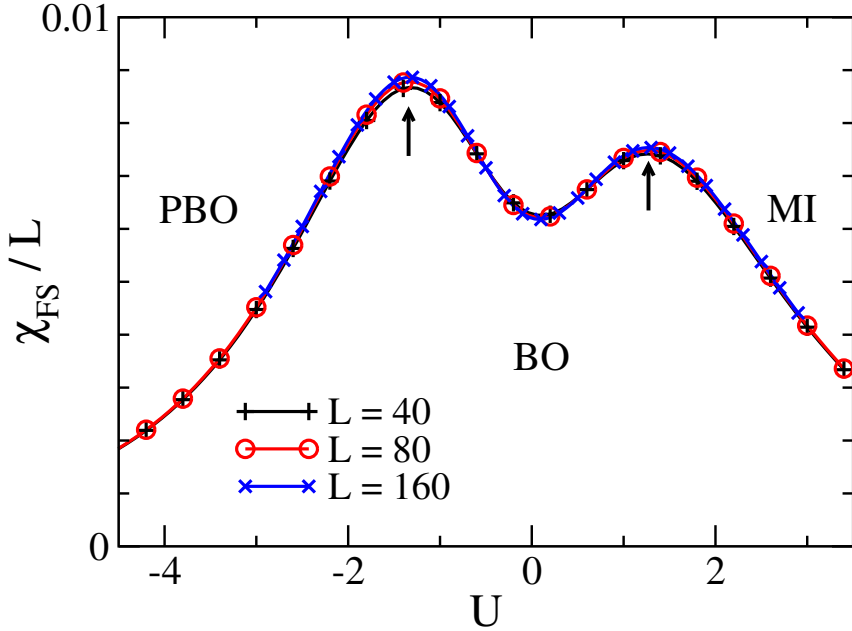


**Figure 5.11:** Fidelity susceptibility  $\chi_{FS}$  as function of the interaction strength  $U$  ( $\rho = 1$ ,  $t_2 = 0.2$ ) for  $L = 40, 80$  and  $160$ .

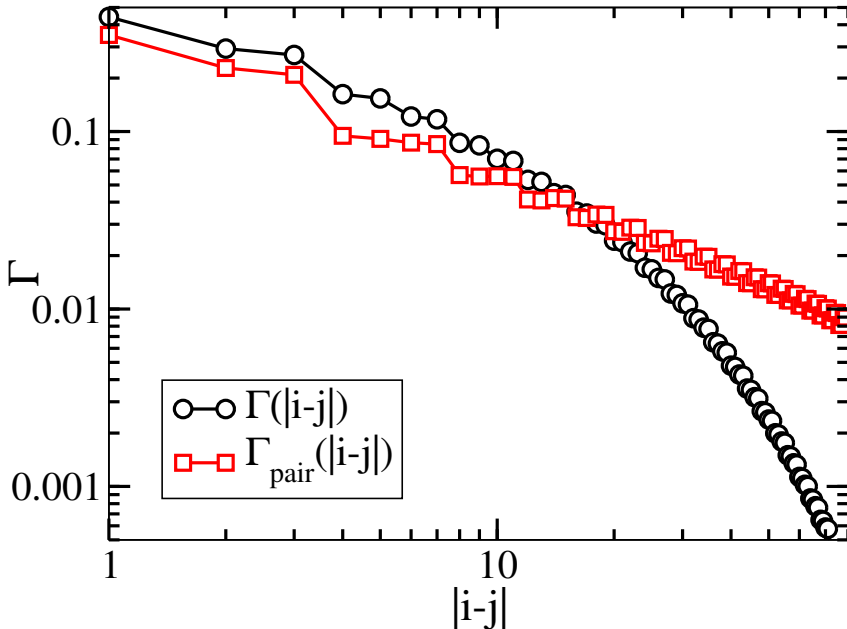


**Figure 5.12:** Single particle correlation function  $\Gamma(|i - j|)$  (black circles) and pair correlation functions  $\Gamma_{pair}(|i - j|)$  for  $t_2 = 0.2$  are plotted for  $U = -4.0$  at  $\rho = 1.5$  for a system of length  $L = 160$  (see text for details).

The gapped BO phase which continues from the repulsive side for  $\rho = 1.5$  closes at a critical value  $U \sim -2.6$ . It is interesting to note that as the interaction becomes more and more attractive, the pair formation occurs and a PSF phase is stabilized

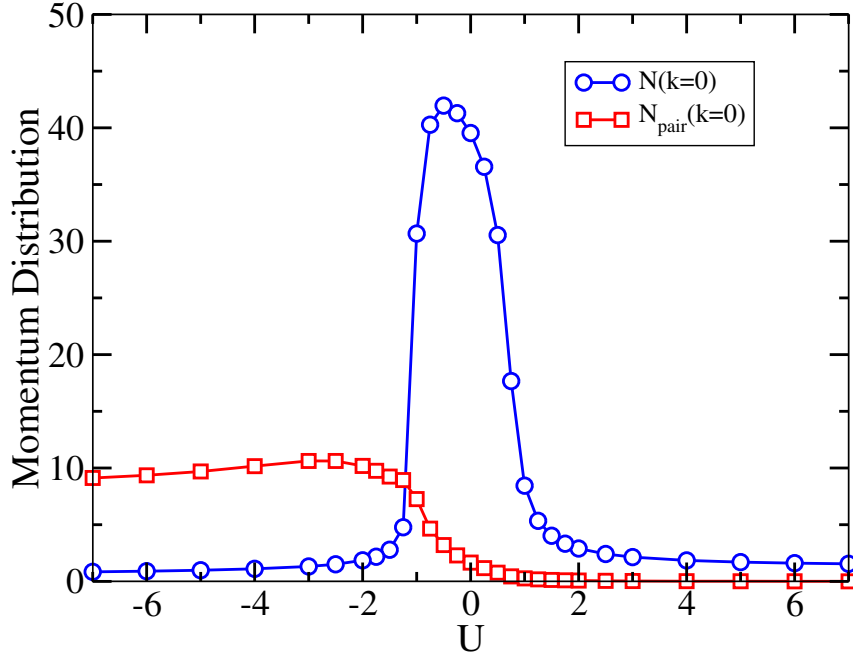


**Figure 5.13:** The peak heights of  $N(k = 0)$  (blue circles) and  $N_{pair}(k = 0)$  (red squares) at  $\rho = 0.5$  using  $L = 160$  for  $t_2 = 0.2$  show the transition from PSF to SF and then to BO phases as discussed in the text.

for all densities around  $\rho = 1.0$  [30, 44]. The PSF and SF phases are separated by the red circles as depicted in the phase diagram of Fig. 5.6. The signature of PSF phase can be obtained from the  $\rho - \mu$  plot where the density jumps in steps of two particle at a time to minimize the energy. This is clearly visible in the insets of Fig. 5.9 where the densities for two different values of  $U$  are plotted. For  $U = -1.5$ , the system is in a PSF phase in the region below the  $\rho = 1$  gapped phase and rest of the region is in the SF phase for incommensurate densities. However, for  $U = -4$  the system is in the PSF phase for all values of density except  $\rho = 1$ . Apart from the  $\rho - \mu$  curve, we compute the single particle and pair correlation functions and corresponding momentum distribution to confirm the existence of the PSF phase. Fig. 5.12 shows the behaviour of  $\Gamma(i, j) = \langle a_i^\dagger a_j \rangle$  (black circles) and  $\Gamma_{pair}(i, j) = \langle (a_i^\dagger)^2 (a_j)^2 \rangle$  (red squares) with respect to the distance  $|i - j|$  for  $U = -4$  and  $\rho = 1.5$ . It can be clearly seen that the single particle correlation function decays faster where as the pair correlation function behaves like a power-law in the logarithmic scale which indicates the presence of the PSF phase.

We also compute the momentum distribution function as

$$N(k) = \frac{1}{L} \sum_{i,j} e^{ikr} \Gamma(i, j), \quad (5.7)$$

to complement the SF phases. Where  $\Gamma(i,j) = \langle a_i^\dagger a_j \rangle (\langle a_i^{\dagger 2} a_j^2 \rangle)$  is the single particle(pair) correlation function. The peak heights of the momentum distribution function  $N(k=0)$  for single particle and pairs are plotted against  $U$  corresponding to  $\rho = 0.5$  of the phase diagram 5.6. This shows that for large attractive interaction  $N_{pair}(k=0)$  is dominant indicating the PSF phase. As the value of  $U$  becomes less attractive then the value of  $N_{pair}(k=0)$  decreases and  $N(k=0)$  increases showing the signatures of the SF phase. The SF phase continues till the critical point for SF-BO transition on the repulsive side where both the momentum distribution functions are extremely small. The SF-BO transitions are of Berezinskii-Kosterlitz-Thouless(BKT) type transition which can be seen from the smooth opening up of the gap in Fig. 5.6. The transition points can be accurately obtained by performing a finite size scaling of the single particle momentum distribution function which varies as  $N(k=0) \propto L^{1-\frac{1}{2K}}$  [247, 248], where  $K = 2$  is the Luttinger parameter. In Fig. 5.14 we plot  $N(k=0)L^{-0.75}$  for different lengths( $L = 80, 120, 160$ ) and all the curves intersect at the critical point  $U \sim 0.44$ .

At this point we analyse the system without the three-body hardcore constraint to see the effect finite three-body interactions ( $W/6 \sum_i n_i(n_i - 1)(n_i - 2)$ ) in the presence of the double-well potentials. As already mentioned before, for softcore bosons and vanishing two-body interaction i.e.  $U = 0$ , the system is a gapless

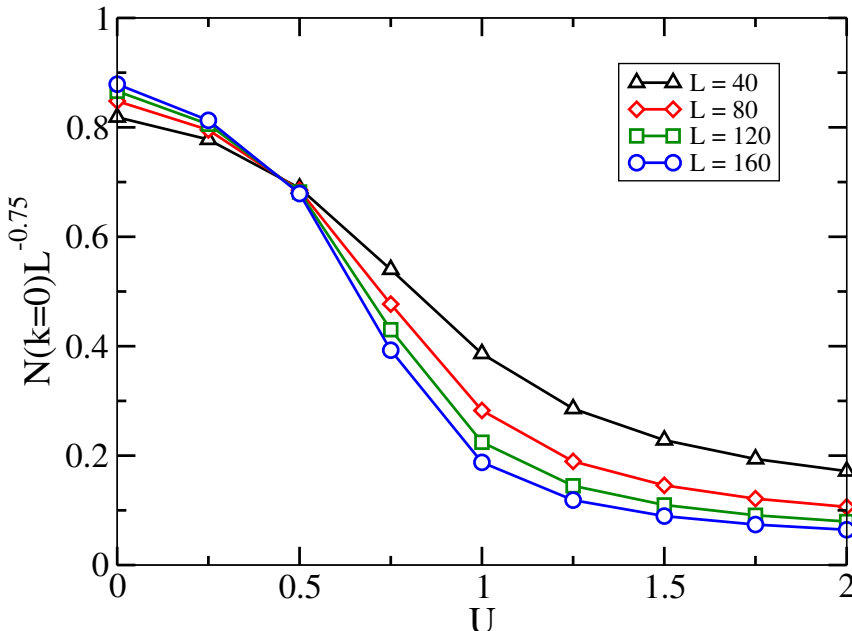


**Figure 5.14:** Finite size scaling of  $N(k=0)$  for  $t_2 = 0.2$  shows that the curves for different lengths ( $L = 40, 80, 120, 160$ ) intersect at the critical point  $U \sim 0.44$  for the SF-MI transition at  $\rho = 0.5$ .

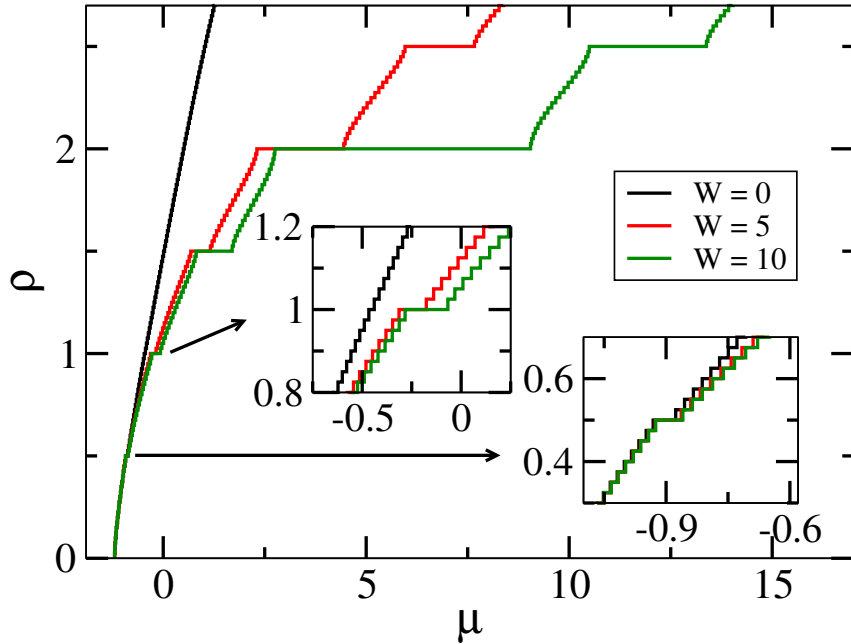


**Figure 5.15:** Behaviour of  $\rho$  with respect to  $\mu$  for  $U = 1$ ,  $t_2 = 0.2$  and  $W = 0$ (black curve),  $W = 5$ (red curve) and  $W = 10$ (green curve) for the case of softcore bosons. Here maximum number of particle per site is taken to be 5. Inset shows the zoomed in view of  $\rho = 1$  and  $0.5$  regions.

superfluid for any value of hopping dimerization which is in contrast to the case of three-body constrained bosons. To see the effect of finite  $W$  we analyse the  $\rho$  vs.  $\mu$  plot for different values of  $W = 0$ ,  $5$  and  $10$  considering  $L = 40$  with small onsite interaction  $U = 1$ , which is shown in Fig 5.15. Here we can see that for  $W = 0$  the system is in the SF phase for integer and half integer densities except at half filling where there exists a small plateau. This is consistent with the result obtained in Ref [249]. However, as the value of  $W$  increases the plateaus at other integer and half integer densities appear indicating various gapped phases. The plateau lengths increase in size with increase in  $W$ . Therefore, we would like to highlight that although the three-body hardcore constraint is essential to stabilise the gapped phases on the attractive  $U$  side, it is not that crucial for the repulsive  $U$  case.

### 5.2.5 Finite $U$ and $t_2 = 0.6$ case

After analyzing the phase diagram for the  $t_2 = 0.2$  case where the effect of staggered hopping is large, we repeat the calculation for another cut through the phase diagram of Fig. 5.5 at  $t_2 = 0.6$ . The motivation to consider  $t_2 = 0.6$  lies in the fact that there is no gap at  $\rho = 1$  for  $U = 0$  as depicted in Fig. 5.5 and it will be interesting to see

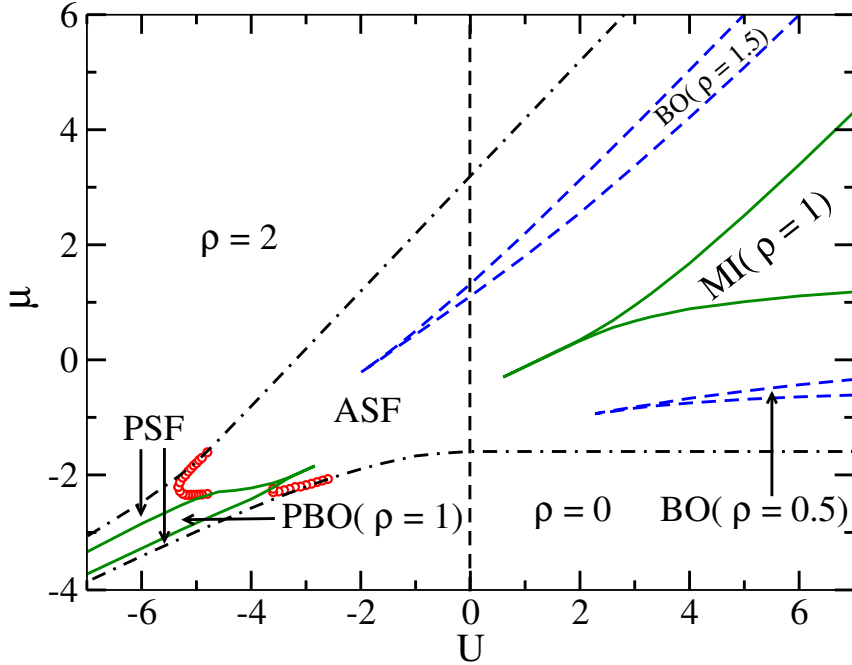


**Figure 5.16:** Phase diagrams for  $t_2 = 0.6$ . The region bounded by the continuous green curves are the gapped phases at  $\rho = 1$  and the regions bounded by the blue dashed curves are the gapped bond order phases at  $\rho = 0.5$  (upper) and  $1.5$  (lower). On the negative  $U$  side the PSF is separated from the SF phase by the red circles. The black dot-dashed lines represent the empty and full states.

how the system evolves by moving away from this limit. A similar analysis along the line of  $t_2 = 0.2$  case leads to the phase diagram as shown in Fig. 5.16. It can be seen that the overall picture of the phase diagram is similar to that of  $t_2 = 0.2$  for  $\rho = 0.5$  and  $\rho = 1.5$ . However, interesting thing to note that there are clear phase transitions from the SF phase to the MI phase on the repulsive side of  $U$  and to a PBO phase on the attractive side of  $U$ . These signatures can be clearly seen from various order parameters plotted in Fig. 5.17. It can be seen that the PBO structure factor, gap and the parity order(see Sec. 5.2.6 for detail) remain finite in the gapped MI and PBO phases where as they vanish in the SF phase.

### 5.2.6 Parity order

Another physical quantity of interest which can be directly accessed in the state-of-the art experiment [5, 6] is the parity order parameter which is defined as

$$O_P^2(i, j) = \langle e^{i \sum_{i < k < j} \pi n_k} \rangle \quad (5.8)$$

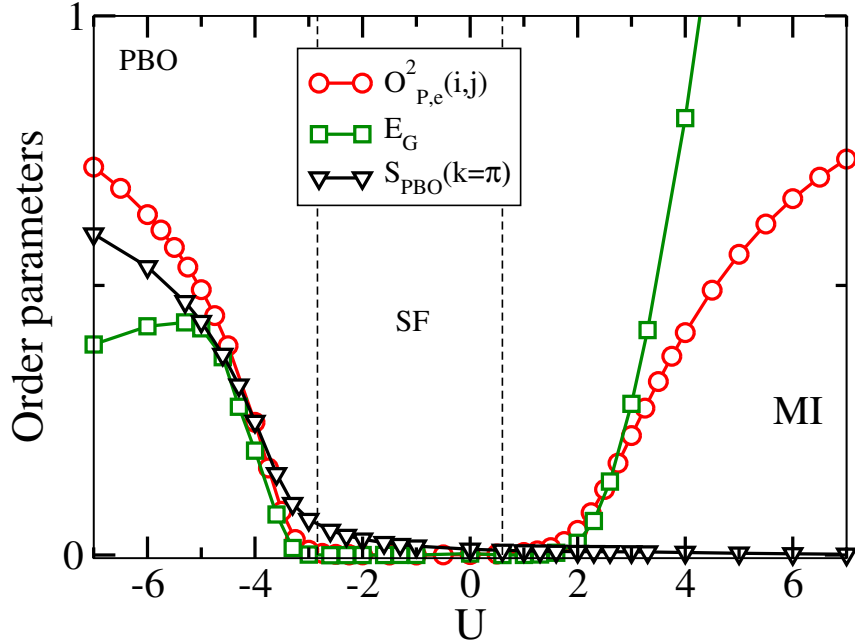


**Figure 5.17:** Order parameters depicting different phases for  $t_2 = 0.6$ . The red circles, green squares and black down triangles show the values of  $O_{P,e}^2(i,j)$ ,  $E_G(L)$  and  $S_{PBO}(k = \pi)$  respectively for different values of  $U$ .

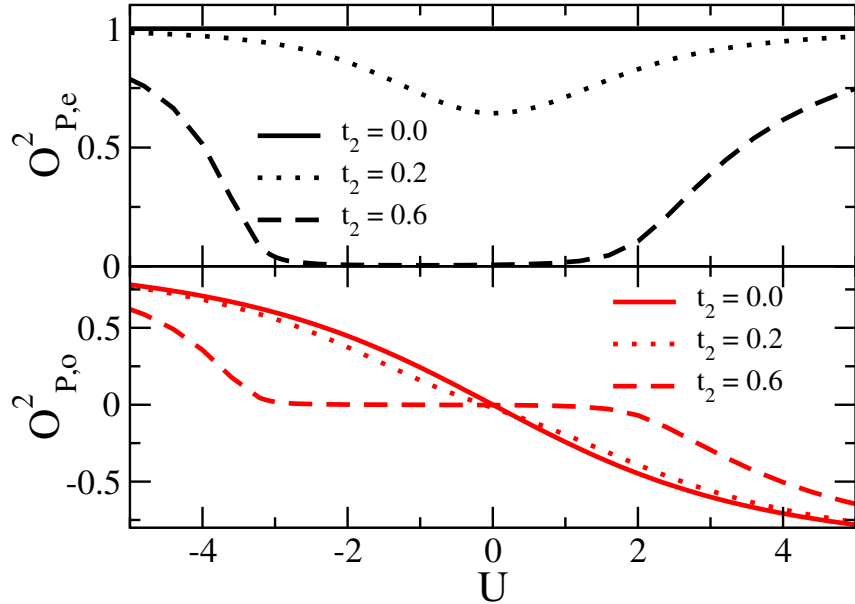


**Figure 5.18:** Parity order  $O_P^2(i,j)$  for odd and even distances  $|i - j| \gg 1$  are plotted for different values of  $t_2$  with respect to  $U$ .  $t_2 = 0$  lines correspond to the analytical results as discussed in the main text,  $t_2 = 0.2$  and  $t_2 = 0.6$  curves depict the data obtained for  $L = 160$  sites.

To complement our findings we compute  $O_P^2(i,j)$  which is finite in the MI phase due to particle-hole excitations. For small  $t_2 \rightarrow 0$  we may understand the emergence of

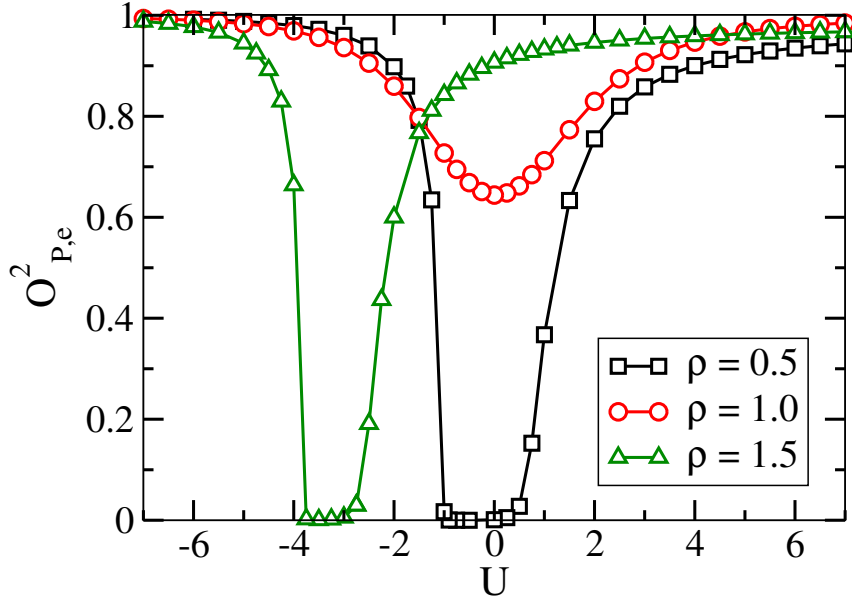


**Figure 5.19:**  $O_{P,e}^2$  at  $\rho = 0.5, 1.0$  and  $1.5$  for  $t_2 = 0.2$  is plotted for different values of  $U$ .

parity order from the properties of isolated double wells as discussed in Sec. 5.2.2. For a ground-state at  $\rho = 1$  given by a product of  $|\psi_1\rangle$ , one easily estimates the parity order to be exactly  $O_{P,e} = 1$  on even distances  $|i-j|$ . For odd distances, however, one observes an interesting dependence of the parity order on the interaction strength,  $O_{P,o} = -\frac{U}{\sqrt{16t_1^2+U^2}}$ . We plot the odd and even distance parity orders as  $O_{P,e}$  and  $O_{P,o}$  respectively with respect to  $U$  for different values of  $t_2$  in Fig. 5.18. The black and red curves correspond to  $O_{P,e}$  and  $O_{P,o}$  respectively. The solid lines correspond to the limit of isolated double wells i.e for  $t_2 = 0$ . The dotted lines are the  $t_2 = 0.2$  and the dashed curves are for  $t_2 = 0.6$ . It is very clear from this figure that the odd and even distance parities show two different behaviour and the parity order is finite in the MI, BO and PBO phases where as it is zero in the SF phase. Analogously one also finds for the gapped phases at half filling a finite oscillating parity order which is 0 for even and  $\pm 1$  for odd distances. The parity order parameter also vanishes in the SF phase. This can be seen from the Figure. 5.19 where  $O_{P,e}^2$  is plotted as a function of  $U$  for different fillings.

### 5.3 Conclusions

We have investigated the ground state phase diagram of a system of three-body constrained bosons in a double well optical lattice. By analysing the competition between the dimerized hopping and onsite interactions we have obtained the com-

plete phase diagram both in the regime of attractive as well as repulsive interactions. The phase diagram exhibits various gapped phases such as the BO and MI phases at commensurate densities. At unit filling and small hopping ratios the system exhibits a BO phase of pairs in the attractive interaction regime which we call the PBO phase and there exists smooth crossover from MI-BO (BO-PBO) on the repulsive (attractive) side of the phase diagram. For large values of the hopping ratios, the gapped phases melt for small values of interactions and there exist an intermediate SF phase. The appropriate finite size scaling shows that the superfluid to gapped phase transitions are of BKT type. The findings presented in this work addresses an interesting problem which involves the physics of strongly correlated bosons in a double well optical lattice both in attractive and repulsive regime. As the double well optical lattices have already been created and manipulated using cold atoms, it will be possible to observe these phases in the experiments.

As mentioned before, this kind of double well optical lattice resembles the topological SSH model which possess two types of dimerizations depending on the hopping ratios. Depending on the dimerization, the SSH model exhibits topological phase transition. The topological aspects of this model have been analysed recently in various contexts [242, 250–253]. One of the interesting phenomenon which signals these topological phase transition is the Thouless charge pumping mechanism [254–257]. In the present scenario the PBO phase consists of hardcore boson pairs and it is in principle possible to map the system to an effective SSH model for the spinless fermions. In Chapter 6, we discuss the topological features of the bound bosonic pairs.



# Chapter 6

## Topological properties of bound bosonic pairs in the SSH model

### 6.1 Introduction

Composite particles often exhibit fundamentally different properties, e.g. charge or exchange statistics, from the ones of their constituents, which may strongly influence the properties of many body states of these composite objects. A paradigmatic example of this is the composite fermions picture of fractional quantum Hall states [258, 259]. In particular, these phases have triggered a paramount interest in topological phases of matter influencing the field of condensed matter physics, material sciences and quantum computation [114].

As already mentioned, the simplest system which exhibits topological phase transition is the one dimensional SSH model. Although, the SSH model is known to exhibit a phase transition from the trivial to topological phase in a system of non-interacting fermions, recently it has been extensively studied in the context of fermionic and bosonic systems with interactions [242–244, 252, 252, 260–263, 263–265], dynamical fields [250, 251, 266], as well as finite temperatures, non-equilibrium and mixed states [267–269]. As already discussed in 1.4, the topological phases of the SSH model are characterized by the existence of polarized edge states. The existence of such localized edge modes can be probed by the presence of adiabatic transport or pumping of a quantized topological charge. This concept was first introduced by Thouless [270], and may be studied by the generalization of the SSH to the Rice-Mele (RM) model [271]. Recently, with the observation of charge pumping in cold-atom experiments [254, 255, 272, 273], the fate of Thouless-pumping in interacting systems, such as the interacting fermionic or bosonic RM model has attracted

a lot of interest [256, 257, 274–278].

In this chapter, we study the topological phase transitions of a system of bound bosonic pairs in a one dimensional SSH model. which can be written as :

$$H = - \sum_i (t + \delta t (-1)^i) a_i^\dagger a_{i+1} + \text{H.c.} + H_{\text{int}} \quad (6.1)$$

The first two terms in Eq. 6.1 corresponds to the SSH model written in terms of  $t = \frac{t_1+t_2}{2}$  and  $\delta t = \frac{t_1-t_2}{2}$  for convenience with hopping rates  $t_1$  and  $t_2$  from odd and even sites respectively. H.c stands for the Hermitian conjugate.  $H_{\text{int}}$  introduces interaction is the SSH model which in our case is the onsite two particle interaction of bosons of the form;

$$H_{\text{int}} = \frac{U}{2} n(n-1). \quad (6.2)$$

where  $n_i$  is the number operator. As we intend to study the case of bound bosonic pairs, we consider  $U < 0$  and impose three-body constraint i.e.  $(a_i^\dagger)^3 = 0$  in order to stabilize the system against collapse due to the attractive onsite interactions. In the rest of the chapter we typically choose parameters in units of  $t_\alpha = 1$  where  $t_\alpha = t_1$  (or  $t_2$ ) for the dimerization  $t_1 > t_2$  (or  $t_2 > t_1$ ).

## 6.2 Results

The limit of strong attractive interactions  $-U \gg t$  at unit filling is dual to the hard-core boson limit  $U \rightarrow \infty$  with renormalized hopping coefficients  $t_i^{\text{eff}} = t_i^2/|U|$  and half filling. As effective on-site pairs are formed, one can define the corresponding operator  $c_i^\dagger = (a_i^\dagger)^2$  and hence, the paired boson model can be mapped to the free fermion Model

$$H_f = - \sum_j (t + \delta t (-1)^j) c_j^\dagger c_{j+1} + \text{H.c..} \quad (6.3)$$

As this model exhibits well defined non-trivial topological properties at half-filling, we can expect to find similar properties of the paired-boson model in the limit  $-U \gg t$  at unit-filling. In the following we analyze the ground state phase diagram and the topological properties of paired bosons for finite on-site two-body interactions by using the DMRG method. We consider typically system sizes up to 160 sites and keeping bond dimension equal to 800 .

We show that the system of bound bosonic pairs, even though not protected

by symmetry, exhibits remarkable effective topological features such as edge states and Thouless charge pumping of pairs in a region of attractive finite  $U > -\infty$ , which is adiabatically connected to a region with trivial effective topology. In the end we discuss how some features of this phenomenology could be observed without implementation of a three-body hardcore constraint in cold atomic quantum gases.

### 6.2.1 Bulk properties

In the SSH model shown in Eq. 6.1, two types of hopping dimerization are possible for corresponding to  $t_1 < t_2$  and  $t_1 > t_2$ , which exhibit identical bulk properties. At half filling, the single particle spectrum is gapped for any imbalance in hopping between the unit cells  $t_1 \neq t_2$  [125]. In the limit of large interactions  $U \rightarrow \infty$ , the bosons are hardcore in nature and in this limit the Model (6.1), after a Jordan-Wigner transformation to free fermions  $c_i^{(\dagger)}$  can be considered as the topological SSH model as mentioned before. Hence, one gets a BO phase of bosons at half filling i.e.  $n = N/L = 1/2$  particles per lattice site as a result of natural dimerization due to the Peierls instability. Presence of chiral symmetry in the model leads to the emergence of gapless topological edge states for  $t_1 < t_2$  which are characterized by a nontrivial winding number (or Zak phase) [261, 262, 279]. This paradigmatic example of bulk-boundary correspondence can be extended to the case of softcore bosons at half filling [242].

### 6.2.2 Phase diagram

Detailed ground state bulk properties of three-body constrained bosonic SSH model in a grand canonical ensemble are discussed in Chapter 5. Here, we will summarize the phases and phase transitions of the model focusing on the phase diagram at unit-filling i.e.  $n = N/L = 1$  particles per lattice site. In the case of  $\delta t = 0$  of Model (6.1) is known to exhibit a Berezinskii-Kosterlitz-Thouless(BKT) type phase transition from a gapless SF to a gapped MI phase for strong repulsive interactions  $U > U_c > 0$  (where  $U_c$  is the critical point for the SF-MI phase transition). For negative values of the interaction  $U < 0$ , the three-body constrained system exhibits an Ising-type phase transition to a SF phase of paired bosons called the pair superfluid(PSF) phase. In the limit of strong attractions  $-U \gg t$  the system is a stable ensemble of bosonic pairs  $(a_i^\dagger)^2 |0\rangle$  [280] dual to the hardcore boson limit  $U \rightarrow \infty$  with renormalized hopping coefficients of bound pairs  $t_i^{eff} = t_i^2/|U|$ . The complete ground state phase diagram of the bosonic constrained SSH model is

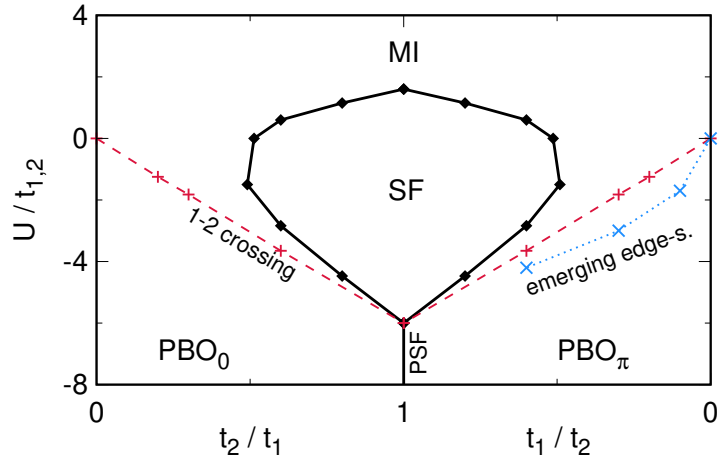


**Figure 6.1:** Phase diagram of the bosonic three-body constraint SSH model at unit filling  $n = 1$  as function of  $t_2/t_1$  and  $U/t_1$  (on the left) and  $t_1/t_2$  and  $U/t_2$  (right part). The solid line with black diamonds marks BKT phase transitions between gapped and gapless phases. The dashed line depicts the crossing between single and two particle excitations and defines the crossover between MI and PBO phases. The dotted line depicts the emergence of polarized edge states due to the nontrivial effective topology of the model in the attractive regime (see text).

shown in Fig. 6.1 as a function of the hopping ratios  $t_2/t_1$  as well as  $t_1/t_2$  and the interaction strength  $U/t_1$  and  $U/t_2$  respectively.

The phase diagram shows various quantum phases such as the gapped MI phase on the repulsive  $U$  regime and the PBO<sub>0</sub> and PBO<sub>π</sub> phases in the attractive regime, which will be discussed in more detail in the following. Apart from this there also exist the gapless SF and PSF phases. The black diamonds depict the phase transition to the SF phase and there exist smooth crossovers from the MI to the PBO phase denoted by the red plus-dashed lines. The blue cross-dotted line represents the emergence of edge states as will be discussed below.

In Fig. 6.1, the gap to gapless phase transitions and crossovers are determined by using the finite size scaling of the momentum distribution function;

$$N(k) = \frac{1}{L} \sum_{i,j} e^{ik|i-j|} \langle a_i^\dagger a_j \rangle \quad (6.4)$$

The BKT type SF-MI transition points are obtained by means of the finite size scaling of the momentum distribution function as discussed in Chapter 5 [247, 248].

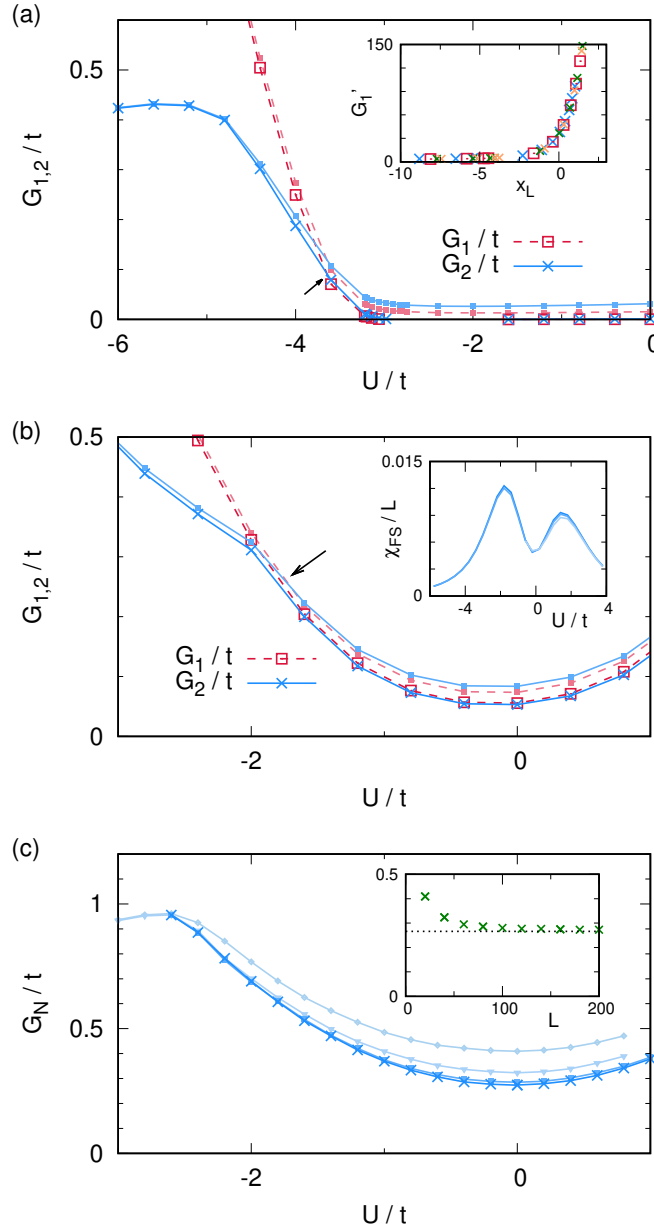


**Figure 6.2:** Single and two particle energy gaps  $G_1$  (red dashed lines) and  $G_2$  (blue solid lines) respectively are shown as function of  $U/t$ . We show the data for system size of  $L = 160$  (light filled squares) together with the extrapolation to the thermodynamic limit (open square for  $G_1$  and cross for  $G_2$ ) using  $L = 40, 80, 120$  and  $160$  sites. DMRG data for (a)  $t_2/t_1 = 0.6$  and (b)  $t_2/t_1 = 0.3$ . The arrow marks the crossing between  $G_1$  and  $G_2$ . The Inset in (a) shows the BKT-compatible scaling of the single particle energy gap with a critical value of  $U_c = -2.9t_1$  (see text). The Inset in (b) depicts the fidelity susceptibility  $\chi_{FS}/L$  for  $t_2/t_1 = 0.3$  as function of  $U$ . Panel (c) shows the neutral excitation gap  $G_N$  at  $t_2/t_1 = 0.2$  for  $L = 20, 40, 80$  and  $160$  sites (top to bottom curve). The inset in (c) shows the extrapolation of the gap-minimum for system sizes up to  $L = 200$  sites which extrapolates to a finite value  $G_N \sim 0.26t_1$ .

We further compute the excitation gap of the single particle  $G_1$  and two-particle sector  $G_2$  with

$$G_m(L) = (E_0(N+m, L) - 2E_0(N, L) + E_0(N-m, L))/m, \quad (6.5)$$

where  $E_0(N, L)$  is the ground-state energy of a system of  $N$  particles and  $L$  sites and  $m \in [1, 2]$ . In order to verify the BKT character of the phase transitions we analyze the finite size scaling of the energy gaps in the negative  $U$  regime using the approach used in Ref. [281, 282]. In the inset of Fig. 6.2 (a) the rescaled single particle energy gap

$$G'_1 = G_1 L (1 + 1/(\log(L) + C)) \quad (6.6)$$

for  $t_2 = 0.6$  exhibits the expected scaling close to the BKT transition point ( $U_c = -2.9$ ). This leads to a collapse of data points plotted against

$$x_L = \log L - \log B / \sqrt{|U - U_c|}, \quad (6.7)$$

with fitting parameters  $C$ ,  $B$  and  $U_c$  [281, 282].

For a strong staggered hopping  $\delta t$ , as shown in Fig. 6.2 (b), we do not observe any closing of the excitation gap  $G_{1,2}$  upon changing  $U$  from the PBO to the MI phase. We furthermore calculate the neutral excitation gap  $G_N(L) = E_1(N, L) - E_0(N, L)$  for strong  $\delta t$ , as depicted in Fig. 6.2 (c), which also remains finite. This shows that - interestingly - both phases remain adiabatically connected, as discussed already in Chapter 5. In the inset of Fig. 6.2 (b) we depict the fidelity susceptibility defined as

$$\chi_{FS}(U) = \lim_{U-U' \rightarrow 0} \frac{-2 \ln |\langle \psi_0(U) | \psi_0(U') \rangle|}{(U - U')^2}, \quad (6.8)$$

where  $|\psi_0\rangle$  is the ground-state wave-function.  $\chi_{FS}/L$  exhibits local maximum which stays finite as function of the system size, consistent with the finite excitation gaps. The presence of a second local maximum may be attributed to an intermediate bond-ordered (BO) region (see Chapter 5), which we will not discuss here further. We may quantify the crossover points from the MI-region to the PBO phase by a more detailed analysis of the excitation gap. As shown in Fig. 6.2 (a) and (b) we observe a crossing between the single particle gap  $G_1$  (red dashed lines) and two-particle gap  $G_2$  (blue solid lines) which indicates the crossover points. In the figure we show the data for  $L = 160$  along with the extrapolated data for  $t_2 = 0.6$  (Fig. 6.2 (a)) and 0.3 (Fig. 6.2 (b)). The extrapolation is performed using the data

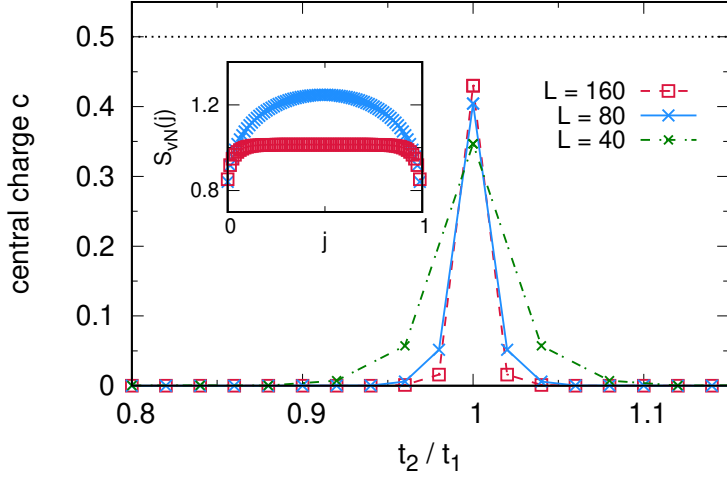


**Figure 6.3:** Estimate of the central charge for the PSF to PBO phase transition ( $U = -8$ ) for different system sizes. The figure shows results of a fit to the bipartite entanglement entropy  $S_{vN}(j)$ , as shown in the inset for  $L = 160$  for two examples  $t_2 = t_1$  (top curve) and  $t_2 = 0.98t_1$  (bottom curve).

for  $L = 40, 80, 120, 160$ . The arrow defines the crossover between MI-like and dimerized PBO states. The crossover position to a PBO region can also be seen in the bond order structure factors, shown in Chapter 5.

Finally, in Fig. 6.3 we present numerical results for the phase transition to the PSF phase at large negative  $U = -8t_1$ . By fitting the bipartite von-Neumann entanglement entropy  $S_{vN}(j)$  to its conformal description [283]

$$S_{vN} = \frac{c}{3} \log \left[ \frac{L}{\pi} \sin \frac{\pi l}{L} \right] + g \quad (6.9)$$

we obtain estimates of the central charge  $c$  for several system sizes. The central charge seems to converge to a value of  $c = 1/2$  at the critical point  $t_1 = t_2$  in the thermodynamic limit, as expected for a PSF-phase. For a finite  $\delta t > 0$ , the central charge drops to  $c = 0$  and the system enters into the gaped PBO regime.

### 6.2.3 Topological properties

As argued above, for  $U \rightarrow -\infty$ , the Model (6.1) is equivalent to a model of hardcore bosons or free fermions given in Eq. (6.3). At half-filling, this exhibits non-trivial topological properties for  $t_2 > t_1$ , such as edge states. In the following we discuss the fate of these features for finite interactions.

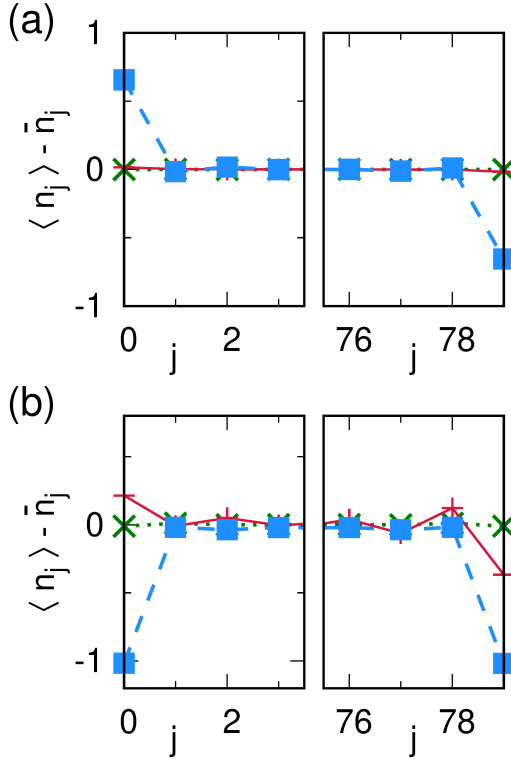


**Figure 6.4:** Polarized edge states for the RM model at (a)  $U = -10$  and (b)  $U = -2$  ( $t_1 = 1$ ,  $t_2 = 0.2$ ) after subtracting the overall density modulation  $\bar{n}_i = \langle n_{L/2+(i \bmod 2)} \rangle$  for clarity. The different curves are for different values of  $\tau = 0.0$ (blue dash-square),  $0.25\pi$ (red plus-solid),  $0.5\pi$ (green dot-cross).

### 6.2.3.1 Edge states

In our numerical simulations, we observe the presence of polarized edges also at finite values of  $U > -\infty$ , in the region marked as PBO $_\pi$  phase in Fig. 6.1. In Fig. 6.4, we sketch the edge density for a generalized RM model at  $t_1/t_2 = 0.2$  for different values of  $U$ . We will come to the RM model later, and here we will focus on  $\tau = 0$  curves which show the edge densities of the corresponding SSH model. In order to visualize the properties of the edges, for clarity, we subtract the background average density  $\bar{n}_j = \langle n_{L/2+(j \bmod 2)} \rangle$  and plot the density for different values of  $\tau$ . For smaller values of  $U$  (Fig. 6.4 (b)), the polarization vanishes abruptly and symmetric (Friedel-like) density oscillations are found at the boundaries of the system.

In order to quantify the edge properties in more detail, we calculate the polar-

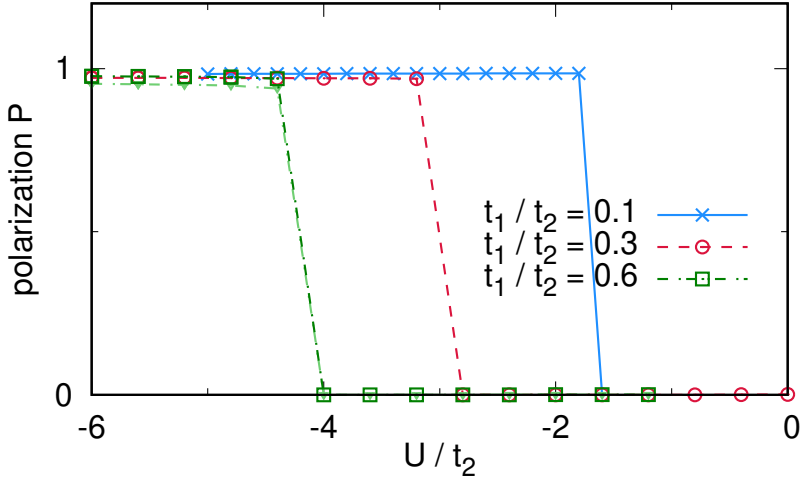


**Figure 6.5:** Polarization  $P$  for  $t_1/t_2 = 0.1, 0.3$  and  $0.6$  as function of the interaction strength for  $L = 160$  and  $L = 80$  sites (light colored lines).

ization

$$P = \frac{1}{L} \sum_{i=0}^L \langle \psi | (i - i_0) n_i | \psi \rangle \quad (6.10)$$

with  $i_0 = (L - 1)/2$  and the ground state  $|\psi\rangle$  of Model (6.1) or (6.13) at  $\tau = 0$ . We plot this quantity for different values of  $t_1/t_2$  with respect to  $U$  as shown in Fig. 6.5. In order to facilitate the numerical simulations, we add a small symmetry breaking potential to the boundary sites, corresponding to the evolution of the RM model at small value of  $\delta\tau = 0.001$ . Comparisons to results with a smaller  $\delta\tau = 0.0001$  and different system sizes indicate that our choice does not influence the physics of the system. Interestingly, we observe a sudden sharp transition between a region of  $U < U_e$  with polarized edges and a polarization close to  $P = 1$  and unpolarized systems with  $P = 0$  for larger values of  $U > U_e$ .

In the phase diagram of Fig. 6.1, we depict the point of emergence of edge states  $U_e$  as the blue cross-dotted line. This transition line differs from the crossing position of 2-particle and 1-particle excitations (red dashed line in Fig. 6.1). The reason for this can be attributed to the bosonic enhancement which is energetically favorable to first delocalize a single doublon on the MI phase before the polarized edge states are formed [243].

### 6.2.3.2 Winding number

The concept of bulk-boundary correspondence states that the presence of topological edge states should be related to a non-trivial topological invariant of the bulk system. For the SSH-model, this is the winding number [242] defined in the many-body context as

$$\omega = \int_0^{2\pi} d\theta \langle \psi(\theta) | \partial_\theta \psi(\theta) \rangle \quad (6.11)$$

from the ground state  $|\psi\rangle$  of the effective model with twisted boundary conditions  $a_i \rightarrow e^{i\theta/L} a_i$ . With this definition, we find that  $\omega$  vanishes in all the gapped phases and in the SF phase it is accurately characterized by the winding number  $\omega \neq 0$ . However, we observe no distinction between the  $t_1 < t_2$  and the  $t_2 < t_1$  region as shown in Fig. 6.6 (a).

To circumvent this we may identify  $c_i \rightarrow (a_i^\dagger)^2$  and, hence, a single fermion hopping corresponds to two boson tunneling and will involve twice the phase. This simple argument already explains why we observe  $\omega = 0$  also for  $t_2 < t_1$  as we are winding effectively twice around the parameter space. Hence, the winding number correctly describing the topological properties in this limit should be defined over half the period as

$$\omega_{1/2} = \int_0^\pi d\theta \langle \psi(\theta) | \partial_\theta \psi(\theta) \rangle, \quad (6.12)$$

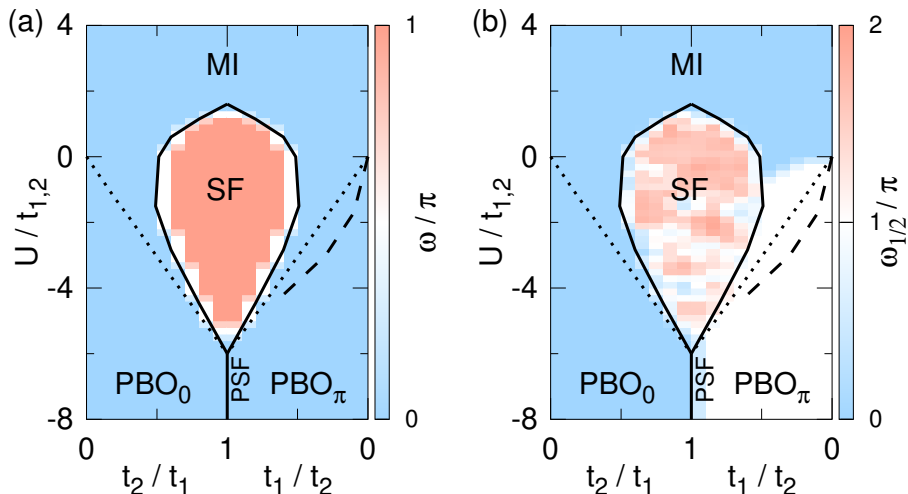


**Figure 6.6:** Estimates of the winding numbers (a)  $\omega$  and (b)  $\omega_{1/2}$  from small system size simulation ( $L = 8$  sites, exact diagonalization) for the SSH-model as function of  $U/t$  and  $t_1/t_2$  as well as  $t_2/t_1$ . Black lines correspond to the lines of Fig. 6.1.

in analogy to a  $Z_2$  index used for the description of e.g. quantum spin Hall effect [284]. In Fig. 6.6 (b) we calculate  $\omega_{1/2}$  for the full phase diagram for small system sizes and observe that, interestingly,  $\omega_{1/2}$  stays remarkably close to a quantized value in all gapped regions. We also observe an extended region where  $\omega_{1/2} = \pi$ , which coincides roughly with the emergence of the edge states. We want to stress that  $\omega_{1/2}$  is not protected by symmetry in the attractive boson model, but its robustness can be related to an effective chiral symmetry of the bound bosonic pairs. This is why the emerging topological properties without closing of many-body gap apparently seems to contradict the bulk-boundary correspondence. It allows us to discriminate between the  $PBO_0$  and a  $PBO_\pi$  regions with non-trivial and trivial effective topology,  $\omega_{1/2} = 0$  and  $\omega_{1/2} = \pi$  and an abrupt jump between them.

### 6.2.3.3 Thouless charge pumping of bound pairs

In the absence of external electric or magnetic fields, a quantum pump can transport a quantized amount of charge in a cycle, with the adiabatic cyclic evolution of the Hamiltonian of the system. The technique of this quantum pump was introduced by Thouless in 1983 [270]. This quantized charge pumping is robust against small perturbation and related to the topology of the system [270, 285]. In this section, we will utilize the Thouless charge pumping to characterize the topological properties.

Thouless pumping, for interacting bosons, can be performed in the framework

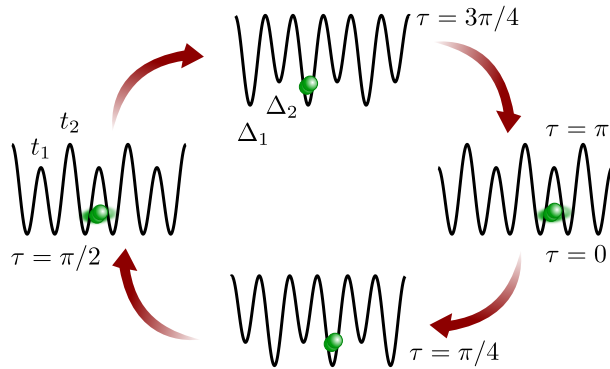


**Figure 6.7:** Sketch of a charge pumping cycle of the RM model in a one dimensional optical superlattice. The SSH-model corresponds to a dimerized hopping  $\delta t = (t_1 - t_2)/2$  as shown in the configurations  $\tau = 0$  and  $\tau = \pi/2$ . The cases of  $\tau = \pi/4$  and  $\tau = 3\pi/4$  depict a staggered potential with  $\delta\Delta = \Delta_2 - \Delta_1$ .

of a generalized RM model given by (compare Fig. 6.7)

$$H_{\text{RM}} = - \sum_i (t - (-1)^i \delta t \cos(2\tau)) a_i^\dagger a_{i+1} + \text{H.c.} + \frac{\delta\Delta}{2} \sin(2\tau) \sum_i (-1)^i n_i + H_{\text{int}} \quad (6.13)$$

with  $a_i^{(\dagger)}$  being the bosonic annihilation(creation) operators on site  $i$  and  $n_i = a_i^\dagger a_i$  is the number operator.  $\tau$  is a cyclic parameter which will be utilized for the pumping protocol. Onsite interactions  $H_{\text{int}} = \frac{U}{2} \sum_i n_i(n_i - 1)$  are characterized by the term  $U$ . Note, that the RM model reduces for  $\tau = 0$  and  $\pi/2$  to the SSH model,

$$H_{\text{SSH}} = - \sum_i (t + \delta t(-1)^i) a_i^\dagger a_{i+1} + \text{H.c.} + H_{\text{int}} \quad (6.14)$$

with  $t = \frac{t_1+t_2}{2}$  and  $\delta t = \frac{t_1-t_2}{2}$ , where  $t_1$  and  $t_2$  are the staggered hopping rates from odd and even sites respectively.

In the RM model  $\tau$  connects the two regions of different topology by breaking the chiral symmetry of the SSH model that allows the addition of  $h_z$  in the Hamiltonian shown in Eq. 1.38. This breaking of symmetry helps to keep the bulk energy gap open during the whole pumping cycle, which is a necessary condition for topological charge pumping. In this scenario, with varying  $\tau$  from 0 to  $\pi$  adiabatically, one can expect pumping of a quantized charge. The phenomenon of charge pumping can be evident from the single-particle spectrum of a finite system, which is given in Fig. 6.8. Here we can see that during the pumping cycle, the edge state located at

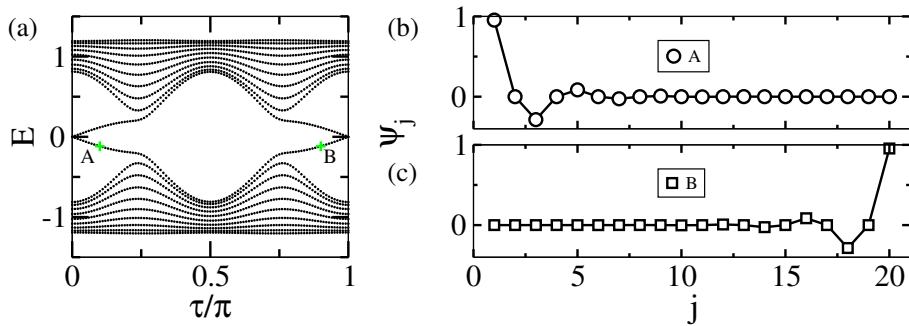


**Figure 6.8:** The figure depicts the charge pumping in the Rice-Mele model. Figure (a) shows the single-particle energy spectrum of model (6.13) for a system of length  $L = 20$  where  $\delta t = \delta\Delta = 0.4$  and  $t = 0.6$ . (b-c) Show the wavefunctions for the parameters indicated by the green plus signs in figure(a).

one edge is transferred to the other edge without closing the bulk gap.

In the single particle picture (i.e. for  $U \rightarrow -\infty$ ) the pumped charge can be related to a Chern number of the RM model (in momentum  $k$  and  $\tau$  space). Hence, here the pumped charge is quantized and directly linked to the non-trivial topology of the model if non-vanishing. In the following, we will analyze how the topological feature of the attractive bosons at unit filling can give rise to a pumping of bosonic pairs and will analyze the breakdown of the pair-pumping upon approaching the crossover to the MI-regime.

Following Ref. [257] we study the charge pumping for finite systems with open-boundary conditions by monitoring the polarization  $P(\tau)$  (Eq. 6.10) with respect to Model (6.13). The total transferred charge is given by

$$Q = \int_0^1 d\tau \partial_\tau P(\tau) \quad (6.15)$$

and hence, directly linked to the presence of polarized edge state for the SSH-model. We plot the polarization over the pumping cycle in Fig. 6.9 for several values of the interactions. While for strong attractive interactions  $U = -10t$ , we observe a clear pumping of a charge  $Q = 2$  corresponding to a bosonic pair, for  $U > U_{P1} \approx -2.6$  (i.e. for the curves  $U = -2, -1$  and  $4$ ) we find zero pumped charge i.e.  $Q = 0$ ,

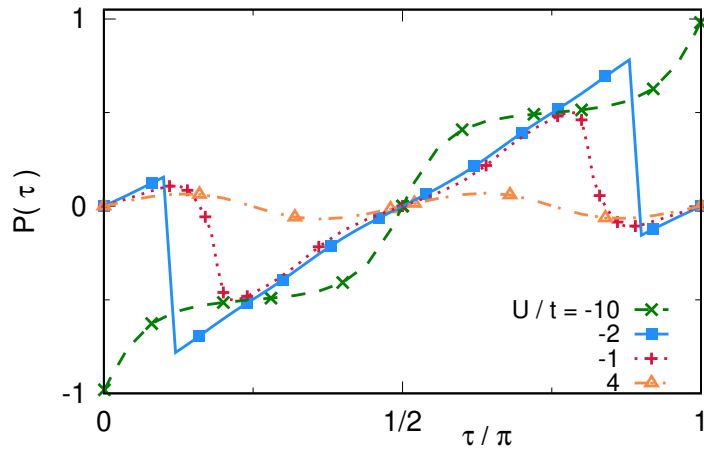


**Figure 6.9:** Polarization  $P$  for the RM model (6.13) as function of the adiabatic parameter  $\tau$  for several values of  $U$  ( $\delta\Delta = \delta t$ ). Note that,  $\tau = 0$  and  $\pi$  correspond to  $t_1 = 0.2$  and  $t_2 = 1$  and for  $\tau = \pi/2$  we have  $t_1 = 1.0$  and  $t_2 = 0.2$ . We consider system size of  $L = 180$  sites and for comparison we consider  $L = 80$ (not shown) for  $U = -1$  and observe no change in the result. For  $U = 4$  we plot  $10 \times P$  for clarity.

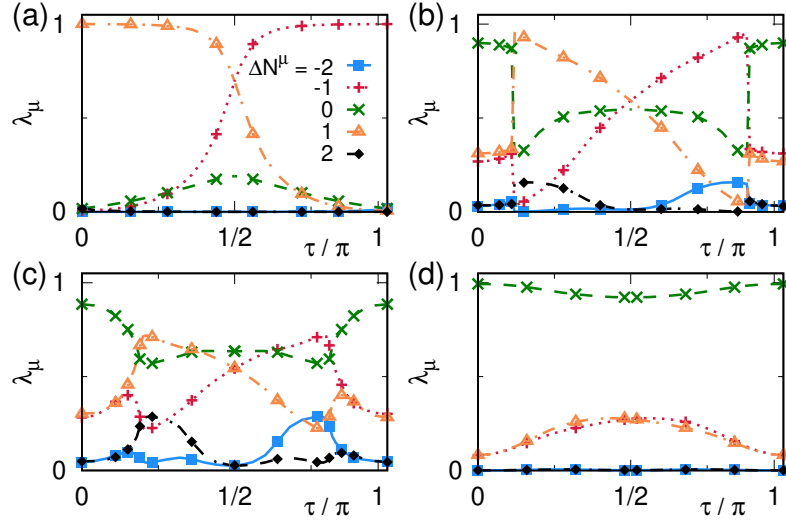


**Figure 6.10:** Largest values of the entanglement spectrum  $\lambda_\mu$  of the reduced density matrix in the center of a finite system of size  $L = 160$  for the RM model shown in Eq. (6.13) of the main text as a function of the adiabatic parameter  $\tau$  for (a)  $U = -10$ , (b)  $U = -2$ , (c)  $U = -1$  and (d)  $U = 4$  (compare Ref. [276]). The eigenvalues  $\lambda_\mu$  have been sorted by the particle number sector  $N_\mu$  in the center of the chain and for convenience labeled by  $\Delta N_\mu = N_\mu - L/2$ .

corresponding to the abrupt vanishing of the polarized edge states discussed in the previous section. Again, we cannot directly link the breakdown of the charge pumping to a gap closing in the pumping cycles.

Interestingly, we can identify an intermediate pumping regime  $U_{P1} < U < U_{P2}$ , where the polarization during one cycle exhibits a discontinuous jump, as can be seen from the  $U = -2$  curve in Fig. 6.9 around  $\tau = 0.1\pi$ . The position and size of the jump are stable with increase of system size (note that in Fig. 6.9 the lines contain more calculated data points than shown by the symbols). For  $U \gtrsim -1.5$ , the discontinuity vanishes and the polarization becomes a smooth function of  $\tau$ .

As discussed by Hayward et al. [276], the charge-pumping in the RM model may as well be visualized by the evolution of the entanglement spectrum  $\lambda_\mu$ . In Fig. 6.10, we plot the largest eigenvalues  $\lambda_\mu$  of the reduced density matrix in the center of the system. Due to the total particle number conservation of the model, the eigenvalues may be labeled by  $\Delta N_\mu = N_\mu - N_0$ , where  $N_\mu$  corresponds to the quantum number of the eigenvalues  $\lambda_\mu$  and  $N_0 = N/2$ . As shown in Fig. 6.10 (a), for strong attractive interaction  $U = -10t$ , the  $\Delta N_\mu = \pm 1$  eigenstates dominate, leading to a non-zero pumped charge. With increasing  $U$ , we observe a crossover to the MI regime where the  $\Delta N_\mu = 0$  state has the largest contribution and no charge is pumped (Fig 6.10 (d)).

### 6.2.4 Experimental realization

While there has been an active research on the bosonic systems with three-body hardcore constraint and attractive interactions [42, 46, 48, 49, 280, 286, 287], important features of the pair-pumping and its breakdown can be studied with state-of-the-art bosonic quantum gas experiments without these properties. We discuss this scenario by considering a system of repulsively bound pairs in the following subsection. The pumping of attractive pairs can to some extent be simulated by repulsively bound particles: For a deep staggered potential, ( $\delta t = 0.9$  and  $\delta\Delta = 2.0$ ), the ground state for  $\tau = -\pi/4$  with good accuracy given by a Fock-state of two bosons in every second lattice site. In a deep optical superlattice, this state can be accurately prepared [288] with unconstrained bosons with a small repulsive interaction  $U > 0$ . After initialization, we assume a quench to large repulsive interactions  $U_q \gg t, \delta t, \delta\Delta$  by means of a Feshbach resonance. These repulsively bound pairs as studied in Refs. [153, 289] are stable due to energy conservation and propagate

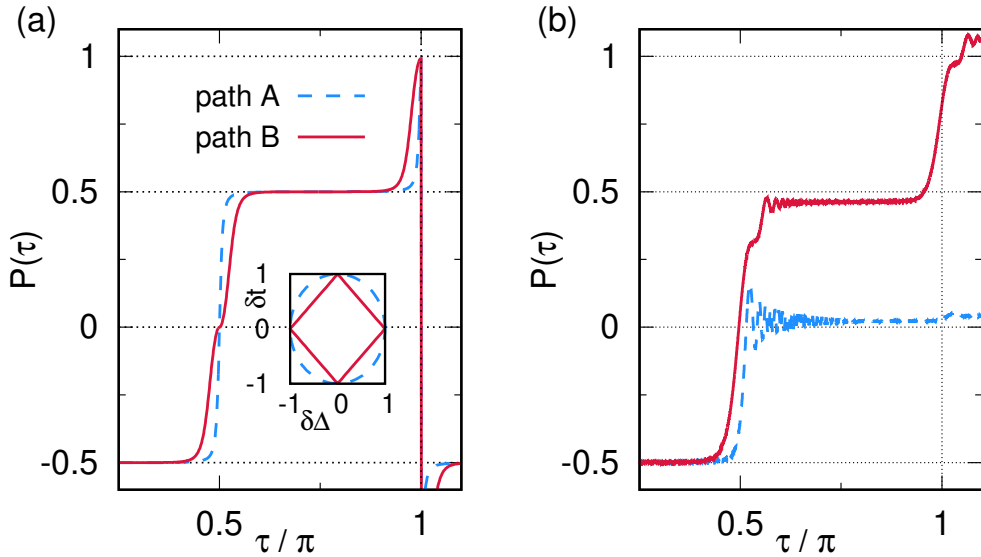


**Figure 6.11:** Pumping of repulsively bound pairs along different paths A and B (sketched in the inset of (a) as parametric plot in  $\tau$ ). (a) Fully adiabatic evolution (ground state calculation of the effective model of attractively bound pairs,  $L = 120$  sites). (b) Simulation of an actual real time evolution, which is sufficiently slow to stay close to the adiabatic regime in path B but too fast for path A (exact diagonalization,  $L = 6$  sites,  $N = 6$  particles,  $U_q = 36t$ , time evolution initialized at  $\tau = \pi/4$ ). Up to  $\tau = 1$  the curve for path B resembles well the one for the fully adiabatic evolution and totally pumped polarization is close to 1.

with a reduced hopping rate in a second order tunneling process  $t_{eff} \sim 2t^2/U$ . One may now try to perform a pumping cycle with these repulsively bound pairs which can simulate the physics of the attractively bound bosonic pairs. Note that the pumping process has to be slow compared to the effective tunneling rate but fast enough compared to the effective lifetime of the pairs.

In Fig. 6.11 we perform the time dependent exact-diagonalization (ED) simulation of the pumping process after a quench of the interaction  $U \rightarrow U_q$  and compare to the pumping of attractively bound pairs. Generally we choose a relatively fast evolution  $\tau = \tau(\tau') = \pi \frac{\tau'}{10t}$ , with the real time  $\tau'$ . Interestingly, if we change the precise path through the phase space (path B as sketched in the inset of Fig. 6.11) the (partial) pumping cycle can be performed accurately as shown in Fig. 6.11. Instead of the elliptical path of Eq. (1) of main text we choose a more rectangular contour (path B), connecting still the same intermediate points at  $\tau \bmod \pi/4$ . On this path, our real time evolution is able to pump a repulsively bound pair, where as on path A, the evolution is too fast and the system evolves to an unpolarized state.

In Fig. 6.12 we study the pumping of repulsively and attractively bound pairs for various interaction strengths. The effective adiabaticity condition may depend strongly on the precise path through the phase space chosen during the time of

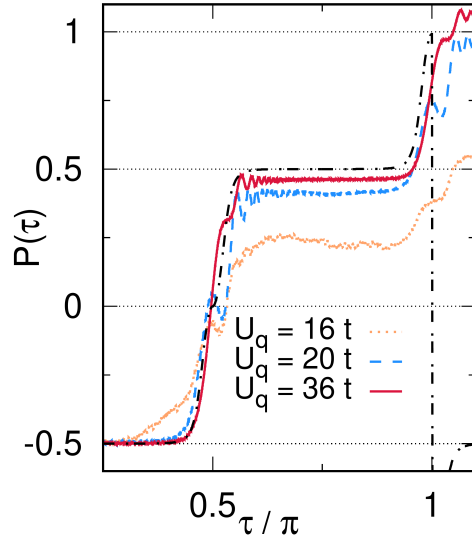


**Figure 6.12:** Pumping of repulsively bound pairs for different values of the quenched interactions  $U_q = 16t$ ,  $20t$  and  $36t$  (real-time evolution,  $L = 6$ ,  $N = 6$ , initialized at  $\tau = \pi/4$ ). The dash-dotted line depicts the fully adiabatic evolution of the effective model of attractively bound pairs ( $L = 120$  sites).

evolution. For the given examples,  $U_q \gtrsim 20t$  is sufficient to pump one pair during the time-evolution. Interestingly, we observe that slightly lower values of  $U_q$  quickly lead to a completely distinct evolution without quantized pumped charges.

### 6.3 Conclusions

In summary, we have investigated the ground-state phase diagram and topological properties of attractive bosons in the context of the SSH model at unit filling. For strong attractive interactions the bosons pair up and dimerize to form the PBO phases, with different effective topological properties and winding numbers  $\omega_{1/2} = 0$  and  $\omega_{1/2} = \pi$ , being linked to interesting edge states of paired bosons. Even though the effective topological properties of the bound pairs are not protected by symmetry, they remain remarkably robust across a wide range of parameters. Without closing a many-body gap the system exhibits a crossover between regions with trivial and non-trivial effective topology [290].

We have further established the topological properties of bound pairs in the context of Thouless charge pumping in the context of the RM model. While the aspects of the topological pumping of bosonic pairs could be reproduced with current set-ups of unconstrained bosons as we have shown, the flexibility to tune the interactions from attractive to repulsive regimes and the techniques to engineer three and higher order local interactions [42, 46, 48, 49, 280, 286] and recent experimental observation [291] have broadened the scope of simulating the physics of many-body systems by several folds. With the existing state-of-the-art facilities the current prediction can in principle be experimentally accessible in ultracold atom experiments along the line of recent experiment on Rydberg atoms in SSH model [265].



# Chapter 7

## Topological inheritance in multi-component bosons

### 7.1 Introduction

In the previous chapter, we discuss the topological properties of the single component interacting bosons in the context of the SSH model. As already mentioned in Chapter 3, multi-component systems may reveal interesting physics due to the presence of competing inter-particle interactions, correlation effects, particle statistics, which is still not well investigated in the literature. Recently, in Ref. [277], it has been shown that in an SSH-Hubbard (SSHH) model at half-filling, there exists a strongly correlated edge pair. The long time evolution of the correlation function between the edge states corresponding to both the spin and charge exhibits strong entanglement between them. It is to be noted that in the SSHH model, both the spin degrees of freedom are subjected to the hopping dimerization, which spontaneously stabilizes four-fold degenerate edge modes in the absence of interspecies interaction. Finite interaction reduces the degeneracies to two-fold and leads to the entangled

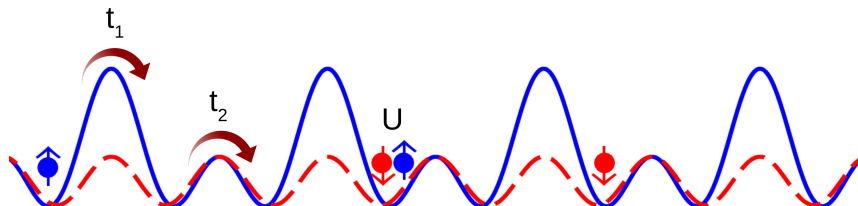


**Figure 7.1:** Two different species  $\{\uparrow, \downarrow\}$  in the Model (7.1). Whereas  $\uparrow$  experiences SSH hopping dimerization with  $t_1 \neq t$ ,  $\downarrow$  is in a homogeneous lattice with uniform hopping amplitude  $t$ . The inter-component interaction is denoted as  $U$ .

edge pairs [277].

In this chapter, we show how, due to interactions, a topological system may induce topological features in a non-topological one. In particular, we consider a two-component system in which one of the components experiences dimerized hopping, and hence an SSH model, whereas the other presents non-dimerized hopping, and would be hence topologically trivial if considered alone. This system can be described as a Half-SSH-Hubbard (HSSH) model, as depicted in Fig. 7.1. We show that a finite interaction (attractive or repulsive) coupling the two species maps topological properties into the a-priori non-topological component, resulting in the formation of strongly-correlated edge pairs.

## 7.2 Half-SSH Hubbard (HSSH) model

We consider two Bose components  $\{\uparrow, \downarrow\}$ , such that  $\uparrow$  experiences SSH dimerization, whereas  $\downarrow$  is not dimerized. The interacting many-body system is described by the model:

$$\begin{aligned} \mathcal{H} = & -t_1 \sum_{i \in \text{odd}} (c_{i\uparrow}^\dagger c_{i+1\uparrow} + \text{H.c.}) - t_2 \sum_{i \in \text{even}} (c_{i\uparrow}^\dagger c_{i+1\uparrow} + \text{H.c.}) \\ & - t \sum_i (c_{i\downarrow}^\dagger c_{i+1\downarrow} + \text{H.c.}) + U \sum_i n_{i\uparrow} n_{i\downarrow} \end{aligned} \quad (7.1)$$

where  $c_{i\sigma}^\dagger$  and  $c_{i\sigma}$  are the creation and annihilation operators for  $\sigma = \uparrow, \downarrow$  at site  $i$ ,  $n_{i\sigma} = c_{i\sigma}^\dagger c_{i\sigma}$  are the number operators,  $t_1$  and  $t_2$  are the tunneling rates of  $\uparrow$  from odd and even sites, respectively,  $t$  is the hopping rate of  $\downarrow$ , and  $U$  characterizes the inter-component interaction. We consider the hard-core constraint,  $n_{\uparrow,\downarrow} \leq 1$ . Note that model (7.1) can be mapped to a Fermi mixture, which presents the same spectrum and diagonal correlations.

In absence of interactions ( $U = 0$ ) model (7.1) reduces to two uncoupled models, an SSH model for  $\uparrow$ , and a trivial Hubbard model for  $\downarrow$ . The quantized Zak phase of  $\uparrow$  is zero for  $t_1 > t_2$  (trivial phase) and  $\pi$  for  $t_1 < t_2$  (topological phase). While the bulk remains gapped for both phases, only the latter possesses zero energy edge modes. In our studies we show that after a critical threshold value of interaction  $U$ , the topological properties of the  $\uparrow$  component gets induced in the  $\downarrow$  component. We utilize the DMRG method for this simulations. In our DMRG calculations below, we consider half-filling, in which the number of particles in both components  $N_{\uparrow,\downarrow} = L/2$ , for a lattice with  $L$  sites. In the analysis, we consider system sizes up

to  $L = 120$  sites and retaining bond dimension up to 500. We set  $t_2 = t = 1$  as energy unit, and fix  $t_1 = 0.2$ , within the non-trivial regime for  $\uparrow$ .

### 7.3 Induced bulk properties

Before discussing the topological properties of the system, in this subsection, we show how the bulk properties of the  $\downarrow$  component gets affected by the  $\uparrow$  component which experiences the dimerized hopping.

In the absence of any interactions, the  $\downarrow$  component is a gapless superfluid, whereas due to the hopping dimerization, the bulk of the  $\uparrow$  component is in a gapped dimer phase. It is shown in Chapter 5 that, this dimer phase can be characterized by the bond energy along the length of the system, which is defined on the  $i^{\text{th}}$  bond as

$$D_{i\sigma} = c_{i\sigma}^\dagger c_{i+1\sigma} + H.c. \quad (7.2)$$

for component  $\sigma = \uparrow$  and  $\downarrow$ . If the system is dimerized, one expects finite oscillations in  $D_i$  when plotted with respect to bond index  $i$ . Here we show how finite interaction plays an important role in inducing the dimer order from one component on to the

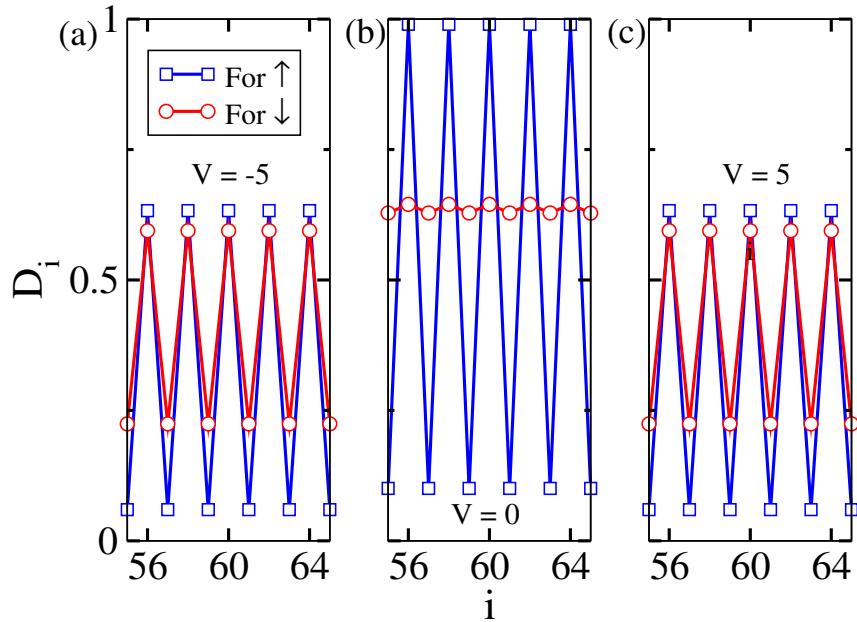


**Figure 7.2:** The dimer order parameters ( $D_{i\sigma}$ ) are plotted with respect to the bond index  $i$  for different values of interaction (a)  $U = -5$  (b)  $U = 0$  and (c)  $U = 5$  with  $t_1 = t = 1$  and  $t_2 = 0.2$  using a system of length  $L = 120$ . Here black square (red circle) stand for spin- $\uparrow$  ( $\downarrow$ ) component.

other. We plot  $D_{i\sigma}$  around the center of a system of  $L = 120$  for three values of interactions such as  $U = -5.0$ ,  $0.0$  and  $5.0$  in Fig. 7.2.

It can be seen that when  $U = 0.0$ (Fig. 7.2(b)), there exist finite oscillations in  $D_{i\uparrow}$  due to the hopping dimerization. On the other hand, for  $\downarrow$  component, there is no oscillation in  $D_{i\downarrow}$  because of the homogeneous hoppings. However, when the interaction is turned on, finite oscillations appear in  $D_{i\downarrow}$  indicating the induced dimer order in the  $\downarrow$  component as shown in Fig. 7.2(a) and (c).

The dimer phase can be further characterized by the dimer structure factor defined as;

$$S_{D\sigma}(k) = \frac{1}{L^2} \sum_{i,j} e^{ikr} \langle D_{i\sigma} D_{j\sigma} \rangle \quad (7.3)$$

The finite values of  $S_{D\sigma}(k)$  at  $k = \pi$  reveal the presence of dimer order in the system as already discussed in Chapter 5. Along with  $S_{D\sigma}(k)$ , we also calculate the charge gap of each component as

$$\Delta_\sigma = E(L, N_\sigma + 1) + E(L, N_\sigma - 1) - 2E(L, N_\sigma). \quad (7.4)$$

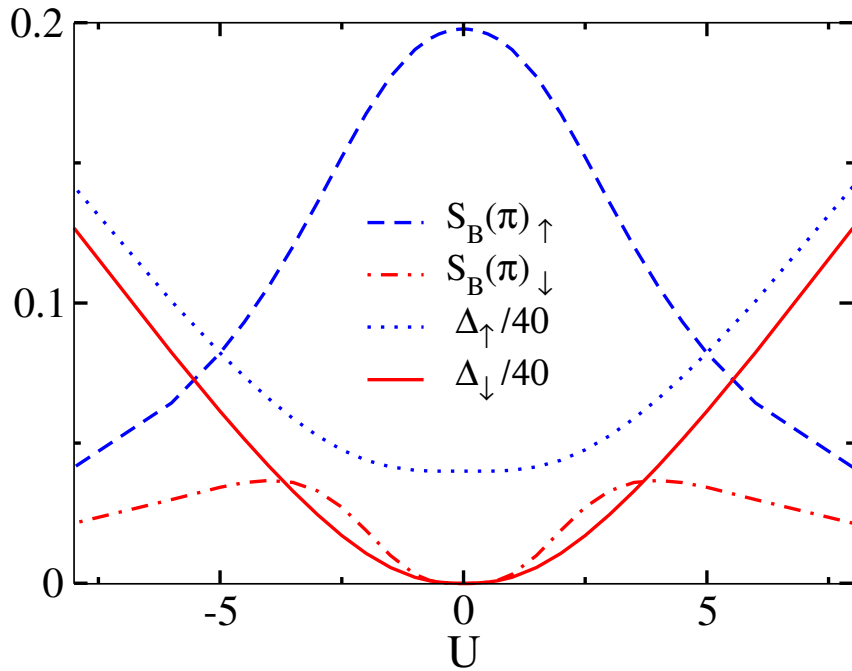


**Figure 7.3:** Bulk gaps  $\Delta_\sigma$  (blue dotted and red continuous), and dimer structure factors  $S_{D\sigma}(\pi)$  (blue dashed and red dot-dashed) for  $\uparrow$  and  $\downarrow$  components, respectively, as a function of  $U$ . The observables are extrapolated to  $L \rightarrow \infty$  using our DMRG results for system sizes of length  $L = 40, 60, 80, 100$  and  $120$ .

The dotted blue (solid red) curve in Fig. 7.3 depicts the extrapolated charge gap and the dashed blue (dot-dashed red) curve depicts the extrapolated dimer structure factor for the  $\uparrow(\downarrow)$  component. Large  $|U|$  exactly replicates the bulk properties of the  $\uparrow$  component on the  $\downarrow$  component asymptotically. Note, however, that any  $U \neq 0$  (either repulsive or attractive) results in a finite bulk gap and dimer order in the spin- $\downarrow$  component. Any finite interaction drives the bulk of the  $\downarrow$  component into a gapped dimer phase.

## 7.4 Induced topological properties

Before going to the details of the results, we examine the physics resulting from the strong interactions in such two component systems. For a sufficiently strong  $U < 0 (> 0)$  a particle of one component pairs on-site with a particle (hole) of the other. To monitor the pairing, we define a quantity defined as ;

$$\eta = \frac{4}{L} \sum_i \left( \langle n_{i\uparrow} n_{i\downarrow} \rangle - \frac{1}{4} \right) \quad (7.5)$$

which is plotted in Fig. 7.4. For large-enough  $|U| > 8$ ,  $|\eta| \simeq 1$  indicates strongly localized on-site pairing. For strong particle-particle pairing (particle-hole pairing

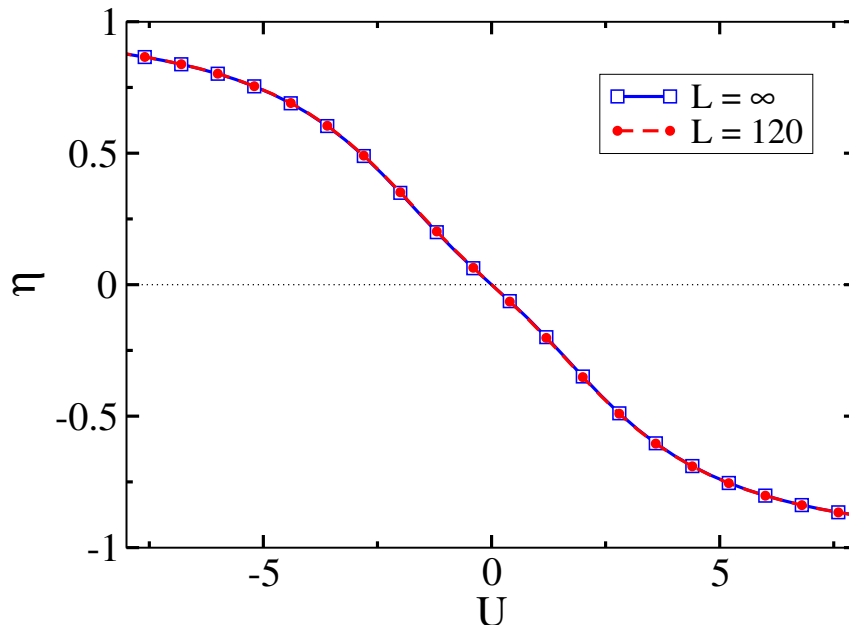


**Figure 7.4:** Pairing  $\eta$  as a function of  $U$ .

is treated analogously), the combined system can be described by an effective SSH model for on-site hard-core pairs:

$$\mathcal{H} = \frac{2t_1 t}{U} \sum_{i \in odd} P_i^\dagger P_{i+1} + \frac{2t_2 t}{U} \sum_{i \in even} P_i^\dagger P_{i+1} + \text{H.c.}, \quad (7.6)$$

with  $P_i = c_{i\uparrow} c_{i\downarrow}$ . Model (7.6) is topological if the SSH model for  $\uparrow$  is topological. Hence, the pairs (and with them the second component) inherit the topology of the first component. Interestingly, in the following we show that, much weaker pairing  $\eta \ll 1$ , and hence very moderate  $|U|$ , already suffices to induce full topological inheritance.

### 7.4.1 Edge states

As a first check of bulk-edge correspondence, we compute the local particle densities  $\langle n_{i,\sigma} \rangle$  for both the components which allows to gain insights about the non-trivial edge states which may exist in the system. In Fig. 7.5(a,b) we plot  $\langle n_{i,\sigma} \rangle$  versus  $i$  for both attractive and repulsive values of interactions for a system of length  $L = 120$ . In Fig. 7.5(a), it can be seen that for attractive interaction  $U = -5$ , both the spin components show equal densities at the left end and zero on the right end of the lattice. This is a clear indication that the spin- $\downarrow$  now exhibits topological edge modes along with the bulk gap which was discussed before. Due to the influence of the attractive interaction, one can consider the two particles from both the spin components form doublons( $\uparrow\downarrow$ ) and therefore, the entire system behaves like an SSH model of doublons. In such a scenario, the edge state on the opposite side of the lattice is composed of holons( $\circ\circ$ ). On the other hand, when  $U$  becomes repulsive in nature the two spins tend to avoid each other and therefore, the edge states corresponding to particle and holes of each component respectively appear on the opposite ends of the lattice as depicted in Fig. 7.5(b).

The inheritance of the edge states by the  $\downarrow$  component is best monitored by the polarization

$$P_\sigma = \frac{1}{L} \sum_{i=0}^L \langle \psi | (i - L/2) n_{i\sigma} | \psi \rangle \quad (7.7)$$

for the ground state  $|\psi\rangle$ , which we depict in Fig. 7.5(c) for  $L = 120$  for different values of  $U$ . Note that  $P_\uparrow = -1/2$  due to the topological character of the  $\uparrow$  component. The  $\downarrow$  component shows maximally polarized edges,  $|P_\downarrow| \simeq 1/2$ , already for  $|U| \sim 1$ . Hence, the  $\downarrow$  component fully inherits the topological edge modes for values of  $|U|$

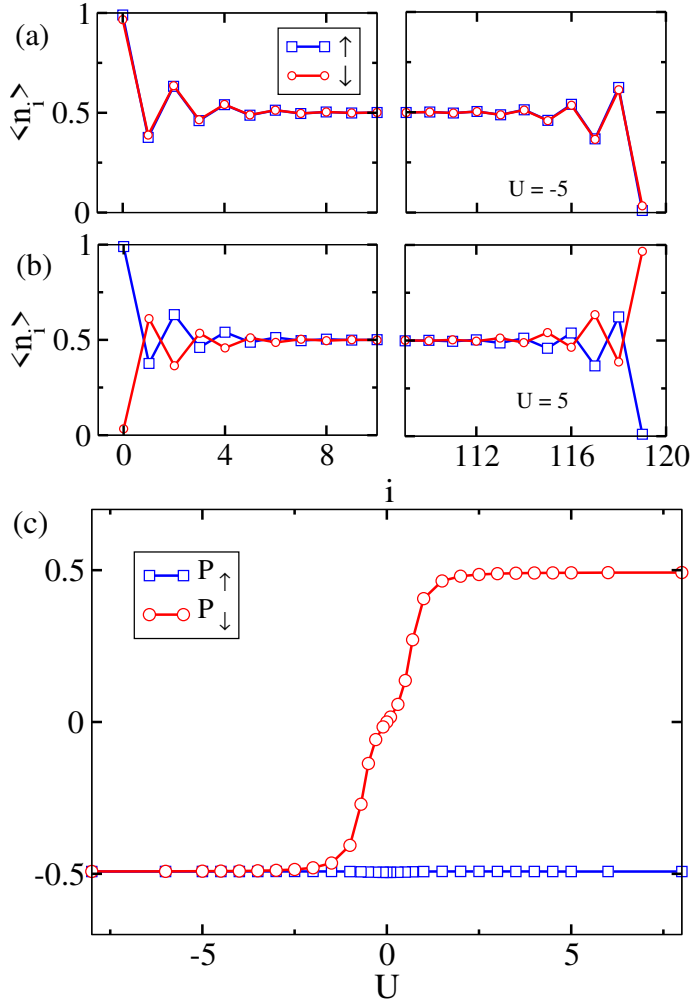


**Figure 7.5:** (a-b) Edge states for both component for  $U = -5$  and 5 for a system with  $L = 120$ ; (c) Polarization  $P_\sigma$  for  $\uparrow$  (blue squares) and  $\downarrow$  (red circles) as a function of  $U$ , obtained for  $L = 120$ .

well below those needed for strong pairing (compare Fig 7.4).

#### 7.4.2 Mean chiral displacement

Topological inheritance may be easily probed experimentally by monitoring the dynamical evolution after a quench. The mean-chiral displacement (MCD), recently utilized in the context of quantum walk on a graph, can be utilized to measure the topological winding number in photonic and ultracold atomic systems [292–295]. The MCD is defined as

$$C_\sigma(\tilde{t}) = 2\langle \Psi(\tilde{t}) | \Gamma_\sigma m_\sigma | \Psi(\tilde{t}) \rangle \quad (7.8)$$

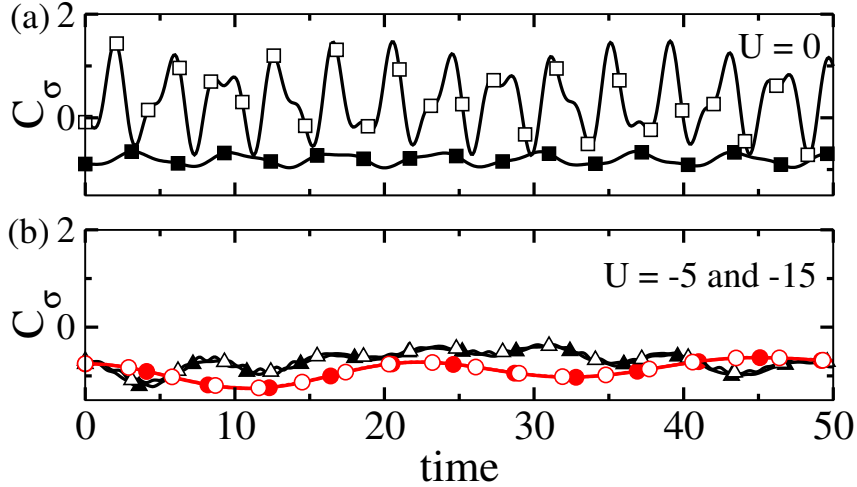


**Figure 7.6:** (a) MCD for a system with  $L = 6$  for  $U = 0$  for  $\uparrow$  (filled symbols) and  $\downarrow$  (hollow symbols); (b) Same for  $U = -15$  (red circles) and  $U = -5$  (black triangles). Here solid and empty symbols are corresponding to  $\uparrow$  and  $\downarrow$  respectively. For  $|U| = 5(15)$  the MCD evolution curves are marked by symbol triangle(circle). In all cases we employ as initial state  $|\Psi(0)\rangle = c_{0\uparrow}c_{0\downarrow}|\Psi_{GS}\rangle$ .

where  $\Gamma_\sigma$  and  $m_\sigma$  are the chiral and unit cell operators, respectively, and  $|\Psi(\tilde{t})\rangle$  is the time-evolved state. The MCD displays an oscillatory behavior, but after a sufficiently large time its time averaging converges to the winding number  $\omega$ . We compute the winding number,  $\omega = \int_0^\pi d\theta \langle \psi(\theta) | \partial_\theta \psi(\theta) \rangle$ , of the ground state  $|\psi\rangle$  of Model (7.1) with twisted boundary conditions  $a_{i,\sigma} \rightarrow e^{i\theta_\sigma/L} a_i$ . The modified limit of integration and the two different twisting angles take care of the two different components [296]. Our exact numerical calculation for  $L = 8$  shows that the winding number in the topological phase is appropriately captured as  $\omega = 1$  for  $|U| = 5$  with the choice of twist angle  $\theta_\uparrow = \pm\theta_\downarrow$ .

We analyze the MCD by considering an initial state

$$|\Psi(0)\rangle = O|\Psi_{GS}\rangle \quad (7.9)$$

with  $|\Psi_{GS}\rangle$  the ground-state, and  $O = c_{0\uparrow}c_{0\downarrow}$  ( $O = c_{0,\uparrow}^\dagger c_{0,\downarrow}$ ), i.e. pair annihilation (spin flip) at the central site, for  $U < 0$  ( $> 0$ ). Quantum walks from these initial states provide insights about the charge and spin winding numbers, respectively. Figures 7.6 show our results of  $C_\sigma(\tilde{t})$ , evaluated with the pair annihilation, for a system of size  $L = 6$  with open boundary conditions. For  $U_{\uparrow,\downarrow} = 0$  (Fig. 7.6(a)),  $C_\uparrow(\tilde{t})$  (filled squares) oscillates around the winding number  $-1$ , as expected from the topological character of the  $\uparrow$  component. In contrast,  $C_\downarrow(\tilde{t})$  oscillates around

zero (open squares), showing no topological behavior. When increasing the inter-component interaction, the MCD of both components become identical oscillating around the winding number (Fig. 7.6(b)) revealing the inheritance by the  $\downarrow$  component of the topological properties of the  $\uparrow$  component. Note that the deviations from the true winding numbers can be attributed to the finite size and interaction effects [297].

### 7.4.3 Thouless charge pumping

Alternatively, topological inheritance may be dynamically probed by investigating Thouless charge pumping, i.e. the transport of quantized charge as a result of an adiabatic periodic modulation of the system parameters. This process has been discussed in Chapter 6 already for a single component system. In this section, we will utilize this concept for the two component system in the context of the HSSH model. Here, we consider that only the  $\uparrow$  component is driven following a Rice-Mele (RM) model [271] given as;

$$\begin{aligned} \mathcal{H}_{\uparrow} = & - \sum_i \left[ (t - (-1)^i \delta t \cos(2\tau)) c_{i,\uparrow}^\dagger c_{i+1,\uparrow} + \text{H.c.} \right] \\ & + \frac{\delta\Delta}{2} \sin(2\tau) \sum_i (-1)^i n_{i,\uparrow}. \end{aligned} \quad (7.10)$$

where  $\tau$  is a cyclic parameter used for the pumping protocol. As already mentioned in the Chapter 6, the RM model reduces for  $\tau = \pi/4$  and  $3\pi/4$  to the SSH model [276, 296].

The pumping is best evaluated by monitoring the polarizations

$$P_\sigma(\tau) = \frac{1}{L} \sum_{i=0}^L \langle \psi(\tau) | (i - L/2) n_{i\sigma} | \psi(\tau) \rangle \quad (7.11)$$

The total charge pumped during the cycle can be obtained by computing

$$Q_\sigma = \int_0^1 d\tau \partial_\tau P_\sigma(\tau) \quad (7.12)$$

As expected,  $P_{\uparrow}(\tau)$  (Fig. 7.7(a)) shows the robust pumping of one particle, indicating the existence of edge states. While no pumping occurs in  $\downarrow$  for  $|U| = 0$ , increasing  $|U|$  leads to a finite pumping (Fig. 7.7(b)), despite the fact that only  $\uparrow$  is externally modulated. For  $|U| \gtrsim 1$  the pumping of a full  $\downarrow$  particle marks the complete topo-

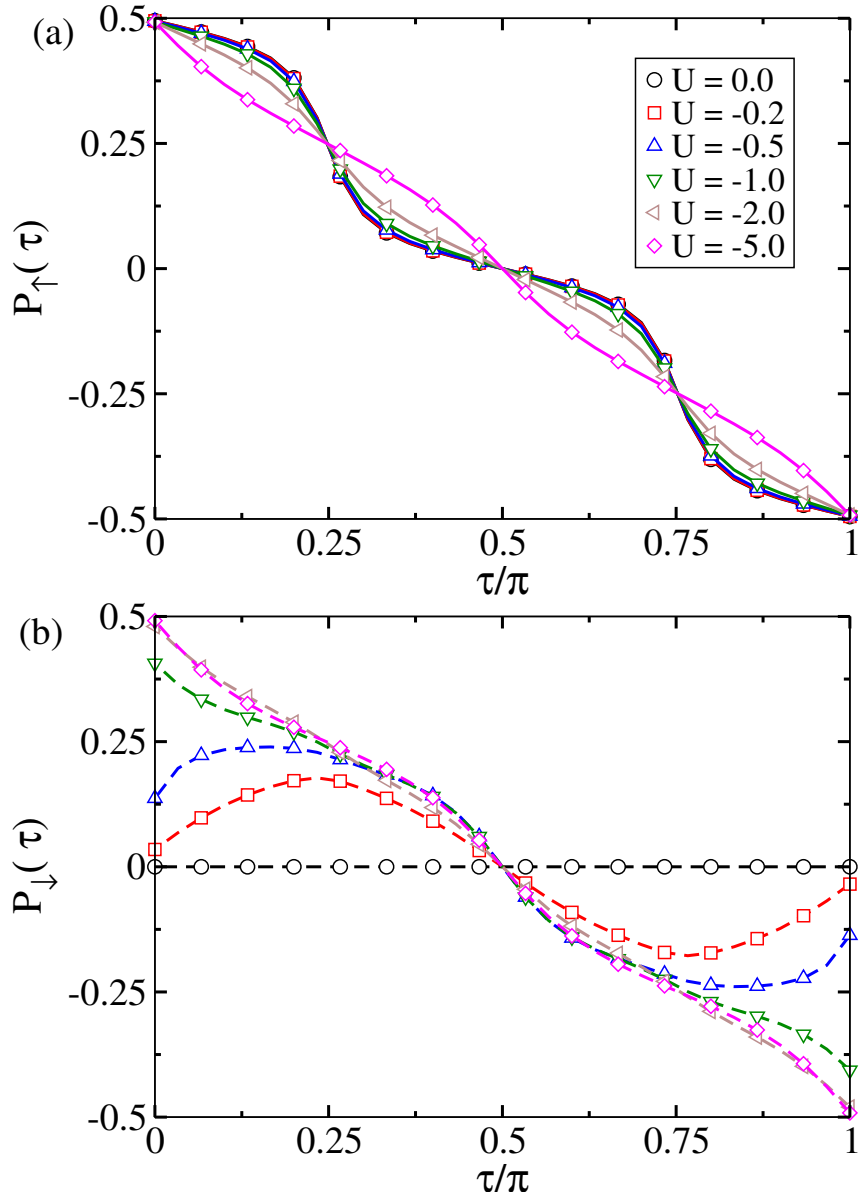


**Figure 7.7:** Polarizations  $P_{\uparrow}(\tau)$  (a) and  $P_{\downarrow}(\tau)$  (b) for different  $U$  values and  $L = 120$ .

logical inheritance. To see the change in the character of charge pumping, which may quantify the critical point of complete inheritance, we calculate the slope of  $P_{\downarrow}(\tau)$  at  $\tau = 0$  which is shown in Fig. 7.8. It can be seen that near  $|U| \sim 1$  there is a change in the nature of the curve, showing the position of complete inheritance of topology.

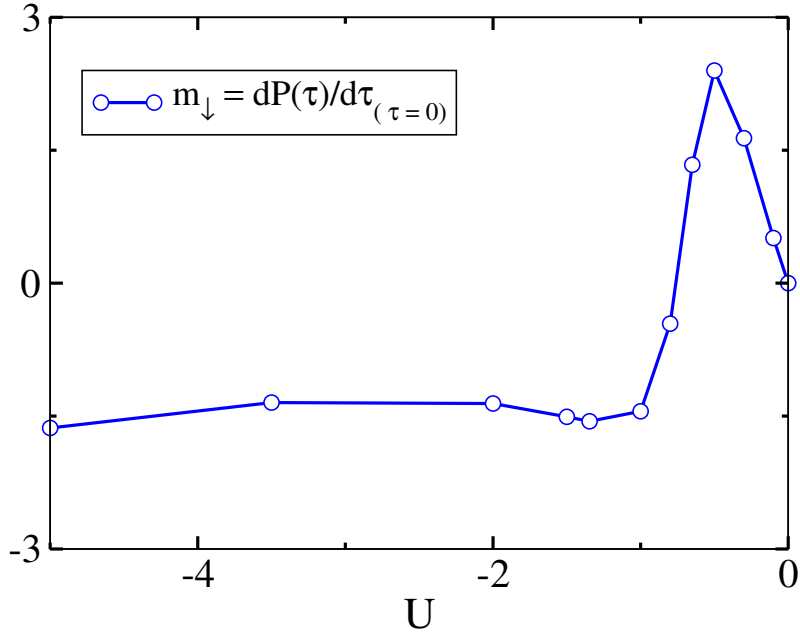


**Figure 7.8:** Initial gradient of polarization  $m_{\downarrow} = \frac{dP_{\downarrow}}{d\tau}(\tau = 0)$  as a function of  $U < 0$  shows the signature of topological inheritance.

#### 7.4.4 Inheritance threshold

The previous results show that the  $\downarrow$  component fully inherits the topological properties of the  $\uparrow$  component (edge states, winding number, MCD, full-particle Thouless pumping) for inter-particle interactions beyond a given threshold. Such an inheritance threshold is not only revealed by the edge polarization (Fig. 7.5 (c)) and the change of character of the charge pumping (Fig. 7.7 (b) and Fig. 7.8), but also by the analysis of the fidelity susceptibility,

$$\chi = \lim_{(U-U') \rightarrow 0} \frac{-2 \ln |\langle \psi_0(U) | \psi_0(U') \rangle|}{(U - U')^2}. \quad (7.13)$$

As shown in Fig. 7.9,  $\chi/L$  shows a clear maximum, that marks the inheritance threshold. Such a threshold approaches asymptotically  $|U| \simeq 1.06$  for growing  $L$ . At the threshold, the pairing correlation  $\eta \simeq 0.2$  (Fig. 7.4), and hence, remarkably, the on-set of full topological inheritance occurs when the components are not yet paired.

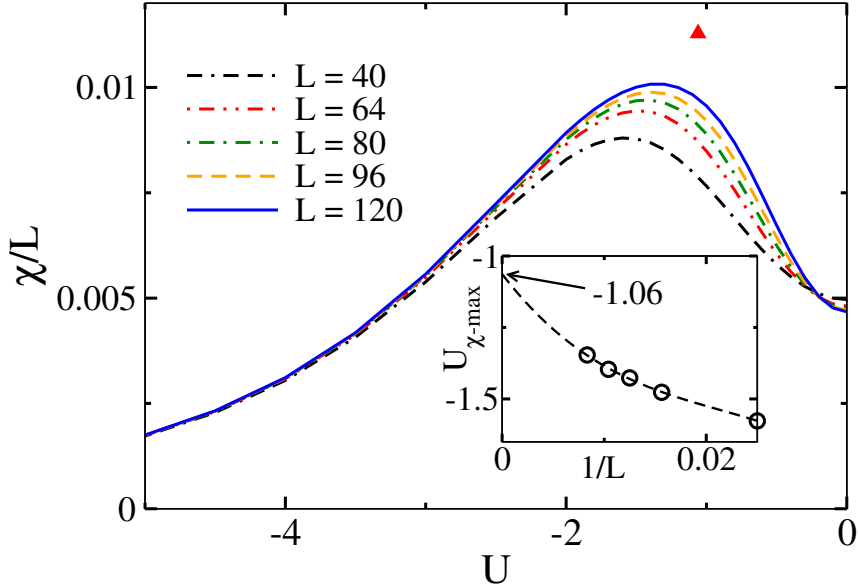


**Figure 7.9:** Fidelity susceptibility  $\chi$  as a function of  $U$  for different  $L$ . The inset shows the extrapolation of the value  $U$  at which  $\chi/L$  has a maximum. This value marks the onset of full topological inheritance. Here, the filled red triangle corresponds to the extrapolated position of the peak.

## 7.5 Experimental feasibility

A possible experimental realization of Model (7.1) may be achieved by employing two neighboring one dimensional lattices of hardcore dipolar bosons, which act like the two components  $\{\uparrow, \downarrow\}$ . Hopping dimerization in one of the chains can be introduced by using a secondary lattice on an already isolated ladder obtained using the primary lasers, as sketched in Fig. 7.10 (a). The Hubbard interaction can be simulated by aligning the dipoles in individual chains at the so-called magic angle, such that in-leg interactions vanish, and only inter-leg interactions are relevant.

Alternatively, state dependent optical lattices [298, 299] may allow for a direct experimental realization of Model (7.1).

Interestingly, it is possible to study the topological inheritance in a system of more than two components in state dependent optical lattices. In general, an  $M$  component system can be written as a  $SU(M)$  symmetric Hamiltonian give by

$$\mathcal{H}_M = -t \sum_{i,\sigma} (c_{i,\sigma}^\dagger c_{i+1,\sigma} + \text{H.c.}) + U_{SU(M)} \sum_i n_i^2 \quad (7.14)$$

where  $n_i = \sum_\sigma n_\sigma$ . The different components correspond to different hyperfine states of the atoms. If one of the components is in a topologically non-trivial phase,

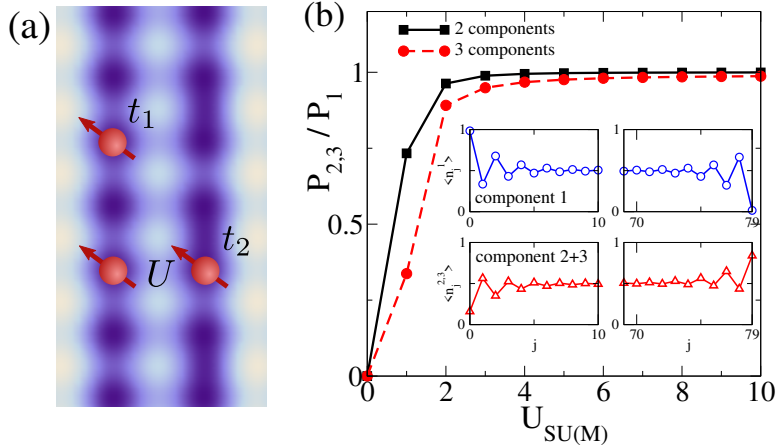


**Figure 7.10:** (a) Experimental scheme to realize Model (7.1) using two-leg optical ladder systems of hardcore dipolar bosons using dipolar particles (see text); (b) Induced polarization for a three-species system in an state-dependent super-lattice in the presence of on-site all-to-all ( $SU(3)$ -symmetric) interactions. The inset shows the replication of the edge state to the second and third species for  $U_{SU(3)} = 6$

as a result of dimerized hopping, it is possible to induce the topological properties in the other components which are topologically trivial with inter-species interaction  $U_{SU(M)}$ . As an example, Fig. 7.10 (b) shows our results for a three-component system (assuming  $SU(3)$ -symmetric all-to-all interactions,  $U_{SU(3)}$ ), in which only one component is topological. As for the two-component case, the trivial components fully inherit the topological properties for relatively weak interactions.

## 7.6 Conclusions

In this chapter, we have shown that due to interactions, a topological system may induce topological features in a non-topological one, as we have illustrated for a Hubbard model in which a component experiences SSH dimerization and the other not. Although, for strong interactions topological inheritance may be readily understood from the formation of on-site localized inter-component pairs which experience an effective SSH model, we have shown that, interestingly, the threshold for full topological inheritance occurs for much weaker interactions, for which the two components are not yet paired.



## Chapter 8

# Conclusions and Future Directions

In this thesis, we have studied the equilibrium, non-equilibrium and topological properties of the systems of interacting bosons in periodic potentials in different physical situations. In this context, we have addressed some of the problems of current importance while keeping in mind about their experimental feasibility in ultracold atomic systems in optical lattices.

Motivated by the theoretical and experimental developments in systems of ultracold atoms in optical lattices and the recent proposal to access multi-body onsite interactions in optical lattice systems, we have investigated the ground state properties of multi-body interacting bosons in a two-dimensional optical lattice in Chapter 2. Assuming a repulsive two-body and four-body interaction and attractive three-body interaction, we have obtained the signatures of two-body repulsive bound pairs in the regions between the Mott insulator lobes in the phase diagram. These repulsively bound bosonic pairs form a region of pair superfluid phase sandwiched between the Mott lobes. We have further shown that this pair superfluid phase is robust against density induced tunneling, which usually has significant effects on the system.

Large onsite repulsive interaction between atoms leads to the two- (three-) body hardcore constraint where the per site occupation of more than one (two) particle is prohibited. In Chapter 3, we have studied the quantum phase transitions in a system of constrained dipolar bosons in a non-locally coupled ladder. While in one leg of the ladder the bosons are allowed to experience two-body hardcore constraint, in the other leg three-body hardcore constraint is imposed. Allowing dipole-dipole interaction between the legs only, we have obtained the ground-state phase diagram of the system for attractive interchain interaction. The competition between the repulsive onsite and attractive nearest-neighbor interactions between the chains yields

three kinds of superfluids, namely the trimer superfluid, pair superfluid and the usual single-particle superfluid along with the insulating Mott phase at the commensurate density. Besides, we have also realized the simultaneous existence of Mott insulator in one chain and superfluid phases on the other for the two- and three-body constrained bosons, respectively. Further, we have shown that these quantum phases are stable in the presence of an external harmonic trap potential.

After discussing the equilibrium properties of different interacting systems in previous chapters, in Chapter 4, we have studied the non-equilibrium properties of different systems of interacting bosons in the context of the quantum random walk. In this chapter, first we have analyzed the quantum walk of single particle and single hole defects on top of a uniform bosonic Mott insulator in a one-dimensional lattice. We have shown that the quantum walk of a single particle or hole defect exhibits a quantum walk similar to single-particle on an empty lattice. However, the expansion speed gets enhanced with the density of the Mott insulator. In the next part of this chapter, we have investigated the quantum walk of two particle-defects on an MI1 state in the presence of both two and three-body interactions. This shows the interesting phenomenon of quantum walk reversal as a function of attractive three-body interaction. We have shown that for small three-body attraction, the defects form repulsively bound pair and with increasing three-body attraction, the pair dissociate at some intermediate values and reappear in the large three-body attraction. In the end, we have analyzed the case of two particle-defects located at two nearest-neighbor sites on top of an MI1 state in the presence of the nearest neighbor interaction. Interestingly, we have shown the signature of bosonic antibunching for vanishing nearest-neighbor interaction and nearest neighbor dimer formation for large interactions.

In Chapter 5, we have analyzed the groundstate properties of the three-body constrained bosons in a one-dimensional optical lattice with staggered hoppings and finite onsite interactions. By considering attractive and repulsive onsite interactions between the bosons, we have obtained the phase diagram exhibiting various quantum phases. Due to the double-well geometry and three-body constraint, several gapped phases, such as the Mott insulator and dimer/bond-order phases emerge at commensurate densities in the repulsive interaction regime. Attractive interaction leads to the pair formation and these pairs in the presence of staggered hopping form the pair bond order phase at unit filling. We have shown that there exist smooth crossovers between the Mott insulator and the bond order phase in the repulsive interaction regime. However, on the attractive side, there exists a crossover from

the bond order phases of single particles and pairs. At incommensurate densities, we have shown the signatures of the gapless pair superfluid phase.

In Chapter 6, we have discussed the topological properties of the bound bosonic pairs whose signatures have been obtained in Chapter 5. In this context, we have analyzed the physics of bound bosonic pairs in the context of the one dimensional Su-Schrieffer-Heeger (SSH) model. We have obtained a detailed phase diagram in both the trivial and nontrivial regimes of the SSH model depicting various quantum phases and transitions among them. We have shown that the bosonic pairs, which form the pair-bond-order phase in the presence of staggered hopping associated with the SSH model, exhibit effective topological properties such as the presence of polarized edge states of pairs. We have identified this topological property by analyzing the phenomenon of Thouless charge pumping. At the end, we have shown how the pumping of paired bosons can be probed in state-of-the-art experiments, for example with repulsively bound bosonic pairs.

Finally, in Chapter 7 we have studied a system of a one-dimensional two-component bosonic Hubbard model in which one component is subjected to the SSH type hopping dimerization, whereas the other one is not. We have shown that due to inter-component interactions the topological properties of one component are induced in the originally trivial one. Although the topological inheritance at strong interspecies interaction can be expected due to onsite pairing, have shown that the topological inheritance occurs at a weak interspecies interaction. We have illustrated this inheritance by discussing both bulk and edge properties, as well as dynamical observables such as mean chiral displacement and Thouless charge pumping.

## 8.1 Future Directions

The topics covered in the thesis deals with some of the timely problems which are of current importance in the context of strongly correlated systems. The outcome of the thesis promises several possible extension which can be addressed immediately. We list some of them in the following.

The prediction of the two-body repulsively bound bosonic pairs in multi-body interacting Bose-Hubbard model may allow for the study of the supersolid phases of repulsively bound pairs by introducing dipole-dipole interactions. It will be possible to investigate this phenomenon in the case of bilayer systems and other lattice geometries and frustrated systems to explore the physics of repulsively bound bosonic pairs.

The outcome from the constrained dipolar bosons in a non-locally coupled chains can be extended to understand various interesting physics related to binary mixtures. It will be worthwhile to look for physics by introducing the long-range interaction along the legs of the ladder. The attractive interaction along the legs may lead to spatial phase separation of dimers or trimers depending on the onsite interaction of the three-body constrained bosons. By considering three-body constrained bosons in both the legs and taking different onsite interactions, it will be possible to achieve the induced supersolid phase if one of the particles in one of the legs are taken to be dipolar in nature.

A novel scenario is discussed to study the quantum walk of interacting particles. Here instead of a few particles in an empty lattice, we have considered a MI background where defects interact with themselves and also with the MI background. This scenario opens up a new class of problems in the field of the quantum walk. An immediate extension of this could be to study the quantum walk of both particle-hole excitation in the presence of onsite and nearest neighbor interactions. Further extension can be made in terms of dimensions such as the quantum walk of defects in quasi-one-dimensional and two-dimension, multiple species, in the presence of external gauge field and disordered lattice etc.

In the thesis, we have also studied the bulk and topological properties of interacting bosons in the framework of the SSH model. We have presented to the topological phase transition in the presence of local interaction. This work can be extended to study the topological properties in the presence of the nearest neighbor interaction among the bosons, which may reveal interesting phenomena due to the competition between local and non-local interaction in the presence of staggered hopping strengths. It is also possible to investigate the topological phase transition in the context of binary bosonic mixtures. By considering different combinations of interactions in both the components, it will be interesting to see the phase separated topological phases of bosons.

In the end, we have studied the system of two-component hardcore bosons/spin-polarized fermions and shown the phenomenon of topological inheritance in the presence of interspecies interaction. It will be possible to extend this concept to the system of softcore bosons and also in the presence of dipole-dipole interactions. It will be interesting to see the effect of disorder in such systems by allowing disorder for one or both components of the systems.

Apart from these immediate extensions, it will be possible to explore several other novel physics in other systems using the techniques developed to accomplish

the thesis work. It will be possible to address the topological phenomena in a two-leg ladder SSH model in the presence of interactions and rung hopping. One can, in principle, allow disorder along the legs and also along the rungs to investigate the effect of disorder on the topological phase transitions. While interacting bosons in SSH model models show exciting trivial and non-trivial phases, one can extend the study in extended SSH models such as SSH3 and SSH4 models [294, 300–302]. Apart from the cold atomic systems in the optical lattice, these many-body methods can be applied to other systems such as superconducting circuits and trapped ions.



# Bibliography

- [1] D. Bitko, T. F. Rosenbaum, and G. Aeppli, Phys. Rev. Lett. **77**, 940 (1996).
- [2] B. Zimmermann, T. Müller, J. Meineke, T. Esslinger, and H. Moritz, New Journal of Physics **13**, 043007 (2011).
- [3] N. Gemelke, X. Zhang, C.-L. Hung, and C. Chin, Nature **460**, 995 (2009).
- [4] K. D. Nelson, X. Li, and D. S. Weiss, Nature Physics **3**, 556 (2007).
- [5] W. S. Bakr, J. I. Gillen, A. Peng, S. Fölling, and M. Greiner, Nature **462**, 74 (2009).
- [6] J. F. Sherson, C. Weitenberg, M. Endres, M. Cheneau, I. Bloch, and S. Kuhr, Nature **467**, 68 (2010).
- [7] T. Gericke, P. Würtz, D. Reitz, T. Langen, and H. Ott, Nature Physics **4**, 949 (2008).
- [8] M. Endres et al., Science **334**, 200 (2011).
- [9] P. M. Preiss et al., Science **347**, 1229 (2015).
- [10] C. Gross and I. Bloch, Science **357**, 995 (2017).
- [11] M. Lewenstein, A. Sanpera, V. Ahufinger, B. Damski, A. Sen(De), and U. Sen, Advances in Physics **56**, 243 (2007).
- [12] W. Hofstetter and T. Qin, Journal of Physics B: Atomic, Molecular and Optical Physics **51**, 082001 (2018).
- [13] L. Tarruell and L. Sanchez-Palencia, Comptes Rendus Physique **19**, 365 (2018).
- [14] R. Grimm, M. Weidemüller, and Y. B. Ovchinnikov, *Optical Dipole Traps for Neutral Atoms*, volume 42, pages 95–170, Academic Press, 2000.
- [15] I. Bloch, Nature Physics **1**, 23 (2005).
- [16] C. Becker, P. Soltan-Panahi, J. Kronjäger, S. Dörscher, K. Bongs, and K. Sengstock, New Journal of Physics **12**, 065025 (2010).
- [17] M. P. A. Fisher, P. B. Weichman, G. Grinstein, and D. S. Fisher, Phys. Rev. B **40**, 546 (1989).
- [18] D. Jaksch, C. Bruder, J. I. Cirac, C. W. Gardiner, and P. Zoller, Phys. Rev. Lett. **81**, 3108 (1998).
- [19] M. Greiner, O. Mandel, T. Esslinger, T. W. Hänsch, and I. Bloch, Nature **415**, 39 (2002).
- [20] C. J. Pethick and H. Smith, *Bose-Einstein condensation in dilute gases*, Cambridge university press, 2008.
- [21] H. A. Gersch and G. C. Knollman, Phys. Rev. **129**, 959 (1963).

## BIBLIOGRAPHY

---

- [22] J. Hubbard and B. H. Flowers, Proceedings of the Royal Society of London. Series A. Mathematical and Physical Sciences **276**, 238 (1963).
- [23] I. Bloch, J. Dalibard, and W. Zwerger, Rev. Mod. Phys. **80**, 885 (2008).
- [24] H. Feshbach, Annals of Physics **5**, 357 (1958).
- [25] K. Sheshadri, H. R. Krishnamurthy, R. Pandit, and T. V. Ramakrishnan, Europhysics Letters (EPL) **22**, 257 (1993).
- [26] J. K. Freericks and H. Monien, Europhysics Letters (EPL) **26**, 545 (1994).
- [27] S. Will, T. Best, U. Schneider, L. Hackermüller, D.-S. Lühmann, and I. Bloch, Nature **465**, 197 (2010).
- [28] M. J. Mark, E. Haller, K. Lauber, J. G. Danzl, A. J. Daley, and H.-C. Nägerl, Phys. Rev. Lett. **107**, 175301 (2011).
- [29] A. J. Daley, J. M. Taylor, S. Diehl, M. Baranov, and P. Zoller, Phys. Rev. Lett. **102**, 040402 (2009).
- [30] L. Bonnes and S. Wessel, Phys. Rev. Lett. **106**, 185302 (2011).
- [31] M. Singh, A. Dhar, T. Mishra, R. V. Pai, and B. P. Das, Phys. Rev. A **85**, 051604 (2012).
- [32] B.-l. Chen, X.-b. Huang, S.-p. Kou, and Y. Zhang, Phys. Rev. A **78**, 043603 (2008).
- [33] T. Sowiński, Phys. Rev. A **85**, 065601 (2012).
- [34] T. Sowiński, R. W. Chhajlany, O. Dutta, L. Tagliacozzo, and M. Lewenstein, Phys. Rev. A **92**, 043615 (2015).
- [35] A. Safavi-Naini, J. von Stecher, B. Capogrosso-Sansone, and S. T. Rittenhouse, Phys. Rev. Lett. **109**, 135302 (2012).
- [36] S. Ejima, F. Lange, H. Fehske, F. Gebhard, and K. z. Münster, Phys. Rev. A **88**, 063625 (2013).
- [37] J. Silva-Valencia and A. Souza, Eur. Phys. J. B **85**, 161 (2012).
- [38] C. Avila, R. Franco, A. Souza, M. Figueira, and J. Silva-Valencia, Physics Letters A **378**, 3233 (2014).
- [39] A. F. Hincapie-F, R. Franco, and J. Silva-Valencia, Phys. Rev. A **94**, 033623 (2016).
- [40] J. Silva-Valencia and A. M. C. Souza, Phys. Rev. A **84**, 065601 (2011).
- [41] T. Sowiński, Central European Journal of Physics **12**, 473 (2014).
- [42] A. Safavi-Naini, J. von Stecher, B. Capogrosso-Sansone, and S. T. Rittenhouse, Phys. Rev. Lett. **109**, 135302 (2012).
- [43] F. Dalfovo, S. Giorgini, L. P. Pitaevskii, and S. Stringari, Rev. Mod. Phys. **71**, 463 (1999).
- [44] M. Singh, T. Mishra, R. V. Pai, and B. P. Das, Phys. Rev. A **90**, 013625 (2014).
- [45] Y.-C. Chen, K.-K. Ng, and M.-F. Yang, Phys. Rev. B **84**, 092503 (2011).
- [46] P. R. Johnson, E. Tiesinga, J. V. Porto, and C. J. Williams, New Journal of Physics **11**, 093022 (2009).
- [47] A. J. Daley and J. Simon, Phys. Rev. A **89**, 053619 (2014).
- [48] D. S. Petrov, Phys. Rev. A **90**, 021601 (2014).
- [49] D. S. Petrov, Phys. Rev. Lett. **112**, 103201 (2014).
- [50] C. Trefzger, C. Menotti, B. Capogrosso-Sansone, and M. Lewenstein, Journal of

- Physics B: Atomic, Molecular and Optical Physics **44**, 193001 (2011).
- [51] A. Griesmaier, J. Werner, S. Hensler, J. Stuhler, and T. Pfau, Phys. Rev. Lett. **94**, 160401 (2005).
- [52] M. Lu, N. Q. Burdick, S. H. Youn, and B. L. Lev, Phys. Rev. Lett. **107**, 190401 (2011).
- [53] K. Aikawa, A. Frisch, M. Mark, S. Baier, A. Rietzler, R. Grimm, and F. Ferlaino, Phys. Rev. Lett. **108**, 210401 (2012).
- [54] M. Saffman, T. G. Walker, and K. Mølmer, Rev. Mod. Phys. **82**, 2313 (2010).
- [55] T. F. Gallagher and P. Pillet, *Dipole–Dipole Interactions of Rydberg Atoms*, volume 56 of *Advances in Atomic, Molecular, and Optical Physics*, pages 161–218, Academic Press, 2008.
- [56] J. B. Balewski et al., Nature **502**, 664 (2013).
- [57] J. B. Balewski, A. T. Krupp, A. Gaj, S. Hofferberth, R. Löw, and T. Pfau, New Journal of Physics **16**, 063012 (2014).
- [58] N. Henkel, R. Nath, and T. Pohl, Phys. Rev. Lett. **104**, 195302 (2010).
- [59] G. Pupillo, A. Micheli, M. Boninsegni, I. Lesanovsky, and P. Zoller, Phys. Rev. Lett. **104**, 223002 (2010).
- [60] B. Yan et al., Nature **501**, 521 (2013).
- [61] A. de Paz et al., Phys. Rev. Lett. **111**, 185305 (2013).
- [62] O. Dutta et al., Reports on Progress in Physics **78**, 066001 (2015).
- [63] T. Lahaye, C. Menotti, L. Santos, M. Lewenstein, and T. Pfau, Reports on Progress in Physics **72**, 126401 (2009).
- [64] H. Weimer, M. Müller, I. Lesanovsky, P. Zoller, and H. P. Büchler, Nature Physics **6**, 382 (2010).
- [65] H. Weimer, M. Müller, H. P. Büchler, and I. Lesanovsky, Quantum Information Processing **10**, 885 (2011).
- [66] S. Baier et al., Science **352**, 201 (2016).
- [67] E. H. Lieb and D. W. Robinson, Comm. Math. Phys. **28**, 251 (1972).
- [68] S. Bravyi, M. B. Hastings, and F. Verstraete, Phys. Rev. Lett. **97**, 050401 (2006).
- [69] M. B. Hastings and T. Koma, Communications in Mathematical Physics **265**, 781 (2006).
- [70] M. Greiner, O. Mandel, T. W. Hänsch, and I. Bloch, Nature **419**, 51 (2002).
- [71] S. Trotzky, Y.-A. Chen, A. Flesch, I. P. McCulloch, U. Schollwöck, J. Eisert, and I. Bloch, Nature Physics **8**, 325 (2012).
- [72] S. Braun et al., Proceedings of the National Academy of Sciences **112**, 3641 (2015).
- [73] W. S. Bakr et al., Science **329**, 547 (2010).
- [74] M. Cheneau et al., Nature **481**, 484 (2012).
- [75] U. Schneider et al., Nature Physics **8**, 213 (2012).
- [76] J. P. Ronzheimer et al., Phys. Rev. Lett. **110**, 205301 (2013).
- [77] D. Chen, M. White, C. Borries, and B. DeMarco, Phys. Rev. Lett. **106**, 235304 (2011).
- [78] S. Trotzky et al., Nature Physics **6**, 998 (2010).

## BIBLIOGRAPHY

---

- [79] T. Esslinger, Annual Review of Condensed Matter Physics **1**, 129 (2010).
- [80] D. Pertot et al., Phys. Rev. Lett. **113**, 170403 (2014).
- [81] F. Meinert, M. J. Mark, E. Kirilov, K. Lauber, P. Weinmann, A. J. Daley, and H.-C. Nägerl, Phys. Rev. Lett. **111**, 053003 (2013).
- [82] C. Weitenberg et al., Nature **471**, 319 (2011).
- [83] Y. Wang, X. Zhang, T. A. Corcovilos, A. Kumar, and D. S. Weiss, Phys. Rev. Lett. **115**, 043003 (2015).
- [84] N. Strohmaier, Y. Takasu, K. Günter, R. Jördens, M. Köhl, H. Moritz, and T. Esslinger, Phys. Rev. Lett. **99**, 220601 (2007).
- [85] Y. Aharonov, L. Davidovich, and N. Zagury, Phys. Rev. A **48**, 1687 (1993).
- [86] S. E. Venegas-Andraca, Quantum Information Processing **11**, 1015 (2012).
- [87] A. M. Childs, D. Gosset, and Z. Webb, Science **339**, 791 (2013).
- [88] A. M. Childs, Phys. Rev. Lett. **102**, 180501 (2009).
- [89] A. Ambainis, A. Baćkurs, N. Nahimovs, R. Ozols, and A. Rivosh, Search by quantum walks on two-dimensional grid without amplitude amplification, in *Theory of Quantum Computation, Communication, and Cryptography*, edited by K. Iwama, Y. Kawano, and M. Murao, pages 87–97, Berlin, Heidelberg, 2013, Springer Berlin Heidelberg.
- [90] A. Ambainis, A. Backurs, N. Nahimovs, R. Ozols, and A. Rivosh, arXiv e-prints , arXiv:1112.3337 (2011).
- [91] N. B. Lovett, S. Cooper, M. Everitt, M. Trevers, and V. Kendon, Phys. Rev. A **81**, 042330 (2010).
- [92] M. S. Underwood and D. L. Feder, Phys. Rev. A **82**, 042304 (2010).
- [93] E. Farhi and S. Gutmann, Phys. Rev. A **58**, 915 (1998).
- [94] A. Ambainis, Quantum walk algorithm for element distinctness, in *45th Annual IEEE Symposium on Foundations of Computer Science*, pages 22–31, 2004.
- [95] A. Ambainis, International Journal of Quantum Information **01**, 507 (2003).
- [96] N. Shenvi, J. Kempe, and K. B. Whaley, Phys. Rev. A **67**, 052307 (2003).
- [97] R. Yao and J. Zakrzewski, arXiv:2007.04745 (2020).
- [98] D. Wiater, T. Sowiński, and J. Zakrzewski, Phys. Rev. A **96**, 043629 (2017).
- [99] D. L. Shepelyansky, Phys. Rev. Lett. **73**, 2607 (1994).
- [100] H. Schmitz, R. Matjeschk, C. Schneider, J. Glueckert, M. Enderlein, T. Huber, and T. Schaetz, Phys. Rev. Lett. **103**, 090504 (2009).
- [101] F. Zähringer, G. Kirchmair, R. Gerritsma, E. Solano, R. Blatt, and C. F. Roos, Phys. Rev. Lett. **104**, 100503 (2010).
- [102] M. Karski, L. Förster, J.-M. Choi, A. Steffen, W. Alt, D. Meschede, and A. Widera, Science **325**, 174 (2009).
- [103] T. Fukuhara, P. Schauß, M. Endres, S. Hild, M. Cheneau, I. Bloch, and C. Gross, Nature **502**, 76 EP (2013).
- [104] K. Manouchehri and J. Wang, Physical Implementation of Quantum Walks, Springer (2014).

- [105] S. Hoyer, M. Sarovar, and K. B. Whaley, New Journal of Physics **12**, 065041 (2010).
- [106] M. Mohseni, P. Rebentrost, S. Lloyd, and A. Aspuru-Guzik, The Journal of Chemical Physics **129**, 174106 (2008).
- [107] C. M. Chandrashekar, arXiv e-prints , arXiv:1001.5326 (2010).
- [108] O. Mülken and A. Blumen, Phys. Rev. E **71**, 036128 (2005).
- [109] X.-P. Xu, Phys. Rev. E **77**, 061127 (2008).
- [110] A. Wójcik, T. Luczak, P. Kurzyński, A. Grudka, and M. Bednarska, Phys. Rev. Lett. **93**, 180601 (2004).
- [111] K. v. Klitzing, G. Dorda, and M. Pepper, Phys. Rev. Lett. **45**, 494 (1980).
- [112] K. von Klitzing, Rev. Mod. Phys. **58**, 519 (1986).
- [113] D. C. Tsui, H. L. Stormer, and A. C. Gossard, Phys. Rev. Lett. **48**, 1559 (1982).
- [114] M. Z. Hasan and C. L. Kane, Rev. Mod. Phys. **82**, 3045 (2010).
- [115] X.-L. Qi and S.-C. Zhang, Rev. Mod. Phys. **83**, 1057 (2011).
- [116] E. J. Bergholtz and Z. Liu, International Journal of Modern Physics B **27**, 1330017 (2013).
- [117] Y. Ando, Journal of the Physical Society of Japan **82**, 102001 (2013).
- [118] C.-Z. Chang et al., Science **340**, 167 (2013).
- [119] D. Hsieh, D. Qian, L. Wray, Y. Xia, Y. S. Hor, R. J. Cava, and M. Z. Hasan, Nature **452**, 970 (2008).
- [120] Y. Xia et al., Nature Physics **5**, 398 (2009).
- [121] D.-W. Zhang, Y.-Q. Zhu, Y. X. Zhao, H. Yan, and S.-L. Zhu, Advances in Physics **67**, 253 (2018).
- [122] M. Aidelsburger, S. Nascimbene, and N. Goldman, Comptes Rendus Physique **19**, 394 (2018).
- [123] H. Zhai, Reports on Progress in Physics **78**, 026001 (2015).
- [124] J. Dalibard, *Introduction to the physics of artificial gauge fields*, volume 191, Quantum Matter at Ultralow Temperatures, edited by M. Inguscio, W. Ketterle, and S. Stringari (IOS Press), 2016.
- [125] W. P. Su, J. R. Schrieffer, and A. J. Heeger, Phys. Rev. Lett. **42**, 1698 (1979).
- [126] J. Asbóth, L. Oroszlány, and A. Pálvi, *A Short Course on Topological Insulators: Band Structure and Edge States in One and Two Dimensions*, Springer International Publishing, 2016.
- [127] J. Zak, Phys. Rev. Lett. **62**, 2747 (1989).
- [128] K. Sheshadri, H. R. Krishnamurthy, R. Pandit, and T. V. Ramakrishnan, Europhysics Letters (EPL) **22**, 257 (1993).
- [129] T. McIntosh, P. Pisarski, R. J. Gooding, and E. Zaremba, Phys. Rev. A **86**, 013623 (2012).
- [130] D. Yamamoto, A. Masaki, and I. Danshita, Phys. Rev. B **86**, 054516 (2012).
- [131] S. R. Hassan and L. de' Medici, Phys. Rev. B **81**, 035106 (2010).
- [132] M. Singh, S. Greschner, and T. Mishra, Phys. Rev. A **98**, 023615 (2018).
- [133] I. Affleck, T. Kennedy, E. H. Lieb, and H. Tasaki, Phys. Rev. Lett. **59**, 799 (1987).
- [134] I. Affleck, T. Kennedy, E. H. Lieb, and H. Tasaki, Communications in Mathematical

## BIBLIOGRAPHY

---

- Physics **115**, 477 (1988).
- [135] M. Fannes, B. Nachtergael, and R. F. Werner, Europhysics Letters (EPL) **10**, 633 (1989).
- [136] U. Schollwöck, Annals of Physics **326**, 96 (2011).
- [137] S. R. White, Phys. Rev. Lett. **69**, 2863 (1992).
- [138] U. Schollwöck, Rev. Mod. Phys. **77**, 259 (2005).
- [139] E. Jeckelmann, Computational Many-Particle Physics, Springer , 597 (2008).
- [140] P. Pippal, S. R. White, and H. G. Evertz, Phys. Rev. B **81**, 081103 (2010).
- [141] I. P. McCulloch, arXiv e-prints , arXiv:0804.2509 (2008).
- [142] G. Vidal, Phys. Rev. Lett. **98**, 070201 (2007).
- [143] S. Yan, D. A. Huse, and S. R. White, Science **332**, 1173 (2011).
- [144] S. Depenbrock, I. P. McCulloch, and U. Schollwöck, Phys. Rev. Lett. **109**, 067201 (2012).
- [145] M. A. Cazalilla and J. B. Marston, Phys. Rev. Lett. **88**, 256403 (2002).
- [146] M. A. Cazalilla and J. B. Marston, Phys. Rev. Lett. **91**, 049702 (2003).
- [147] H. G. Luo, T. Xiang, and X. Q. Wang, Phys. Rev. Lett. **91**, 049701 (2003).
- [148] G. Vidal, Phys. Rev. Lett. **91**, 147902 (2003).
- [149] G. Vidal, Phys. Rev. Lett. **93**, 040502 (2004).
- [150] M. Suzuki, Progress of Theoretical Physics **56**, 1454 (1976).
- [151] H. F. Trotter, P. Am. Math. Soc **10**, 545 (1959).
- [152] P. Calabrese and J. Cardy, Journal of Statistical Mechanics: Theory and Experiment **2005**, P04010 (2005).
- [153] K. Winkler et al., Nature **441**, 853 (2006).
- [154] A. Tomadin, V. Giovannetti, R. Fazio, D. Gerace, I. Carusotto, H. E. Türeci, and A. Imamoglu, Phys. Rev. A **81**, 061801 (2010).
- [155] J. Jordan, R. Orús, G. Vidal, F. Verstraete, and J. I. Cirac, Phys. Rev. Lett. **101**, 250602 (2008).
- [156] F. Verstraete and J. I. Cirac, arXiv e-prints , cond (2004).
- [157] P. Corboz, R. Orús, B. Bauer, and G. Vidal, Phys. Rev. B **81**, 165104 (2010).
- [158] H. J. Liao et al., Phys. Rev. Lett. **118**, 137202 (2017).
- [159] T. Picot and D. Poilblanc, Phys. Rev. B **91**, 064415 (2015).
- [160] T. Picot, M. Ziegler, R. Orús, and D. Poilblanc, Phys. Rev. B **93**, 060407 (2016).
- [161] A. Kshetrimayum, T. Picot, R. Orús, and D. Poilblanc, Phys. Rev. B **94**, 235146 (2016).
- [162] A. Kshetrimayum, C. Balz, B. Lake, and J. Eisert, arXiv e-prints , arXiv:1904.00028 (2019).
- [163] C. Boos, S. P. G. Crone, I. A. Niesen, P. Corboz, K. P. Schmidt, and F. Mila, Phys. Rev. B **100**, 140413 (2019).
- [164] C. Boos, S. P. G. Crone, I. A. Niesen, P. Corboz, K. P. Schmidt, and F. Mila, arXiv e-prints , arXiv:1903.07887 (2019).
- [165] P. Corboz, Phys. Rev. B **93**, 045116 (2016).
- [166] P. Corboz, T. M. Rice, and M. Troyer, Phys. Rev. Lett. **113**, 046402 (2014).

## BIBLIOGRAPHY

---

- [167] A. Kshetrimayum, H. Weimer, and R. Orús, *Nature Communications* **8**, 1291 (2017).
- [168] P. Czarnik, L. Cincio, and J. Dziarmaga, *Phys. Rev. B* **86**, 245101 (2012).
- [169] P. Czarnik and J. Dziarmaga, *Phys. Rev. B* **92**, 035152 (2015).
- [170] P. Czarnik, M. M. Rams, and J. Dziarmaga, *Phys. Rev. B* **94**, 235142 (2016).
- [171] A. Kshetrimayum, M. Rizzi, J. Eisert, and R. Orús, *Phys. Rev. Lett.* **122**, 070502 (2019).
- [172] C. Hubig and J. I. Cirac, *SciPost Phys.* **6**, 31 (2019).
- [173] P. Czarnik, J. Dziarmaga, and P. Corboz, *Phys. Rev. B* **99**, 035115 (2019).
- [174] A. Kshetrimayum, M. Goihl, and J. Eisert, arXiv e-prints , arXiv:1910.11359 (2019).
- [175] A. Kshetrimayum, M. Goihl, D. M. Kennes, and J. Eisert, arXiv e-prints , arXiv:2004.07267 (2020).
- [176] H. C. Jiang, Z. Y. Weng, and T. Xiang, *Phys. Rev. Lett.* **101**, 090603 (2008).
- [177] M. Singh, S. Mondal, B. K. Sahoo, and T. Mishra, *Phys. Rev. A* **96**, 053604 (2017).
- [178] O. Jürgensen, F. Meinert, M. J. Mark, H.-C. Nägerl, and D.-S. Lühmann, *Phys. Rev. Lett.* **113**, 193003 (2014).
- [179] D.-S. Lühmann, O. Jürgensen, and K. Sengstock, *New Journal of Physics* **14**, 033021 (2012).
- [180] T. Kinoshita, T. Wenger, and D. S. Weiss, *Science* **305**, 1125 (2004).
- [181] M. A. Cazalilla, R. Citro, T. Giamarchi, E. Orignac, and M. Rigol, *Rev. Mod. Phys.* **83**, 1405 (2011).
- [182] L. Bonnes, Quantum phase transitions in constrained bose systems, 2011.
- [183] M. A. Baranov, M. Dalmonte, G. Pupillo, and P. Zoller, *Chemical Reviews* **112**, 5012 (2012).
- [184] A. Argüelles and L. Santos, *Phys. Rev. A* **75**, 053613 (2007).
- [185] C. Trefzger, C. Menotti, and M. Lewenstein, *Phys. Rev. Lett.* **103**, 035304 (2009).
- [186] T. Giamarchi, *Quantum physics in one dimension*, volume 121, Clarendon press, 2003.
- [187] M. S. Luthra, T. Mishra, R. V. Pai, and B. P. Das, *Phys. Rev. B* **78**, 165104 (2008).
- [188] M. A. Cazalilla, A. F. Ho, and T. Giamarchi, *New Journal of Physics* **8**, 158 (2006).
- [189] D. C. Johnston, J. W. Johnson, D. P. Goshorn, and A. J. Jacobson, *Phys. Rev. B* **35**, 219 (1987).
- [190] M. Azuma, Z. Hiroi, M. Takano, K. Ishida, and Y. Kitaoka, *Phys. Rev. Lett.* **73**, 3463 (1994).
- [191] E. Dagotto, *Reports on Progress in Physics* **62**, 1525 (1999).
- [192] I. Danshita, J. E. Williams, C. A. R. Sá de Melo, and C. W. Clark, *Phys. Rev. A* **76**, 043606 (2007).
- [193] E. Altman, W. Hofstetter, E. Demler, and M. D. Lukin, *New Journal of Physics* **5**, 113 (2003).
- [194] A. Kuklov, N. Prokof'ev, and B. Svistunov, *Phys. Rev. Lett.* **92**, 050402 (2004).
- [195] M. Lewenstein, L. Santos, M. A. Baranov, and H. Fehrmann, *Phys. Rev. Lett.* **92**, 050401 (2004).
- [196] T. Mishra, R. V. Pai, and B. P. Das, *Phys. Rev. A* **76**, 013604 (2007).

## BIBLIOGRAPHY

---

- [197] T. Mishra, B. K. Sahoo, and R. V. Pai, Phys. Rev. A **78**, 013632 (2008).
- [198] T. Mishra, R. V. Pai, and B. P. Das, Phys. Rev. B **81**, 024503 (2010).
- [199] L. Mathey, Phys. Rev. B **75**, 144510 (2007).
- [200] I. Titvinidze, M. Snoek, and W. Hofstetter, Phys. Rev. Lett. **100**, 100401 (2008).
- [201] M. Iskin and C. A. R. S. de Melo, Phys. Rev. Lett. **99**, 080403 (2007).
- [202] G.-H. Chen and Y.-S. Wu, Phys. Rev. A **67**, 013606 (2003).
- [203] K. Günter, T. Stöferle, H. Moritz, M. Köhl, and T. Esslinger, Phys. Rev. Lett. **96**, 180402 (2006).
- [204] S. Ospelkaus, C. Ospelkaus, O. Wille, M. Succo, P. Ernst, K. Sengstock, and K. Bongs, Phys. Rev. Lett. **96**, 180403 (2006).
- [205] T. Best, S. Will, U. Schneider, L. Hackermüller, D. van Oosten, I. Bloch, and D.-S. Lühmann, Phys. Rev. Lett. **102**, 030408 (2009).
- [206] J. Catani, L. De Sarlo, G. Barontini, F. Minardi, and M. Inguscio, Phys. Rev. A **77**, 011603 (2008).
- [207] B. Gadway, D. Pertot, R. Reimann, and D. Schneble, Phys. Rev. Lett. **105**, 045303 (2010).
- [208] M. Taglieber, A.-C. Voigt, T. Aoki, T. W. Hänsch, and K. Dieckmann, Phys. Rev. Lett. **100**, 010401 (2008).
- [209] S. Sugawa, K. Inaba, S. Taie, R. Yamazaki, M. Yamashita, and Y. Takahashi, Nature Physics **7**, 642 (2011).
- [210] R. Islam, R. Ma, P. M. Preiss, M. Eric Tai, A. Lukin, M. Rispoli, and M. Greiner, Nature **528**, 77 (2015).
- [211] J. Simon, W. S. Bakr, R. Ma, M. E. Tai, P. M. Preiss, and M. Greiner, Nature **472**, 307 (2011).
- [212] M. Miranda, R. Inoue, N. Tambo, and M. Kozuma, Phys. Rev. A **96**, 043626 (2017).
- [213] P. M. Preiss et al., Science **347**, 1229 (2015).
- [214] A. Peruzzo et al., Science **329**, 1500 (2010).
- [215] Y. Lahini, M. Verbin, S. D. Huber, Y. Bromberg, R. Pugatch, and Y. Silberberg, Phys. Rev. A **86**, 011603 (2012).
- [216] Y. Ye et al., Phys. Rev. Lett. **123**, 050502 (2019).
- [217] Z. Yan et al., Science **364**, 753 (2019).
- [218] Y. Bromberg, Y. Lahini, R. Morandotti, and Y. Silberberg, Phys. Rev. Lett. **102**, 253904 (2009).
- [219] L. Sansoni, F. Sciarrino, G. Vallone, P. Mataloni, A. Crespi, R. Ramponi, and R. Osellame, Phys. Rev. Lett. **108**, 010502 (2012).
- [220] M. A. Broome, A. Fedrizzi, S. Rahimi-Keshari, J. Dove, S. Aaronson, T. C. Ralph, and A. G. White, Science **339**, 794 (2013).
- [221] J. B. Spring et al., Science **339**, 798 (2013).
- [222] M. Tillmann, B. Dakic, R. Heilmann, S. Nolte, A. Szameit, and P. Walther, Nature Photonics **7**, 540 EP (2013).
- [223] A. Crespi et al., Nature Photonics **7**, 545 EP (2013).
- [224] M. Ben Dahan, E. Peik, J. Reichel, Y. Castin, and C. Salomon, Phys. Rev. Lett.

- 76**, 4508 (1996).
- [225] D. Jaschke, M. L. Wall, and L. D. Carr, Computer Physics Communications **225**, 59 (2018).
- [226] A. Müller-Hermes, J. I. Cirac, and M. C. Bañuls, New Journal of Physics **14**, 075003 (2012).
- [227] W. S. Dias, E. M. Nascimento, M. L. Lyra, and F. A. B. F. de Moura, Phys. Rev. B **76**, 155124 (2007).
- [228] R. Khomeriki, D. O. Krimer, M. Haque, and S. Flach, Phys. Rev. A **81**, 065601 (2010).
- [229] M. Singh, S. Greschner, and T. Mishra, Phys. Rev. A **98**, 023615 (2018).
- [230] S. Mondal, A. Kshetrimayum, and T. Mishra, arXiv e-prints , arXiv:2002.11317 (2020).
- [231] T. Mishra, R. V. Pai, S. Ramanan, M. S. Luthra, and B. P. Das, Phys. Rev. A **80**, 043614 (2009).
- [232] M. Hafezi, P. Adhikari, and J. M. Taylor, Phys. Rev. B **90**, 060503 (2014).
- [233] I. B. Spielman, W. D. Phillips, and J. V. Porto, Phys. Rev. Lett. **98**, 080404 (2007).
- [234] D. van Oosten, P. van der Straten, and H. T. C. Stoof, Phys. Rev. A **63**, 053601 (2001).
- [235] G. Vidal, Phys. Rev. Lett. **93**, 040502 (2004).
- [236] J. Sebby-Strabley, M. Anderlini, P. S. Jessen, and J. V. Porto, Phys. Rev. A **73**, 033605 (2006).
- [237] J. Sebby-Strabley, B. L. Brown, M. Anderlini, P. J. Lee, W. D. Phillips, J. V. Porto, and P. R. Johnson, Phys. Rev. Lett. **98**, 200405 (2007).
- [238] Cruz, G J, Franco, R, and Silva-Valencia, J, Journal of Physics: Conference Series **687**, 012065 (2016).
- [239] M. Greiner, O. Mandel, T. Esslinger, T. W. Hänsch, and I. Bloch, Nature **415**, 39 (2002).
- [240] J. Sebby-Strabley, B. L. Brown, M. Anderlini, P. J. Lee, W. D. Phillips, J. V. Porto, and P. R. Johnson, Phys. Rev. Lett. **98**, 200405 (2007).
- [241] Anderlini Marco, Lee Patricia J., Brown Benjamin L., Sebby-Strabley Jennifer, Phillips William D., and Porto J. V., Nature **448**, 452 (2007).
- [242] F. Grusdt, M. Höning, and M. Fleischhauer, Phys. Rev. Lett. **110**, 260405 (2013).
- [243] M. Di Liberto, A. Recati, I. Carusotto, and C. Menotti, Phys. Rev. A **94**, 062704 (2016).
- [244] M. Di Liberto, A. Recati, I. Carusotto, and C. Menotti, The European Physical Journal Special Topics **226**, 2751 (2017).
- [245] M. Singh, A. Dhar, T. Mishra, R. V. Pai, and B. P. Das, Phys. Rev. A **85**, 051604 (2012).
- [246] S.-J. Gu, Int. J. Mod. Phys. B **24**, 4371 (2010).
- [247] A. Dhar, M. Maji, T. Mishra, R. V. Pai, S. Mukerjee, and A. Paramekanti, Phys. Rev. A **85**, 041602 (2012).

## BIBLIOGRAPHY

---

- [248] S. Greschner, L. Santos, and T. Vekua, Phys. Rev. A **87**, 033609 (2013).
- [249] D. Muth, A. Mering, and M. Fleischhauer, Phys. Rev. A **77**, 043618 (2008).
- [250] D. González-Cuadra, P. R. Grzybowski, A. Dauphin, and M. Lewenstein, Phys. Rev. Lett. **121**, 090402 (2018).
- [251] D. González-Cuadra, A. Dauphin, P. R. Grzybowski, P. Wójcik, M. Lewenstein, and A. Bermudez, arXiv preprint arXiv:1811.08392 (2018).
- [252] T. Yoshida, R. Peters, S. Fujimoto, and N. Kawakami, Phys. Rev. Lett. **112**, 196404 (2014).
- [253] T. Yoshida, I. Danshita, R. Peters, and N. Kawakami, Phys. Rev. Lett. **121**, 025301 (2018).
- [254] C. Schweizer, M. Lohse, R. Citro, and I. Bloch, Phys. Rev. Lett. **117**, 170405 (2016).
- [255] S. Nakajima et al., Nature Physics **12**, 296 (2016).
- [256] Y. E. Kraus, Y. Lahini, Z. Ringel, M. Verbin, and O. Zilberberg, Phys. Rev. Lett. **109**, 106402 (2012).
- [257] M. Nakagawa, T. Yoshida, R. Peters, and N. Kawakami, Phys. Rev. B **98**, 115147 (2018).
- [258] J. K. Jain, Phys. Rev. Lett. **63**, 199 (1989).
- [259] B. I. Halperin, P. A. Lee, and N. Read, Phys. Rev. B **47**, 7312 (1993).
- [260] S. Ryu and Y. Hatsugai, Phys. Rev. Lett. **89**, 077002 (2002).
- [261] P. Delplace, D. Ullmo, and G. Montambaux, Phys. Rev. B **84**, 195452 (2011).
- [262] L.-J. Lang, X. Cai, and S. Chen, Phys. Rev. Lett. **108**, 220401 (2012).
- [263] S. R. Manmana, A. M. Essin, R. M. Noack, and V. Gurarie, Phys. Rev. B **86**, 205119 (2012).
- [264] M. Atala, M. Aidelsburger, J. T. Barreiro, D. Abanin, T. Kitagawa, E. Demler, and I. Bloch, Nature Physics **9**, 795 (2013).
- [265] S. de Léséleuc et al., Science **365**, 775 (2019).
- [266] G. Magnifico, D. Vodola, E. Ercolessi, S. Kumar, M. Müller, and A. Bermudez, Phys. Rev. D **99**, 014503 (2019).
- [267] C. Bardyn, M. Baranov, C. Kraus, E. Rico, A. İmamoğlu, P. Zoller, and S. Diehl, New Journal of Physics **15**, 085001 (2013).
- [268] C.-E. Bardyn, L. Wawer, A. Altland, M. Fleischhauer, and S. Diehl, Physical Review X **8**, 011035 (2018).
- [269] M. Heyl and J. Budich, Physical Review B **96**, 180304 (2017).
- [270] D. Thouless, Phys. Rev. B **27**, 6083 (1983).
- [271] M. Rice and E. Mele, Phys. Rev. Lett. **49**, 1455 (1982).
- [272] Lohse M., Schweizer C., Zilberberg O., Aidelsburger M., and Bloch I., Nature Physics **12**, 350 (2015).
- [273] M. Lohse, C. Schweizer, H. M. Price, O. Zilberberg, and I. Bloch, Nature **553**, 55 (2018).
- [274] E. Berg, M. Levin, and E. Altman, Phys. Rev. Lett. **106**, 110405 (2011).
- [275] L. Taddia, E. Cornfeld, D. Rossini, L. Mazza, E. Sela, and R. Fazio, Phys. Rev. Lett. **118**, 230402 (2017).

## BIBLIOGRAPHY

---

- [276] A. Hayward, C. Schweizer, M. Lohse, M. Aidelsburger, and F. Heidrich-Meisner, arXiv preprint arXiv:1810.07043 (2018).
- [277] L. Barbiero, L. Santos, and N. Goldman, Phys. Rev. B **97**, 201115 (2018).
- [278] Y. Kuno, K. Shimizu, and I. Ichinose, New Journal of Physics **19**, 123025 (2017).
- [279] J. Zak, Phys. Rev. Lett. **62**, 2747 (1989).
- [280] A. J. Daley, J. M. Taylor, S. Diehl, M. Baranov, and P. Zoller, Phys. Rev. Lett. **102**, 040402 (2009).
- [281] T. Mishra, J. Carrasquilla, and M. Rigol, Phys. Rev. B **84**, 115135 (2011).
- [282] M. Dalmonte, J. Carrasquilla, L. Taddia, E. Ercolessi, and M. Rigol, Phys. Rev. B **91**, 165136 (2015).
- [283] P. Calabrese and J. Cardy, Journal of Statistical Mechanics: Theory and Experiment **2004**, P06002 (2004).
- [284] C. L. Kane and E. J. Mele, Physical review letters **95**, 146802 (2005).
- [285] Q. Niu and D. J. Thouless, Journal of Physics A: Mathematical and General **17**, 2453 (1984).
- [286] A. J. Daley, J. M. Taylor, S. Diehl, M. Baranov, and P. Zoller, Phys. Rev. Lett. **102**, 040402 (2009).
- [287] S. Greschner and L. Santos, Physical review letters **115**, 053002 (2015).
- [288] B. Yang et al., arXiv preprint arXiv:1901.01146 (2019).
- [289] D. Petrosyan, B. Schmidt, J. R. Anglin, and M. Fleischhauer, Phys. Rev. A **76**, 033606 (2007).
- [290] N. J. Robinson et al., Phys. Rev. Lett. **122**, 027201 (2019).
- [291] Sebastian Will, Thorsten Best, Ulrich Schneider, Lucia Hackermüller, Dirk-Sören Lühmann, and Immanuel Bloch, Nature **465**, 197 (2010).
- [292] E. J. Meier, F. A. An, A. Dauphin, M. Maffei, P. Massignan, T. L. Hughes, and B. Gadway, Science **362**, 929 (2018).
- [293] F. Cardano et al., Nature Communications **8**, 15516 (2017).
- [294] D. Xie, W. Gou, T. Xiao, B. Gadway, and B. Yan, npj Quantum Information **5**, 55 (2019).
- [295] D. Xie, T.-S. Deng, T. Xiao, W. Gou, T. Chen, W. Yi, and B. Yan, Phys. Rev. Lett. **124**, 050502 (2020).
- [296] S. Greschner, S. Mondal, and T. Mishra, Phys. Rev. A **101**, 053630 (2020).
- [297] A. Haller, P. Massignan, and M. Rizzi, Phys. Rev. Research **2**, 033200 (2020).
- [298] P. Soltan-Panahi et al., Nature Physics **7**, 434 (2011).
- [299] B. Yang, H.-N. Dai, H. Sun, A. Reingruber, Z.-S. Yuan, and J.-W. Pan, Phys. Rev. A **96**, 011602 (2017).
- [300] Y. He, K. Wright, S. Kouachi, and C.-C. Chien, Phys. Rev. A **97**, 023618 (2018).
- [301] Y. He and C.-C. Chien, arXiv e-prints , arXiv:2007.02468 (2020).
- [302] M. Maffei, A. Dauphin, F. Cardano, M. Lewenstein, and P. Massignan, New Journal of Physics **20**, 013023 (2018).

## BIBLIOGRAPHY

---

# **Curriculum Vitae**

### **Address**

Home Address : Hanskhali, Nadia, West Bengal, India, 741505

Phone : +91 9800069494

Email : suman.m@iitg.ac.in

### **Personal profile**

Date of Birth : 19/02/1993

Place of Birth : Hanskhali

Gender : Male

Marital Status : Unmarried

Nationality : Indian

Language : Bengali, English, Hindi

### **Education**

B.Sc (2010-2013) : Srikrishna College, University of Kalyani

M.Sc (2013-2015) : University of Kalyani

Ph.D (Enrolled in 2016) : Indian Institute of Technology Guwahati

Earned the Senior Research Fellowship in 2018 by Indian Institute of Technology Guwahati.

Graduate Aptitude Test in Engineering (GATE) qualified in 2016.

National Eligibility Test (NET) qualified in 2016(CSIR Fellow).